A Study of Field Electron Emission From Composite Micro-Regimes.

MARWAN SULEIMAN MOUSA B.Sc. , M.Sc.

A Thesis submitted for the Degree of Doctor of Philosophy.

The University of Aston in Birmingham.

October, 1984.

I dedicate this thesis

to my family

who supported me patiently

during the course of this work.

The University of Aston in Birmingham

A Study of Field Electron Emission from Composite Micro-Regimes

Marwan Suleiman Mousa B.Sc., M.Sc.

A Thesis submitted for the Degree of Doctor of Philosophy, 1984.

SUMMARY

An experimental study has been made of the field emission of electrons from various composite microemitters. The majority of the work has been carried out using electrolytically etched tungsten micropoints, coated with 0.04 - 0.2 μ m thick layers of various insulating materials (e.g. epoxylite resin, hydrocarbon, lacomit).

The aim of the investigation was two-fold: firstly, to identify a hot-electron emission mechanism resulting from field penetration in the insulating film. Secondly, to evaluate the performance of such devices as practical electron sources.

The radius of the substrate micropoint and the thickness of the insulating overlayers were measured in a transmission electron microscope; the current-voltage characteristics and emission images were studied with a field emission microscope, whilst an advanced Van Oostrom retarding potential analyser was used to measure the energy spectra of the composite emitters. In general, virgin emitters initially switched-on at fields of 3×10^{8} - 3×10^{9} V m^{-1} , depending on the insulating film thickness, to give smooth reversible current-voltage characteristics, obeying the Fowler-Nordheim equation at low fields and saturating at high fields. The emission images generally consisted of a small single-spot, i.e. corresponding to a high source brightness, while the electron energy spectra were shifted by $\gtrsim$ 0.2 e V from the cathode Fermi level and had half-widths of $\geq$ 0.2 e V, with both parameters increasing with applied field. These findings have been explained in terms of a hot-electron emission mechanism involving the creation of a conducting channel in the insulating layer.

Key words: Field Electron Emission. Electron Spectroscopy. Hot-Electron Emission. Metal-Insulator Electron Microsource.

CONTENTS

		Page No.
	Title Page	1
	Dedication	2
	Summary	3
	List of Contents	4
	List of Figures	7
	List of Tables	13
1.	INTRODUCTION	14
2.	THERMIONIC AND FIELD ELECTRON EMISSION	17
2.1	Introduction	17
2.2	Electron Emission from Metals	17
2.2.1	Thermionic Emission	17
2.2.2	Field Assisted Thermionic Emission	20
2.2.3	Field Electron Emission	22
2.2.3.1	The Fowler-Nordheim Theory	24
2.2.3.2	Total Energy Distribution of Field Emitted Electrons	27
2.3	Field Electron Emission from Semiconductors- Theoretical Models	32
2.4	Field Emission from Composite Metal-Semiconductor/ Insulator Micro-Regimes	45
2.4.1	Hot-Electron Model	46
2.4.2	Conducting Filament Model	50
2.4.3	Revised Hot-Electron Model	54
3.	EXPERIMENTAL STUDIES OF FIELD ELECTRON EMISSION FROM COMPOSITE MICROPOINT EMITTERS	62
3.1	Introduction	62
3.2	Emitter Fabrication Techniques	63
3.2.1	Coated Tungsten Micropoint Emitters	63
3.2.1.1	Aluminium Oxide Coating	65
3.2.1.2	Miscellaneous Coatings (Wax, Zinc Oxide, Plastic and Araldite Resin)	68

		Page No.
3.2.1.3	Lacomit Coating	68
3.2.1.4	Epoxylite Resin Coating	69
3.2.1.5	Hydrocarbon Coating	78
3.2.2	Metal-Glass Emitters	82
3.2.2.1	Tungsten Micropoint Emitters Coated with Glass	82
3.2.2.2	Extrusion of Internally-Conducting Glass Capillary tubes	84
3.3	Development of a High Resolution Electron Spectrometer	88
3.3.1	Instrumental Design	88
3.3.1.1	Electron Spectrometer Systems	88
3.3.1.2	Spectrometer Design	91
3.3.1.3	Specimen Holder and Manipulator	104
3.3.1.4	Electronic Systems	109
3.3.2	Instrumental Performance	120
3.3.2.1	Optimising the Resolution	121
3.3.2.2	Energy Calibration	124
3.4	Ancillary Field Emission Microscope Facility	126
4.	EXPERIMENTAL RESULTS	131
4.1	Introduction	131
4.2	Current-Voltage Characteristics	131
4.2.1	Typical Behaviour of Composite Emitters	132
4.2.2	Resin-Coated Tungsten Emitters	134
4.2.3	Collated Data from a Selection of Composite Emitting Structures	145
4.2.4	Atypical Emission Characteristics	149
4.3	Emission Images of Composite Emitters	156
4.3.1	Axially-Symmetrical Single-Spot Images	156
4.3.2	Multiple-Spot Images	161
4.4	Electron Energy Spectra of Composite Emitters	169
4.4.1	Spectra of Single-Spot Sources	169

Page No.

4.4.2	Spectra of Multi-Spot Sources	170
4.5	Effect of Ion Beam Etching	175
5.	DISCUSSION	177
5.1	Introduction	177
5.2	Technological Implications	179
5.2.1	The Field Emission Electron Source	180
5.2.1.1	Background and Development	180
5.2.1.2	Emitter Types and Recent Advances	182
5.2.1.3	Uses and Applications	187
5.2.2	A Comparison of the Performance of Composite Micro-Emitters with that of Conventional Metallic Micropoint Emitters	188
5.2.2.1	Source Brightness	188
5.2.2.2	Emission Images	189
5.2.2.3	Emission Current	190
5.2.2.4	Stability	191
5.2.2.5	Energy Spread of Emitted Electrons	191
5.2.2.6	Life-Time	192
5.2.2.7	Emitter Profile	193
5.2.2.8	Ease of Fabrication	194
5.3	Theoretical Implications	194
6.	CONCLUSION	204
6.1	Principal Experimental Conclusions	204
6.2	Future Work	206
	References	210
	Acknowledgements	221
	Appendix	222

LIST OF FIGURES

Figure No.		Page No.
2.1	The energy model for a metal at 0 K with energy levels filled up to the Fermi level F.L..	18
2.2	The surface potential barrier and Schottky effect.	21
2.3	A schematic representation of the quantum mechanical tunnelling whereby a field emitted electron escapes from the surface of a metal.	25
2.4	Typical Fowler-Nordheim plot for a metallic emitter.	28
2.5	Theoretical and experimental total-energy distributions of field-emitted electrons at room temperature. The theoretical normal-energy distribution is shown for comparison. All three curves are arbitrarily normalized.	31
2.6	The energy band schematic diagrams for (a) Insulator (b) Semiconductor and (c) Metal.	34
2.7	The Fermi function f_{FD} for an n-type intrinsic and an extrinsic semiconductor.	35
2.8	The conduction band bending at the semiconductor/vacuum interface (a) due to low field penetration (b) shows the effect of high field (c) energy diagram showing an internal potential drop (ΔV_R) due to field penetration and bulk resistivity. Where $ - E_f$ is the Fermi energy of bulk material.	37
2.9	Surface states of germanium according to Handler's model.	41
2.10	The bands bending (a) upwards when field applied to the semiconductor = 0 (b) downwards when field applied to the semiconductor $\gg 0$.	41
2.11	Theoretical energy spectra according to Modinos.	43
2.12	Typical energy distribution from the center of the (100) facet of Ge. Clean, annealed end form.	44
2.13	(a) Electron energy spectra obtained from (i) a reference tungsten micropoint emitter, and (ii) an emission site on a broad-area copper electrode: in both cases, the spectra are referred to the Fermi level FL of the substrate cathode. (b) Electron energy spectra from a site on a broad-area copper-chromium specimen at 293 K (——) showing single-or double-peak characteristics; for comparison, --- shows the distribution from a clean tungsten emitter. FL represents the position of the Fermi level in the bulk	47

Figure No.		Page No.
	of the electrode.	
2.14	(a) A one-dimensional diagram of a composite surface consisting of a metal substrate and an overlaying semiconducting microstructure. $\emptyset$ and FL are respectively the work-function and Fermi level of the metal substrate. The --- indicates the position of the Fermi level, which is continuous between the metal and semiconductor. (b) The same one-dimensional energy diagram showing the effect of field penetration into the semiconducting layer and the proposed tunnelling mechanisms.	49
2.15	Spectra of radiation from typical K-spots.	51
2.16	Production of electroluminescence, vacuum breakdown and electron emission from electroformed conducting filaments in oxide impurities. (a) Electron emission. (b) Electroluminescence. (c) vacuum breakdown.	53
2.17	Energy band and surface barrier configurations of the metal-insulator micro-emitting regime under varying field conditions: (i) zero field; (ii) high field prior to switching and electron emission; (iii) high field stable electron emission regime.	56
2.18	Energy band configuration of the 'on' state of an electron emitting regime providing multi-peaked spectra.	58
2.19	Variation of the spectral shift and half-width (F.W.H.M.) with site current. □ represents the shift of the maximum of the energy distribution from the substrate Fermi level. o represents the half-width (F.W.H.M.) of the energy distribution.	60
3.1	The experimental apparatus used for electrolytically etching of tungsten micropoint emitters.	64
3.2	Stages in the etching process of a tungsten field emitter.	64
3.3	A scanning electron micrograph of an etched tungsten micropoint emitter.	65
3.4	Scanning electron micrographs of tungsten tip (a) before and (b) after coating with $\sim$4 microns of Alumina.	66
3.5	The anodising process in an electrolytic cell.	67
3.6	Optical micrograph of tungsten tip coated with a ball of Zinc oxide.	69
3.7	Micrographs of (a) tungsten tip covered with a ball of lacomit before baking (b) after baking to $\sim$ 200°C.	70

Figure No.		Page No.
3.8	(a) Optical micrograph of tungsten tip coated with a ball of resin (b) optical micrograph of the coated tip in (a) after ion beam etching.	72
3.9	Schematic diagram of the ion beam etching regime.	73
3.10	A diagram showing the T.E.M. electron beam falling on the tungsten tip coated with resin.	74
3.11	The modified specimen holder of the T.E.M.	75
3.12	Transmission electron micrographs of tungsten tip (a) before coating (b) after coating with a 0.06 μ m layer of resin.	76
3.13	Electron micrographs of tungsten tips coated with various thicknesses of resin.	77
3.14	Electron micrographs of (a) tungsten tip free from contamination (b) after been contaminated with hydrocarbon.	79
3.15	A sequence of micrographs showing the building of a hydrocarbon contaminate layer on a tungsten tip.	80
3.16	The X-ray energy spectra obtained from (a) the shank of the tungsten emitter (b) the contaminated tip.	81
3.17	(a) Schematic diagram of the specially designed system which provided means of extracting molten glass to cover the tungsten tip. (b) A micrograph of tungsten tip coated with glass.	83
3.18	(a) A schematic diagram of capillary glass tube pulling technique (b) the glass tube before being fixed into the puller (c) coated glass tips after the pulling process.	85
3.19	Glass tip before and after etching in hydrofluoric acid.	87
3.20	Optical micrograph of a glass tip with an internal film of electrodag.	87
3.21	The electrode configuration of a Van Oostrom retarding potential analyser where A is the anode with a phosphored screen P, L is the lens electrode, S is the earthed shield, C is the collector and O is the electron source.	92
3.22	Diagram showing the electron beam (e^-) trajectories due to field enhancement from the sharp point of the cathode and the equipotential lines (dotted) between cathode and anode.	93

Figure No.		Page No.
3.23	(a) A typical schematic integral plot showing the variation of the collector current Ic as a function of the cathode voltage Vc, and (b) its corresponding differential plot.	95
3.24	General section through spectrometer chamber.	97
3.25	A general exterior view of the spectrometer and the associated equipment.	99
3.26	A photograph showing a close-up view of the analyser.	101
3.27	A photograph showing a close-up view of the experimental chamber.	103
3.28	(a) The original specimen holder, (b) a standard electron microscope tungsten thermionic emitter with the required insulation and fittings for carrying the heating current, and (c) a 0.1 mm diameter tungsten microemitter, spot welded to a 0.2 mm diameter bridge wire.	105
3.29	Rotatable specimen holder, showing a 0.1 mm diameter tungsten microemitter fitted into a 0.11 mm stainless steel tube.	106
3.30	A photograph illustrating the specimen holder, the manipulator and the ancillary anode.	108
3.31	The circuit used to produce integral plots for field emitting sources (full line) and a thermionic electron source (chain-dotted lines).	110
3.32	The electrometer schematic diagram.	112
3.33	Ramp generator A and a unity gain inverting amplifier B. The signal generator SG is incorporated for modulating the ramp when a differential plot is required. (see section 3.3.1 4 (b)).	114
3.34	A negative going ramp at the output of integral circuit A.	116
3.35	A schematic plot representing the relationship between the integral and differential plots.	117
3.36	A circuit to produce automatically the differential plots for field emission.	119
3.37	A simplified block diagram of the lock-in amplifier.	120
3.38	(a) The integral plot obtained with a thermionic source and (b) the corresponding differential plot.	122

Figure No.		Page No.
3.39	A series of spectra taken at a range of temperatures from a thermionic emitter.	123
3.40	The calibration of the analyser using a tungsten field emitter with an associated thermionic emission (T ~ 2410 K); (N.B. The distributions are plotted on different energy scales).	125
3.41	A comparison of the electron energy spectra obtained from a tungsten emitter (a) before and (b) after coating with a 0.2 μ m thick layer of resin at identical emission currents of 2 μ A (FL = Fermi level of the substrate cathode).	128
3.42	Schematic diagram of a field emission microscope.	129
4.1	The general form of current-voltage (I-V characteristics of a composite emitter.	133
4.2	A comparison of the I-V characteristics of an uncoated tungsten emitter of tip radius ~38 nm (curve A), and that obtained after coating with a 0.2 μ m thick layer of epoxylite resin (curve B).	135
4.3	Fowler-Nordheim plots of the uncoated (curve A) and resin-coated (curve B) emitters whose I-V characteristics are presented in Fig. 4.2 .	137
4.4	The relation between the film coating thickness Δd and the tip switching field factor E_{SW} (α V_{SW} / r).	140
4.5	The relation between the film coating thickness Δd and the tip saturation field factor E_{SAT} (α V_{SAT} / r).	141
4.6	The relation between the film coatings of thickness Δd and the saturated current I_{SAT} .	142
4.7	I-V plot of 'type A' atypical behaviour.	150
4.8	I-V plot of 'type B' atypical behaviour.	151
4.9	I-V plot of 'type C' atypical behaviour.	152
4.10	I-V plot of 'type D' atypical behaviour.	153
4.11	I-V plot of 'type E' atypical behaviour.	154
4.12	Projector images obtained from (a) a clean tungsten emitter and (b) after coating with a 0.2 μ m layer of resin. Both images were recorded with the same tip-to-screen separation and the same emission current of 4.5 μ A.	157

Figure No.		Page No.
4.13	A T.E.M. micrograph of deformed tungsten microelectrode coated with resin after tip "explosion".	159
4.14	A sequence of projector images showing how the spot size changed with emission current.	160
4.15	A sequence of images showing emission originating from more than one sub-emission centre "before" and "after" various tip treatments.	162
4.16	A sequence of cine-film frames showing the change with time (t) in the multi-spot images of thin insulating layers.	164
4.17	Micrographs of internally conducting glass tip, where tip (1) (a) before exploding and (b) after exploding.	166
4.18	Micrographs showing glass tips (2 and 3) after exploding.	167
4.19	(a) Multi-spot emission image obtained from tungsten microemitter coated with 0.2 μ m resin coating (b) the same image after 24 hours relaxation process.	168
4.20	A sequence of spectra obtained from tungsten micro-emitter coated with 0.2 μ m resin, illustrating how the shift and half-width (F.W.H.M.) vary with the emission current (increasing from 1.1 μA to 4.5 μA).	172
4.21	Plot shows the variation of the spectral shift and the half-width (F.W.H.M.), with respect to the tungsten substrate Fermi level, with emission current.	173
4.22	The super impressed energy spectra recorded at constant applied voltage from the individual spots of the emission image shown in Fig. 4.15 .	174
5.1	Illustrating I_e variations and cyclical lifetime criterion, of constant applied potential.	182
5.2	A schematic illustration of how electron emission results from the formation of a conducting channel in the insulating layer. The associated electron field distribution is also shown.	196
5.3	A schematic illustration of how the divergent field associated with close proximity anode can lead to multi-spot images.	200
5.4	Schematic illustration of how the irregularities of the substrate tungsten emitter could lead to a non-uniform surface film and formation of more than one channel.	200

LIST OF TABLES

Table No.		Page No.
4.1	Emission data obtained from composite emitters having various thicknesses of a resin coating.	139
4.2	The collated experimental data obtained from three tungsten microemitters coated with similar thickness of resin (0.2 μ m) and baked at different temperatures.	144
4.3	Collated emission data obtained from a range of composite emitter regimes.	146
4.4	Collated experimental data from emitters exhibiting 'type C' atypical behaviour.	176

CHAPTER 1

INTRODUCTION

The investigation described in this thesis is concerned with the field emission of electrons from metal-insulator-vacuum (M.I.V.) systems, where field penetration in the insulating medium can give rise to hot electrons with sufficient energy to be emitted over the surface potential barrier. Thus, the emission mechanism can be thought of as a quasi thermionic process as described by the Richardson-Schottky model. The motivation for the project stems from recent studies of the microscopically localised field-induced electron emission processes that are responsible for the pre-breakdown currents that flow between vacuum-insulated high voltage electrodes [1,2], it has become evident that electrons can be "cold emitted" from dielectric-like micro-inclusions that are in intimate contact with the substrate metallic cathode or perhaps even partially embedded, at applied electric fields that are often two orders of magnitude lower than the threshold value of $\sim 3 \times 10^9$ V/m which is required for the well-known Fowler-Nordheim "metallic" field electron emission (F.E.E.) tunnelling mechanism [1]. Recently Latham [3] gave an explanation of this abnormal field emission in terms of a field-induced hot-electron emission (F.I.H.E.E.) mechanism involving a composite metal-insulator-vacuum emission regime. According to this model, the applied field penetrates the sub-micron thick dielectric region to the metal substrate producing bending in the band structure. Therefore, for any given micro-inclusion, there will be a critical field at which it will be possible for a stream of electrons to tunnel from the metal substrate into the conduction band of the inclusion. At fields in the range of 10 - 20 MV/m, it will initiate a "switching pro-

cess, where a conducting channel, or filament, is formed in the dielectric by a similar mechanism to that proposed by Dearnaley et al [4] and Adler et al [5] to explain the behaviour of metal-insulator-metal (M.I.M.) switching devices. However, the absence of the "top" metal electrode in the M.I.V. regime excludes the possibility of hole injection, and hence results in the existence of an ambient population of hot-electrons at the insulator vacuum interface, some of which will be able to be "thermionically" emitted over the surface potential barrier [6].

Whilst this model has been shown to provide a satisfactory explanation of typical experimental data [3], like the current-voltage characteristic and the field and temperature-dependence of the electron spectral half-width, it had not been subjected to any direct verification of its validity. Therefore, the present simulation study was undertaken in which it was hoped to replicate, under controlled conditions, the emission regime supposed to exist locally on the surface of high voltage broad area electrodes. Thus, techniques were developed for fabricating and testing composite microemitters, these consist of a metal substrate (mainly tungsten) of known microscopic profile, coated by a sub-micron thick layer of a suitable insulating material (e.g. epoxylite resin, hydrocarbon, lacomit). As will be described, the emission characteristics of these controlled emitters showed several striking similarities to those obtained from the naturally occuring emission processes: however, they also showed some significant and physically interesting differences.

A parallel, but equally important, objective of this study was to determine whether such composite emitters had any technological potential as a "cold" electron source for possible use in such commercial devices as cathode ray tubes [7], electron microscopes [8 - 10] etc.

Thus, their performance has been characterised in terms of such practical parameters as: electron beam brightness, energy spread, short and long-term current stability and emitter life time. From this data, it has also been possible to make a quantitative comparison of the emission characteristics of these composite emitters with other types of "cold emission" electron sources that are currently under development; e.g. carbon fibre [7, 11 - 13] and other micropoint emitter systems [14], M.I.M. hot-electron sources [15 -17], and negative affinity devices [18].

An experimental technique which formed an important part of the present study, was the measurement of the field electron energy distribution (F.E.E.D.) of the electrons emitted from the composite emitters, since this type of data provides valuable information about the basic emission mechanism. For this aspect of the work, it was necessary to develop a fully automated Van Oostrom retarding potential electron spectrometer. Several other techniques have also been developed for this investigation, either for use in conjunction with the spectrometer, or for subsidiary experiments. These include an ancillary field emission microscope facility, an ion beam etching technique to control the insulator coating thickness, and a special specimen holder for a Philips EM 200 transmission electron microscope for mounting the composite emitters and measuring the coating thickness and the radius of curvature of the substrate cathode. In addition a scanning electron microscope, together with its Kevex X - ray spectrometer facility, was extensively used for characterising emitters.

CHAPTER 2

THERMIONIC AND FIELD ELECTRON EMISSION

2.1 Introduction

As the main part of the work described in this thesis is concerned with the process of field electron emission, it was considered essential to include a review of the published literature regarding the theoretical and experimental aspects of field emission from metals, semiconductors and composite metal-semiconductor/insulator materials. However, as the work also includes a study of field-assisted thermionic emission, it was therefore thought appropriate to introduce this review with a brief account of the thermionic emission process. Furthermore, it will be seen later that the fundamental physical concepts associated with the thermionic emission mechanism, also play an important role in the hot-electron model that has been proposed to explain the field emission of electrons from composite emitters.

2.2 ELECTRON EMISSION FROM METALS

2.2.1 THERMIONIC EMISSION

The electric and magnetic properties of solids are mainly determined by the properties of the electrons in them [19]. Each electron has a definite energy and momentum, where the arrangement of the permitted energy levels of the electrons holds the key to the properties of solids. According to the free-electron model, which was introduced by Sommerfield in 1928 [20], it is assumed that the "free" electrons,

i.e. the valence electrons of the free atoms [19] which become detached in the condensed phase to create the conduction electrons [21], find themselves in a potential which is constant everywhere inside the metal. Since no significant electron emission is observed from metals at room temperature [22], it seems evident that the potential energy of an electron at rest inside the metal must be lower than that of an electron at rest outside the metal. This is confirmed by relatively simple theoretical arguments [23]. Now a physical model where the interior of the metal is represented by a potential energy box of depth E_o, is shown in Fig. 2.1. The Fermi energy, E_f, is the energy of the highest filled level in the ground state (i.e. at T = 0 K) [21], while the energy difference between E_o and E_f is known as the work function, ϕ, of the metal. The energy of an electron at rest outside the metal is used as a reference, and referred to as the vacuum level [22].

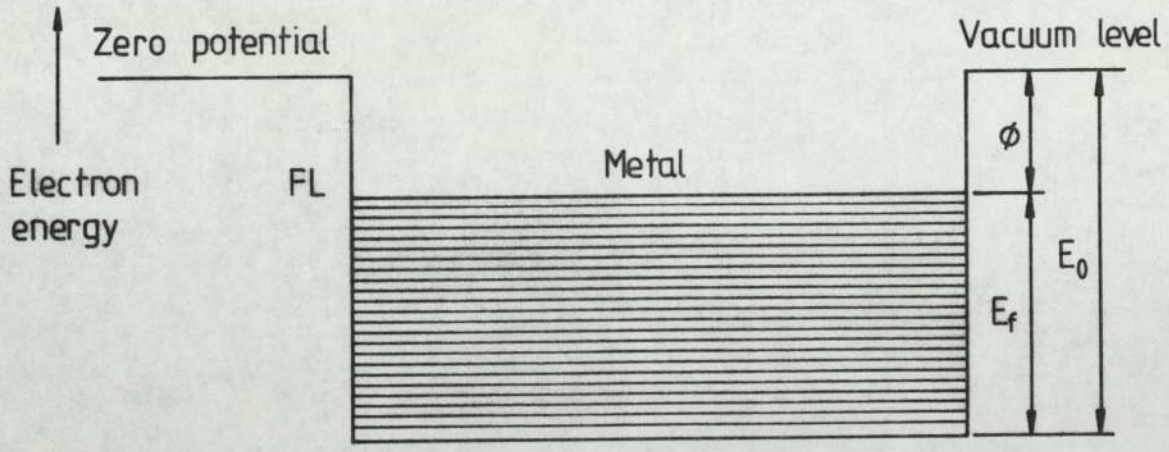

Fig. 2.1 The energy model for a metal at 0 K with energy levels filled up to the Fermi level FL .

When an electron inside a metal moves towards the boundary of the metal with sufficient energy ($\geq E_o$) to overcome the potential barrier, represented by the work function, the electron will be emitted over the barrier into the vacuum [24]. As the temperature of the metal increases the kinetic energy of the electron gas is increased [21], producing some occupied energy levels which were vacant at absolute zero. Because the probability that the electron will have sufficient energy to escape is strongly dependent on temperature, such electron emission is known as thermionic emission [24], and may be explained using the Fermi-Dirac statistics [25]. The emission current density is given by

$$J = e \int_{E_o = E_f + \phi}^{\infty} N(W)\, d\, W \qquad (2.1)$$

where N(W) is the supply function, and is equal to the number of electrons with the x component of their energy within the range W to W + d W, incident on the surface per unit area and time [26]. On substituting a suitable expression for N(W) and integrating, one obtains the Richardson equation [27]

$$J = A\, T^2 \exp\left(-\frac{\phi}{K\, T} \right) \qquad (2.2)$$

[24]

If account is taken of the possibility of reflection of the electron at the boundary (i.e. the potential barrier), equation (2.2) is modified to give the Richardson-Dushman equation,

$$J = A\, (1 - r)\, T^2 \exp\left(-\frac{\phi}{K\, T} \right) \qquad (2.3)$$

where r represents a suitable average of the reflection coefficient [28, 29], and A is a constant defined by,

$$A = \frac{4\, \pi e\, m\, k^2}{h^3} = 1.2 \times 10^6 \text{ A m}^{-2} \text{ K}^{-2}$$

where e, m, h and k have their usual significance, so that the ideal value of A appropriate to a perfect metal-vacuum interface is 1.2×10^6 $A\ m^{-2}\ K^{-2}$. Equation (2.3) gives the electron current that would start to flow if the sample is heated to a temperature T; it would however be limited by the negative space charge which will exist in the vicinity of the emitter, so that it is necessary for the anode potential to be sufficiently positive to prevent the build-up of space charge (22).

2.2.2 FIELD ASSISTED THERMIONIC EMISSION

The model described in the previous section can be further refined by including the effects of (a) the image force and (b) the electric field. Thus, when a metal is approached by an electron it will induce an image charge in its surface so that an attractive force will be exerted on the electron given by the well-known image force

$$\frac{e^2}{4\ \pi\varepsilon_o}\ \frac{1}{(\ 2\ x\ )^2}$$

where e is the electronic charge and x is the normal distance of the electron from the metal surface. This leads to a potential energy of the electron equal to

$$V_{image} = -\frac{e^2}{16\ \pi\varepsilon_o x}$$

which will only have a significant effect on the potential barrier at very close distances from the surface. If now the effects of both an external electric field and the image force are taken into account, the potentials will be added, leading to the modified potential barrier shown in Fig. 2.2 , where there is an apparent reduction $\Delta\phi$ in the

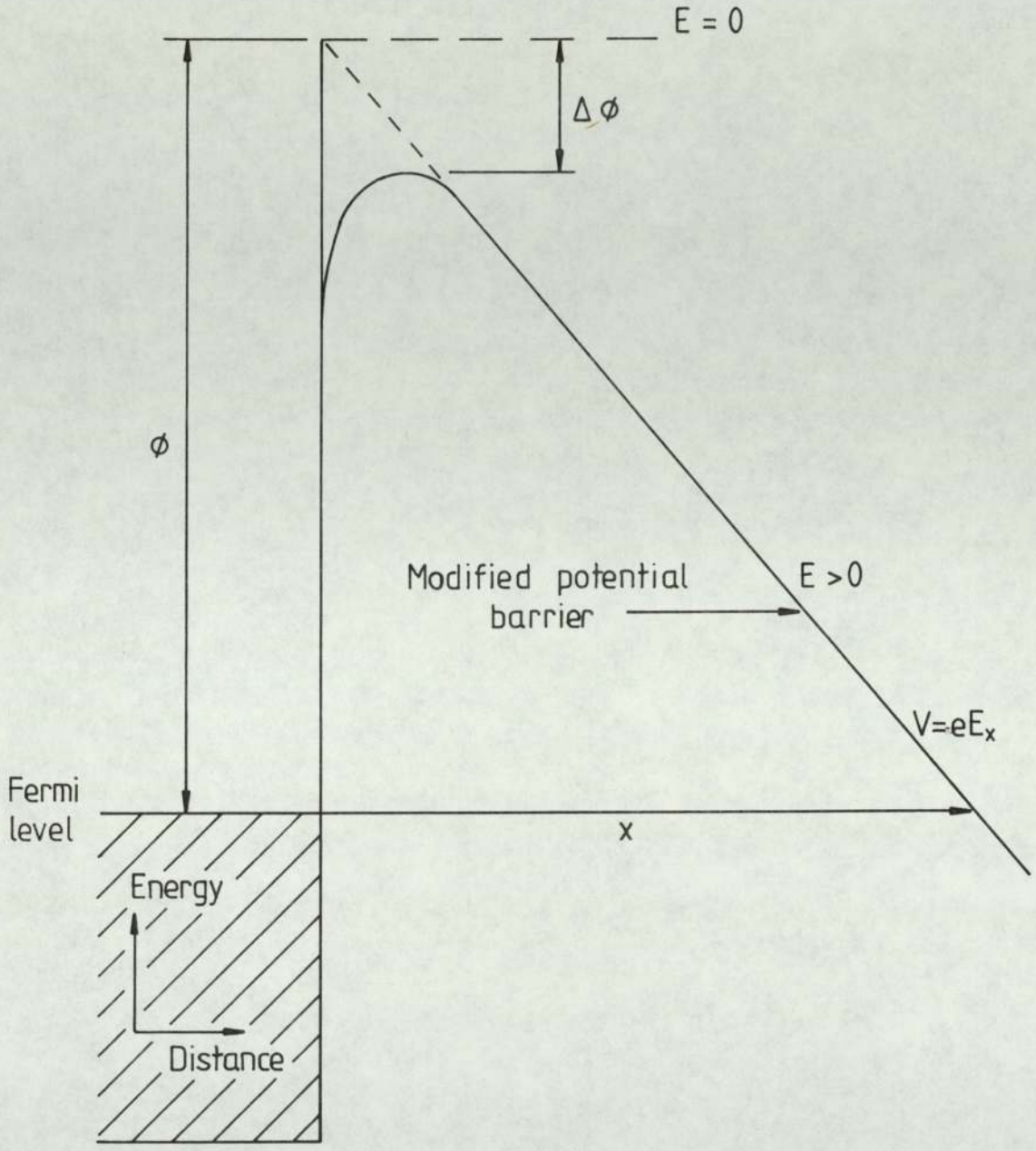

Fig. 2.2 The surface potential barrier and Schottky effect.

work function, which is a phenomenon known as the Schottky effect (30). Equation 2.2 now becomes,

$$J = A T^2 \exp - \left(\frac{\phi - \Delta\phi}{K T} \right)$$

$$= A T^2 \exp \left(- \frac{\phi}{K T} \right) \exp \left(\frac{\Delta\phi}{K T} \right) \qquad (2.4)$$

which, after substituting an expression for $\Delta\phi$ obtained from the image potential and external field, can be expressed as

$$J = A T^2 \exp \left(- \frac{\phi}{K T} \right) \exp - \frac{e^{3/2} E^{1/2}}{K T} \quad (31) \qquad (2.5)$$

Experimental studies confirming the validity of this model have been made for example, by Sommerfield and Bethe (32), Guth and Mullin (33), Dolan and Dyke (34), Dyke et al (35), and Murphy and Good (25).

2.2.3 FIELD ELECTRON EMISSION

It was shown in the previous section that, for an emitter at a high temperature, the presence of relatively low electric fields ($\lesssim 10^5$ V m^{-1}) will cause more electrons to escape over the reduced potential barrier and so enhance the total emission current (36). If the external electric field is increased to the very much higher value of $\gtrsim 10^9$ V m^{-1}, the potential barrier width Δx becomes so thin ($\lesssim 10^{-9}$ m) opposite the metal Fermi level that unexited electrons can tunnel through it, at constant energy, into the vacuum. In quantum mechanical terms, this corresponds to the situation where the barrier width is comparable to the de Broglie wavelength of the electrons near the Fermi level, so that the electron wave function ψ will still be finite on entering the vacuum; i.e. where there is a finite probability of an electron being at either side of the barrier. This condition

can be derived in terms of the Heisenberg uncertainty principal [37] which states that a knowledge of the momentum of an electron with an uncertainty Δp, necessarily implies an uncertainty in position Δx given by

$$\Delta p \quad \Delta x \simeq \hbar \qquad (2.6)$$

where $\hbar = h/2\pi$, h being Planck's constant. Thus, for electrons near the Fermi level, the uncertainty in their momentum corresponds to the barrier height, ϕ, i.e. $\Delta p = (2 m \phi)^{\frac{1}{2}}$, and from equation 2.6 the uncertainty in position will be

$$\Delta x \simeq \frac{\hbar}{\Delta p} = \frac{\hbar}{(2 m \phi)^{\frac{1}{2}}} \qquad (2.7)$$

It follows therefore that if Δx is of the order of the barrier width, there will be a good chance of finding an electron on the outside of the barrier. Neglecting the Schottky effect, and assuming the potential due to the field is equal to the work function at the Fermi level (see Fig. 2.2), the barrier width can be approximated by [37]

$$\Delta x = \frac{\phi}{e E} \qquad (2.8)$$

substituting for ϕ from equation (2.7) the required condition is

$$\Delta x \lesssim \frac{\hbar}{(2 m \phi)^{\frac{1}{2}}} \qquad (2.9)$$

or in terms of the field,

$$E \gtrsim (2 m)^{\frac{1}{2}} \frac{\phi^{3/2}}{e \hbar} \gtrsim 10^9 \text{ V m}^{-1} \qquad (2.10)$$

The first quantum mechanical treatment of field electron emission from metals was presented in 1928, by Fowler and Nordheim [26], and this will be described in detail in the next section. A review of field emission work up to 1956 and a full account of the Fowler-Nordheim theory was published by Good and Muller [38].

2.2.3.1 THE FOWLER-NORDHEIM THEORY

In this theory the field-dependent emission current density J is derived on the basis of the Sommerfield free-electron theory for the case of an ideal planar metal-vacuum interface. As previously discussed, the potential barrier close to the surface in the vacuum region consists of the classical image-force potential and a potential due to the high external applied electric field, and results in the modified potential barrier as shown in Fig. 2.3 . In the Fowler-Nordheim model, electrons from the bulk which are incident on the metal surface and obey Fermi-Dirac statistics, penetrate the potential barrier with a probability which is predicted by a solution of the Schrödinger equation. The derivation of an expression for J progresses in three distinct stages.

(1) The derivation of the electron supply function N(W) d W which gives the flux of electrons with the x-component of their energy within the range W + d W incident on the barrier from within the metal surface per second per unit area.

(2) The derivation of the electron transmission coefficient D(W) which gives the probability that an electron of energy W will be transmitted through the barrier. Thus, the number of electrons with energies in the range between W and W + d W tunnelling from the metal into the vacuum region, usually known as the normal energy distribution P(W) d W, is the product of the previous two functions, viz.

$$P(W)\ d\ W = N(W)\ D(W)\ d\ W$$

(3) The evaluation of the field electron emission current density J ($A\ m^{-2}$) which is the total number of electrons emitted per second per unit area in the energy range W to W + d W, integrated over all energies, and then multiplied by the electronic charge (e), i.e.

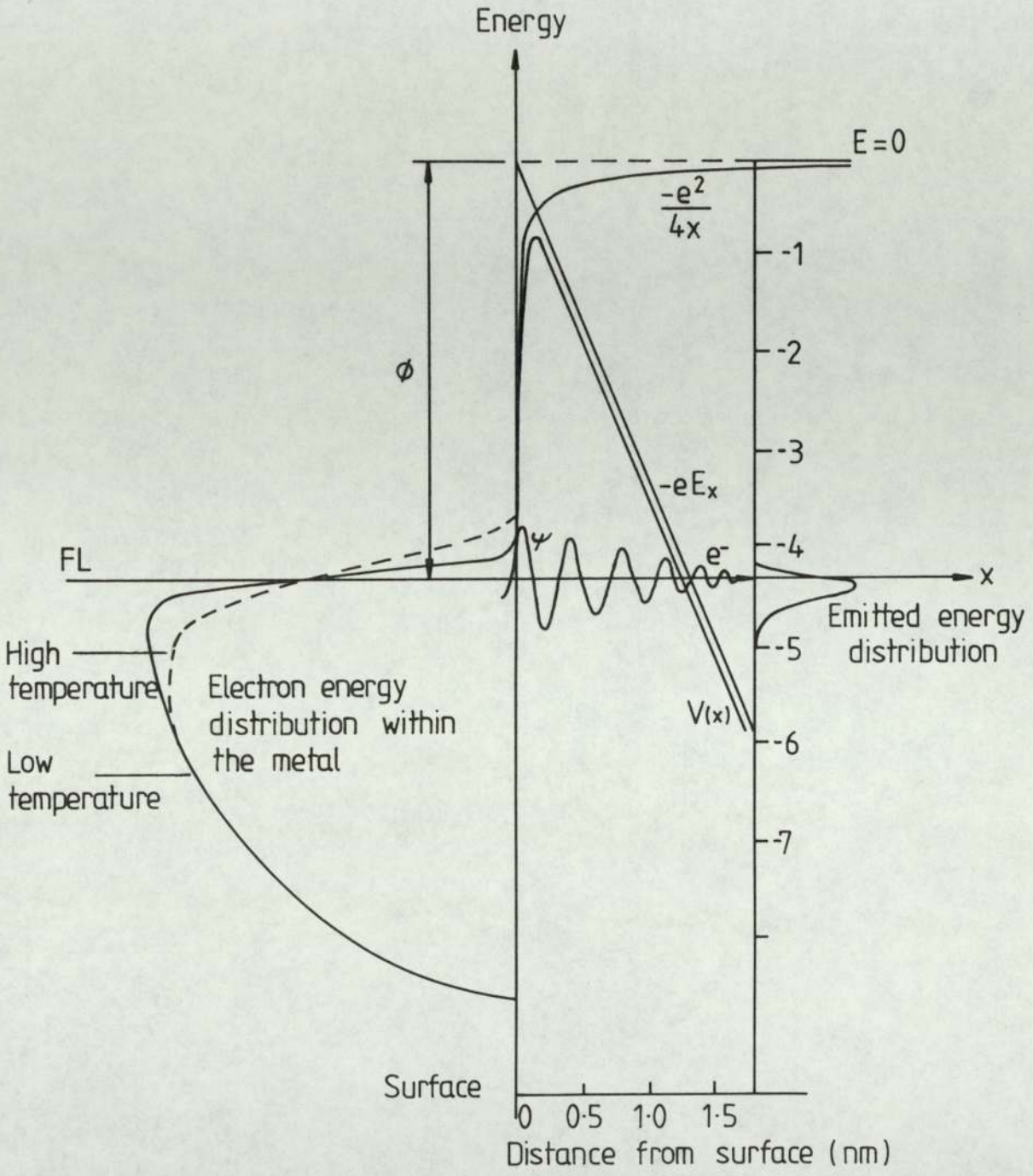

Fig. 2.3 A schematic representation of the quantum mechanical tunnelling mechanism whereby a field emitted electron escapes from the surface of a metal.

$$J = e \int_{\text{all energies}} p(W)\, d\, W \qquad (2.11)$$

For detailed evaluation of N(W), D(W) and the final integral, which is an extended and largely mathematical exercise [1], there are comprehensive modern treatments [38, 39].

At low temperature ($T \leq 300$ K) where few electron states above the Fermi level are occupied, as shown in Fig. 2.3, equation (2.11) leads to the standard Fowler-Nordheim equation

$$J = \frac{1.54 \times 10^{-6}\, E^2}{\phi\, t^2(y)} \exp\left(\frac{-6.83 \times 10^9\, \phi^{1.5}\, v(y)}{E} \right) \qquad (2.12)$$

where E is the surface electric field ($V\ m^{-1}$), ϕ is the work function of metal (e V), while t(y) and v(y) are tabulated dimensionless elliptic functions [38 - 40] of the parameter y given by

$$y = 3.79 \times 10^{-5} \frac{E^{\frac{1}{2}}}{\phi} \qquad (2.13)$$

In practice, t(y) is a slowly varying function of y and for stable field emission range

$$2 \times 10^9 < E < 6 \times 10^9\ V\ m^{-1}$$

$$t(y) \simeq 1 \qquad (2.14)$$

and
$$v(y) \simeq 0.956 - 1.062\, y^2 \qquad (2.15)$$

Thus by substituting the values from equations (2.13), (2.14) and (2.15) into equation (2.12) and taking logarithms, one has

$$\text{Log}\left(\frac{J}{E^2}\right) = \text{Log}\left(\frac{1.54 \times 10^{-6} \times 10^{4.52}\, \phi^{-\frac{1}{2}}}{\phi} \right) - \frac{2.84 \times 10^9\, \phi^{1.5}}{E} \qquad (2.16)$$

If the field acts over an emitting area A_e, then the emission current from this region will be $I = J A_e$, the Fowler-Nordheim equation can be written as,

$$J = A \frac{E^2}{\phi} \exp\left(\frac{-B\, \phi^{\frac{1}{2}}}{E} \right) \qquad (2.17)$$

where A and B are constants.

In 1940 Haefer [41] was the first to test the F-N theory for a point cathode and plane anode geometry. For this case the graph obtained by plotting Log (I/V^2) versus ($10^{-4}/V$), a typical example is shown in Fig. 2.4, is referred to as the Fowler-Nordheim plot, and is the generally accepted method of interpreting experimental observations of field emission from metals. The slope m at any point of the curve is given by

$$m = 2.84 \times 10^9 \, \phi^{1.5} \qquad (2.18)$$

and an intercept

$$c = \text{Log} \left(\frac{1.54 \times 10^{-6} \, A_e \, 10^{4.52 \, \phi^{-\frac{1}{2}}}}{\phi} \right) \qquad (2.19)$$

More recently, in 1953 Dyke et al [42, 43] used micro-point emitters with accurately measured geometry so that the microscopic cathode field could be well determined. The results they obtained were in good agreement with the F-N theory over several orders of magnitude of current density; departures from theory did however occur at high current densities, but these could be explained satisfactorily by taking into account the effects of space charge.

2.2.3.2 TOTAL ENERGY DISTRIBUTION OF FIELD EMITTED ELECTRONS

The earliest measurements of total energy distribution used retarding-potential analysers, where the different types will be discussed in detail in section 3.3.1.1 . Muller [44, 45] and later Muller and Bahadur [46], using a tungsten tip emitter with a spherical retarding-potential analyser, obtained good experimental agreement with the theoretical expression of Fowler-Nordheim for the normal energy distribution. Subsequently, Young and Muller [47], employing

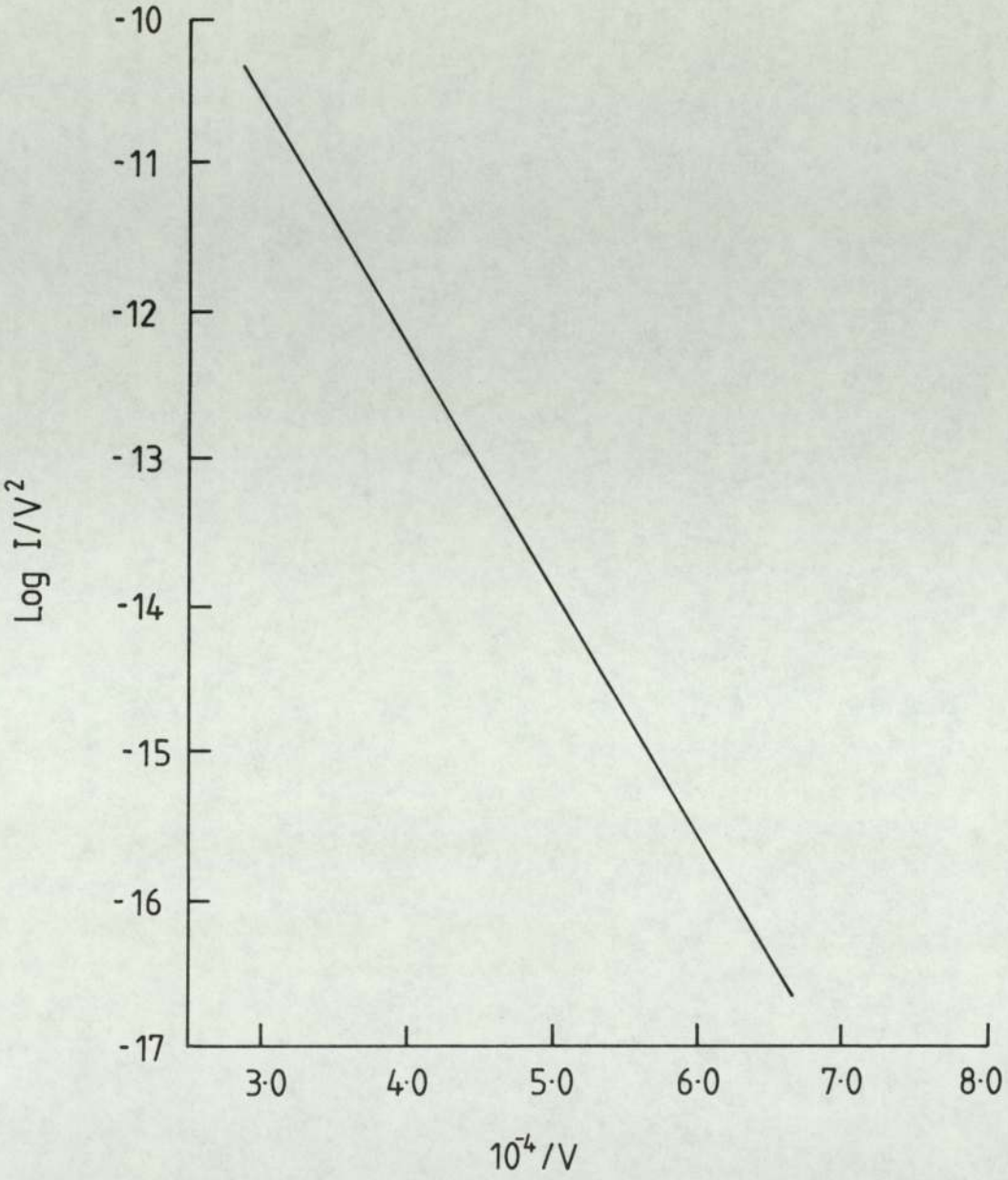

Fig. 2.4 Typical Fowler-Nordheim plot for a metallic emitter.

an improved high-resolution retarding analyser, obtained a much narrower energy distribution than that predicted by the F-N theory. To explain their findings, they had to make the following re-appraisal of the theoretical model used by Fowler and Nordheim:

It was stated earlier that the F-N equation (2.12) was obtained by integrating the normal energy distribution N(W) D(W) d W over all W. This is true for a plane parallel analysing geometry but, for the widely used spherical geometry, the transverse component of energy is conserved in the tunnelling process, but rapidly transferred to the direction of motion once the electron has left the emitter surface, which results in the emitted electrons being incident perpendicular on the collector surface. Therefore, the total rather than the normal energy of the electron is measured. Accordingly, Young (48) used the following reasoning to develop a theoretical expression for the total energy distribution that could be compared with experiment:

(1) The electron supply function N(W , E) d W d E is now equal to the number of electrons with total energy within the range E to E + d E, whose x-part lies in the range W to W + d W incident upon the surface per second per unit area.

(2) The electron transmission coefficient D(W) will be the same as that in the derivation of the normal energy distribution, so the product of N(W , E) D(W) gives the number of electrons in the given energy ranges penetrating the barrier, i.e.

$$P(W , E)\ d\ W\ d\ E = N(W , E)\ D(W)\ d\ W\ d\ E$$

Hence, the total energy distribution is given by

$$P(E)\ d\ E = \int_{W = E}^{W = -W_A} P(W , E)\ d\ W\ d\ E$$

where $-W_A$ is the potential energy within metal. The limit for $P(E)\,dE$ at $-W_A$ can be extended to $-\infty$, since the integrand is zero below $-W_A$, so that after integrating with respect to W one obtains

$$P(E)\,dE = \frac{4\pi m d}{h^3} \exp\left(-c - \frac{E_f}{d}\right) x \frac{\exp\left(\frac{E}{d}\right)}{\frac{(E - E_f)}{KT} + 1} dE \qquad (2.20)$$

where

$$c = \frac{4\,(2m\phi^3)^{\frac{1}{2}}}{3\hbar e F}\, v(y)$$

$$d = \frac{\hbar e F}{2\,(2m\phi)^{\frac{1}{2}}\, t(y)}$$

$\phi = -E_f$ = work function, and F is the electric field acting on the emitting surface while the other parameters are as defined in the previous section 2.2.3.1 .

(3) The field emission current density, J ($A\,m^{-2}$) is found by integrating over all E and multiplying by the electronic charge, so that

$$J = e\int_{-\infty}^{\infty} P(E)\,dE$$

which is the Fowler-Nordheim equation.

To illustrate the significance of the above discussion, Fig. 2.5 shows the total and normal energy distribution curves for two different temperatures, as obtained by Young and Muller [47] . The steeply rising edge of the zero-temperature curve gives the position of the Fermi level, while the exponential drop at lower energies is due to

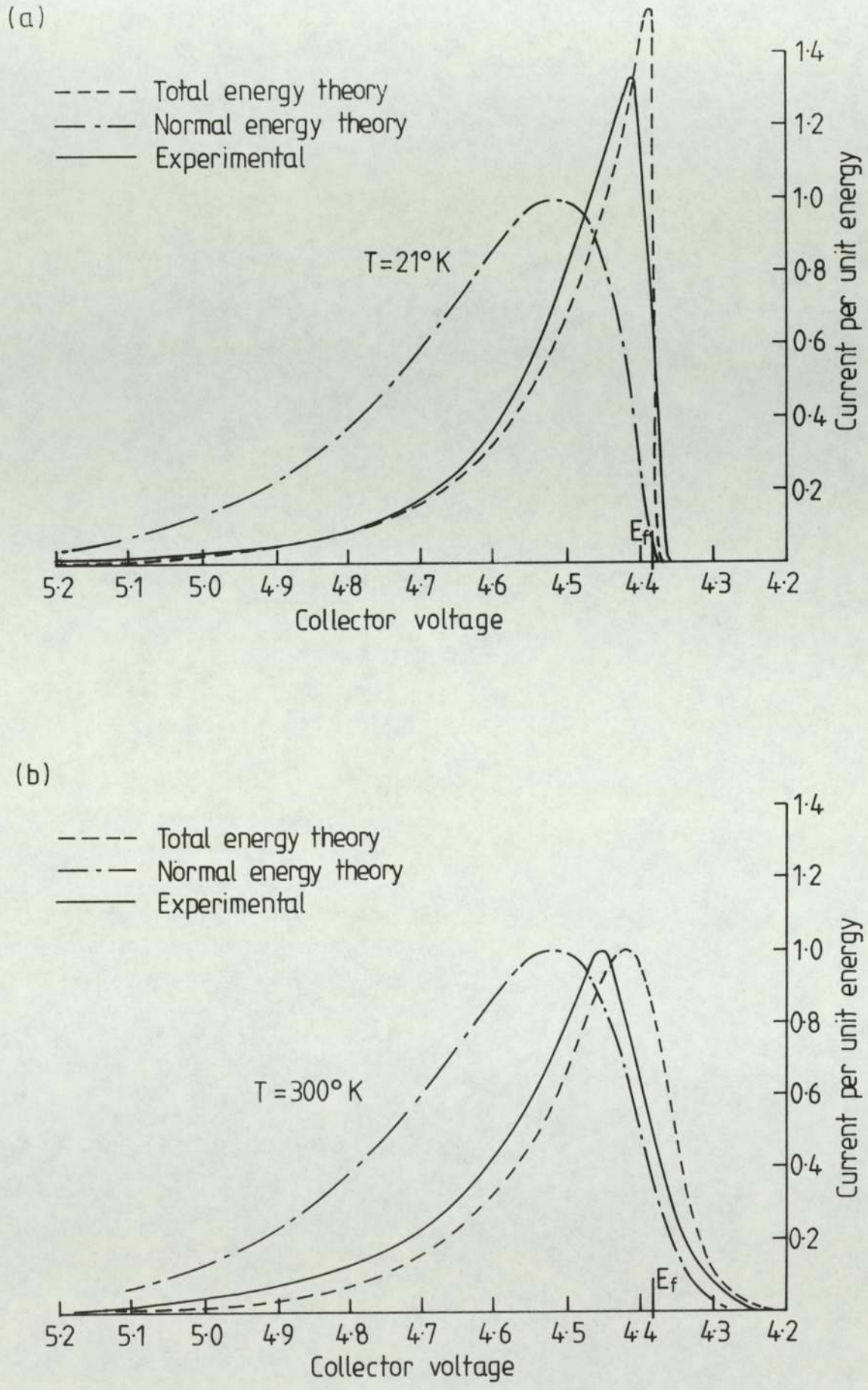

Fig. 2.5 Theoretical and experimental total-energy distributions of field-emitted electrons at room temperature. The theoretical normal-energy distribution is shown for comparison. All three curves are arbitrarily normalized. [47]

the decrease of barrier penetration probability. The maximum value of the total energy distribution E_{MAX} decreases rapidly with temperature, whereas the maximum value of the normal energy distribution remains constant over a wide temperature range. The value of E when P(E) is a maximum can be found by differentiating the exponential part of equation (2.20) with respect to E, which gives

$$E_{MAX} = E_f - K\,T\,Ln\,(\frac{d}{K\,T} - 1\,)$$

which reduces to $E_{MAX} = E_f$ when $T = 0\ K$

The full width at half maximum (F.W.H.M.) of the total energy distribution at zero temperature is found to be,

$$\delta(0) = 0.693\,d \qquad (\ 21\ )$$

2.3 FIELD ELECTRON EMISSION FROM SEMICONDUCTORS

Whilst the free-electron theory can satisfactorily explain most properties of metals, it cannot be applied to insulators and semiconductors. Accordingly, the nearly-free electron theory (or the band theory of solids as it is better known) is used, which is based on the concept that an electron moves in a periodic potential within a crystal. By solving the appropriate Shrödinger equation, the permitted energy states are obtained, but in this case they come out in "bands" of permitted states separated by "forbidden bands". The concept of energy bands is the basis for explaining the properties of semiconductors. It is therefore necessary to give a brief account about conductors, insulators and semiconductors before reviewing the theory of field emission from semiconductors. The schematic band diagrams

of an insulator, a metal and a semiconductor are represented in Fig. 2.6. Each band consists of a very large number of energy levels (one pair of levels for each atom in the crystal); but these overlap to form, in effect, a continuous band of available energies. At sufficiently low temperatures all the electrons will exist in the states of lowest possible energy, and will therefore fill, or partially fill, the lowest available energy band i.e. the valence band. In order to conduct an electric current, some of the valence electrons must be in an energy band which is only partly filled, as in the case of a metal, or alternatively, some electrons must be given sufficient energy to be excited from the valence band into the next lowest energy band, i.e. the conduction band. In the case of an insulator, there is a wide energy gap $\geqslant 4$ eV separating a filled valence band and an empty conduction band, so intrinsic conduction at room temperatures cannot occur. However, the most commonly used semiconductors at present are geranium and silicon [49] which are intrinsic semiconductors, with a small energy gap of 0.72 eV and 1.12 eV respectively. At room temperature therefore, a few electrons can be excited from the top of the valence band to the bottom of the conduction band, and thereby leaving a hole in the valence band. Thus, electrical conduction can take place by both electrons and holes. A rise in temperature increases the rate of production of electron-hole pairs and so increases the number of current carriers; so the conductivity of the semiconductor will increase. In an intrinsic semiconductor at 0 K all the states in the valence band are filled and all the states in the conduction band are empty, with the Fermi level lying midway between the valence band and the conduction band. However, when the temperature increases, the position of the Fermi level changes as shown in Fig. 2.7 (a). In the case of extrinsic semiconductors, say n-type, the corresponding

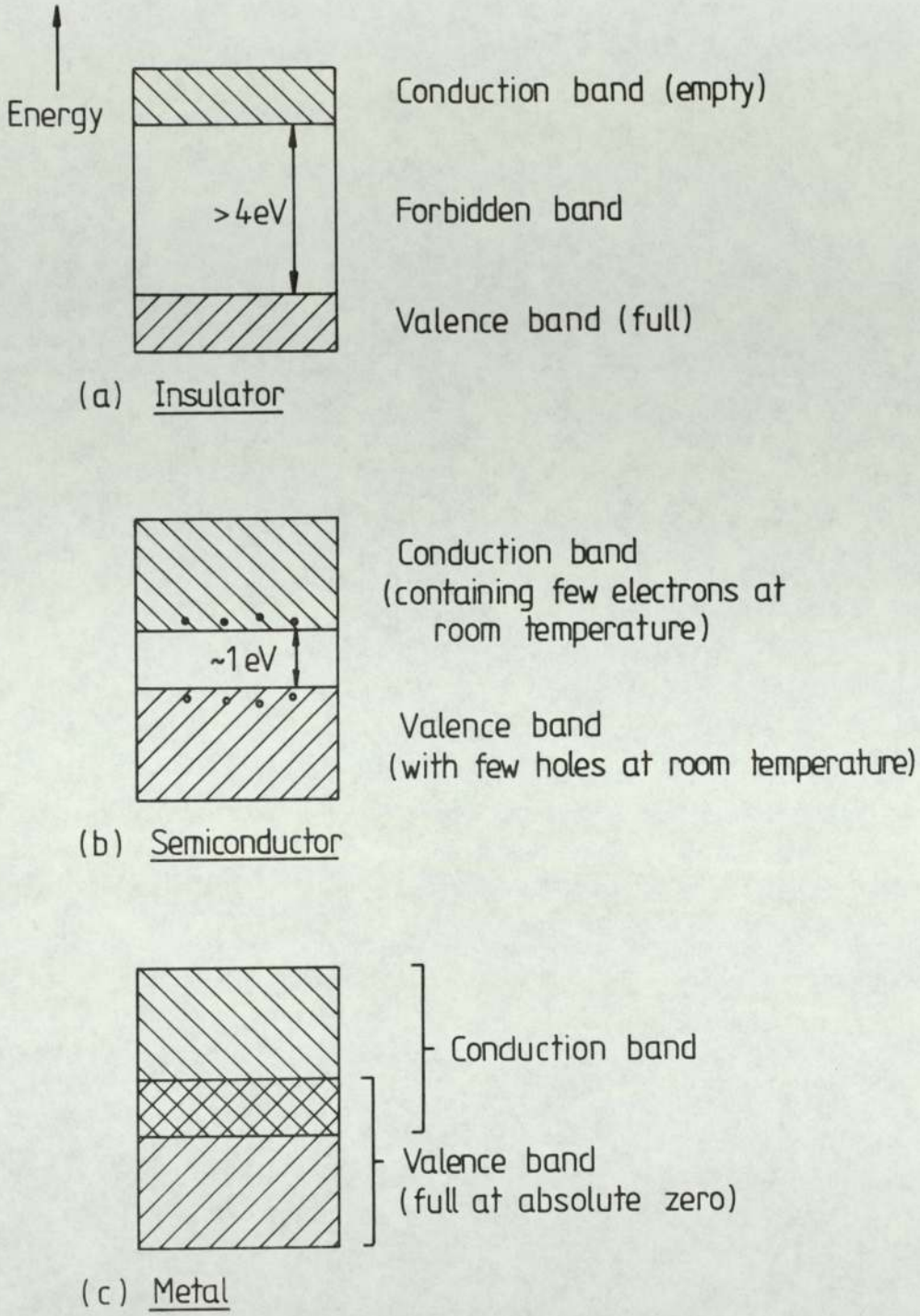

Fig. 2.6 The energy band schematic diagrams for (a) Insulator (b) Semiconductor and (c) Metal.

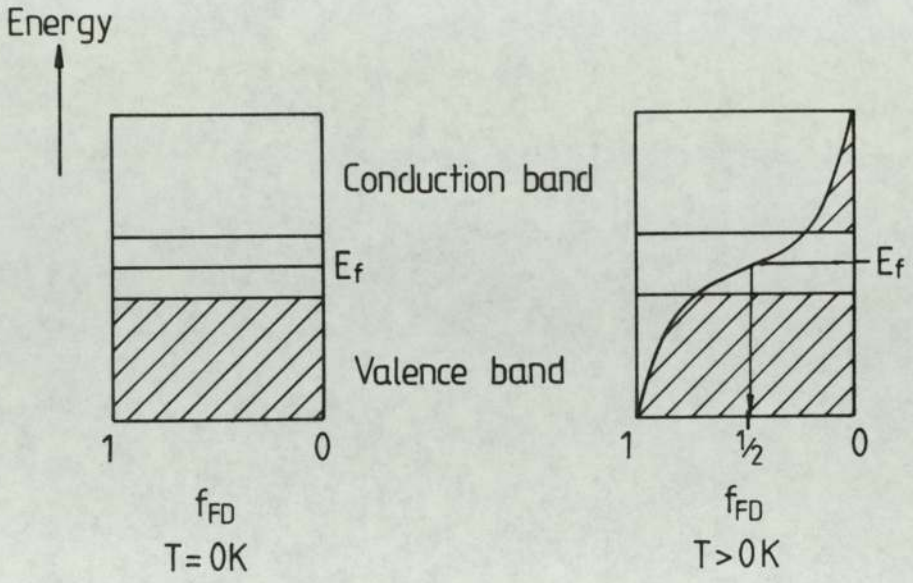

(a) Intrinsic Semiconductor

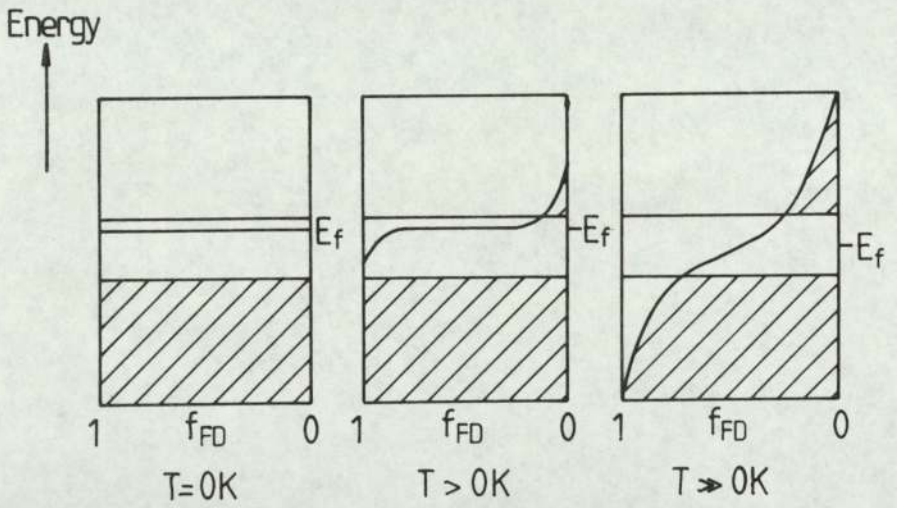

(b) Extrinsic Semiconductor

Fig. 2.7 The Fermi function f_{FD} for an n-type extrinsic and an intrinsic semiconductor.

position of the Fermi level is shown in Fig. 2.7 (b).

Not surprisingly, the theory of the field electron emission from semiconductors is more complicated than for metals. In particular, there will be an ill-defined distribution of surface states that will have a major influence on the field penetration depending on their level of occupancy. These states may themselves also give rise to emission, and so account must be taken of the fact that these surface states need not necessarily be in thermal equilibrium (i.e. Fermi level may not be constant) with the bulk. Further difficulties influence the experimental work in this field; for instance, it is hard to obtain clean semiconductor surfaces, and since semiconductors have a much higher resistance than metals, the voltage drop across the emitter must be taken into account. Thus, when an electric field is applied to a surface of a metal or semiconductor a surface charge is induced. This will be of negligible effect in the case of a metal, since the number of additional charges is small compared to the number of conduction electrons. However, this is not the case for a semiconductor, where the number of electrons in the conduction band is relatively small, so the induced surface charge results in a decrease in electric potential as the surface is approached from the interior, and hence, a down-bending of the bands, as illustrated in Fig. 2.8 (a). This band-bending can be sufficient, with high enough electric fields, for the bottom of the conduction band to fall below the Fermi level, as shown in Fig. 2.8 (b).

The first theoretical study of field electron emission from semiconductors was due to Stratton (50). According to his model, the large field emission currents flowing through a semiconducting emitter can result in a voltage drop ΔV_R down the shank of the emitter with a consequent variation in the Fermi level (an effect particularly

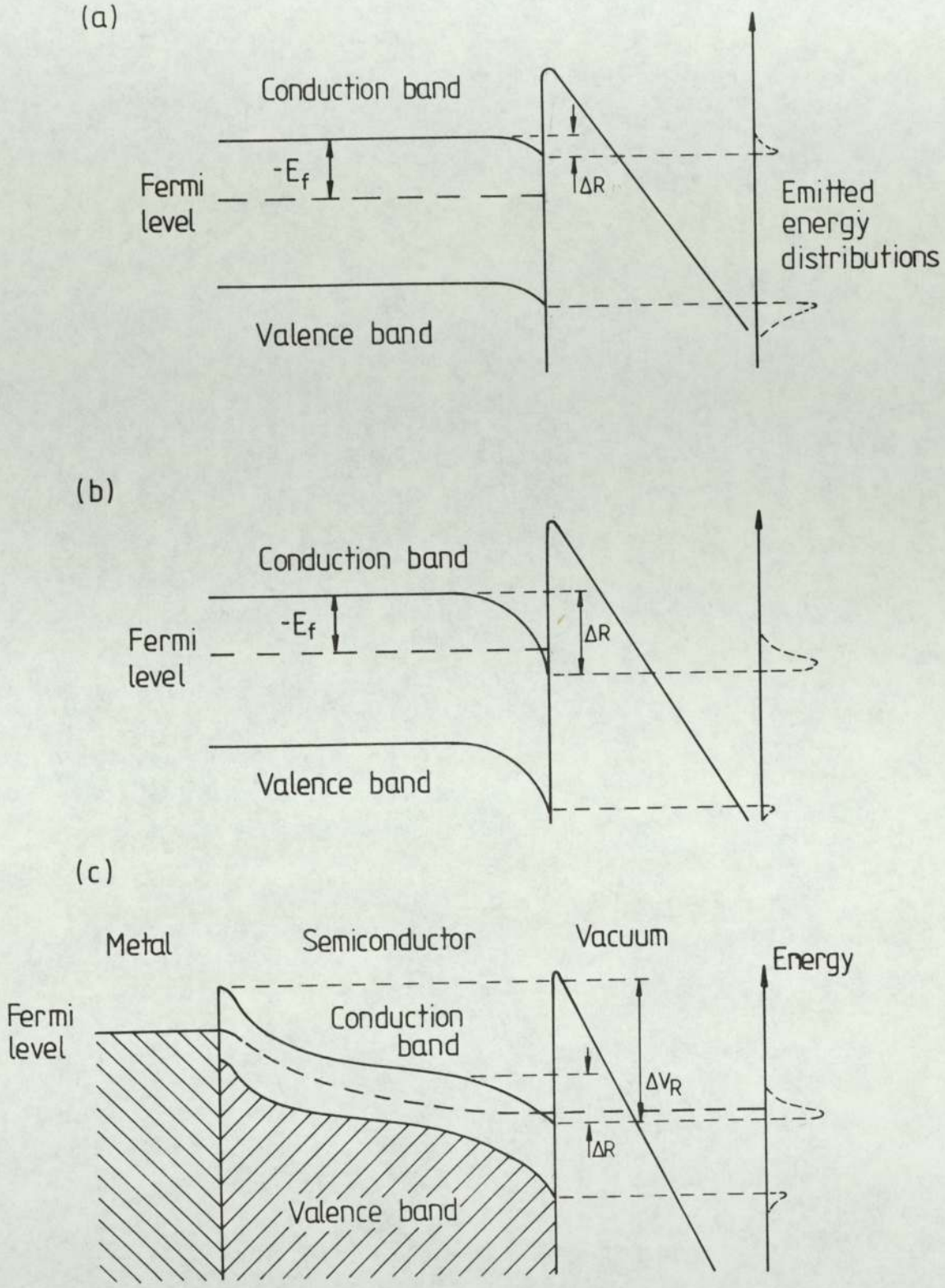

Fig. 2.8 The conduction band bending at the semiconductor / vacuum interface (a) due to low field penetration (b) shows the effect of high field, (c) energy diagram showing an internal potential drop (ΔV_R) due to field penetration and bulk resistivity. Where - E_f is the Fermi energy of bulk material.

associated with semiconductors which have a high resistivity). The voltage drop is concentrated mainly at the apex of an emitter and, as a result, the temperature of this localised region may be raised by Joule heating. Fig. 2.8 (c) [50] presents the electron potential energy diagram of a semiconductor having an internal potential drop due to field penetration and the resistivity of the emitter. Stratton assumed a Fowler-Nordheim type of barrier at the surface and modified the transmission probability to include the dielectric constant of the material. He applied the barrier to different models of a semiconductor surface each with and without field penetration and surface states. In a further publication in 1962, Stratton [51] extended his work, to produce expressions for the emitted current density from both the valence band and the conduction band. This later study used the same type of surface barrier but took account of the variations in the band shapes. He also considered in more detail the effects of surface states, although he did not allow for the probability of emission from these states. The theory broadly predicts, [50, 51] that at low fields, emission will occur predominantly from the valence band (see Fig. 2.8 (a)), and from the conduction band at high fields (see Fig. 2.8 (b)), with linear F-N plots being produced in both situations. In the transition region, the current will increase more rapidly with field as the conduction band population increases. However, most experimental measurements of the current-voltage characteristics did not match with Stratton's theory, in particular a saturation region is observed in the mid-current range where Stratton predicted a pronounced increase in the current. To explain this anomaly Baskin et al [52] considered the electron flow within the semiconductor and showed that there could be a restriction on the emission current caused by the inability of sufficient carriers to arrive at the surface.

Such an effect could either be due to a weakly conducting depletion region, just within the surface for p-type semiconductors, or to the inability of an n-type specimen to generate enough carriers in the bulk. The effects of electron injection at the metal-semiconductor junction were not discussed. Qualitative agreement was shown by numerical calculations based on their expressions.

In 1966 Stratton (53) presented a further study of field electron energy distributions from semiconductors, which can be understood by considering the semiconductor surface and the effect of increasing the applied field, as illustrated by the dotted lines and energy distributions in Fig. 2.8 . This stated that the application of an electric field will induce charge into unoccupied surface states, where if the density of these states is sufficient to accommodate the charge without significantly altering the position of the Fermi level, the external field will be shielded. If any electron emission is obtained it would be expected to come from either the Boltzmann tail of electrons in the conduction band, or from the valence band, depending on factors such as the position of Fermi level, the forbidden energy gap width, and the density of states in the valence band, with the result that two peaks may be observed with an energy separation equal to the gap of the semiconductor, as illustrated in Fig. 2.8 (a). When the field penetration is sufficient for the edge of the conduction band to dip below the Fermi level, the conduction band will become degenerate (i.e. the electrons inside it will obey Fermi-Dirac statistics as opposed to Boltzmann statistics). Accordingly a peak will be observed at the Fermi level and another small one (possibly unobserved) at just below the valence band edge. The first peak would be metal-like and does not shift with increasing the applied field, while the small one may move slightly to lower energies, as shown in

Fig. 2.8 (b). As explained before, when a field emission current flows through a semiconductor emitter a voltage drop ΔV_R will occur within it, with a consequent variation in Fermi level. This effect is ohmic and so ΔV_R is directly proportiional to the bulk resistance of the semiconductor. The additional band-bending at the metal-semiconductor contact (see Fig. 2.8 (c)) is defined by surface states in the semiconductor and work function differences between the two interfaces. Therefore, the distributions obtained would be expected to have an additional shift from the measurable Fermi level of the metal substrate.

In fact, when the field electron energy distribution (F.E.E.D.) from semiconductors were subsequently studied by researchers such as Arthur [54] on germanium, Hughes and White [55] on gallium arsenide, Salmon and Braun [56] on cadmium sulphide, and Lewis and Fischer [57] on silicon, they found that the observed distributions were generally wider and different in shape than the predictions from Stratton's theory. For example, the F.E.E.D. obtained by Arthur [54], in the case of extreme band-bending, was found to approach the result found for metals [48].

In 1974 Modinos [58] proposed the most promising theory of field electron emission from semiconductors, which takes account of emission from surface states. His theory deals particularly with germanium at low current densities, but it should be possible to extend the principles to understand emission from semiconductors in general. Modinos adopted a model for the surface states of germanium, originally suggested by Handler [59] in 1960, which is schematically shown in Fig. 2.9 . The S_1 band is a band of "donor" levels (i.e. it is electrically neutral when occupied), assumed to lie considerably below the top of the valence band; so that it's contribution

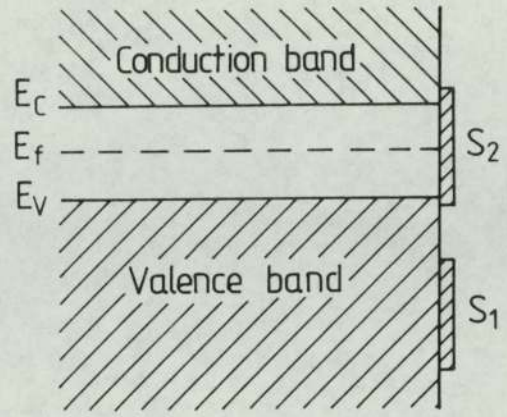

Fig. 2.9 Surface states of germanium according to Handler's model. [59]

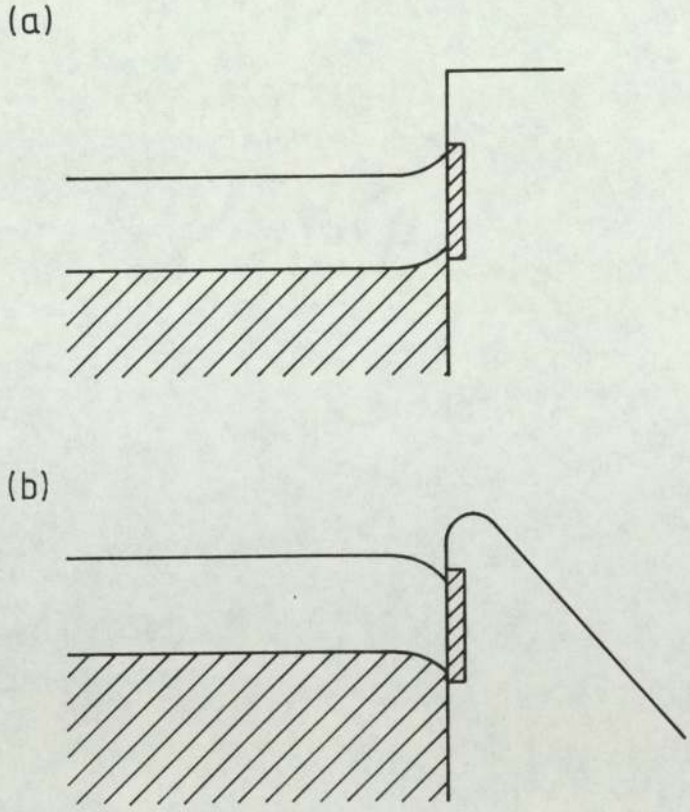

Fig. 2.10 The bands bending (a) upwards when field applied to the semiconductor = 0 (b) downwards when field applied to the semiconductor $\gg 0$. [58]

to the emission current may be entirely neglected. The S_2 band is a band of "acceptor" states (i.e. it is negatively charged when occupied). It is assumed that the band is two-dimensional and circular, with its bottom edge overlapping the valence band. Under zero field conditions, the bands of the semiconductor will bend upwards due to space charge arising from the surface states (Fig. 2.10 (a)). However, if a strong external electric field is applied to the semiconductor surface, the field lines will either terminate on charges in the surface states, or penetrate into the semiconductor and terminate on excess electrons in the space charge region; i.e. the bands may bend downwards, as shown in Fig. 2.10 (b). Modinos calculated the F.E.E.D. corresponding to a p-type, intrinsic and an n-type semiconductor, and these are shown in Fig. 2.11 for three different values of the applied external field. It is obvious that the energy spectra for the three types are practically identical except for a displacement in the energy axis, with respect to the Fermi level. The Modinos theory predicts that at low current densities ($< 10^6$ A m^{-2}), most of the emitted electrons come from surface states and, to a lesser degree, from the valence band. At higher current densities ($\sim 10^7$ A m^{-2}) the emission from the conduction band is a significant, though still small, proportion of the total emission current. At even higher current densities ($> 10^8$ A m^{-2}) the conduction band becomes degenerate and the theory is no longer applicable in its present state. As a consequence of field variation, the energy distributions shift away from the Fermi level towards lower energies as the field is increased, while the relative amplitude of emission from the valence band increases.

A major difference between emission from metals and semiconductors can be seen in the F-N plots. At low fields (i.e. low current

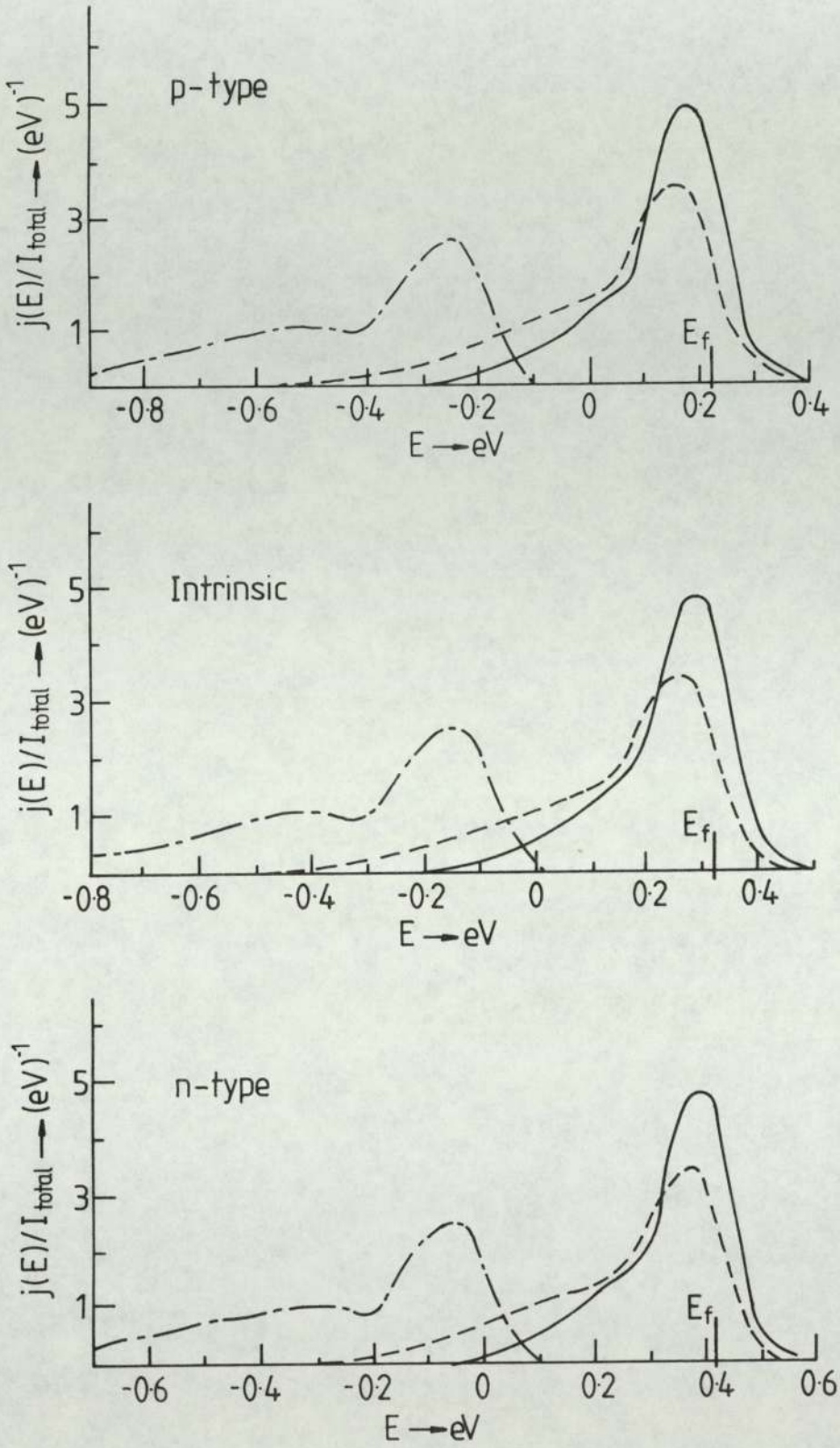

Fig. 2.11 Theoretical energy spectra according to Modinos. [58], for Ge.

densities) the semiconductor plots are linear, but as the field is increased, a saturation region is obtained where the current does not increase with increasing field. Modinos's theory deals only with the linear region before saturation occurs. The F.E.E.D. from germanium obtained by Shepherd and Peria (60) confirmed the main theoretical prediction of the Modinos model, namely that most of the emitted electrons come from the surface states and to a lesser degree from the valence band. The shape of the energy distribution is also confirmed by their results (see Fig. 2.12). More recently, his theory has been used successfully to explain the F.E.E.D. from lead telluride by Sykes and Braun (61) and zinc oxide by Rihon (62), although they did not measure a significant increases in the shift of the distribution from Fermi level with applied field, possibly because they did not reach sufficiently high electric fields.

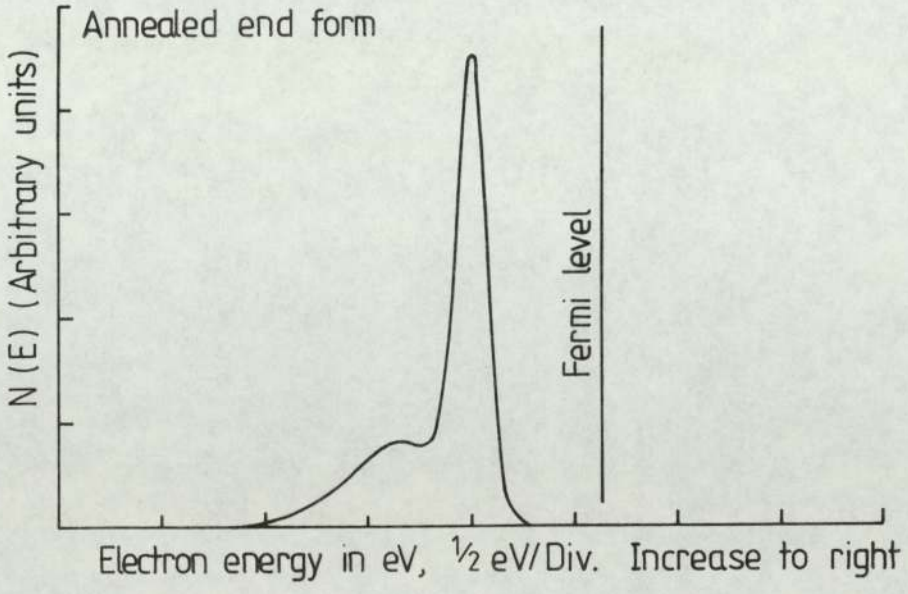

Fig. 2.12 Typical energy distribution from the center of the (100) facet of Ge. Clean, annealed end form.[60]

2.4 FIELD EMISSION FROM COMPOSITE METAL-SEMICONDUCTOR /INSULATOR MICRO-REGIMES

It is generally accepted that the electrical pre-breakdown currents flowing between clean broad area high-voltage electrodes in vacuum arise from localised field electron emission sites [1]. This is supported by the fact that the current-voltage characteristics of these sites give linear Fowler-Nordheim plots. However, the electric field associated with the emission is often two or three orders in magnitude below the threshold value of the field predicted by F-N theory (viz. $\gtrsim 10^9$ V m^{-1}). Accordingly, if the emission is to be explained in terms of the F-N model it is necessary to assume the presence of metallic micro-protrusions, which locally geometrically enhance the field by a factor β to a value greater than the threshold. Although this interpretation was accepted for many decades recent experimental evidence suggests it is incorrect. Thus, in 1975 Cox [63] examined the microtopography of emission sites, and found that the β-values measured indirectly from F-N plots of site currents (typically $\beta > 200$) were very much higher than the geometrical enhancement that could be provided by the surface features directly observed in a S.E.M. (typically $\beta < 10$). Further to this, in 1977 Hurley and Dooly [64] observed electroluminescence from discrete spots on the cathode, and, in 1978, the first measurements of the non-metallic F.E.E.D. from localised sites on broad area copper electrodes were obtained by Allen and Latham [65]. This led both groups, independently, to postulate that the electron emission arose from semiconductor/insulator inclusions in the surface of the cathode, but they proposed different models to explain the phenomena. Those models will be discussed in the following sections.

2.4.1 HOT-ELECTRON MODEL

This model which was proposed in 1978 by Allen and Latham [66], was based upon the electron spectrometry studies referred to above. The crucial finding is illustrated in Fig. 2.13 (a), which compares the spectra obtained from a metallic emitter and a typical broad-area site. This shows that the latter process gives a spectrumthat is displaced from the Fermi level to low energies by 0.2 - 0.5 e V, has a larger half-width (> 0.3 e V) and has a more symmetrical shape than a metallic emitter. Frequently, as illustrated in Fig. 2.13 (b), spectra can be multi-peaked. It has also been shown that the shift from the Fermi level, and half-width of broad-area single-peak spectra, show a strong dependence on the applied field [67].

In seeking a model to explain the "non-metallic" type of electron emission spectra shown in Fig. 2.13, Allen and Latham made reference to the spectra obtained from the semiconducting microemitter studies of Shepherd and Peria [60], Lewis and Fisher [57], and concluded, from certain of their similarities, that the emission mechanism responsible for the pre-breakdown currents was probably based upon some form of semiconductor/insulator regime. However, the possibility that the emission arose from an ambient film of insulating or semi-conducting oxide overlaying the surface was discounted because this does not account for the highly localised nature of the emission site. Instead, it was suggested that the sites were associated with the randomly distributed semiconductor or insulator-like micro-impurities that almost inevitably exist in the surface of an electrode following its various preparation procedures.

Accordingly, it was suggested that the energy band representation

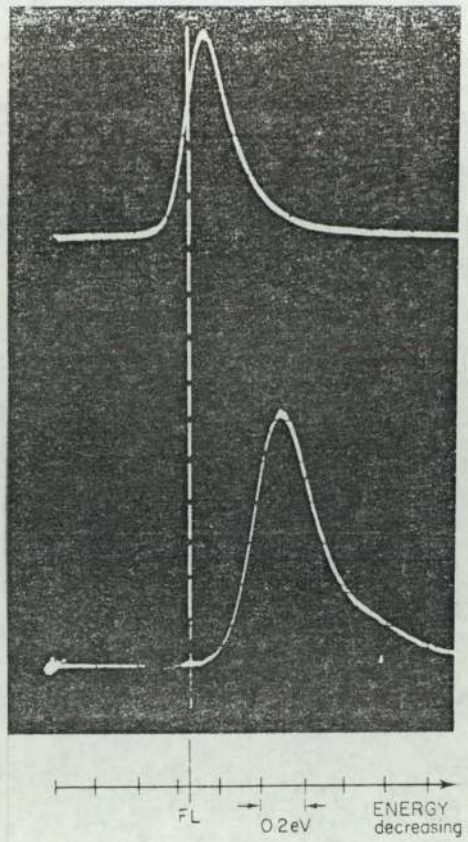

Fig. 2.13 (a) Electron energy spectra obtained from (i) a reference tungsten micropoint emitter, and (ii) an emission site on a broad-area copper electrode: in both cases, the spectra are referred to the Fermi level FL of the substrate cathode. [65]

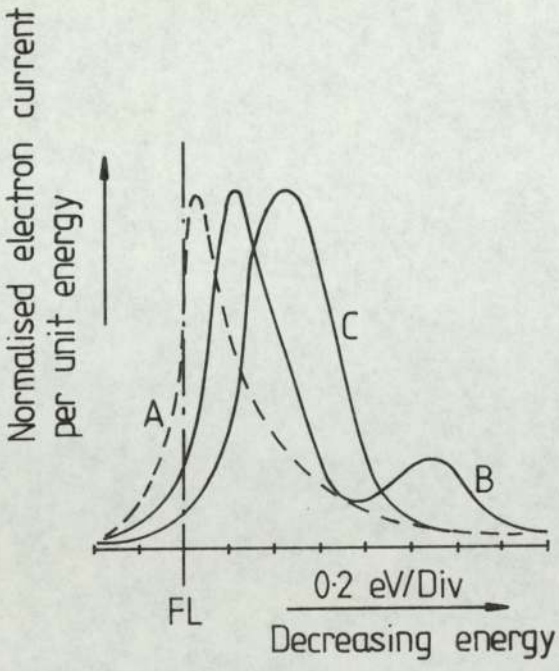

Fig. 2.13 (b) Electron energy spectra from a site on a broad-area copper-chromium specimen at 293 K (———) showing single-or double-peak characteristics; for comparison, ---- shows the distribution from a clean tungsten emitter. FL represents the position of the Fermi level in the bulk of the electrode. [66]

of such a composite surface, together with its associated potential barrier, might appear as shown in Fig. 2.14 (a): In this figure, account has also been taken of the possible presence of surface adatoms, represented in the diagram by a subsidiary potential well associated resonance tunnelling (energy) states ΔE_a of the adsorbed species [68, 69]. When a high field is applied to this composite surface, it is assumed that there is some field penetration so that the band structure is modified to that shown in Fig. 2.14 (b). The three-stages of the electron emission mechanism, which explains how electrons can tunnel from below the Fermi level of the metal substrate, and how an enhanced tunnelling probability is achieved without geometrical field enhancement, are as follows: (i) an initial tunnelling of electrons from the metal substrate to the bottom of the conduction band of the semiconducting layer; (ii) the subsequent 'heating' of these electrons by 2 - 3 e V as a result of their acceleration in the penetrating field; and (iii) a final enhanced tunnelling of the heated electrons into the vacuum from non-equilibrium states (shown dotted in Fig. 2.14(b)) that extend to near the top of the surface potential barrier. On the basis of this model, three possible explanations were proposed for the appearance of the low energy peak. Thus, referring to Fig. 2.14 (b), they would arise from: (i) valence band emission as discussed by Stratton in 1964 [53]; (ii) emission from inter-band surface states; and (iii) adatom resonance tunnelling as described by Duke and Alferieff [68]. Valence band emission is unlikely since the energy difference between the two peaks is much smaller than the band gap of any likely impurity; it would also seem unlikely that the barrier is sufficiently deformed for this type of emission. However, the transient nature of the peak suggests an unstable surface effect, and accordingly the

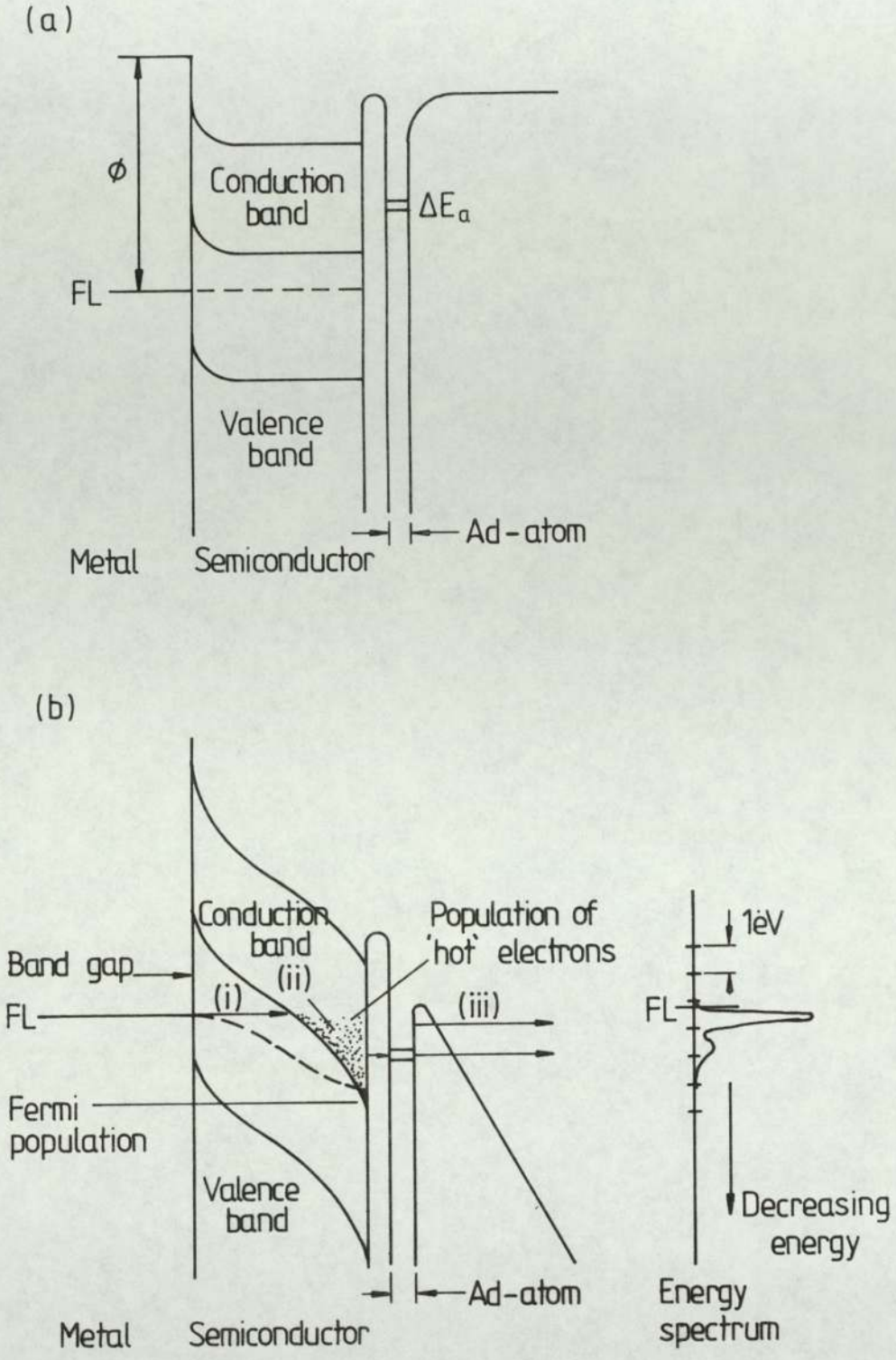

Fig. 2.14 (a) A one-dimensional diagram of a composite surface consisting of a metal substrate and an overlaying semiconducting microstructure. ø and FL are respectively the work-function and Fermi level of the metal substrate. The ---- indicates the position of the Fermi level, which is continuous between the metal and semiconductor. (b) The same one-dimensional energy diagram showing the effect of a field penetration into the semiconducting layer and the proposed tunnelling mechanisms.[66]

favoured explanation is that of ad-atom resonance tunnelling.

Such interpretations of the experimental data were necessarily speculative, however it seems fair to conclude that the field-enhancing microprotrusion model is inapplicable and that the results cannot be interpreted in terms of ordinary metallic emission.

2.4.2 CONDUCTING FILAMENT MODEL.

This model, which was proposed by Hurley [70] in 1979, is based on studies of the electroluminescence associated with this type of electron emission. The experimental arrangements have been fully described by Hurley and Dooley [71], and consist in essence, of a pair of high voltage electrodes (under U.H.V. conditions) were viewed by an image intensifier whilst a pre-breakdown current was flowing between them. He not only observed the well known "anode spots" but also an associated optical emission from the cathode surface, which he called K-radiation. Hurley investigated the spectral distribution of the emitted light from a range of materials, where, as examples, the spectra obtained from O F H C and high purity copper are reproduced in Fig. 2.15. The nature of the spectra of this light shows that it does not arise from black body radiation, and hence cannot be explained in terms of asperity-heating arising from an ohmic conduction processes, as had been traditionally thought. Instead, it was believed to be the direct result of electron energy transitions with associated photon emission. Hurley also found that the intensity of light varied with the applied voltage, which is a further evidence that the emitted current and the electroluminescence are aspects of the same physical phenomena. Discharges were occasionally seen to occur from the light spots and were observed

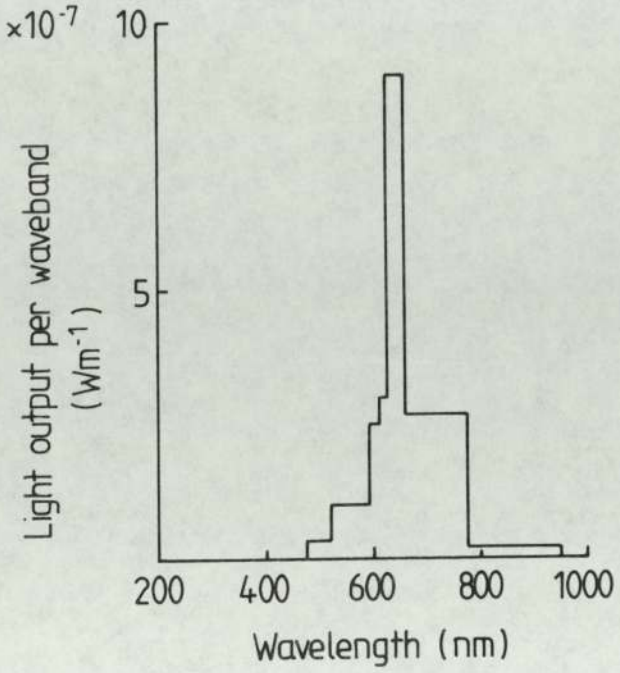

(a) OFHC Copper

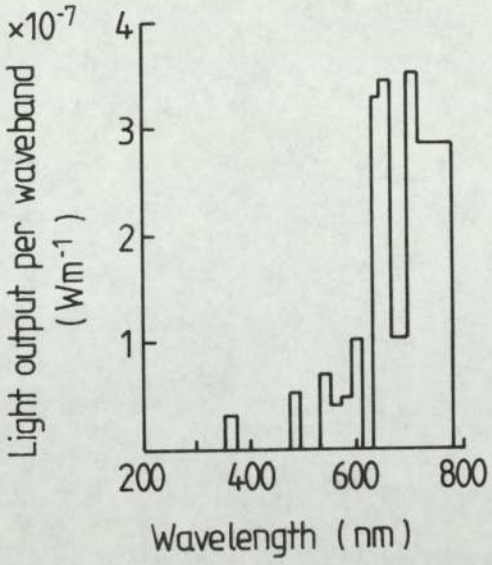

(b) High Purity Copper

Fig. 2.15 Spectra of radiation from typical K-spots.[70]

to precipitate breakdown of the gap. Open shutter photographs revealed that the discharged material was not charged because there was no apparent curvature of its track in the presence of the electric field. The shape of these tracks suggested that particles were being emitted, rather than being a jet of gas. Occasionally, alternating dark and light tracks were observed, such as could be produced by a revolving particle heated on one side only.

The model proposed by Hurley to explain these results was based upon a filament forming mechanism of the type observed to occur in the "memory switching" of amorphous semiconductors [72]. With these systems it had been found that the application of electric fields in the range of 10^6 to 10^7 V m^{-1} to thin films of amorphous semiconductors, with thickness typically between 10 to 2000 n m can result in the formation of thin conducting channels through the films. The "formed channels" have a conductivity which can be 10^8 times greater than the previous unformed-materials. Using these ideas, Hurley believed that a conducting filament is formed through the semiconducting ambient oxide on the surface of an electrode and that as a result, the field is locally enhanced by the geometry of the filament (see Fig. 2.16 (a)) to a value $\geqslant 10^9$ V m^{-1} for the "metallic" field emission of electrons. Some of the high energy electrons are assumed to be scattered into the dielectric to produce lattice excitations, with the recombination processes giving rise to the emission of photons, as shown in Fig. 2.16 (b). An explanation for the discharge events was also given, though Hurley does not seem to be correct in believing the explosion of the filament to be caused by switching. However, the idea that the resistive heating of the filament would cause instability and rupture of the conducting channel, seems more reasonable. In any event, the explosion leads to the

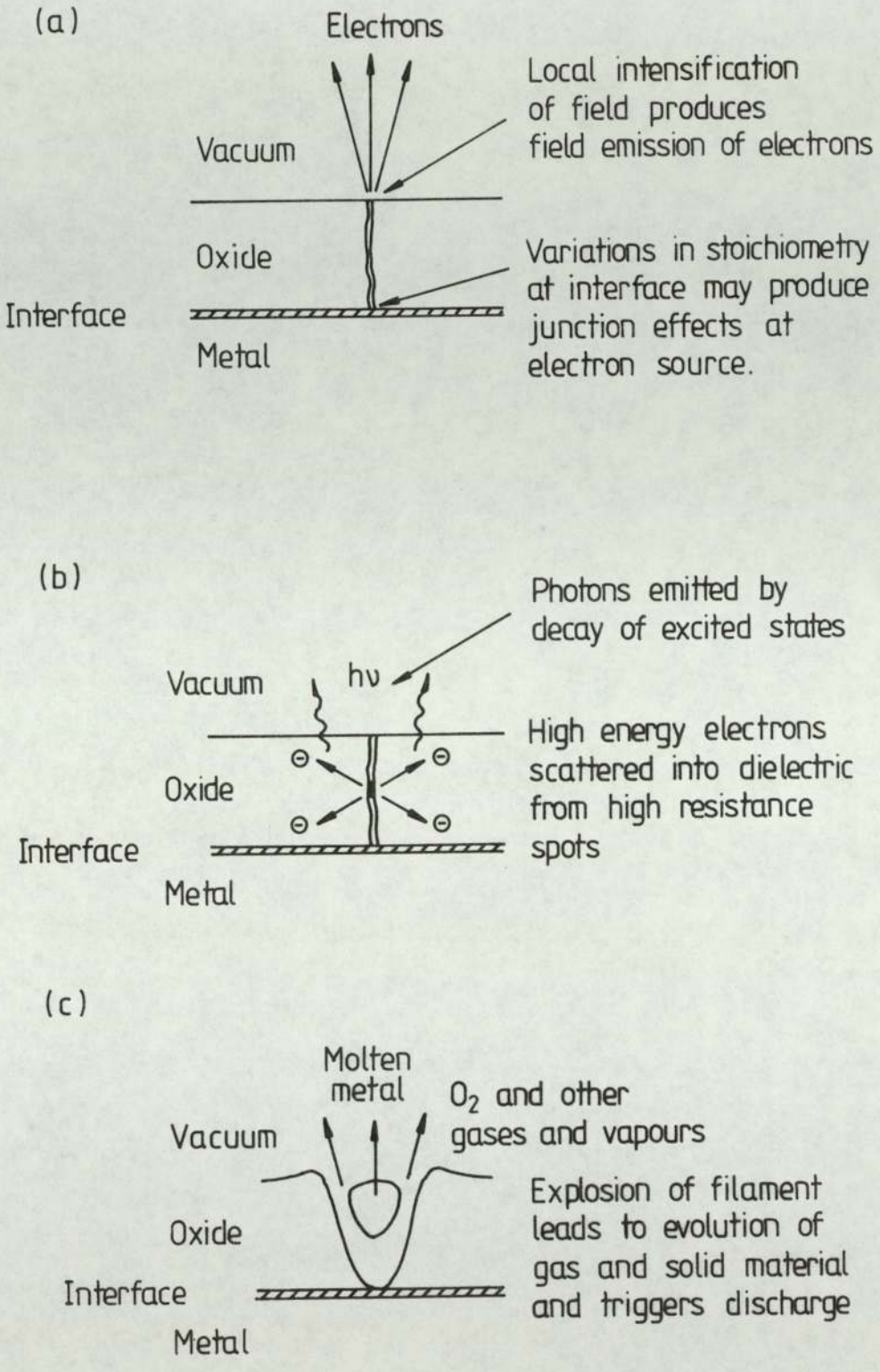

Fig. 2.16 Production of electroluminescence, vacuum breakdown and electron emission from electroformed conducting filaments in oxide impurities. (a) Electron emission.(b) Electroluminescence. (c) Vacuum breakdown.[70]

expulsion of solid and gaseous material into the vacuum, as shown in Fig. 2.16 (c). Finally, it is important to note that Hurley believed that the initial emission of electrons was assumed to be controlled by the metal-semiconductor rather than the semiconductor-vacuum interface.

2.4.3 REVISED HOT-ELECTRON MODEL.

The two models described in the previous two sections, were proposed to explain the emission of electrons from a physical regime consisting of an insulating microimpurity which is in intimate contact with the substrate metallic cathode. Both models were based on restricted experimental data, and may consequently be considered as rudimentary and hence open to some criticism. For instance, the "hot-electron model" does not explain how a significant number of hot electrons will be able to cross the micron-sized impurity without losing most, or all, their energy through phonon scattering processes. Also, the field at the metal-semiconductor interface is not obviously high enough to support tunnelling through the potential barrier at this interface. Equally, the "conducting filament model", which proposes that geometrical field enhancement gives rise to field emission from the top of the filament, does not seem to adequately explain the required field enhancement of $\gtrsim 200$, since the typical radius of filaments in chalcognide glasses was measured, by Adler et al [5], to be $> 2\,\mu$ m. Thus in micron-dimension impurity particles, the geometrical field enhancement from a filament with such dimensions would not be able to give rise to fields high enough for field emission. This model is also vague on (i) how the electrons enter the filament from the metal substrate; (ii) the chemical

nature of the conducting filament; (iii) the optical photon production mechanism; and (iv) the origin of the shifted electron spectra.

In order to overcome these arguments, Athwal and Latham [67] revised the earlier hot-electron model to incorporate some of the fundamental concepts of the dielectric switching model developed by Dearnaly et al [4] and Adler et al [5] to explain the behaviour of M.I.M. switching devices. This approach was suggested by many resemblances in the properties of such devices and the field emission processes on broad-area electrodes. According to this revised model, the energy band configuration of a metal-insulator-vacuum system before a field is applied is typically as shown in Fig. 2.17 (a), where the work function is assumed to be 4.5 e V and the band gap $\gtrsim$ 3 e V. The small band-bending at the two interfaces is determined by the surface energy barriers, which in turn are due to differences in work function and the presence of surface states. As the field is increased, to a value just below the onset of emission, the bands will bend in the way shown in Fig. 2.17 (b) due to the field penetration into the insulator. It is now envisaged that, at the onset of electron emission from the metal, an avalanche occurs in the insulator and causes it to "switch" to a high conductivity state, as is observed to occur in materials such as amorphous oxides and chalcogenide glasses, at fields of this order [4, 73]. It is assumed that on switching there will be a very rapid re-arrangement of the energy band configuration shown in Fig. 2.17 (b) to that shown in Fig. 2.17 (c) which is similar to that postulated by Adler et al [5]. This regime is characterised by two very narrow high-field regions, at the metal-insulator and insulator-vacuum interfaces, separated by an extended low field region. It is also assumed that

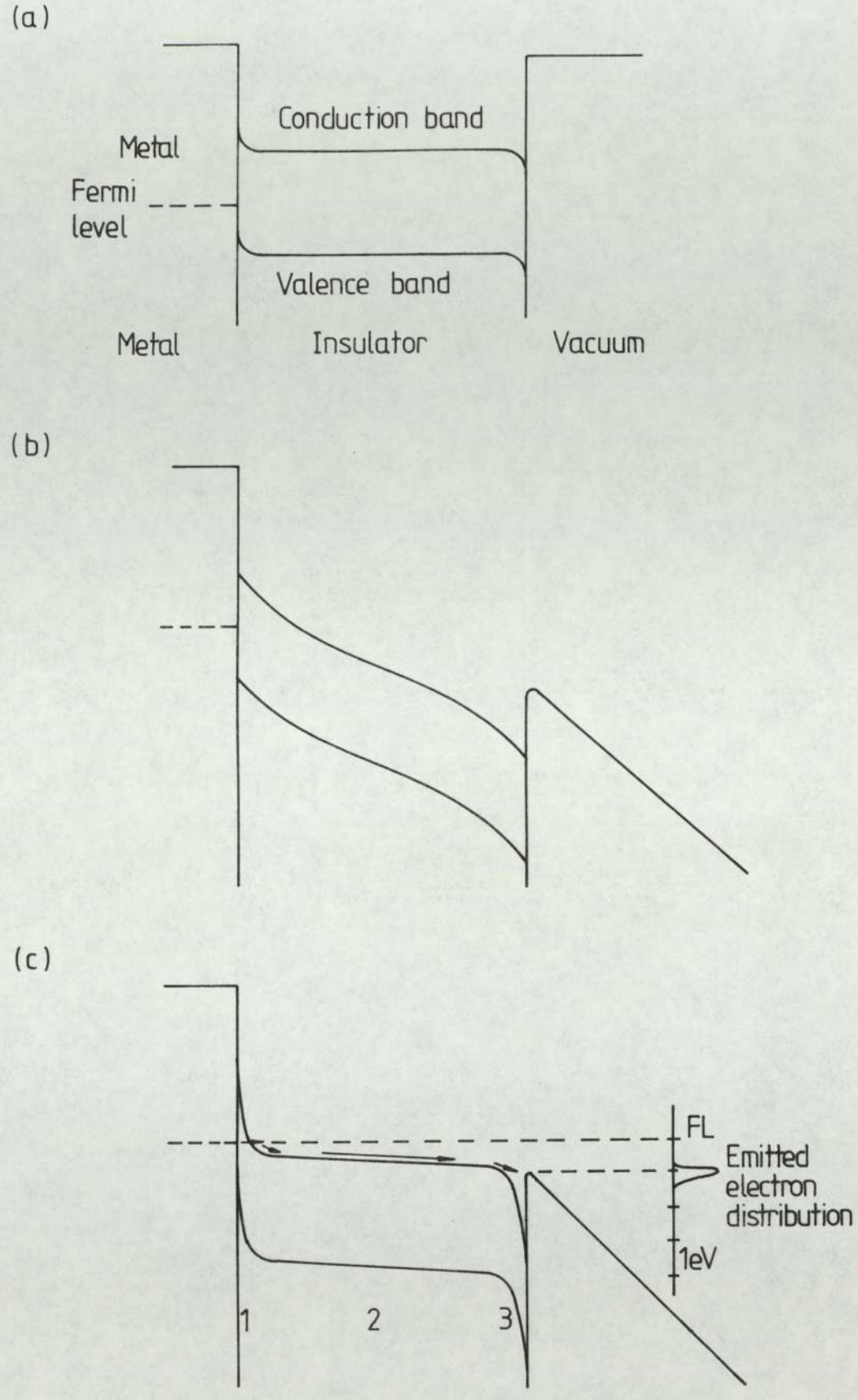

Fig. 2.17 Energy band and surface barrier configurations of the metal-insulator micro-emitting regime under varying field conditions: (*a*) zero field; (*b*) high field prior to switching and electron emission; (*c*) high field stable electron emission regime.[67]

this switching mechanism is assisted by the simultaneous production of positive and negative charge carriers, in the form of electron-hole pairs resulting from impact ionisation events by hot electrons, in localised states at the two interfaces.

Thus, in this revised model, Athwal and Latham postulate that the band configuration is maintained by the following three processes: (i) the trapping of charge carriers in localised sites; (ii) the build up of a "dynamic" space charge in region 1 due to the differing mobilities of electrons and holes there [74]; and (iii) the build up of space charge in regions 1 and 3 due to a solid-state electrolysis process involving the migration of positive ions towards region 1, and negative ions to region 3. It is believed that the process (ii) will dominate near the metal-insulator interface, (i) will be most important near the vacuum interface with (iii) leading to irreversible electroforming.

The process of electron emission, with a band structure as represented in Fig. 2.17 (c), is assumed to take place as follows. Firstly, the electrons tunnel from the metal into the insulator through the potential barrier at the metal-insulator interface and are then rapidly thermalised, in order to cross the extended low field region in the bottom of the conduction band, where their life time can be $\sim 10^{-8}$ second [5]. The electrons now enter the second narrow high field region of ~ 10 n m thickness at the vacuum interface, where they are heated through the 2 - 3 e V necessary to escape over the top of the depressed barrier. Some of them however undergoe scattering processes to excite the electron transitions required for producing the optical spectra, as illustrated in Fig. 2.18.

On the basis of this model, the experimentally measured shift in the energy spectra with applied field [67] illustrated in Fig.

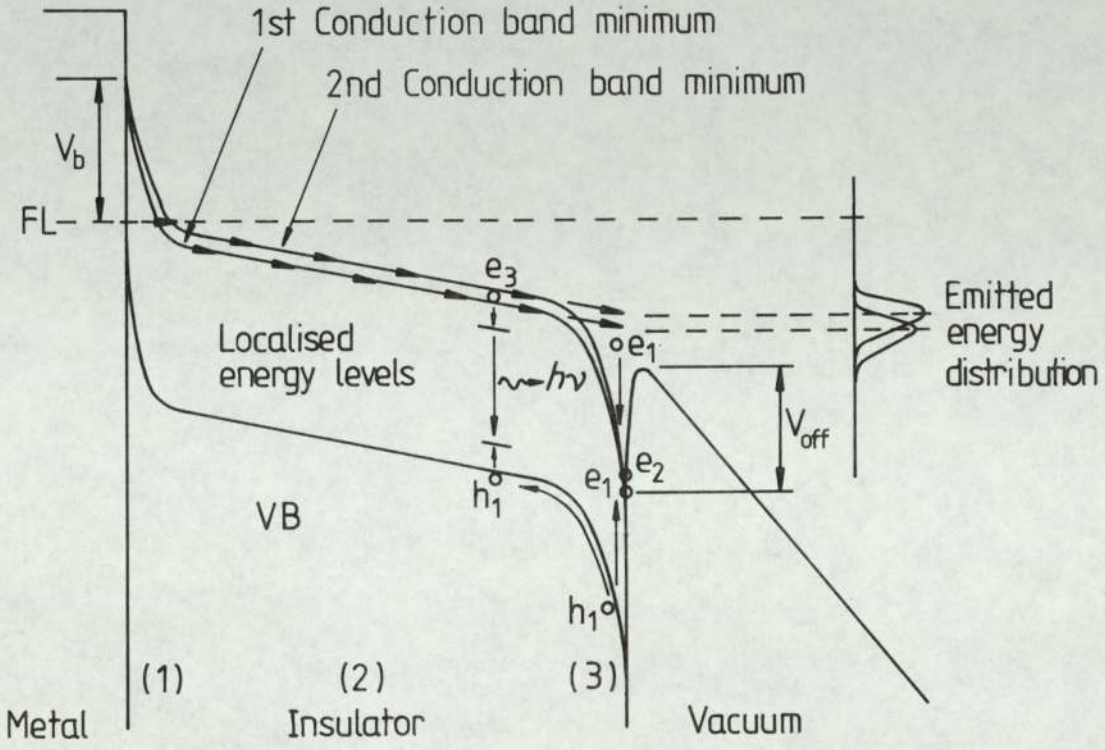

Fig. 2.18 Energy band configuration of the 'on' state of an electron emitting regime providing multi-peaked spectra.[6]

2.19 , will be the sum of three components: (i) the energy lost in thermalising into the conduction band minimum in region 1; (ii) an ohmic energy loss in the low field region 2; and (iii) the energy loss due to phonon scattering in region 3. Each of these losses may be expected to increase with increasing field and current, though the ohmic losses should only be significant at current levels of $\geqslant 10^{-8}$ A. The increase of the full-width at half maximum (F.W.H.M.) of the F.E.E.D. is supposed to be due mostly to phonon scattering of hot-electrons prior to escaping over the potential barrier, since electrons thermalising in a parabolic conduction band would have a half-width of only 1.5 K T (0.04 e V at room temperature) before entering region 3. More precisely, this increase in half-width with current may be due to: (i) an increase in the length of the high field region 3; (ii) an increase in phonon scattering cross-section with the energy of the electrons; and (iii) an introduction of carrier-carrier scattering.

Finally, mention should be made of some other implications of this model. Firstly, the instabilities that are frequently observed in the emission spectra may reflect the inherent instabilities of the space charges in region 1 and 3. Secondly, the double and multi-peaked spectra, which are frequently observed experimentally, are believed to be due either to the presence of more than one conducting channel through a particular impurity, or that they may arise from a more complicated band structure in the insulator, with electrons being able to travel in other conduction band minima or in the continuum of interband states. Lastly, it is generally believed that the typical Fowler-Nordheim characterisitcs which are obtained from these sites may, in all cases, be attributed to electrons tunnelling in region 1. Further details of this and the previous models are

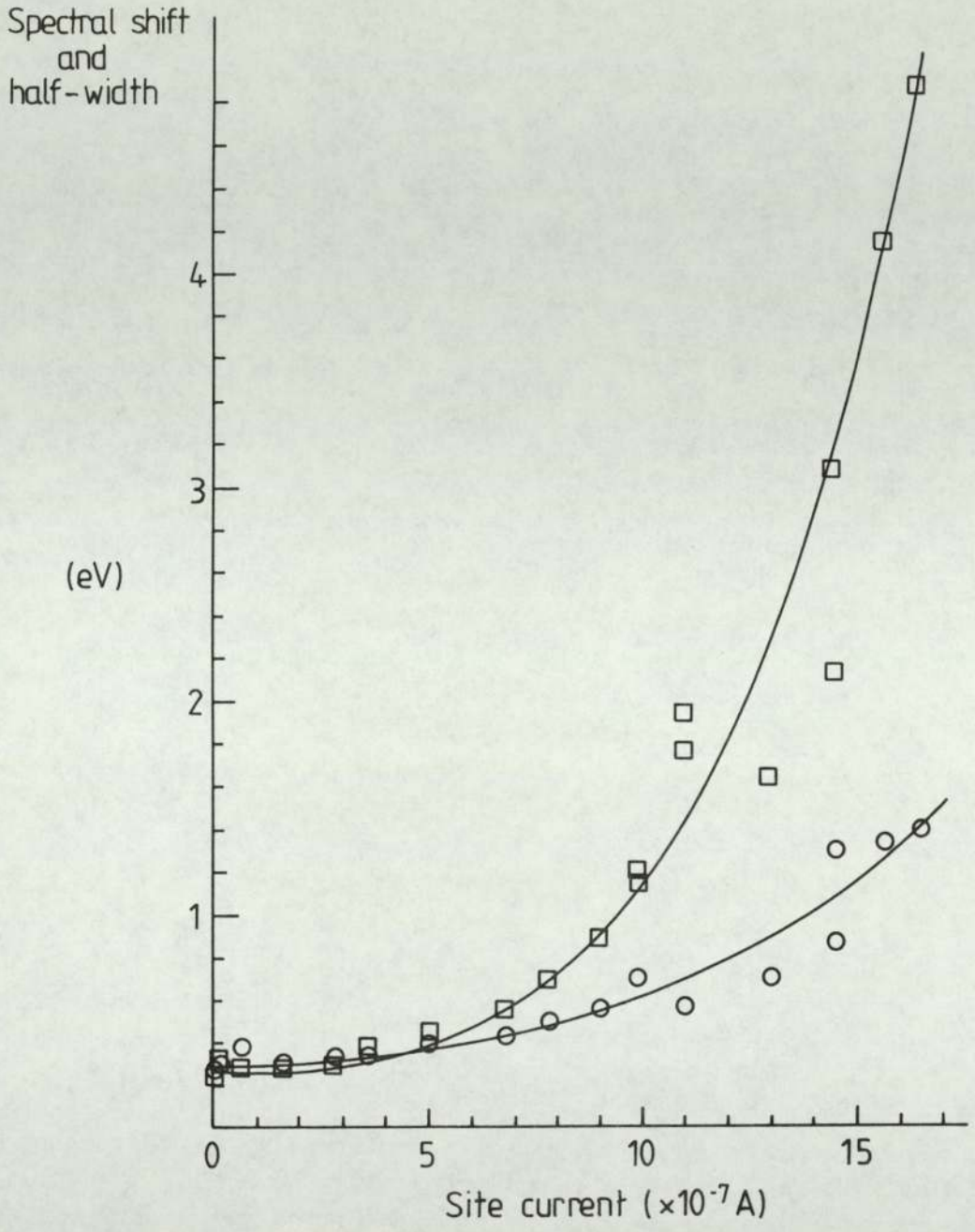

Fig. 2.19 Variation of the spectral shift and half-width (F.W.H.M.) with site current. □ represents the shift of the maximum of the energy distribution from the substrate Fermi level. o represents the half-width (F.W.H.M.) of the energy distribution.[67]

given in chapter 8 [1]. However, more recently Latham [3] using a model in which hot-electrons escape over the potential barrier was able to give a new quantitative significance to the linear Fowler-Nordheim current-voltage characteristic that is typical of a high voltage gap. Also, Athwal and Latham [6] have given a detailed discussion about the switch-on of the emitting state and its subsequent evolution.

CHAPTER 3

EXPERIMENTAL STUDIES OF FIELD ELECTRON EMISSION FROM COMPOSITE MICROPOINT EMITTERS.

3.1 Introduction

This chapter is concerned firstly with the preparation of the composite microregimes discussed in section 2.4 i.e. the emission regime that is thought to promote the hot electron mechanism, and secondly with a description of the instrumental techniques required to evaluate its characteristics. Details will be given concerning the fabrication procedures for several types of composite micropoint field emitters. These include the coating of metallic tungsten micropoints by a range of insulating materials, including alumina, glass, wax, zinc oxide, plastic, araldite resin, lacomit, hydrocarbon and epoxylite resin. In many instances,(e.g. resin) a number of tips were prepared having coatings with thicknesses varying from $\sim .04$ to 50 μm, so that their respective emission characteristics could subsequently be compared. As an alternative and novel approach for producing the required emission regime, advantage was taken of a well known technique for thermaly extruding glass capillary tubes into fine points, where for the present application, the internal walls had to be made conducting. The characteristics of these various types of emitter were evaluated using a combination of a field emission microscope, to obtain current-voltage (I-V) characteristics and for recording their emission images, and a high resolution retarding potential electron spectrometer to measure their field emission energy distributions (F.E.E.D.). Details of the instrumental facilities will be given in the following sections, whilst the properties of the various emitters will be presented in chapter 4.

3.2 EMITTER FABRICATION TECHNIQUES

3.2.1 COATED TUNGSTEN MICROPOINT EMITTERS

This section is concerned with the development of techniques for obtaining composite micropoint field emitters, consisting of a conducting substrate coated with a layer of insulating material of a controlled thickness.

Several approaches were investigated (see later), but the one that proved most successful was based upon the type of tungsten micropoint emitters that are conventionally used in field emission microscopy. Such emitters typically have a tip radius of $\leqslant$ 100nm, and are produced by the electrolytic etching technique illustrated in Fig 3.1 . Here, approximately 4mm of 0.1 mm diameter tungsten wire is immersed below the surface of a 2M. solution of sodium hydroxide [75] and the control circuit adjusted to give an initial etch current of ~4mA. However, as the etching process proceeds this rapidly falls to ~2mA, and then slowly to less than 1mA to give the etched shapes illustrated in Fig 3.2 a to d, at which point the control circuit interupts the current to give the final tip shape shown in e [39] . The rate of decrease in the etch current speeds up considerably just before the tip is "necked off", and this is sensed by the automatic "Schmitt Trigger" circuit [76] , to immediately switch off the voltage source. If this precaution were not taken, the etching action would continue and blunt the tip. Finally these tips are washed in distilled water, or better still, washed ultrasonically in readiness for any of the coating procedures as described below in section 3.2.1.Fig. 3.3 shows a scanning electron micrograph of such a tungsten tip.

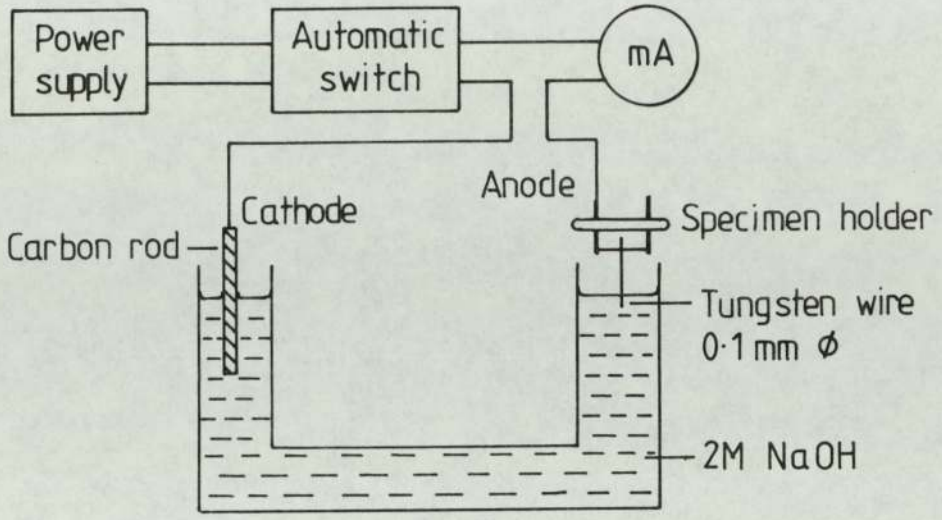

Fig. 3.1 The experimental apparatus used for electrolytically etching of tungsten micropoint emitters.

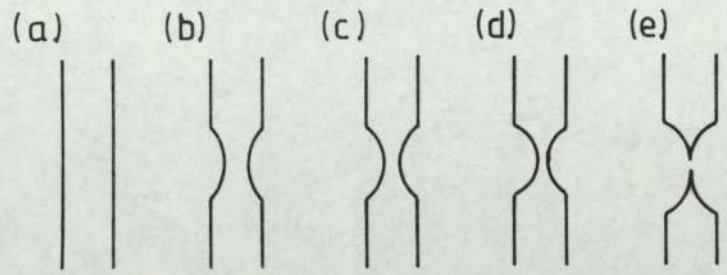

Fig. 3.2 Stages in the etching process of a tungsten field emitter.

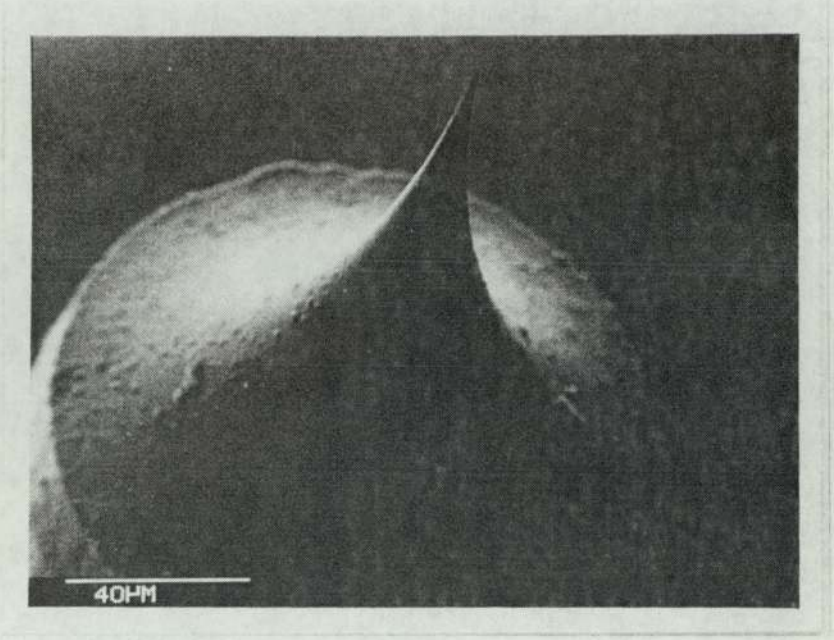

Fig. 3.3 A scanning electron micrograph of an etched tungsten micropoint emitter.

3.2.1.1 ALUMINIUM OXIDE COATING

The first coating material investigated was aluminium oxide Al_2O_3 (Alumina), since this was known to have good insulating properties. The experimental approach involved, firstly, evaporating a thick coating of a few micrometers of metallic Al onto the tungsten tip, where the thickness of this coating could be determined from the "before" and "after" scanning electron micrographs. In the examples of Fig. 3.4, it will be seen that the diameter of the tungsten tip has been coated by a layer of aluminium of ~ 4 microns thickness. Since exposing the emitter to air will only grow a thin ambient oxide layer of ~ 3.5 nm thickness, two methods may be considered to completely oxidize the aluminium coatings. The first is to heat the tip in an oven to a high temperature

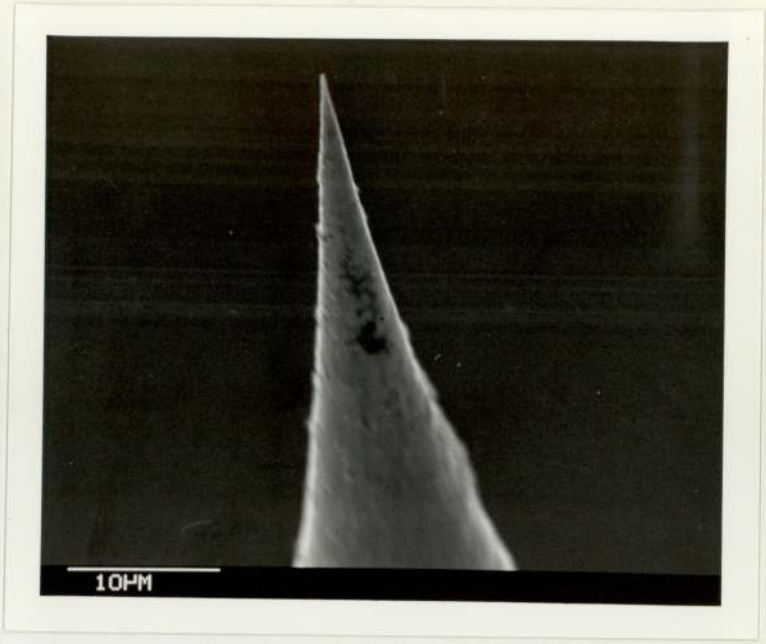

(a)

(b)

Fig. 3.4 Scanning electron micrographs of tungsten tip (a) before and (b) after coating with ~4 microns of Alumina.

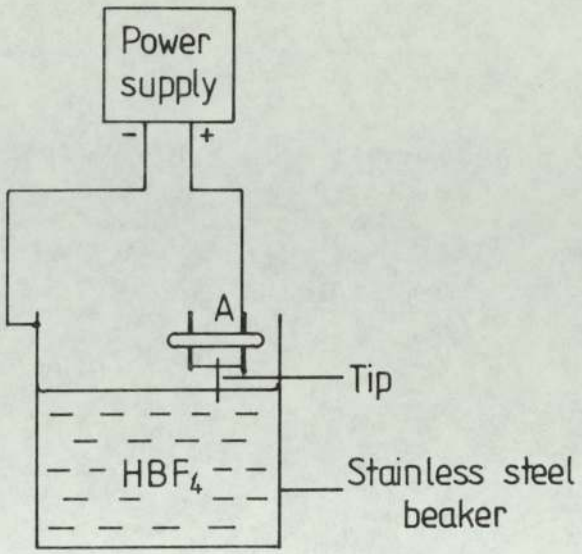

Fig. 3.5 The anodizing process in an electrolytic cell.

(~600°C), whilst the second is to use an anodizing process: however, for this small-area application this latter method proved to be the most successful[77] Referring to Fig. 3.5, the coated tip is made the anode[78] in an electrolytic cell using either chromic, sulphric[79] or hydrofluoroboric acid (HBF_4)[78] i.e. 4 to 5 ml of HBF_4 (48%) and 200 ml of water form the solution, and the tip immersed for 40 to 80 seconds into the electrolyte using 20 Volt bias potential. Relatively thick oxide deposits can be produced by this technique, since even though these coatings are electrically insulating[79] the reaction can continue because the electrolyte is able to reach the metal surface through the small pores which are present in the growing oxide. After anodizing, the pores were sealed by immersing in a boiling distilled water bath which caused

hydration and a resulting volume expansion of the oxide.

Here, it will be recalled from the introduction (chapter 1), that the main aim of manufacturing such composite microemitters was to simulate the hot electron mechanism which best describes the emission from broad area electrodes. However, with this type of composite emitter it was found that the required behaviour for broad area emission, particularly switching was not obtained. Therefore no further work has been done on this material.

3.2.1.2 MISCELLANEOUS COATINGS

Several other commercial insulating materials were tried for coating tungsten tips for example, candle wax, zinc oxide (as used in anti-rust primer paint), plastic (as used to produce a tough transparent flexible surface films) and araldite resin. However in all cases these coatings formed large balls of material over the tips, which offered no possibility of obtaining controlled sub-micron insulating coatings. As an example Fig. 3.6 is an optical micrograph for one of these tips which was coated with zinc oxide, where, because of its opacity, it is not possible to estimate the film thickness.

3.2.1.3 LACOMIT COATING

Lacomit is a petrolium product having good insulating properties. If the tungsten tip is rapidly dipped into and removed from this solution, a ball is formed as shown in the optical micrograph of Fig. 3.7 (a); at this stage the embedded tip is clearly visible $\sim 300\ \mu m$ below the surface of the coating. If the coated tip is now baked in air to a temperature $\sim 200^{\circ}C$, the coating will shrink

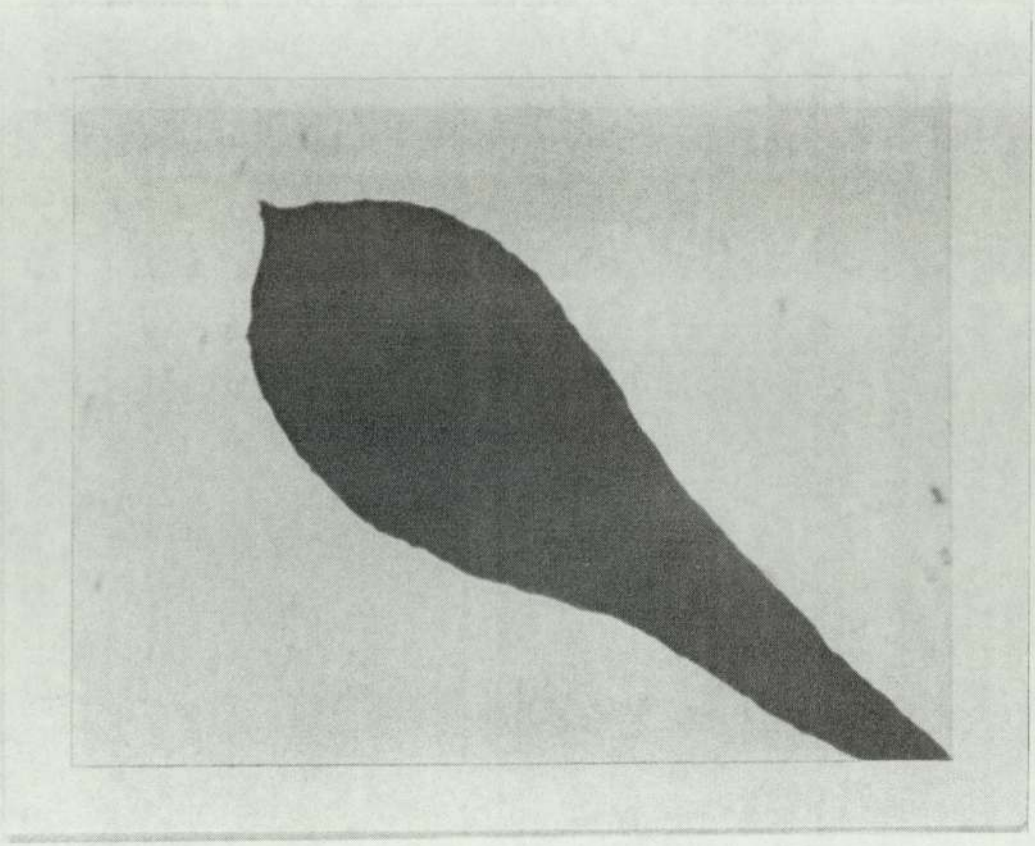

Fig. 3.6 Optical micrograph of tungsten tip coated with a ball of zinc oxide.

as shown in the micrograph of Fig. 3.7 (b), where the estimated layer thickness is a few microns. On the other hand if the tungsten tip is dipped into and removed slowly from this solution, a film is formed the thickness of which could not be estimated due to its opacity.

3.2.1.4 EPOXYLITE RESIN COATING

Epoxylite resin has been shown to provide a very satisfactory insulating coating for microelectrodes in other technological contexts [80], mainly because it is chemically resistant to the most common laboratory solvents and dilute electrolyte solutions. As for the lacomit coating the tungsten microelectrode was dipped into the resin one or more times in order to have a layer of insulator

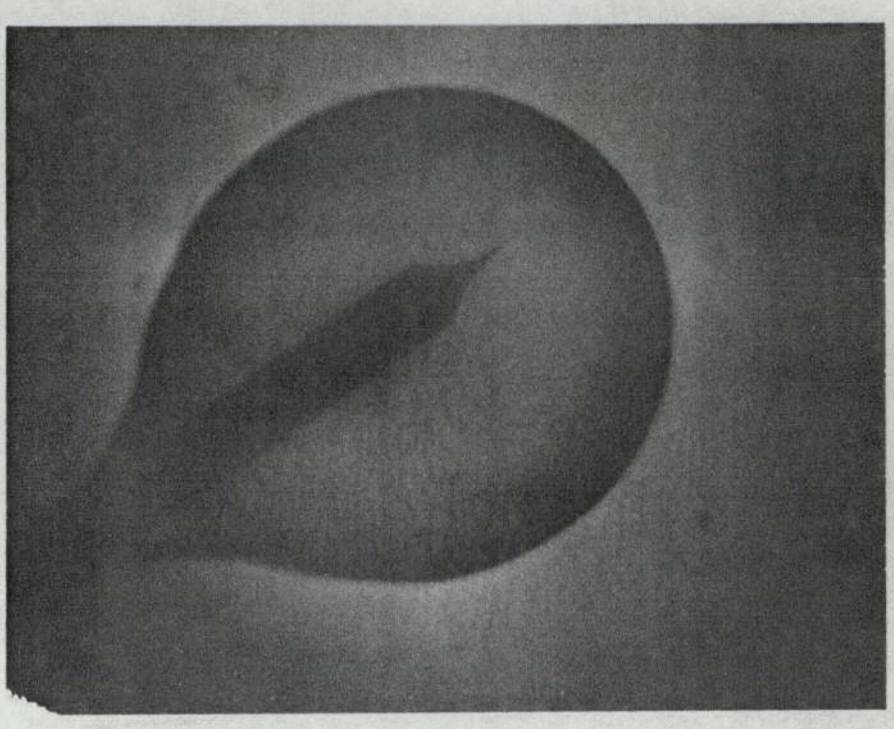

(a) Magnification = 66 X.

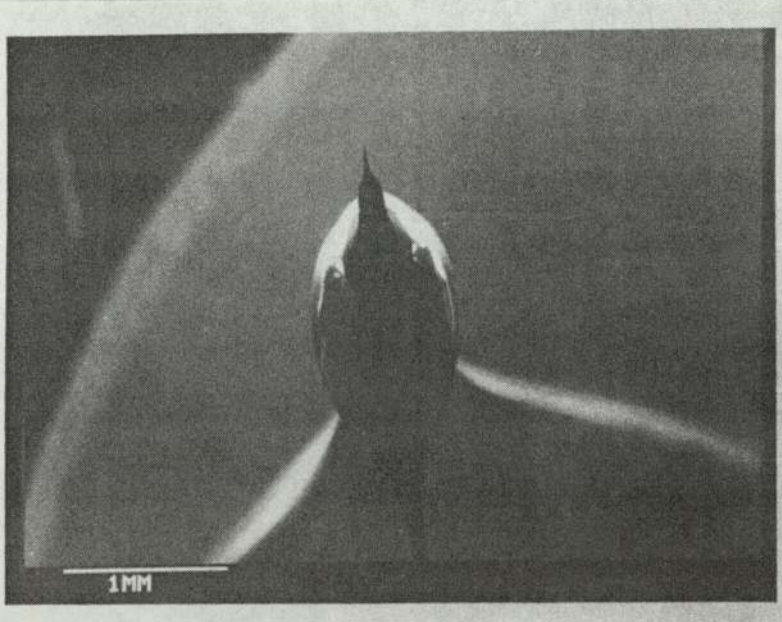

(b)

Fig. 3.7 Micrographs of (a) tungsten tip covered with a ball of lacomit before baking (b) after baking to ~ 200°C.

built on it. Subsequently the coated electrode was heat treated, with the tip pointing vertically upwards, using a curing cycle of 30 minutes at 100°C to drive off the solvents, followed by 30 minutes cure at 175 - 190°C. Since the thickness of the insulating layer is controlled principally by the number of dips into the resin before baking, the actual rate of build up had to be determined by trial and error. In order to investigate this process, a special specimen holder was developed for use with an optical microscope. In the first approach to developing a suitable coating process, a ball of resin initially was built up on the tip. This was acheived by alternately dipping the tip into the resin and pulling it out quickly and then curing it as described above, until a structure such as shown in the optical micrograph Fig. 3.8 (a) was obtained, where the estimated film thickness over the tip appex was $\sim$50 microns. Unfortunately, owing to the image distortion produced by the highly cured resin surface, it was not possible to use the technique for the controlled production of thinner layers ($\lesssim$ 1mm thick) which were required for this study.

As an alternative approach, an attempt was made to remove a certain thickness of the insulating layer over the tip appex in Fig. 3.8 (a) by using the ion beam etching technique illustrated in Fig. 3.9. This used a spherical ion source [81,82] which provided a finely diverging beam of typically 5KV Ar^+ ions, so that by rotating the tip in front of the beam it was possible to achieve uniform etching of the surface, and hence to control the rate of removal of material. Figures 3.8 (a) and (b) are respectively "before" and "after" optical micrographs of a resin coated tip that had been subjected to this treatment. Whilst this technique provided a useful facility for reducing the thickness of the insulation

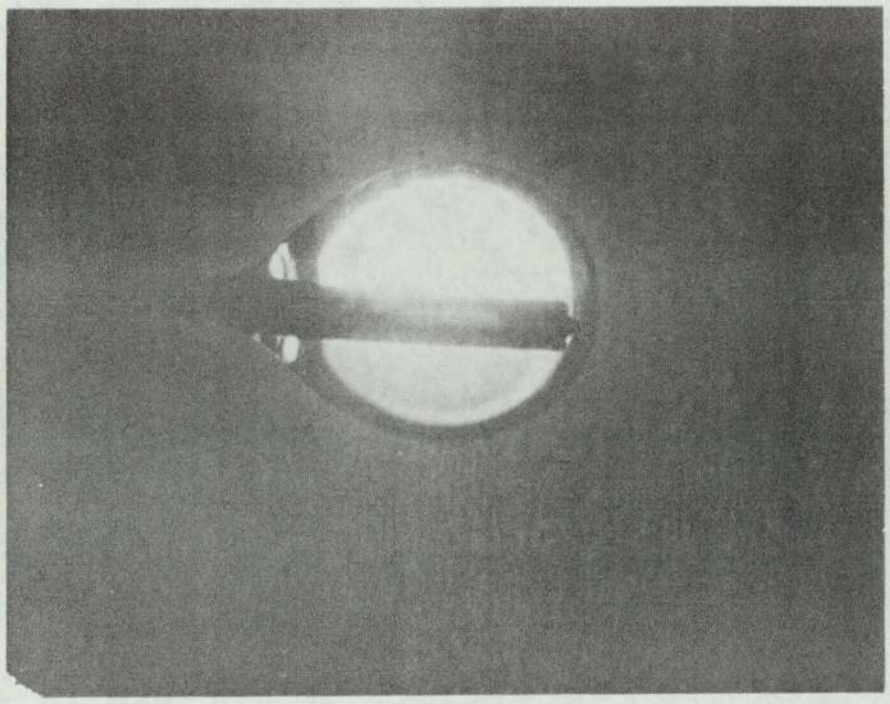

(a)

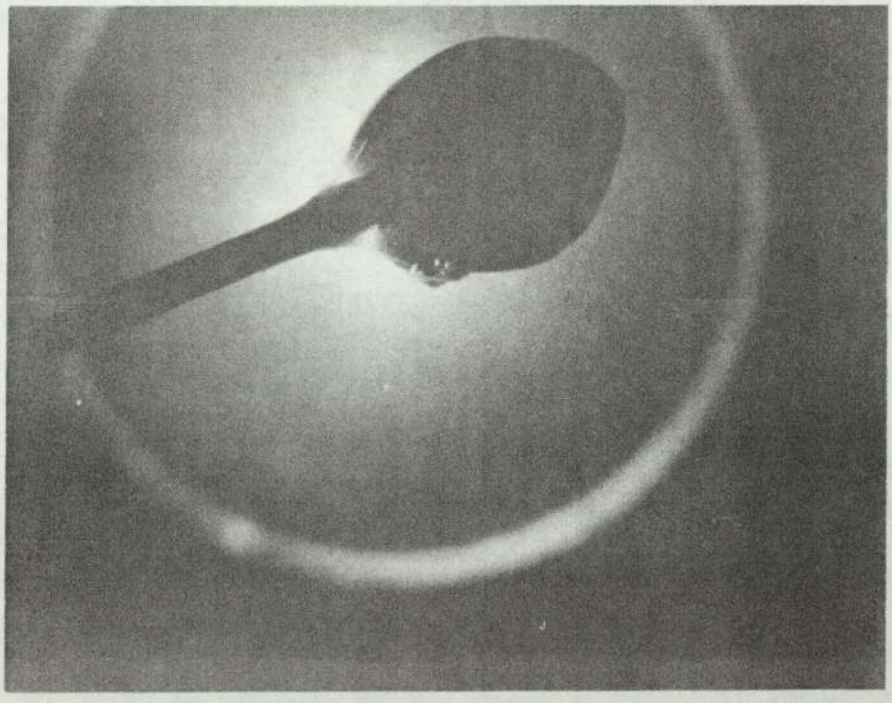

(b)

Fig. 3.8 (a) Optical micrograph of tungsten tip coated with a ball of resin (b) Optical micrograph of a coated tip in (a) after ion beam etching. $M = 24X$.

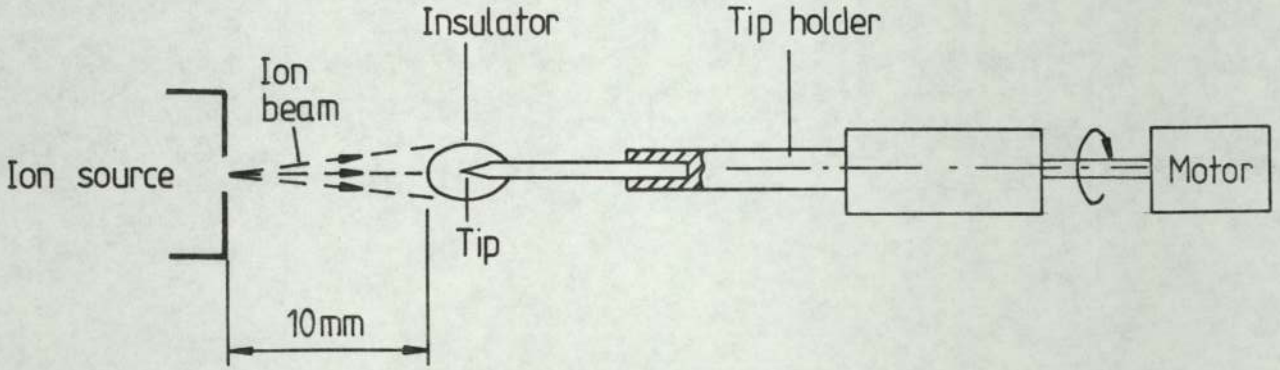

Fig. 3.9 Schematic diagram of the ion beam etching regime.

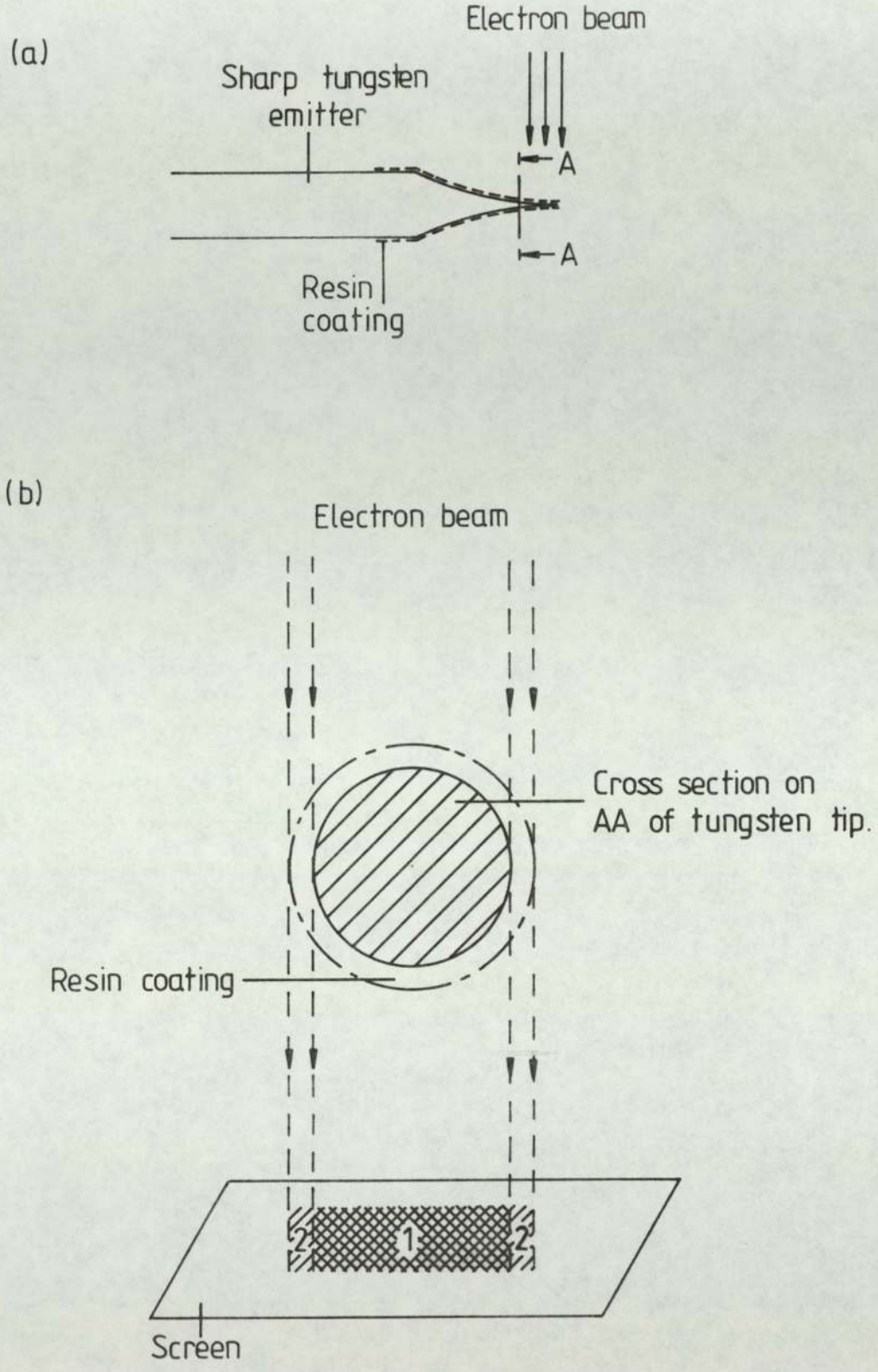

Fig. 3.10 A diagram showing the T.E.M. electron beam falling on the tungsten tip coated with resin.

coating, its value was limited since it was not possible to estimate the final thickness of the layer.

The next approach was to investigate the successive effect of slowly and uniformly dipping a tungsten tip into and out-of the resin, with a view to building up a controlled and uniform sub-micron thick layer. Initially, optical micrographs were taken of the tip before and after each coating of resin, but the resolution of these proved to be too low for accurately measuring the thickness of the film. To solve this problem, an 80 KV transmission electron microscope T.E.M. (Phillips EM 200) was used to obtain a profile image of a tip, whereby the film thickness measurement relied on the differing transmissivities of tungsten and resin. This is illustrated in Fig. 3.10, where region 1 indicates the dark shadow of the tungsten core and region 2 the faint shadow of the insulating coating of the resin. In order to make these measurements, the standard specimen holder of the T.E.M had to be modified as shown in Fig. 3.11 in order to hold these tips. Examples of electron micrographs taken with this facility are shown in Fig. 3.12, where a and b are a pair of images taken "before"

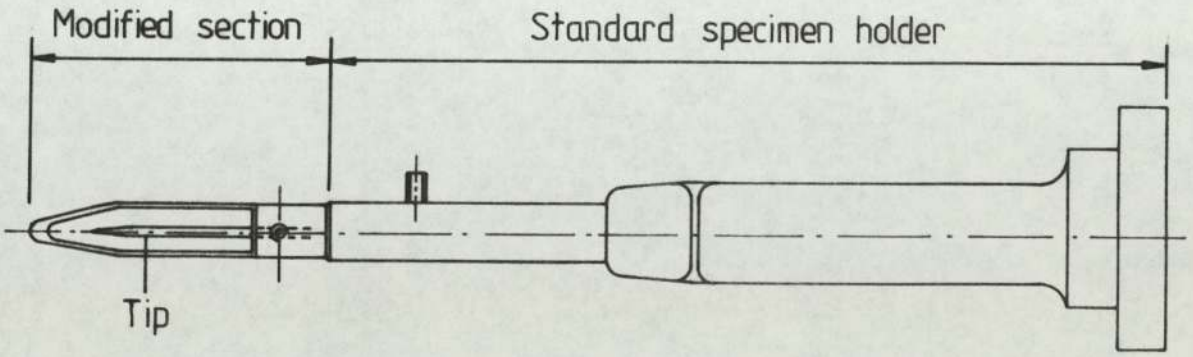

Fig. 3.11 The modified specimen holder of the T.E.M.

(a)

(b)

Fig. 3.12 Transmission electron micrographs of tungsten tip (a) before coating (b) after coating with a 0.06 μm layer of resin. (Magnification = 30240X).

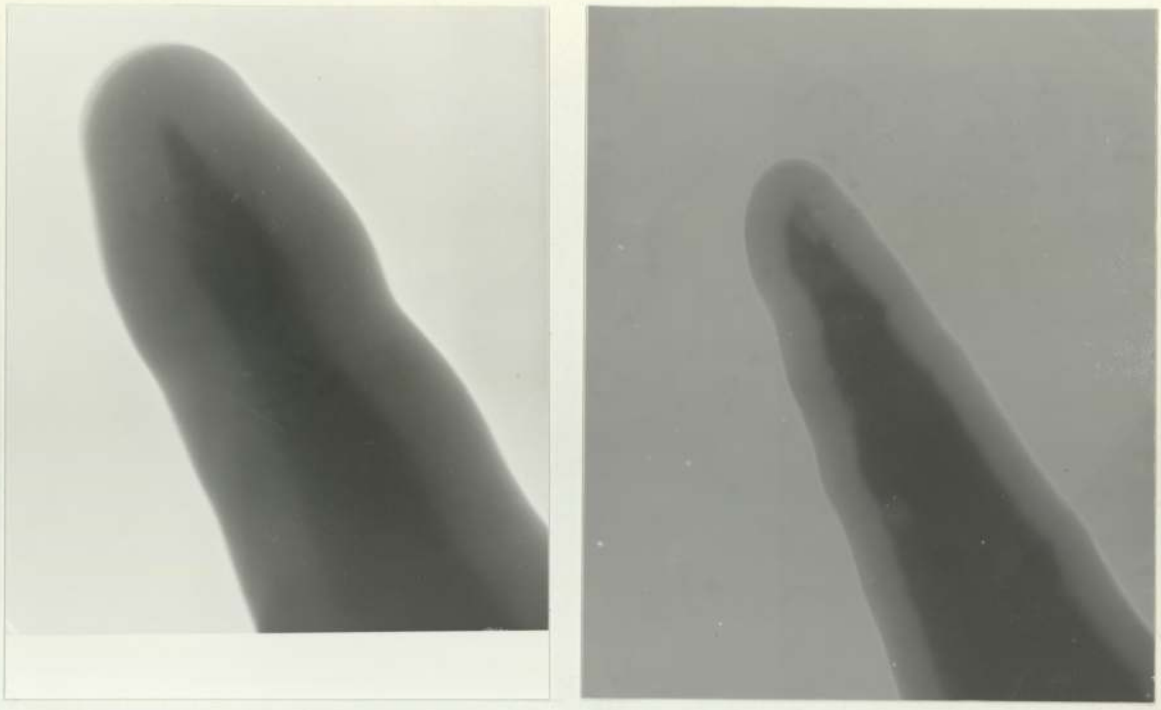

(a) Δd = 0.112 μm.

(b) Δd = 0.095 μm.

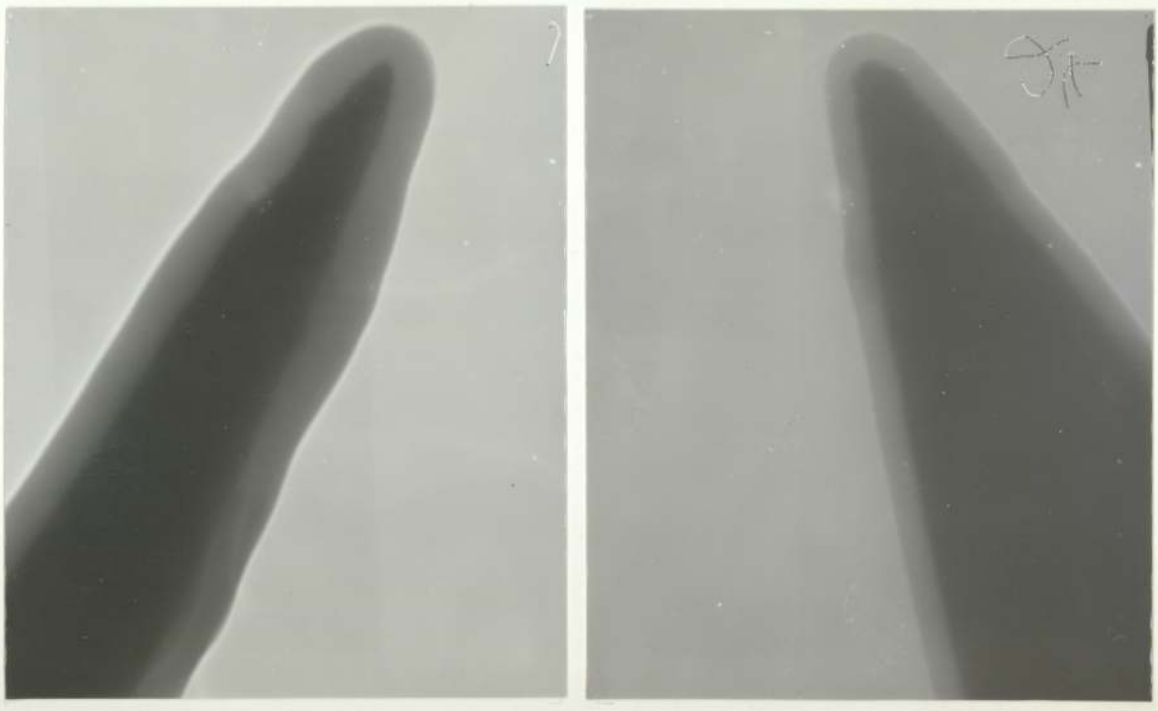

(c) Δd = 0.061 μm.

(d) Δd = 0.042 μm.

Fig. 3.13 Electron micrographs of tungsten tips coated with various thicknesses (Δd) of resin.
(Magnification = 82080X).

and "after" coating with epoxylite resin, while in Fig. 3.13 a, b, c, d are micrographs of tips that have been coated with different thicknesses of the same insulating resin, i.e. ranging from ~0.04 μm to ~0.11 μm (N.B. Further details of the properties of the resin can be found in literature (83).

3.2.1.5 HYDROCARBON COATING

While viewing an uncoated tungsten tip on one occasion in the T.E.M., it was noticed that on focusing the electron beam onto the tip a contaminant layer steadily grew on its surface which was presumed to be formed by polymerised hydrocarbon molecules or silicon base material from the pumping system i.e. the same type of insulating deposits that are well known to "soot up" lens apertures in electron microscopes etc. This effect can be seen in Fig. 3.14, which shows micrographs of the tip before and after contamination, whilst in Fig. 3.15 the sequence (a) to (c) shows the growth of the contaminant film at ~15 second intervals. The most likely origin of this contamination is from the back-streaming organic molecules i.e. either hydrocarbon or silicon arrising respectively from the rotary or diffusion pumps. To verify this, the emitter was subsequently mounted in the S.E.M. and analysed using the X-ray energy dispersive analysis technique. Fig. 3.16 (a) is the spectrum obtained from the shank, well away from the contaminated region of the tip, and shows tungsten peaks; whereas Fig. 3.16 (b) is the spectrum obtained from the tip. Although both spectra were obtained using the same sensitivity, the count rate for the peak at 1.775 Kev is considerably lower in (b), this suggests that some contamination is present on the tip. However, as there are no new peaks present the contamination must consist of elements with an atomic number

(a)

(b)

Fig. 3.14 Electron micrographs of (a) tungsten tip free from contamination (b) after been contaminated with hydrocarbon. (Magnification = 30240X).

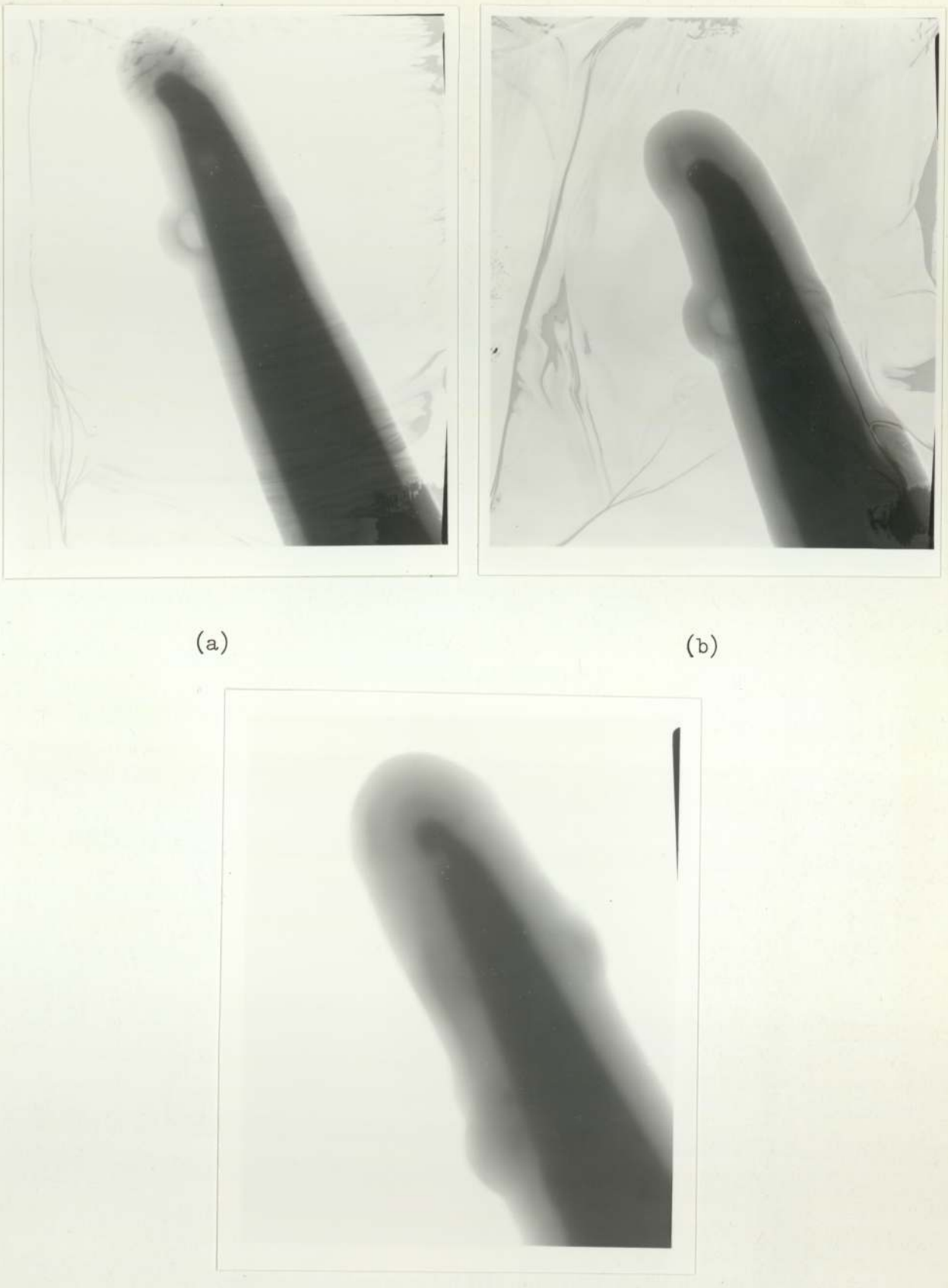

(a) (b)

(c)

Fig. (3.15) A sequence of micrographs showing the building of a hydrocarbon contaminate layer on a tungsten tip. (Magnification = 82080X)

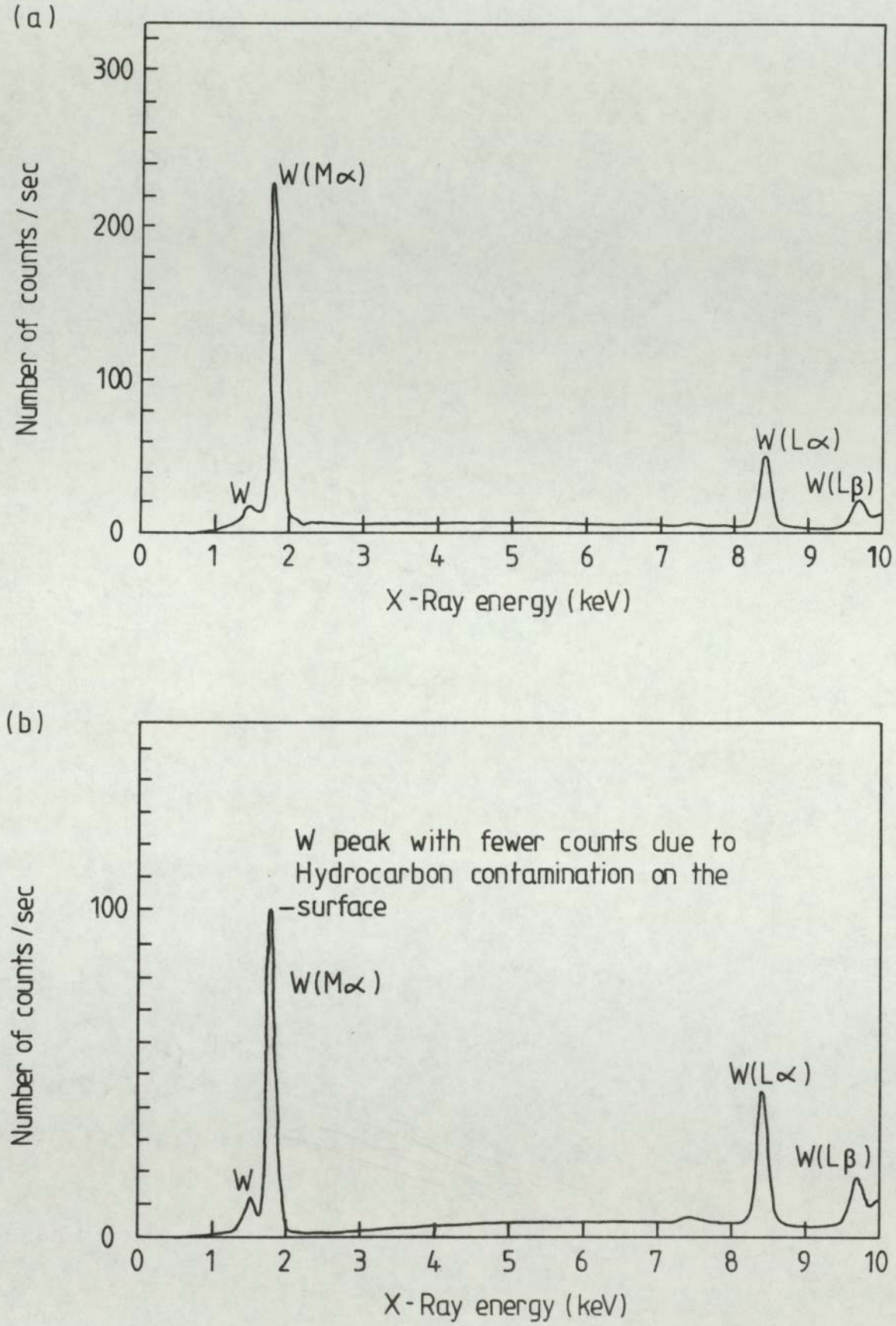

Fig. 3.16 The X-ray energy spectra obtained from

(a) the shank of the tungsten emitter.

(b) the contaminated tip.

less than 9, as this represents the lower threshhold of the analysis technique. By eliminating elements such as nitrogen and oxygen, the contamination can be said to consist predominantly of carbon, in the form of hydrocarbon.

The occurance of such severe contamination was almost certainly due to the poor vacuum conditions in the T.E.M. specimen chamber; in fact this has been independently measured for this instrument and found to be $\sim 10^{-3}$ mbar (84). Since this contamination provides the possibility of accurately controlled coating thickness, the process was potentially very interesting to the present investigation.

It should be noted that in more sophisticated T.E.M.s, using a liquid nitrogen cold finger trap, better pressures are obtainable; so no such contaminant layer forms.

3.2.2. METAL-GLASS EMITTERS

The good insulating properties of glass make it a particularly attractive material for producing composite emitters. Accordingly, a considerable effort was expended to develop a suitable technique for producing a thin layer of glass on a metallic micropoint cathode. Two approaches were investigated, which will be briefly described below.

3.2.2.1 TUNGSTEN MICROPOINT EMITTERS COATED WITH GLASS

For this approach, a tungsten tip was mounted in the specially designed chamber shown in Fig. 3.17 (a) in which the molten glass bead could be electrostatically pulled over the etched sharp tungsten tip, as described below.

A small bead of glass was first deposited as shown at the junction

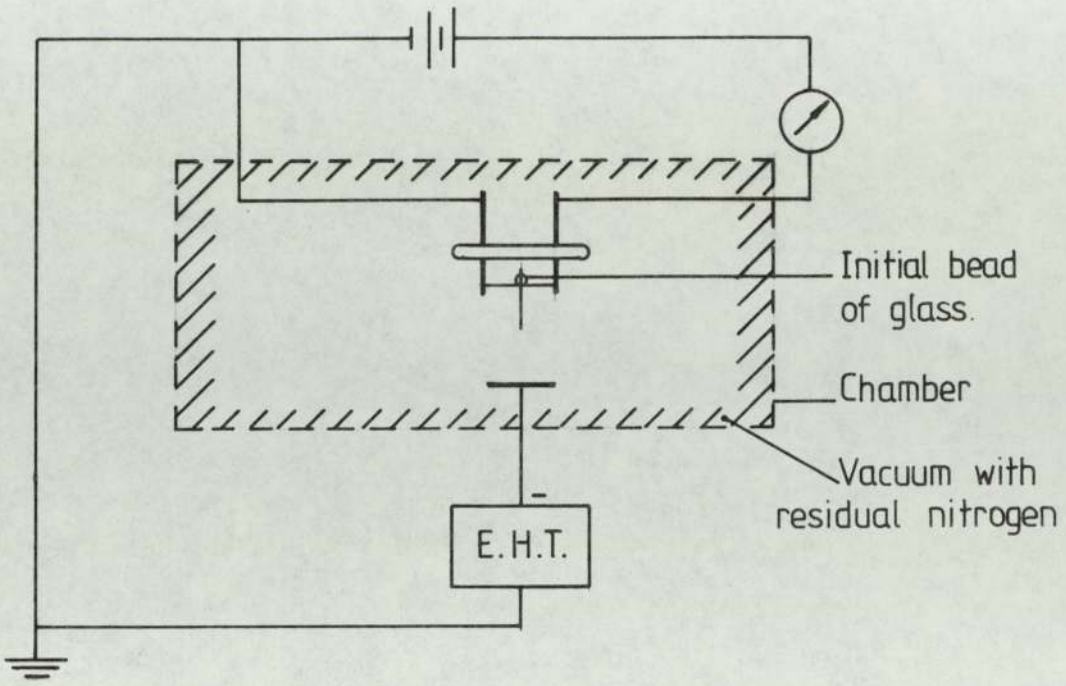

Fig. 3.17 (a) Schematic diagram of the specially designed system which provided the means of extracting molten glass to cover the tungsten tip.

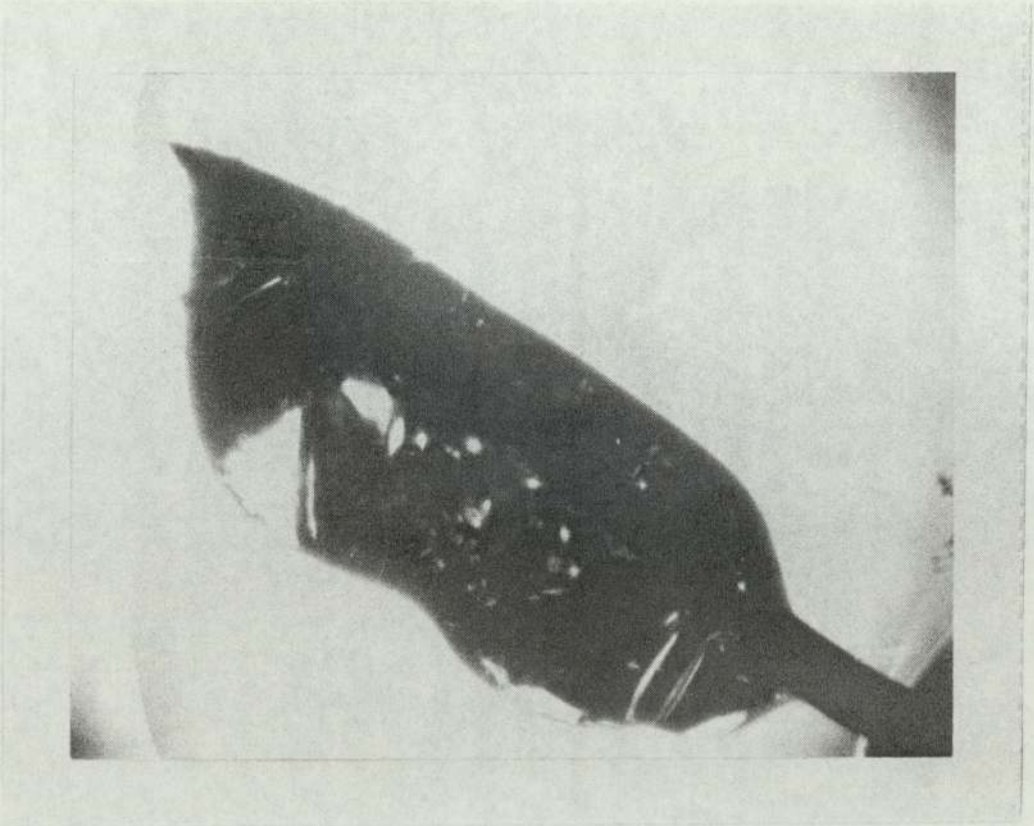

Magnification = 66 X.

Fig. 3.17 (b) A micrograph of tungsten tip coated with glass.

of the tungsten tip and the tungsten bridge, and then a current of $\simeq 2$ A was passed through the bridge in order to melt the glass bead at a temperature of ~ 1400 K. Since it was found that the glowing glass did not move down the emitter shank under gravity to cover the tip, a high voltage was applied to the stainless steel disc which was located perpendicularly to the tip. This caused the whole bead of molten glass to be pulled towards the sharp end of the tip, as shown in the optical micrograph of Fig. 3.17 (b) which is a typical result. It will be seen that this produced a very thick layer of insulator, and although many efforts were made to improve the control of the technique it was not possible to obtain a uniformly thin glass coating of ≤ 5 μm by this method. Subsequent investigations led to another approach which was much more accurate and will be described below.

3.2.2.2 EXTRUSION OF INTERNALLY-CONDUCTING GLASS CAPILLARY TUBES

This approach was based upon a well known capillary tube pulling technique for producing extracted microelectrodes. The basic facility is illustrated in Fig. 3.18 (a) and consists mainly of two bearings, which are located accurately on plates supported by three stainless steel rods fixed rigidly to the frame of the control unit, which serves as a stable base for the instrument. Inside these bearings the lower chuck spindle slides freely and precisely to pull the glass tube (pyrex) down under the action of gravity. The upper chuck can be raised for loading, and the glass tube then located in the furnace loop, the lower chuck is then raised and tightened. If the central section is then heated to ~ 1400 K [85], and a vertical pull applied, the tube will "neck" as illustrated in Fig. 3.18 (b).

For the present application, where the aim is to produce a metal-

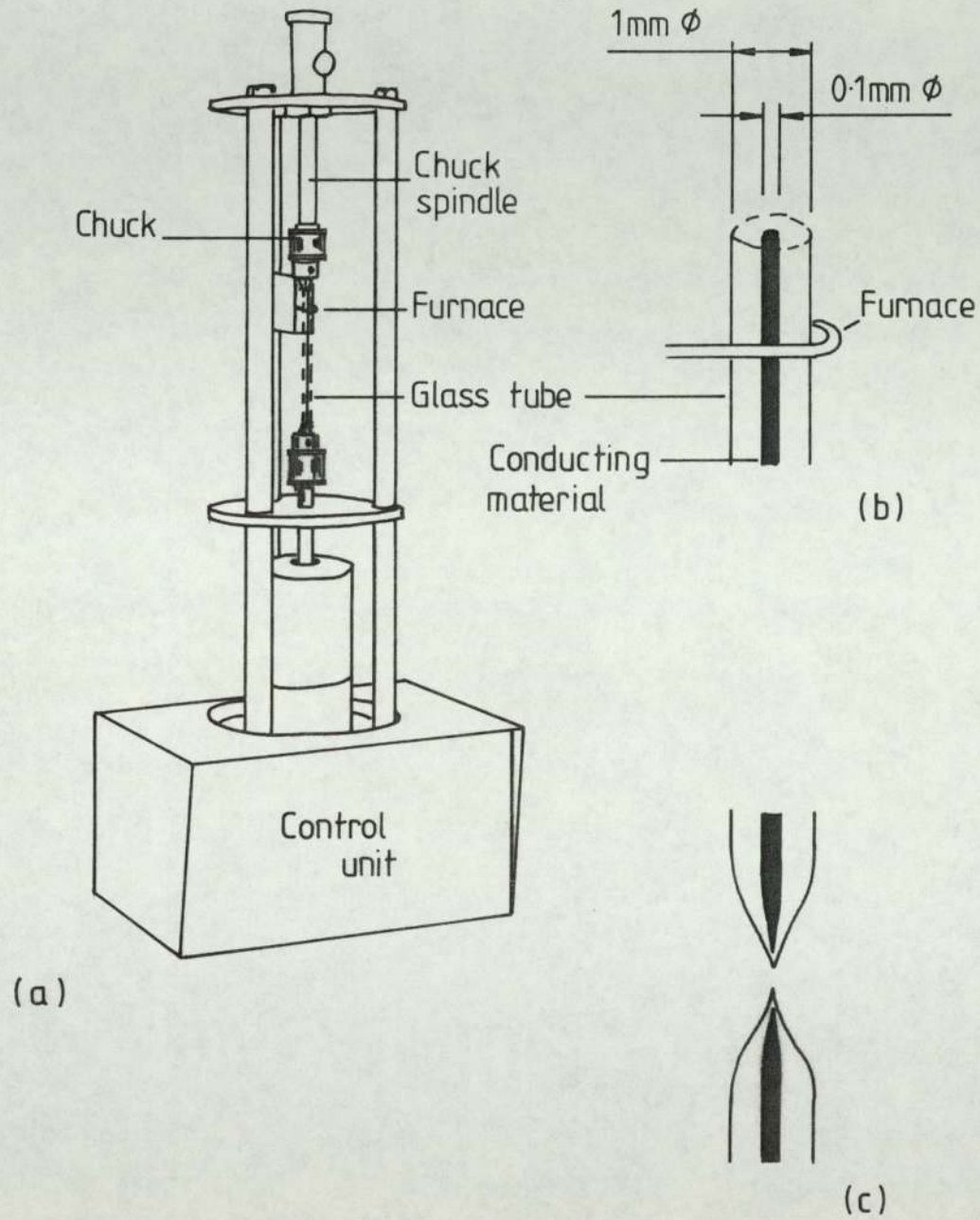

Fig. 3.18 (a) A schematic diagram of capillary glass tube pulling technique

(b) the glass tube before being fixed into the puller

(c) coated glass tips after the pulling process.

insulator structure, it is necessary for the inner wall of the glass tube to have a conducting coating. In order to obtain glass microelectrodes with a conducting central core this core should have a melting point (M.p.) that is less than that of the glass. Several conducting materials were tried, including indium wires (M.p. = 429.8 K), tin wires (M.p. = 505.1 K), tin oxide, gallium (M.p. = 302.9 K) and electrodag 915 (high conductivity silver paint). In the cases of indium and tin it was found that the glass was not wetted by the metal to the extremity of the tip; presumably due to surface tension effects (see Fig. 3.19 (a). To overcome this problem, a subsidiary hydrofluoric acid (HF) etching technique, shown in Fig. 3.19 (b) and (c), was used to remove the surplus glass. It was found experimentally that the tip should be immersed in the acid for the shortest possible time, sufficient to etch the glass protrusion, and then to wash it in water immediately.

Subsequently, this latter procedure was dispensed with by using gallium which was found to be very much more effective in wetting the inner wall of the glass right up to the end of the tip. The only practical problem with using this material was that its very low melting point prevented such tips from being used in bakeable systems. However, an even more satisfactory conducting material than gallium was electrodag 915, this was initially inserted in the glass tube by using a wire plunger, such that after drawning the glass tubes with the puller, sharp tips were obtained which were coated with a film of electrodag, effectively reaching to within few microns of the extremity of the glass tip. An example of such an emitter is shown in the optical micrograph in Fig. 3.20.

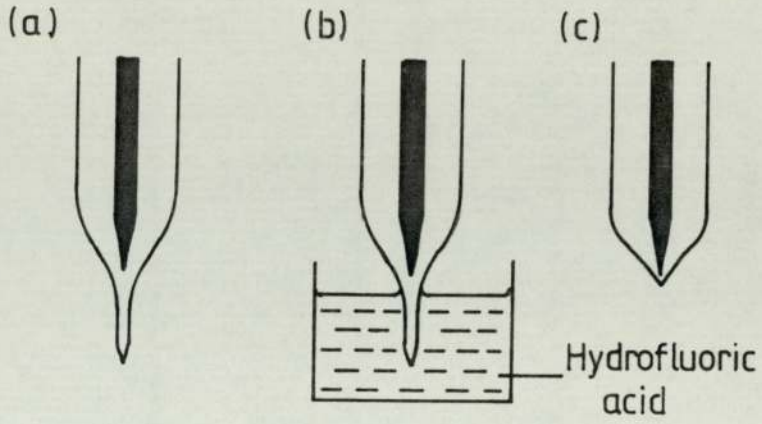

Fig. 3.19 Glass tip before and after etching in hydrofluoric acid.

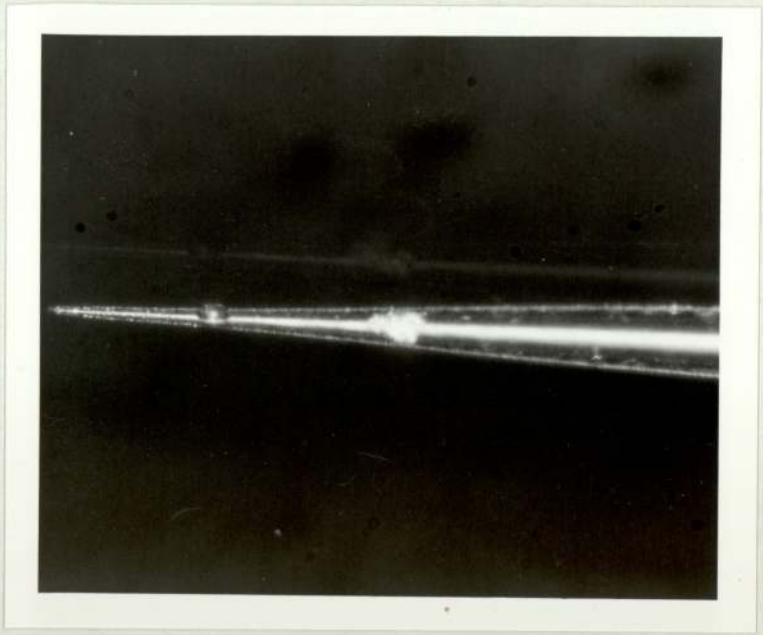

Magnification = 400X

Fig. 3.20 Optical micrograph of a glass tip with an internal film of electrodag.

3.3 DEVELOPMENT OF A HIGH RESOLUTION ELECTRON SPECTROMETER.

The experimental facility described in this section was developed for measuring the field emission energy distributions (F.E.E.D.) of the various types of field electron emission sources whose fabrication techniques were described in the previous section.

3.3.1 INSTRUMENTAL DESIGN.

3.3.1.1 ELECTRON SPECTROMETER SYSTEMS.

The systems used for obtaining the total energy distributions from primary electron sources may be broadly classified according to whether they are the deflecting or retarding potential types. Deflection analysers generally use electrostatic fields to produce energy dispersion, where the energy is determined from a relation between the electron deflection and the applied field strength. Retarding potential analysers however, operate on the principle of an increasing retarding field, such that electrons of increasing energy are progressively repelled before reaching the collector: unlike deflection analysers, these instruments give an integral output which has to be subsequently differentiated to obtain the electron energy spectrum. Several versions of both types of instrument have been described in the literature. The first high-resolution deflector spectrometer was reported by Kuyatt and Plummer (86) who employed a 135° spherical deflecting element to obtain a resolution ~20 m e V: This system was subsequently adopted by Braun et al (87) to use 180° deflection system. Single and double cylindrical deflectors were used respectively by Young and Gomer (88) and Kempin et al (89), giving a wider range of analysed energies: However, operational

problems were encountered, resulting from scattered electrons and stray magnetic fields. Dionne and Rhodin [90] proposed a slightly different type which had the virtue of compact cylindrical symmetry making its assembly and fabrication easier. Isacoon and Gomer [91] described a spectrometer employing electron acceleration to 10 k e V prior to energy analysis: this system minimised the effects of space charge and scattered electrons, whilst maintaining a high resolution (~10 m e V).

Inspite of the fact that the electrostatic deflection analyser is basically a more advanced instrument, having a better performance, a retarding potential analyser was chosen for this investigation because of its simplicity, low cost, ready availability and adequate performance for the project. However, a deflection analyser was also available in the laboratory, should it be necessary to make any high resolution measurements.

An early example of a low resolution retarding potential type of analyser was due to Henderson and co-workers [92, 93] who used a cylindrical geometry to show that field emitted electrons originate from or below the Fermi level. A spherical-geometry retarding-potential device was pioneered by Muller [44, 45], later developed by Muller and Bahadur [46] and finally used by Young and Muller [47] in an improved form with a resolution of $\lesssim$ 30 m e V to measure the total energy distribution of electrons field emitted from a metallic tungsten micropoint emitter. More recently Barnes and Singer [94] used a retarding-potential device for the absolute measurement of the work function of a metallic field emission source.

In 1966, the design by Van Oostrom [39] appeared. This design, which soon became popular, avoided some of the problems connected with the Young and Muller design, e.g. the elimination of

reflected electrons so that it was possible to obtain an improved resolution of ~10 m e V. However, several other workers examined this analyser but they could not obtain a resolution as high as that reported by Van Oostrom, such as Swanson and Crouser [95] where they reported a resolution of ~40 m e V. In a later version Workowski and Czyzewski [96] replaced the electron collector used by Van Oostrom by a hemispherical retarding grid operating in conjunction with an electron multiplier, to achieve a resolution of about 50 m e V; later this was improved by Workowski [97] to 25 m e V. In a computer simulation study, the electron trajectories of the analyser proposed by Van Oostrom were simulated with a digital computer by Hiroshi Adashi et al [98], who showed that it is theoretically possible to obtain much higher resolution than the experimentally obtained value of 10 m e V and that in fact the collector electrode geometry is not very critical and does not need to be hemispherical. Other retarding potential spectrometers have been described by Whitcutt and Blott [99], Plummer and Young [100] and Lea and Gomer [101]. However, except for the design of Plummer and Young, which used a retarding arrangement of a flat condenser symmetry, the others used spherical symmetry arrangements, where typically, the resolution obtained was 10 - 50 m e V.

From the above brief survey, it can be concluded that, whilst the Van Oostrom retarding potential analyser chosen for this study could be expected to have a comparable resolution to that achieved by deflection analysers (viz $\leq$ 30 m e V), it has the disadvantage in its simple form of giving an integral spectral output. Accordingly, considerable effort was expended in developing a sophisticated electronic differentiating system to give the facility a comparable capability to deflection instruments.

It is arguable that it is a disadvantage to use on electrometer as a detector since the electron multiplier is more sensitive, and gives a direct energy distribution output (102, 103, 104). But recently (1980) it was reported that the multiplier is a main source of the signal noise (97) this relates to the statistical character of the secondary emission in the multiplier which depends strongly upon the dynode voltage; therefore the multiplier has to be operated at low gain ($< 10^5$).

3.3.1.2 SPECTROMETER DESIGN.

The basic electron optical design of a Van Oostrom retarding potential analyser is shown schematically in Fig. 3.21 and is seen to consist of a phosphor coated anode A, a lens electrode L and a Faraday cage consisting of a shielding electrode S and a hemispherical collector C. The apertures of the spherical electrodes increase towards the collector and are respectively 1, 2 and 4 mm in diameter, with the radius of the collector being 15 mm. During normal operation an accelerating voltage V_A is applied to the anode A that is sufficient to extract electrons from whatever source is being studied (e.g. a tungsten filament for field assisted thermionic emission or sharp tungsten tip for field emission), whilst a voltage V_L is applied to the lens electrode L such that $V_L/V_A = 0.003$. With this condition satisfied Van Oostrom showed that the electron trajectories will converge to focus near the centre of curvature of the hemispherical collector, so that the electrons will be incident normally on the collector surface, thus the total energy of the electrons will be analysed. In Fig. 3.22 the electrodes of the analyser with the associated equipotentials and the electron trajectories are illustrated. For the electrons to be collected,

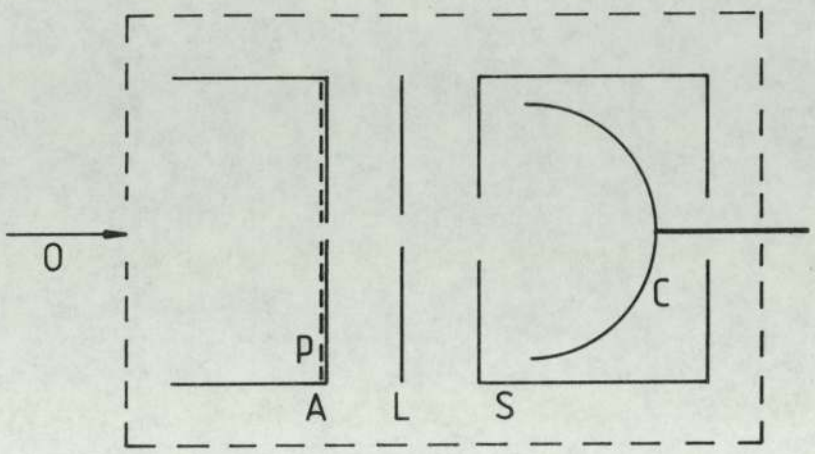

Fig. 3.21 The electrode configuration of a Van Oostrom retarding potential analyser where A is the anode with a phosphored screen P , L is the lens electrode, S is the earthed shield, C is the collector and O is the electron source.

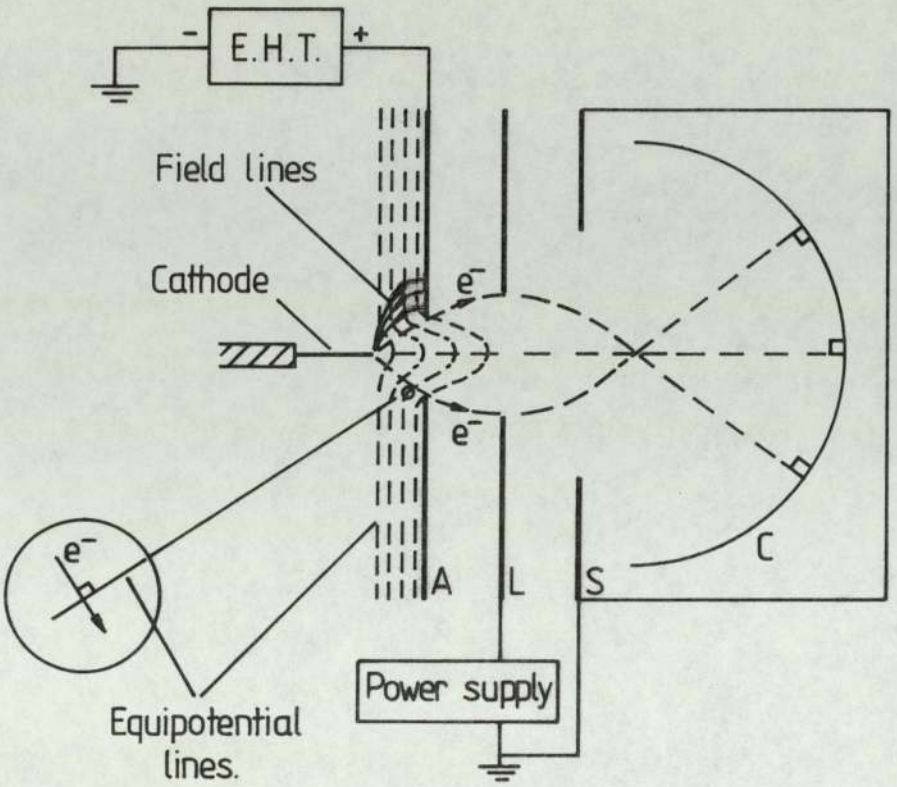

Fig. 3.22 Diagram showing the electron beam (e^-) trajectories due to field enhancement from the sharp point of the cathode and the equipotential lines (dotted) between cathode and anode.

they must have sufficient energy to overcome the work function barrier of the collector, which is effectively at earth potential. Accordingly the cathode has to have a constant negative off-setting bias which is greater than the work function of the emitter (ϕ), i.e. ~ 4.5 volts in practice. To measure the spectrum of an electron source, a slowly increasing positive voltage V_c is applied at the cathode so that the lower energy electrons will be progressively repelled from the collector as V_c is increased, with only the most energetic electrons being collected at the highest value of V_c. A typical integral plot showing the variation of the collector current I_c as the cathode voltage V_c is increased is shown schematically in Fig. 3.23 (a), while, for comparison, the differential of this plot, which represents the free electron energy distribution is shown in Fig. 3.23 (b). (The various electronic systems developed for obtaining such plots will be described in section 3.3.1.4).

A sectional view of the complete spectrometer facility is given in Fig. 3.24 . This shows the stainless steel U H V chamber, the analyser, the specimen holder and manipulating facility, the viewing port for observing emission images, and the electrical feed-throughs for the analyser and other electrode systems. To give a further perspective of the facility, Fig. 3.25 gives an overall external view of the apparatus, whilst Fig. 3.26 shows a close-up view of the analyser itself and Fig. 3.27 the experimental chamber. The various sub-systems will now be discussed in further detail.

THE VACUUM SYSTEM:

This was designed to be capable of achieving ultra high vacuum conditions (i.e. $\lesssim 10^{-9}$ mbar) thus providing the necessary environment to study the emitting properties of clean surfaces. The

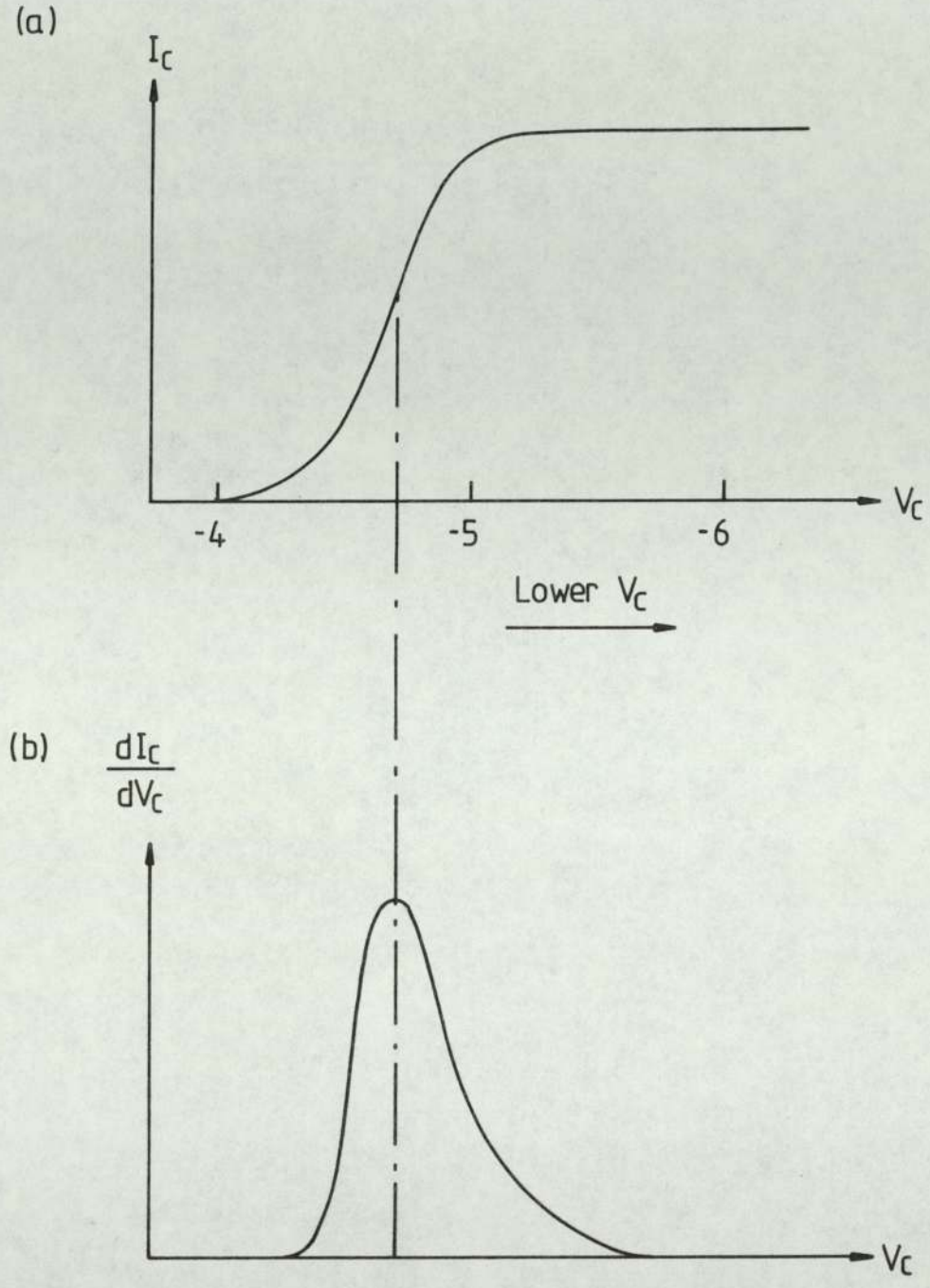

Fig. 3.23 (a) A typical schematic integral plot showing the variation of the collector current I_c as a function of the cathode voltage V_c, and (b) its corresponding differential plot.

(1) Viewing port

(2) Ancillary disc anode

(3) Specimen support rod

(4) Specimen holder

(5) Specimen e.g. field emitting tip

(6) Anode

(7) Analyser lens electrode

(8) Shield

(9) Collector

(10) " Turn Buckle" providing adjustment of the x direction movement of the specimen

(11) High voltage electrical feed-throughs

(12) Bellows

(13) Screws to control the z directional movement of specimen via carriage 14

(14) Threaded carriage which controls the specimen y movement

(15) Rotary drive for specimen manipulation in the x-z plane

Key to Fig. 3.24

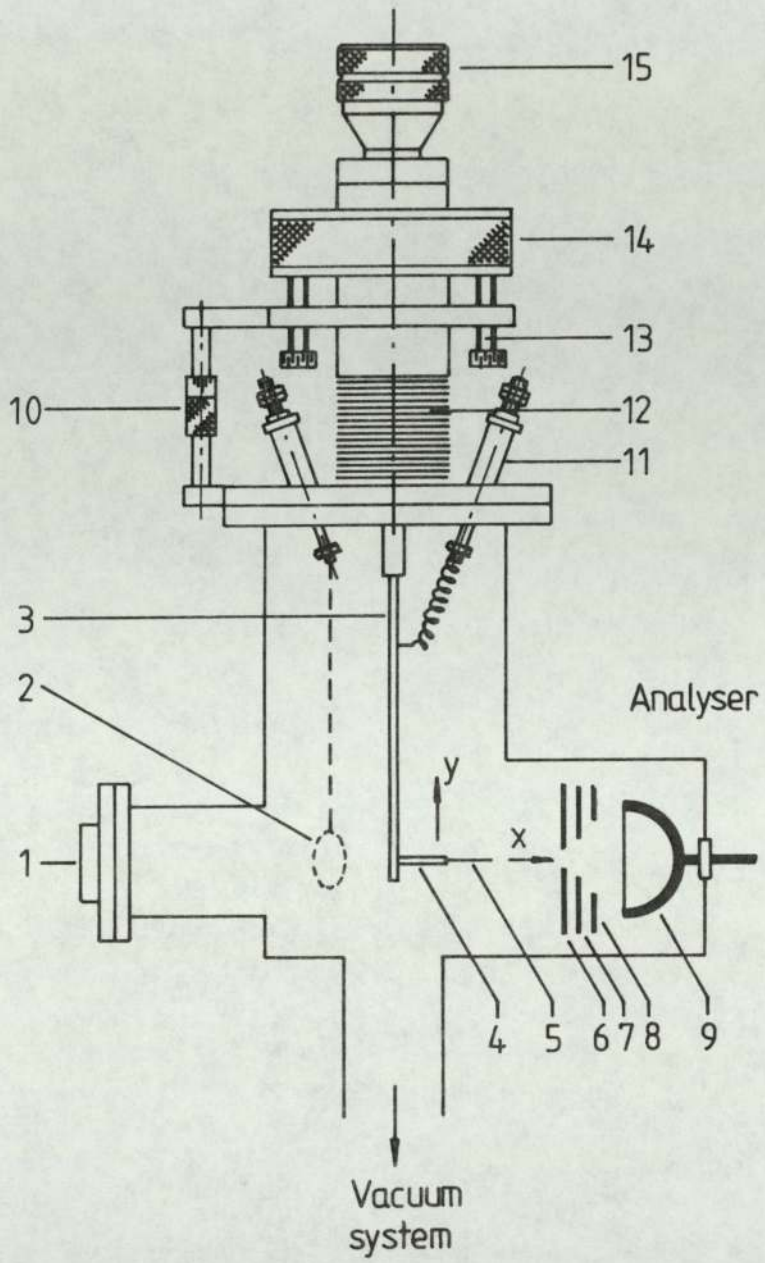

Fig. 3.24 General section through spectrometer chamber.

Fig. 3.25 A general exterior view of the spectrometer and the associated equipment.

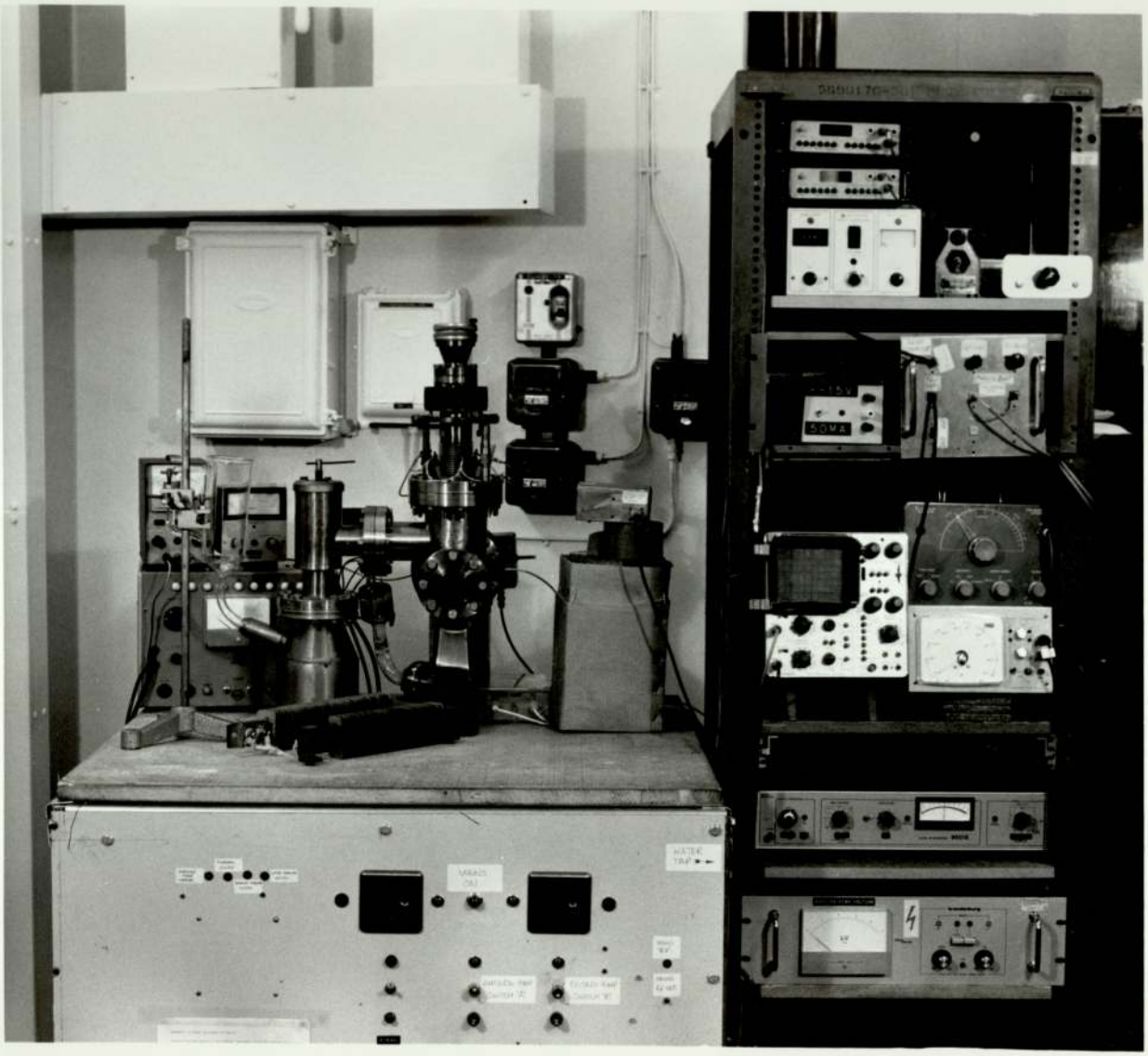
50MA
WATER TAP

Fig. 3.26 A photograph showing a close-up view of the analyser.

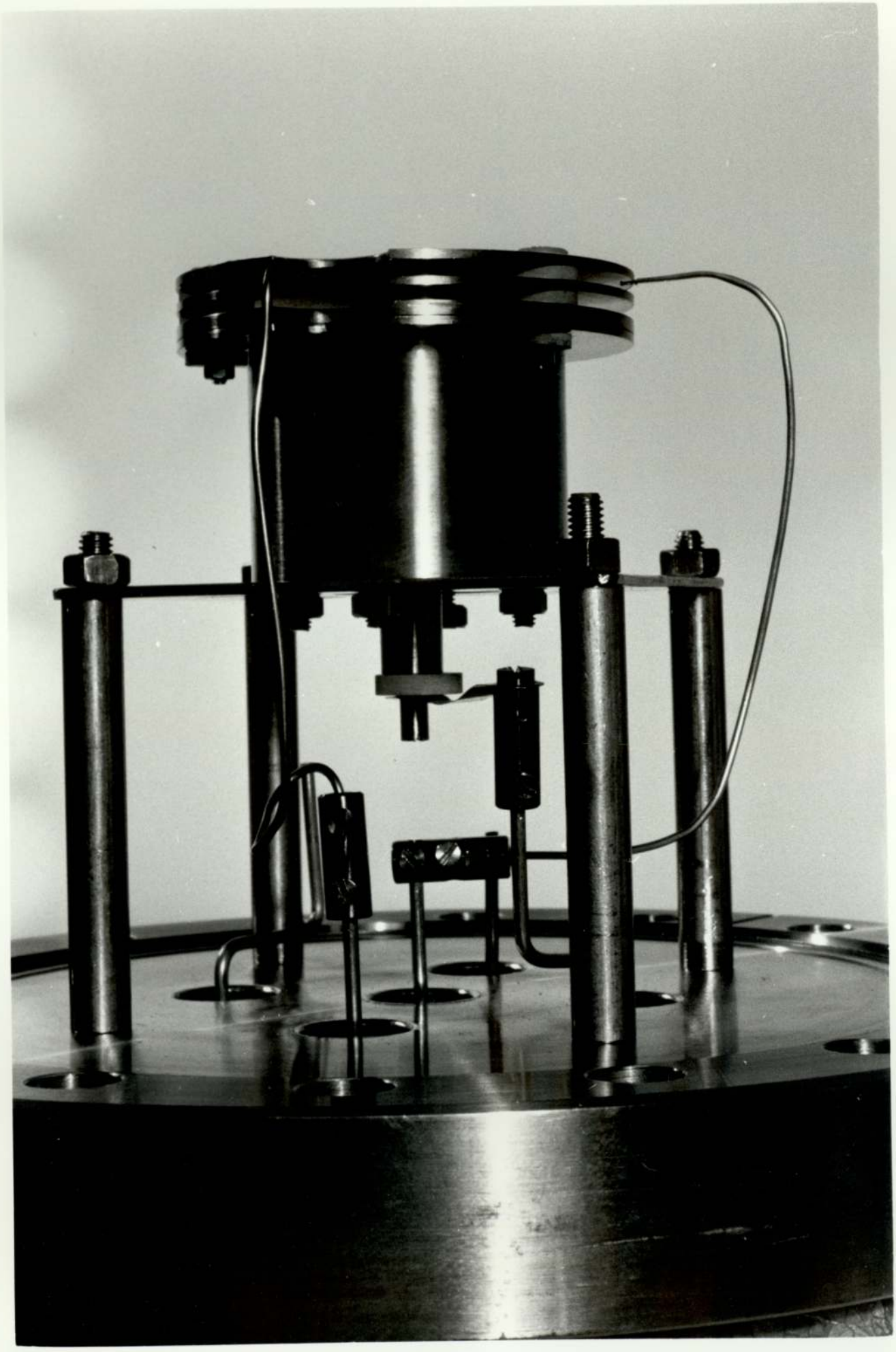

Fig. 3.27 A photograph showing a close-up view of the experimental chamber.

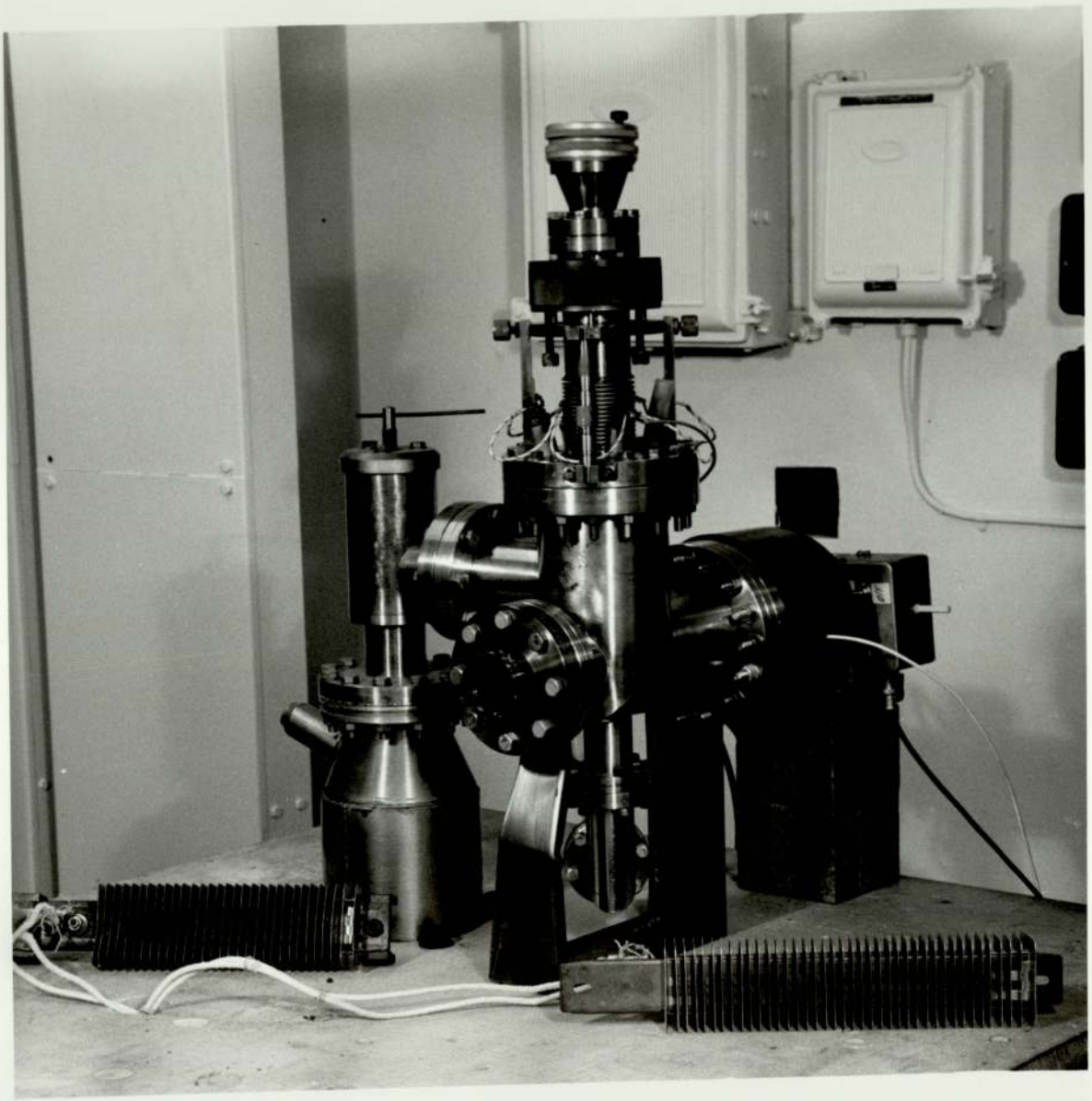

chamber was evacuated by a combination of rotary and diffusion pumps, such that by baking the chamber overnight to a temperature of about 200°C, and then filling the liquid nitrogen trap situated between the diffusion pump and the experimental chamber, a pressure of $\sim 5 \times 10^{-10}$ mbar was achieved. The vacuum system also included various safety devices to protect it from electrical power cuts, water failure or any possible operational error.

3.3.1.3 SPECIMEN HOLDER AND MANIPULATOR.

In order to successfully conduct experiments using microemitters, it is essential to have both a versatile specimen mounting system and an adequate manipulator to allow accurate positioning of the microemitter relative to the anode aperture. The specimen holder used for early experiments, particularly those for thermionic emitters, is fully illustrated in Fig. 3.28 (a). With this system, the specimen manipulation restricted the available movements to the x, y and z axes, thus limiting the view of the emission image on the phosphored anode, due to the large size of the specimen holder. Referring to Fig. 3.24, in order to provide spatial adjustments of the specimen, the screws (13), the brass threaded carriage (14) and the "turn buckle" (10) were used repspectively to provide x, y and z axes movements.

Subsequently, this specimen holder was abandoned as it was found that rotational motion of the specimen holder about a vertical axis was necessary. Accordingly, a smaller version, shown in Fig. 3.29, provided 360° rotation of the specimen holder about a vertical axis, which thus gave complete flexibility when locating any part of an emission image over the anode probe hole. In addition, it allowed a tip to be rotated through 135° and positioned opposite an ancillary

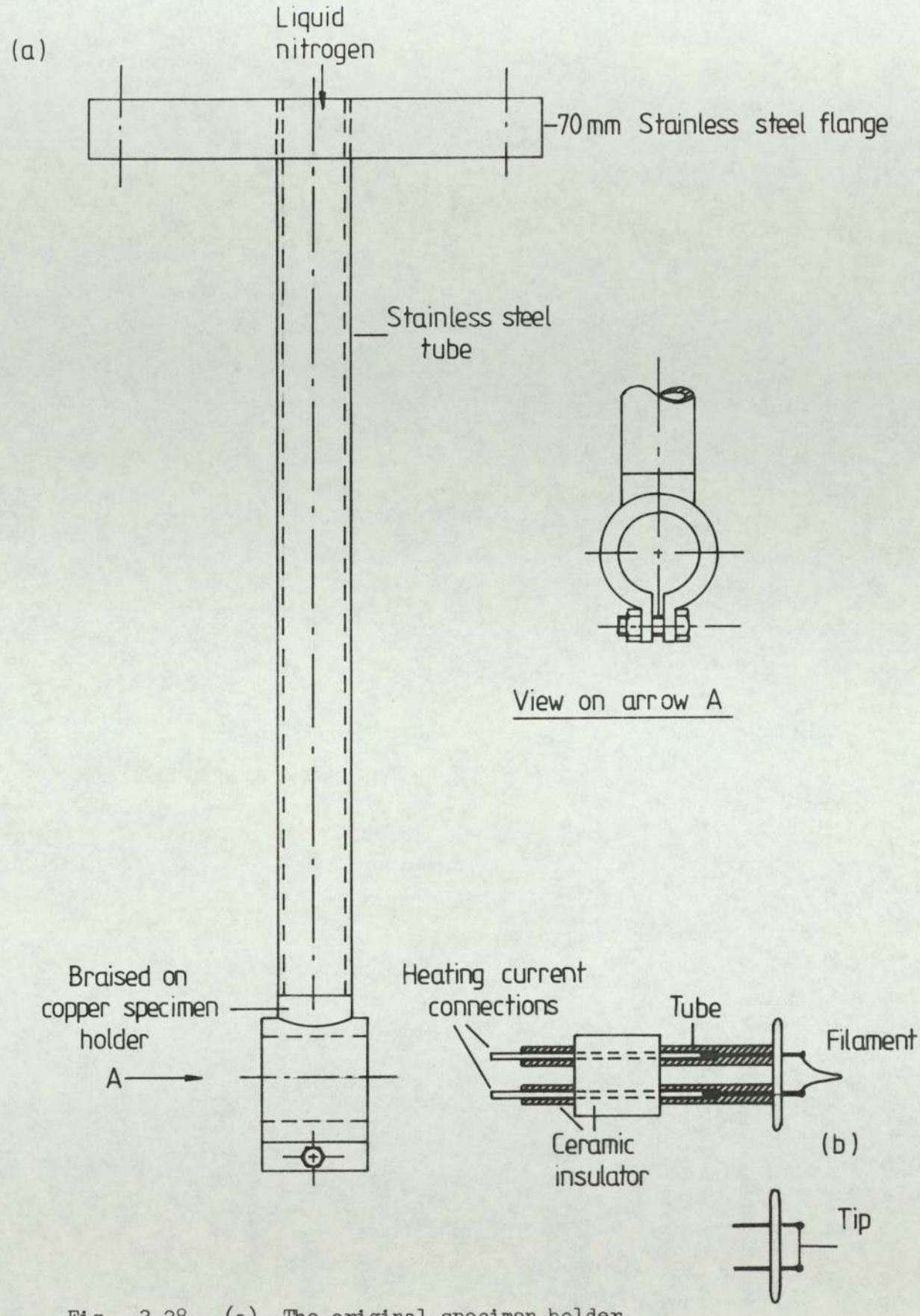

Fig. 3.28 (a) The original specimen holder,

(b) a standard electron microscope tungsten thermionic emitter with the required insulation and fittings for carrying the heating current, and

(c) a 0.1 mm diameter tungsten microemitter, spot welded to a 0.2 mm diameter bridge wire.

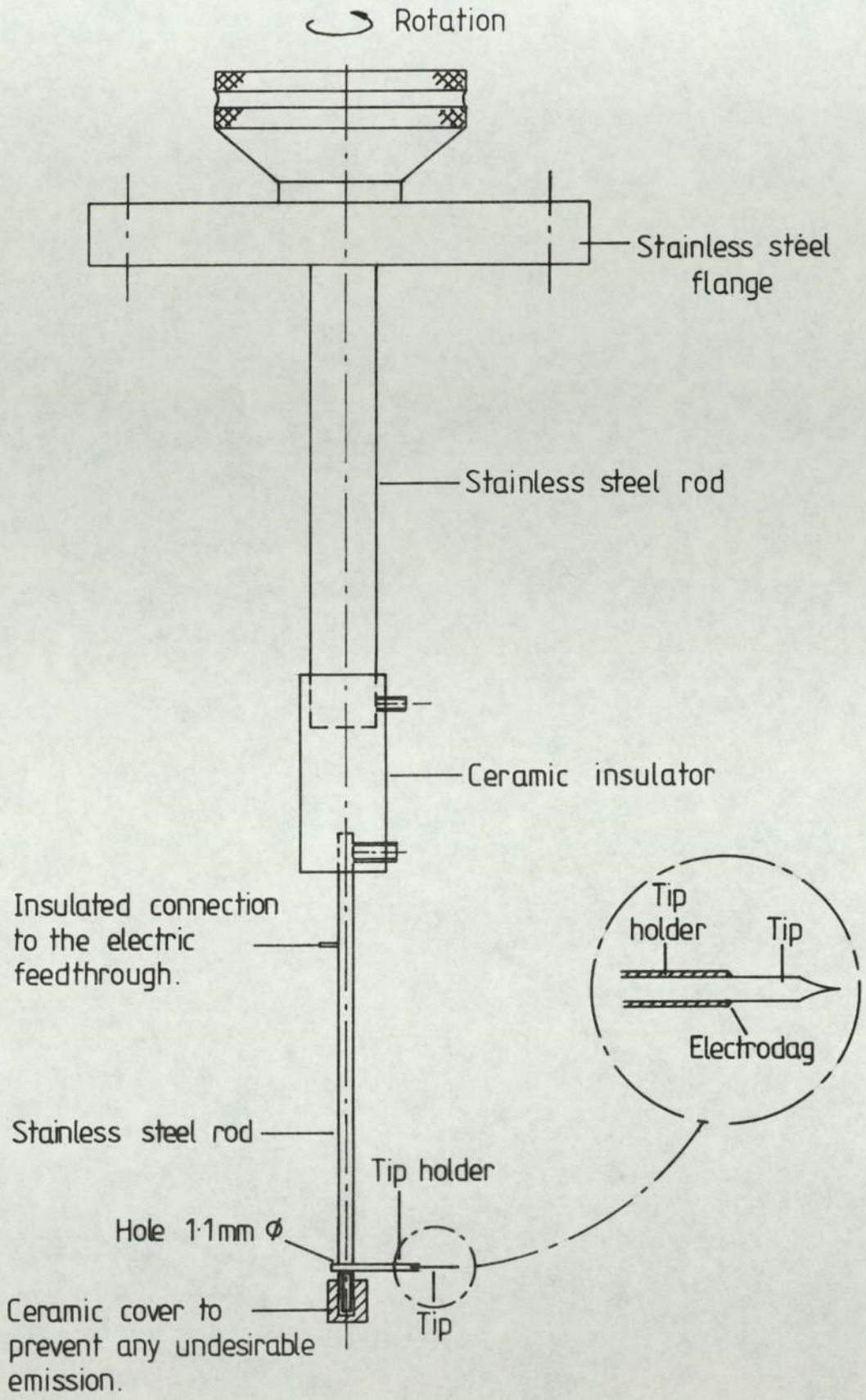

Fig. 3.29 Rotatable specimen holder, showing a 0.1 mm diameter tungsten microemitter fitted into a 0.11 mm stainless steel tube.

Fig. 3.30 A photograph illustrating the specimen holder, the manipulator and the ancillary anode.

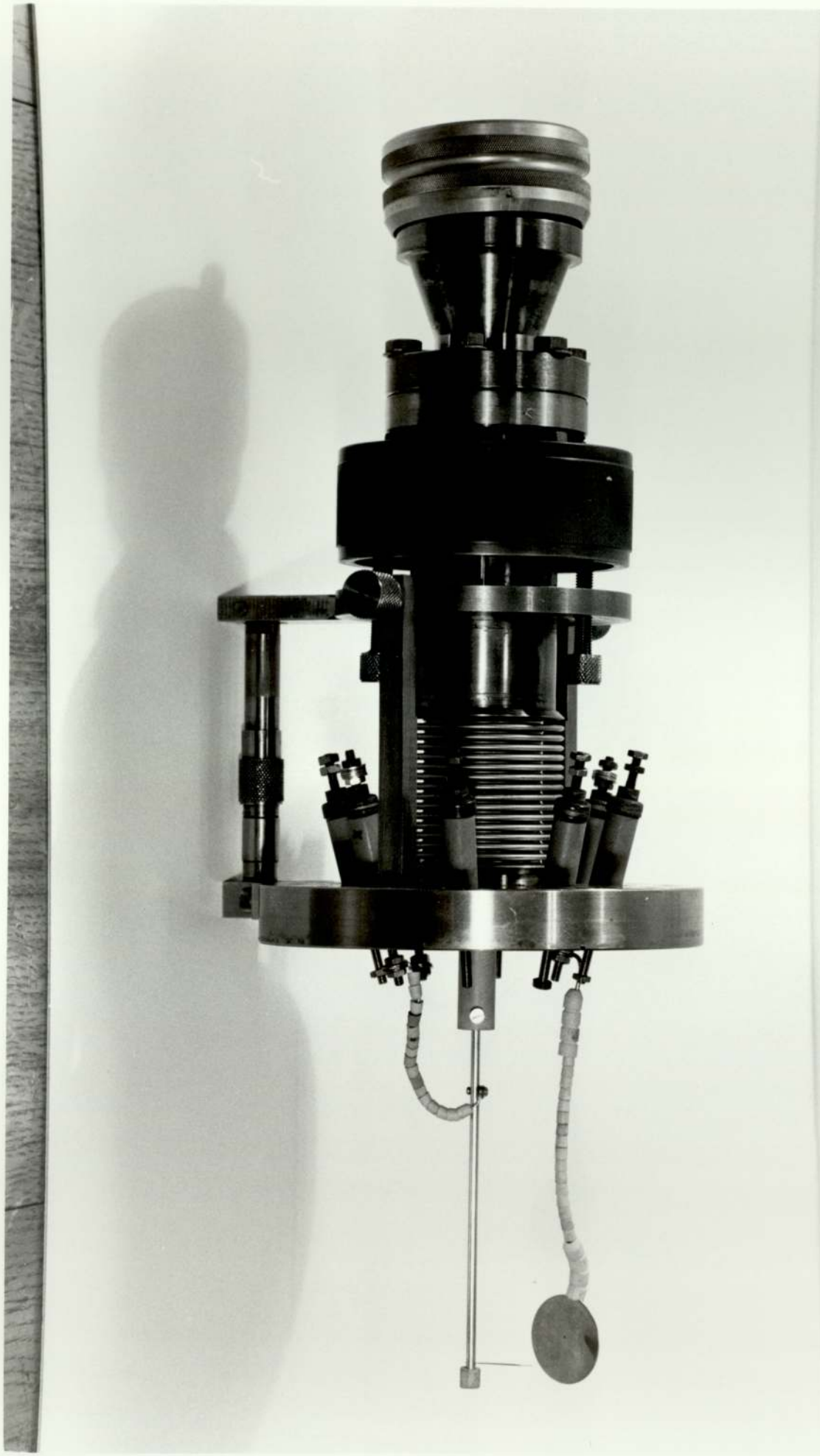

anode either for subsequent observation of any optical effects associated with the emission of electrons, or for studying the long term (Tens of hours) stability of the emission currents. This ancillary anode was used in order to prevent accelerated degeneration of the phosphor screen due to various electron impact phenomena. Finally Fig. 3.30 is a photograph of the final version of specimen stage, showing the manipulator and the ancillary anode, i.e. as shown schematically in Fig. 3.24 .

3.3.1.4 ELECTRONIC SYSTEMS.

As already intimated, the electronic control systems of the analyser provide automatic facilities for measuring either, the "integral" or "differential" form of the energy distributions, of electrons emitted from thermionic or field emission sources.

(a) INTEGRAL PLOTS.

The circuit used for obtaining these plots is shown in Fig. 3.31, for both a field emitting source (full line), and a thermionic electron source in the form of a directly heated hairpin tungsten filament (chain-dotted lines), as was used for the initial calibration of the instrument. It will be seen from Fig. 3.31 that for thermionic measurements the filament was heated by a "floating" 2 volt battery, and also that it was bridged by two resistors of equal value so that their mid-potential corresponded to that of the tip of the emitter. Hence, for both types of source, the cathode-anode E.H.T. voltage (typically $\sim$500 - 1000 Volts) and the retarding ramp voltage (details given below) used for scanning through the range of the electron energies as previously described,

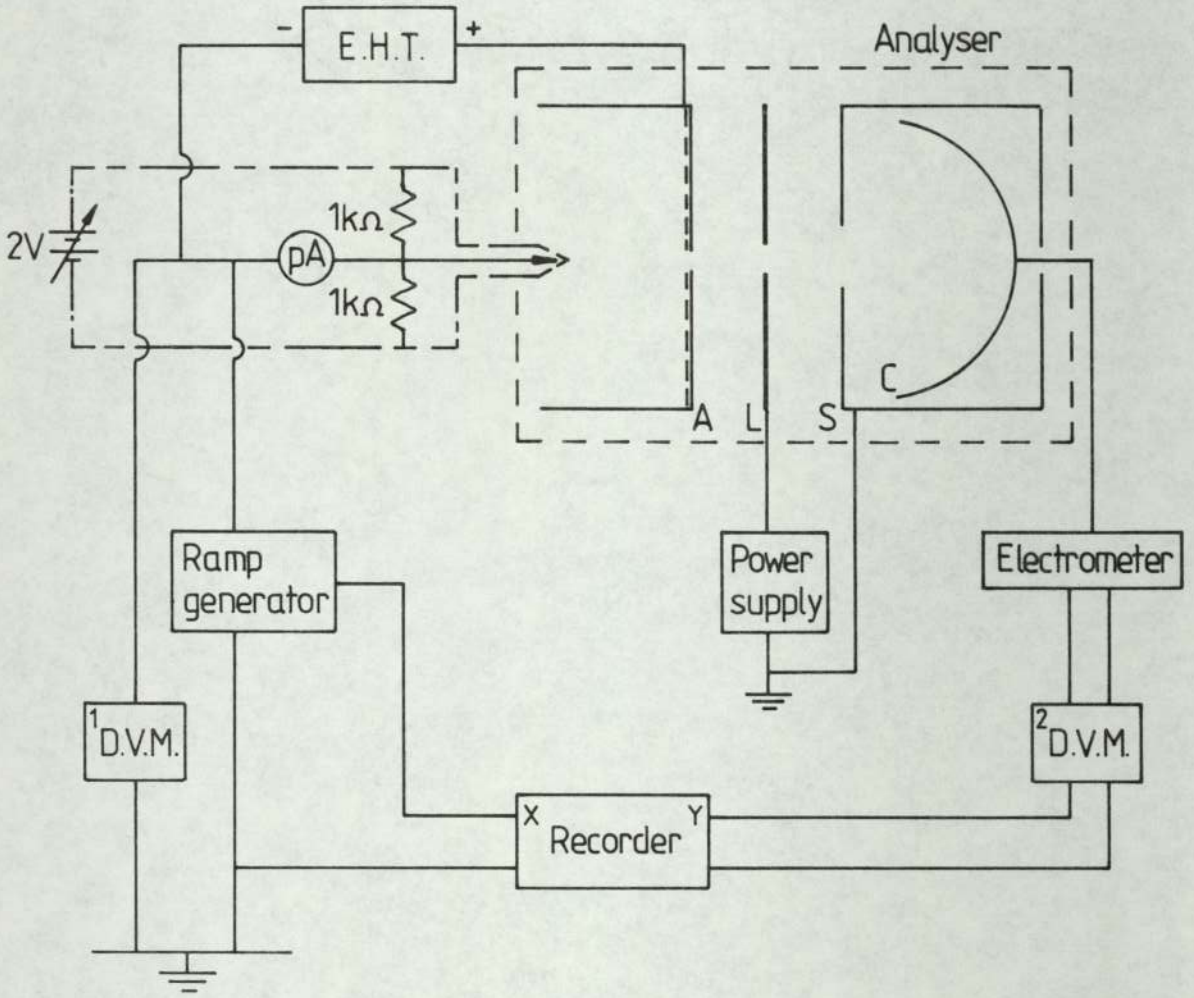

Fig. 3.31 The circuit used to produce integral plots for field emitting sources (full line) and a thermionic electron source (chain-dotted lines).

are effectively applied to the emitting point. This arrangement also has the further important advantage of providing a constant accelerating voltage (and hence constant emission current) during scanning. The collector current I_e (see section 3.3.1.2) was detected by a purpose-built electrometer as described below in conjunction with a D.V.M.$_2$. The E.H.T. was obtained from a 0-5 k v Brandenburg Type 507 R alpha series unit, whilst the lens electrode was fed from a 0 - 30 volts low-voltage supply. An X-Y recorder was initially used to record the spectrum, but this was later replaced by a storage oscilloscope fitted with a poloroid camera to obtain photographs.

ELECTROMETER.

The electrometer input incorporated a Field Effect Transistor (F.E.T.) operational amplifier having a $10^{12}\,\Omega$ input resistance (Type R.S. 307-250) as shown in the circuit diagram of Fig. 3.32 . Since this device also operates as a virtual earth amplifier, the output impendance will be low, and hence it can be assumed that all the input current (I_{in}) flows through the feedback resistor (R_f). Therefore if the switch is in position C, it follows that

$$V_{out} = - I_{in} R_f \qquad (3.1)$$

which is the equation of a current-to-voltage converter. However, the potential divider connected across the output, allows a fraction (N) of V_{out} to be developed across R_f, where N could be chosen to have values 0.01, 0.1 and 1 according to whether the switch was in position A, B, or C.

Equation (3.1) can now be written

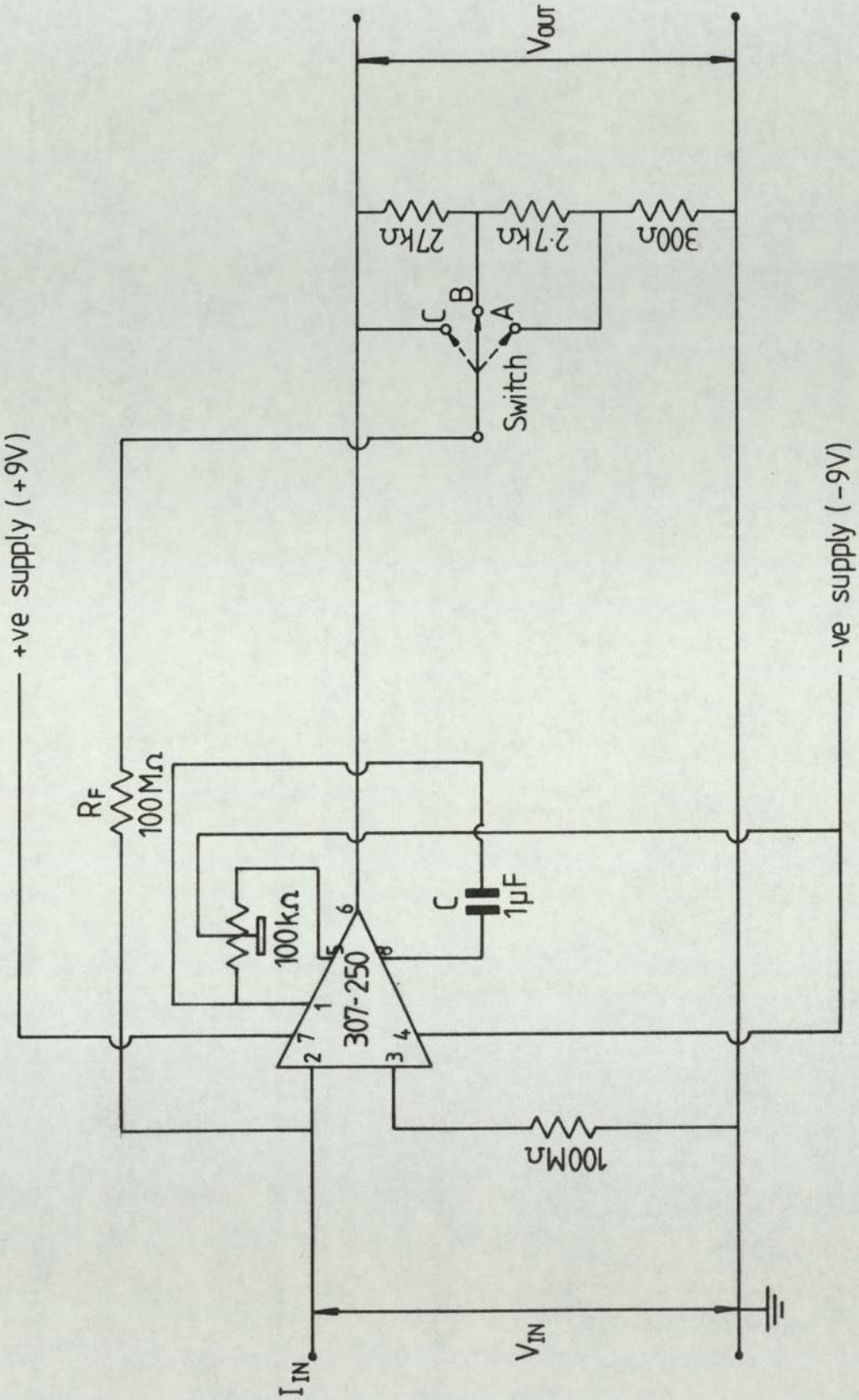

Fig. 3.32 The electrometer circuit diagram.

$$N V_{out} = - I_{in} R_f \qquad (3.2)$$

or $$V_{out} = - I_{in} (R_f / N)$$

so that, with V_{out} = 10 Volts, R_f = 100 MΩ and for the switch positions A, B and C, the current for F.S.D. (full scale deflection) will be 10^{-9}, 10^{-8}, 10^{-7} A respectively. The 1 μ f capacitor C was incorporated to provide operational noise rejection, which was particularly prevalent for the thermionic emission case, however, its value was reduced to 0.22 μ f for field emission use, since a greater bandwidth was required to handle the much faster scan.

RAMP GENERATOR.

As shown in the circuit diagram of Fig. 3.33 the ramp generator consists of two stages. The first stage "A" consists of a 741 operational amplifier connected as an integrator, which is used as follows to generate a controlled ramp voltage (105). Thus if the capacitor current is I_f , one has

$$I_f = \frac{d q}{d t}$$

$$= C \frac{d V_2}{d t} \qquad (3.3)$$

since C is constant

Also, the input impedence of the operational amplifier is high enough to be neglected, and its input voltage V, will be very low in comparison to its output voltage, so that port No 2 is virtually at earth potential. Therefore,

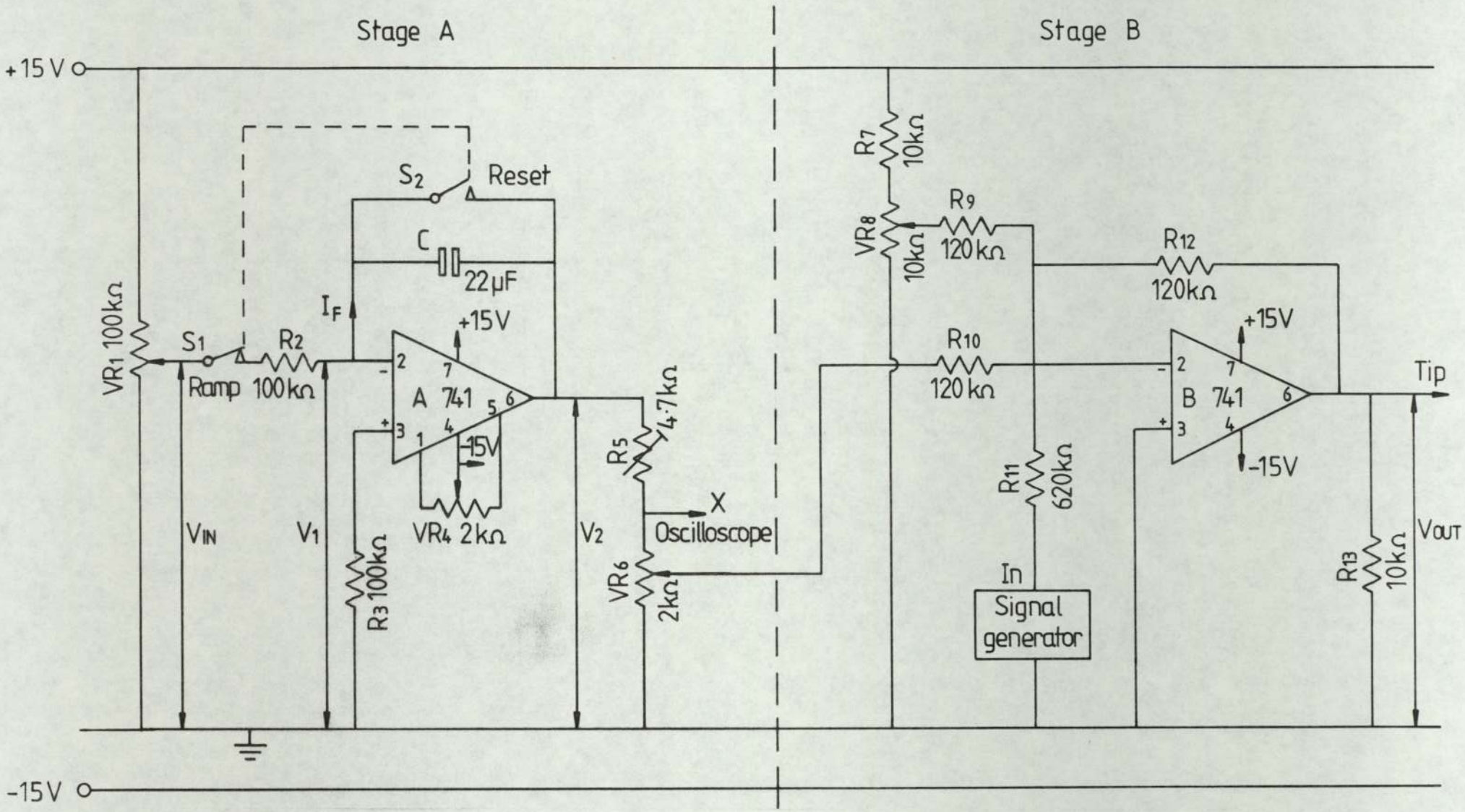

Fig. 3.33 Ramp generater A and a unity gain inverting amplifier B. The signal generater SG is incorporated for modulating the ramp when a differential plot is required (see section 3.3.1. 4(b)).

$$I_f = - \frac{V_{in}}{R_2}$$

or $$\frac{C \, d \, V_2}{d \, t} = - \frac{V_{in}}{R_2} \qquad (3.4)$$

Integrating equation (3.4) gives

$$C \int_0^t \frac{d \, V_2}{d \, t} \, d \, t = - \frac{1}{R_2} \int_0^t V_{in} \, d \, t$$

or $$V_2 = - \frac{1}{C \, R_2} \int_0^t V_{in} \, d \, t$$

which, with V_{in} held constant and $V_2 = 0$ at $t = 0$ gives

$$V_2 = - \frac{1}{C \, R_2} \; V_{in} \; t$$

(N.B. Further details of this type of circuit can be found in references (106, 107, 108)).

The output of I.C. A is thus a negative going ramp as illustrated in Fig. 3.34 , having a gradient of $V_{in} / R_2 \, C$, with V_{in} controlling the ramp rate via the control potentiometer $V.R._1$. The second stage "B" consists of a summing inverting amplifier which takes a fraction of the ramp voltage output of stage "A", as determined by $V.R._6$, and adds it to a fraction of the d.c. supply voltage, determined by $V.R._8$, together with a low amplitude sine-wave from the signal generator. The output of stage "B" thus consists of a variable positive going ramp voltage, having a pre-set starting

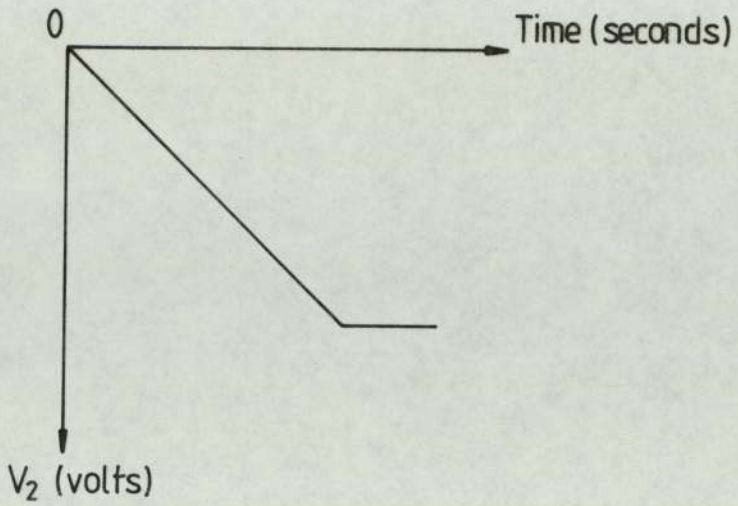

Fig. 3.34 A negative going ramp at the output of Integrated Circuit A.

point, in series with a sinusoidal signal. The X drive for an oscilloscope is provided by tapping off a suitable fraction of the ramp generator output at point X.

(b) DIFFERENTIAL PLOTS.

These were obtained by electronically differentiating the integral signal recorded by the electrometer in the circuit of Fig. 3.31 . The standard procedure which was adopted for differentiation (109) consisted of sinusoidally modulating the emitted current at a given reference frequency ω and then to use a lock-in amplifier to detect the component of the collected current that had this frequency ω : the amplitude of the a.c current will then be proportional to the gradient of the integral plot "d.c" signal. To further clarify this principle, Fig. 3.35 illustrates schematically how the integral signal is differentiated. The actual circuit used

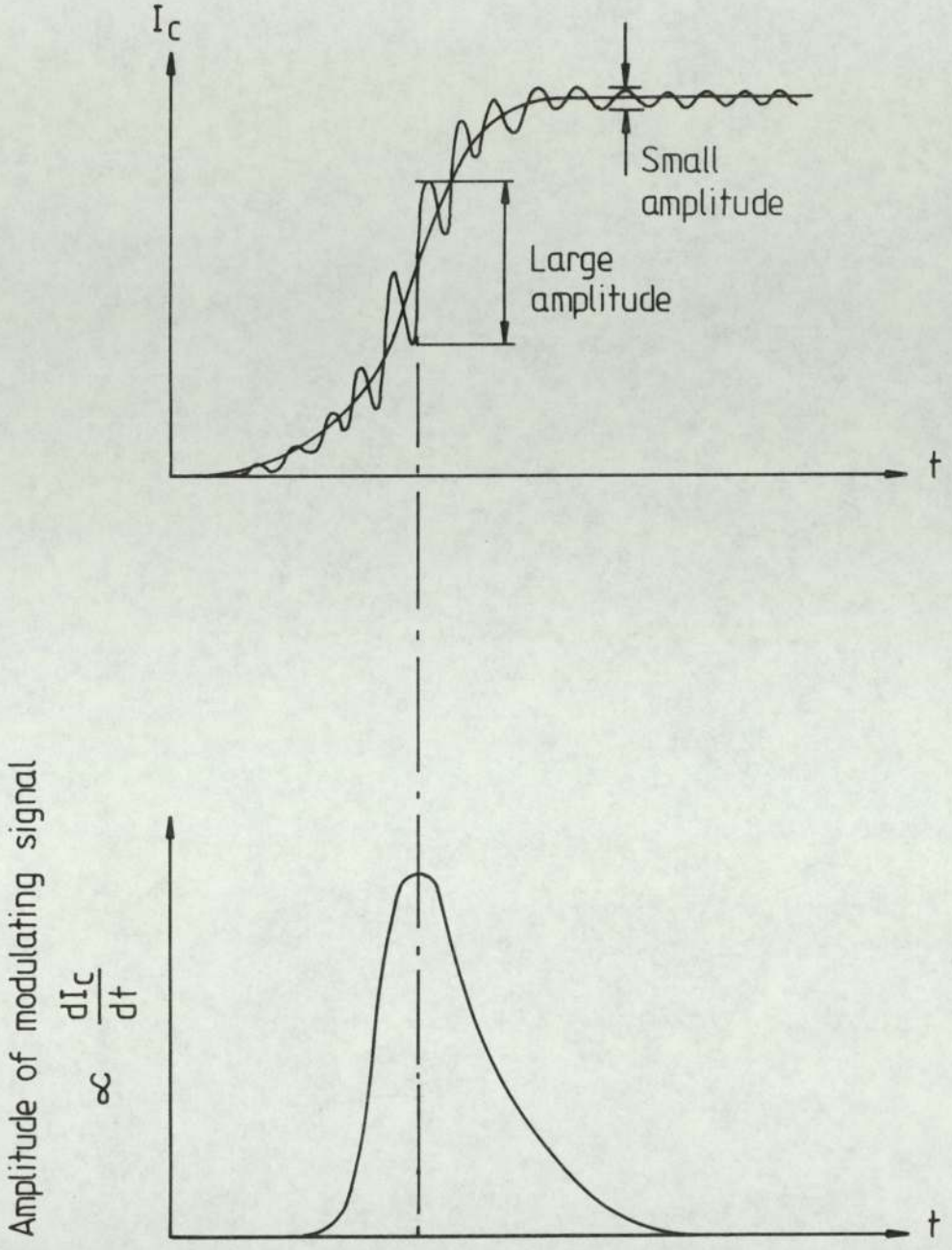

Figure 3.35 A schematic plot representing the relationship between the integral and differential plots.

for recording the differential form of the spectrum is shown in Fig. 3.36 , as applied to a field emitting tip. From this it will be seen that the sine-wave generator is used not only to modulate the ramp voltage (see Fig. 3.33), and hence the collected current I_c , but also to provide the reference signal to the lock-in amplifier, whose operational principle is outlined below.

THE LOCK-IN AMPLIFIER.

The lock-in amplifier output, which gives the differentiated signal, is fed to the Y-input of the X-Y recorder (or oscilloscope). The output of this system, which uses phase sensitive synchronous detection or modulation, is the first derivative of the signal being detected if the amplitude of modulation is made small [110]. The instrument used for this study was an Ortec Brookdeal 9501 E broad-band lock-in amplifier which incorporates a variable gain a.c amplifier, a reference section with phase-shifting facilities, a precision demodulator and output d.c amplification and filtering. A simplified diagram of the system is shown in Fig. 3.37 . Briefly, the a.c amplifier provides gain or attenuation of the signal of interest (the electrometer output in this case), to give a signal input of the correct level to the phase demodulator, and to provide a high impedence interface at the signal input. The reference channel then generates a symmetrical square-wave to drive the reference input of the demodulator; this wave form may be either of the same frequency, or twice the frequency, of the modulated collected current. The demodulator may then be thought of as a linear gating circuit which is controlled by the reference input waveform. A particularly important feature of this circuit is its ability to handle noise signals several million times greater than any error

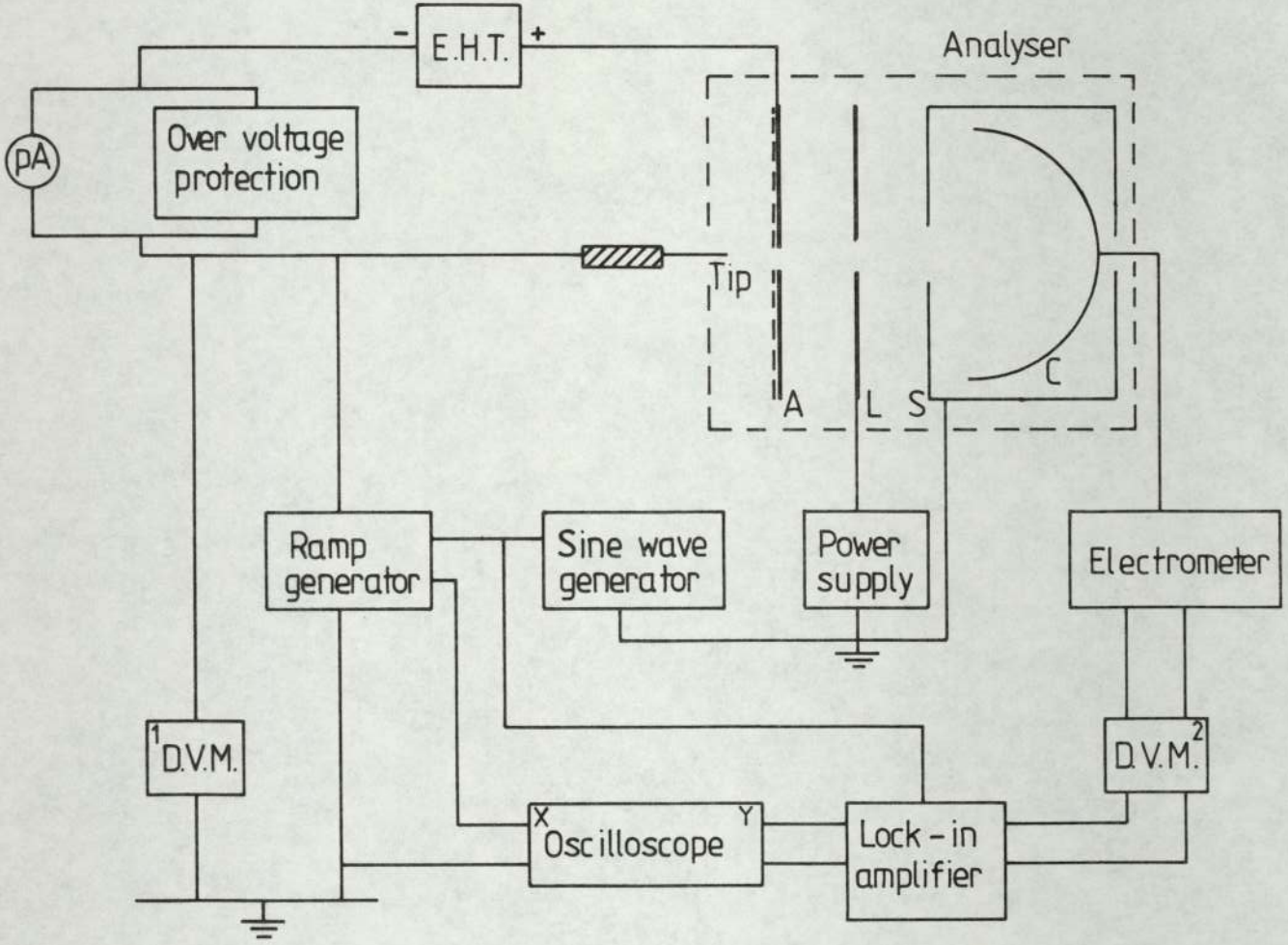

Fig. 3.36 A circuit to produce automatically the differential plots for field emission.

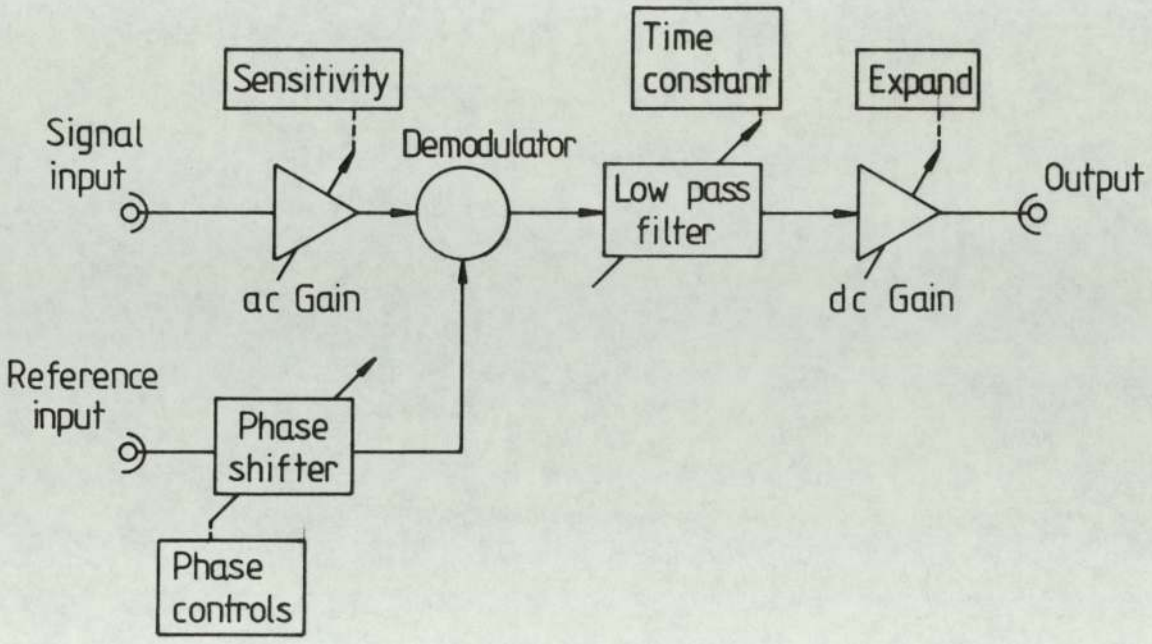

Fig. 3.37 A simplified block diagram of the lock-in amplifier.

signals which may be generated by the internal gating action, or by the subsequent d.c amplification circuits. This is achieved by switching the demodulator output into a low-pass filter section which provides the primary noise attenuation, the effect being altered by the time constant control. The output is then taken to the output expand amplifier which provides a gain of x 1 or x 10, as selected.

3.3.2 INSTRUMENTAL PERFORMANCE.

Before the spectrometer facility could be used for making quantitative measurements of the energy spectra of composite micro-emitters, two commissioning procedures had to be followed. Firstly, its resolution had to be optimised in terms of the known emission characteristics of a thermionic source, and secondly its energy scan

had to be calibrated with reference to the Fermi level of the substrate cathode by using a field emitting source.

3.3.2.1 OPTIMISING THE RESOLUTION.

In his original measurements, Van Oostrom measured the total-energy distribution of a tungsten field emitting source at 4.2 K, where the spectrum is well defined and the resolution can be measured with a high accuracy. He found that the minimum value of the spectral half width occured when the ratio of the lens voltage to the anode voltage $V_L / V_A = 0.003$, and that under these conditions the slope of the high-energy side of a spectrum indicated that the resolution of the analyser was better than 10 m e V [39]. This was also confirmed by computer simulation work by Adachi et al [98], in fact they even showed that it is theoretically possible to obtain a much higher resolution than the experimentally obtained value of 10 m e V. In contrast to deflection analysers, retarding potential analysers suffer from non uniformity of resolution, where the 10 m e V is only attainable at the peak of the distribution; whereas at the low energy end of the integral plot (i.e. Lower V_c values), there is only a relatively small change in the slope of I_c , which results in a poor signal to noise ratio, which in turn produces a greater possibility of error when obtaining the differential plot [102, 103, 111].

Since a liquid He specimen holder was not available, an alternative approach was adopted for optimising the resolution of the present instrument; this was based on the use of a thermionic source. Thus, a standard electron microscope hairpin tungsten filament assembly was mounted on the specimen holder as shown in Fig. 3.28 (b).

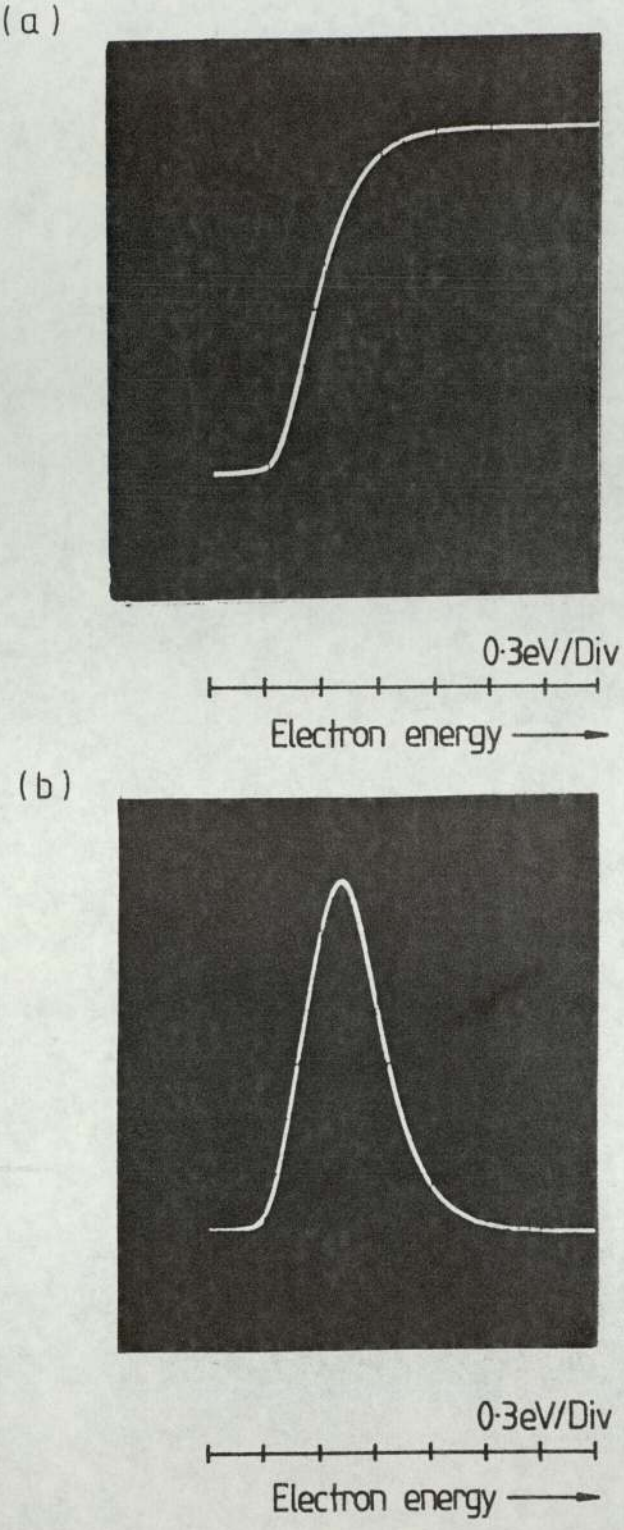

Fig. 3.38 (a) The integral plot obtained with a thermionic source and (b) The corresponding differential plot.

This was then fitted into the specimen chamber shown in Fig. 3.24 which was then evacuated to $\sim 5 \times 10^{-10}$ mbar as described previously in section 3.3.1.2 . However, to maintain this level of vacuum during operation, it was also necessary to outgas the filament by running it at ~ 700 K for several hours.

The resolution was optimised by running the filament at a known temperature T K, as measured with an optical pyrometer, and then, for a given cathode-to-anode accelerating voltage V_a , adjusting the value of the lens voltage V_L until the measured spectral half-width approached as closely as possible to the theoretical value given by Young [48] as

$$(\Delta E)_{\frac{1}{2}} = 2.45 \, k \, T$$

This procedure in fact showed that the optimum value of the ratio V_L / V_A was 0.05 which is somewhat higher than the value recommended by Van Oostrom [39].

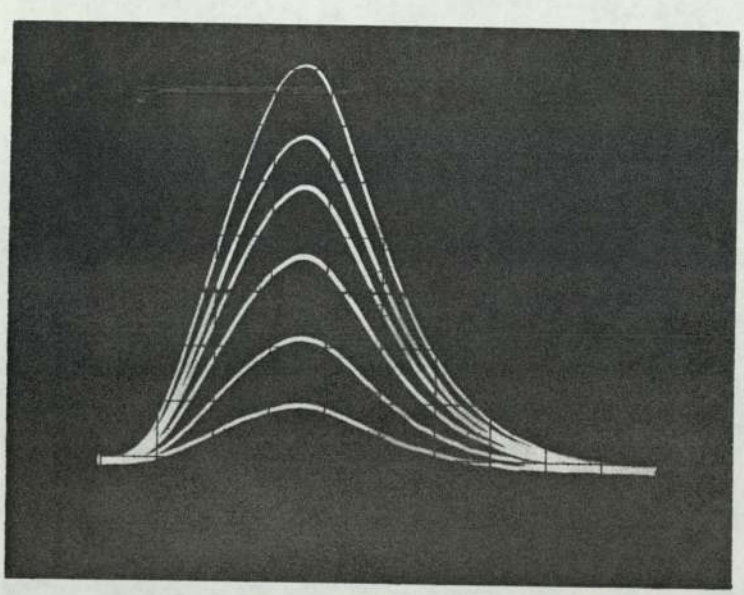

Fig. 3.39 A series of spectra taken at a range of temperatures from a thermionic emitter.

To illustrate the two operational modes of the spectrometer, Fig. 3.38 (a) compares the integral plot obtained with a thermionic source using the circuit of Fig. 3.31 , and (b) the corresponding differential plot obtained with the circuit of Fig. 3.36 . From these traces, it is evident that the integral signal has been faithfully differentiated. The performance of the instrument at optimum resolution is further illustrated in Fig. 3.39 , which shows a series of spectra taken at a range of temperatures (i.e. corresponding to different heating currents), which clearly illustrate the variation of half-width with temperature, i.e. increas linearly with temperature as predicted (48).

3.3.2.2 ENERGY CALIBRATION.

For this important measurement, a tungsten micropoint emitter was mounted in the system as shown in Fig. 3.24 , at a pressure of $\sim 5 \times 10^{-10}$ mbar. After cleaning the tip by field desorbtion , at a gradually increasing voltage up to 9 K V, and then at 9 K V for 30 minutes, the spectra shown in Fig. 3.40 was recorded, where, for comparison the spectrum of a thermionic source at a temperature of ~ 2410 K is also shown in the same figure. Applying the Young criteria (48) i.e. the Fermi level of the tungsten emitter occurs at a point 73% up the high energy slope of its total energy distribution, it is seen that the Fermi level of the cathode occurs at a scan voltage of 4.33 volt. Since this is a constant parameter of the instrument, it is thus possible when composite emitters are used, to relate their spectra to the Fermi level of the substrate cathode. The physical significance of this property will be further discussed in chapter 5.

Referring again to Fig. 3.40 , it has to be noted that the

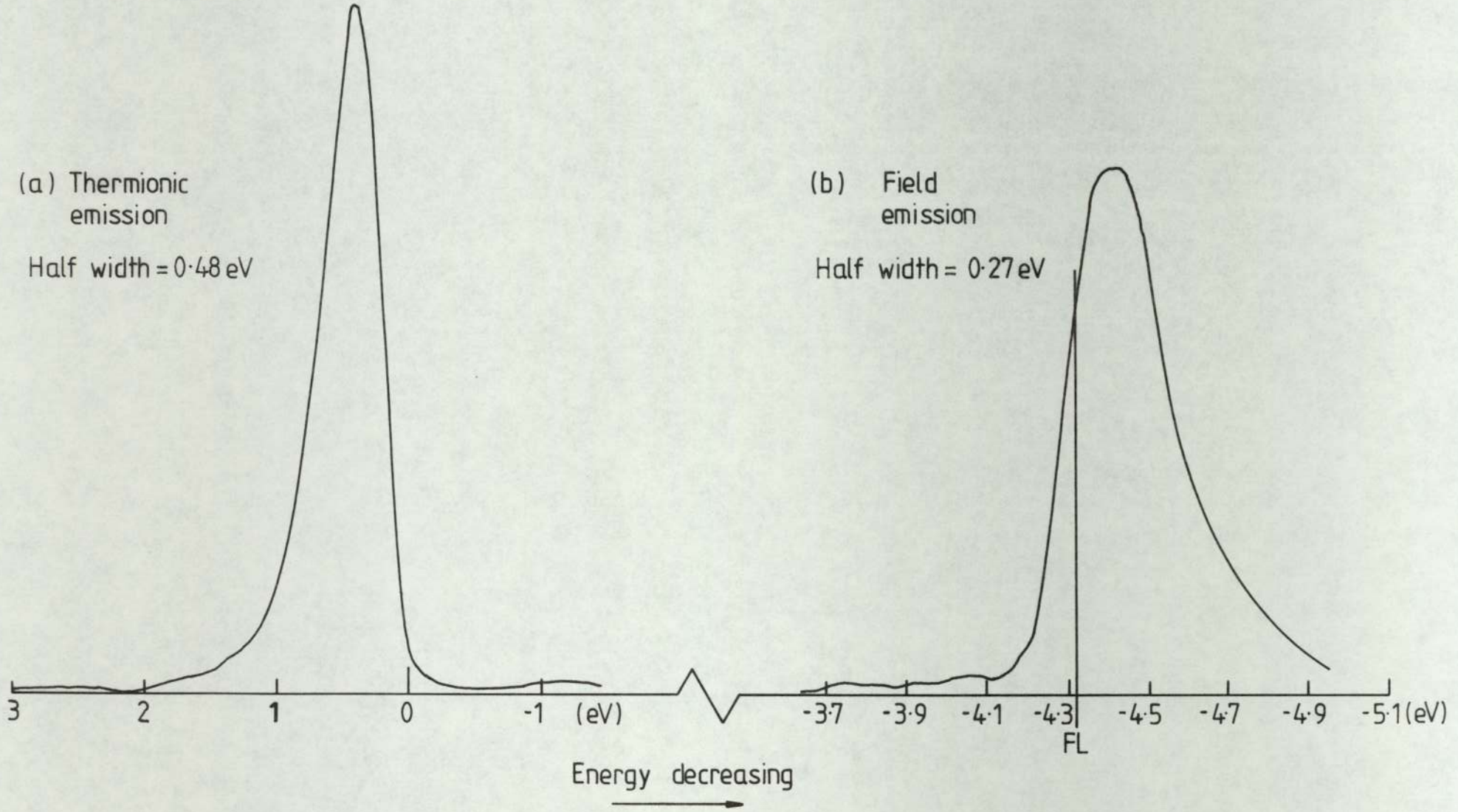

Fig. 3.40 The calibration of the analyser using a tungsten field emitter with an associated thermionic emission ($T_{source} \sim 2410$ K); (N.B. The distributions are plotted on different energy scales).

accuracy of this calibration will depend on the quality of the tungsten field emission spectrum. In fact, even after thorough tip cleaning, the spectrum shown here has a rather large half width, i.e. $(\Delta E)_{\frac{1}{2}} = 270 \pm 1$ m e V, compared with the value for a perfectly clean tip of 230 ± 1 m e V [95]. This therefore means that the calibration can only be assumed to have an accuracy of $\sim 5\ \%$. Finally, if the same type of tungsten is used for the thermionic and field emission sources, the seperation of the spectra on the energy axis indicates the work function of the material to be ~ 4.33 e V.

A comparison of electron spectra from a tungsten emitter before and after coating with a 0.2 μ m thick layer of resin at identical emission currents of 2 μ A is shown in Fig. 3.41 .

3.4 ANCILLARY FIELD EMISSION MICROSCOPE FACILITY.

The field emission microscope is the conventional technique used for studying the field electron emission properties of a micro-point emitter. This consists essentially of a point - to - plane diode device, where the high electric field ($\sim 10^9$ V m^{-1}) necessary for "cold" electron emission is created at the tip of the emitter by a geometrical field enhancement effect. The axial tip - screen seperation is standarised at ~ 10 mm . The spatial distribution of the emitted current density is then visually displayed on a phosphor screen which forms the anode. Such a facility has been used in the present project and is illustrated schematically in Fig. 3.42 . This simple system provides a very convenient and quick method of studying many of the emitting properties of the various composite microtips which were described in section 3.2 , in partic-

Fig. 3.41 A comparison of the electron energy spectra obtained from a tungsten emitter (a) before and (b) after coating with a 0.2 μm thick layer of resin at identical emission currents of 2 μA (FL = Fermi level of the substrate cathode).

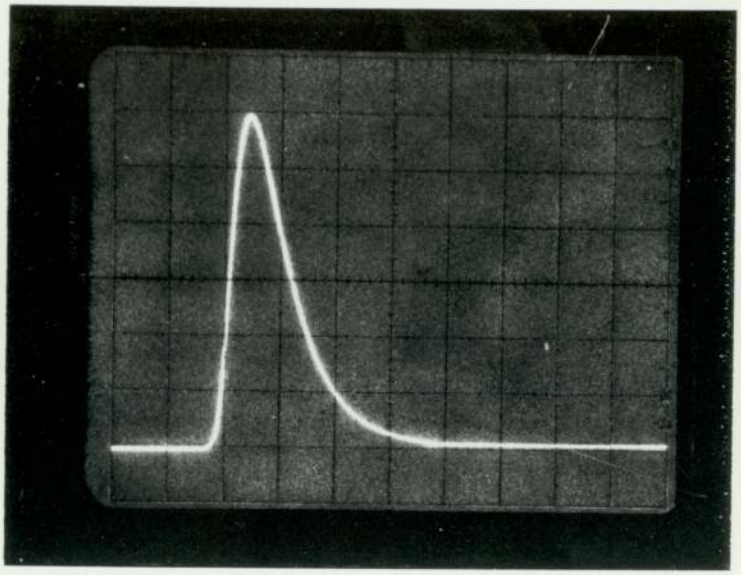

0·23 eV/Div

Fermi level

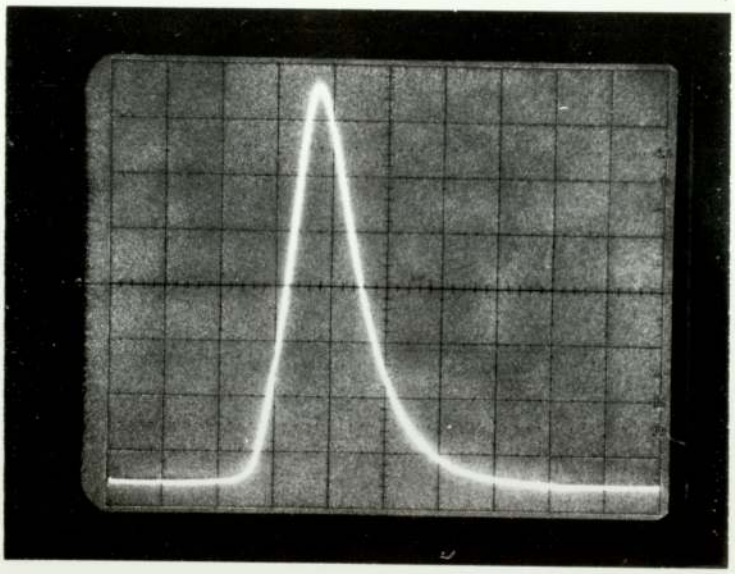

0·23eV/Div

FL

Energy decreasing ⟶

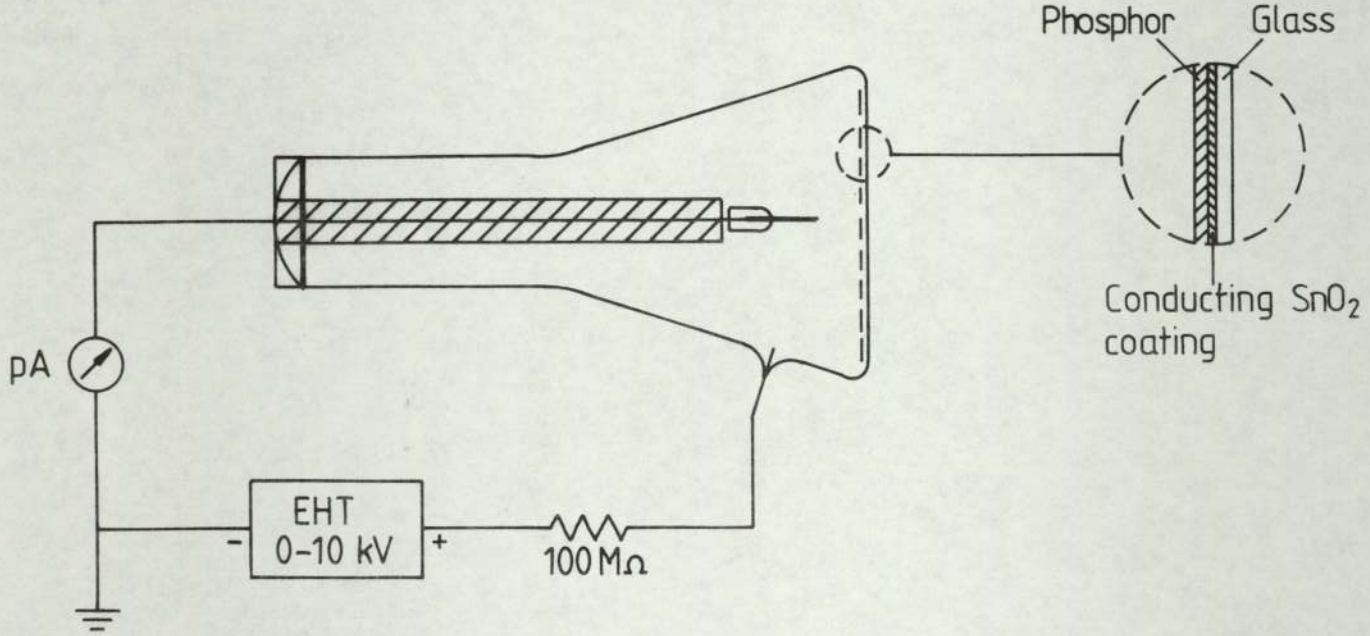

Fig. 3.42 Schematic diagram of a field emission microscope.

ular the stability and form of their emission images and their current-voltage characteristics. It should be noted that, after baking, this system could be operated under U.H.V. conditions.

CHAPTER 4

EXPERIMENTAL RESULTS

4.1 Introduction

This chapter describes the results of experiments on the emission characteristics of the various composite micropoint emitters whose preparation techniques were described in the previous chapter. These results include the current-voltage characteristics, emission images and electron spectra, which were obtained using the experimental combination of a field emission microscope and a high resolution retarding potential electron spectrometer (see sections 3.3 and 3.4). In addition, electron microscopy was used to investigate the details of emitter profile, and the effects of ion beam etching. A full discussion of the physical implication of these findings will be given in chapter 5.

4.2 CURRENT-VOLTAGE CHARACTERISTICS

Two general approaches have been used to present the experimental data. The first is a direct I-V plot, showing how the total measured emission current I depends on the voltage V applied externally between the emitter and anode; such plots are very useful for identifying the important features of the emission behaviour. The second approach follows the conventional practice used in field emission studies where the current-voltage data is given in the form of a Fowler - Nordheim plot, viz. Log I/V^2 versus $1/V$. Such plots have the advantage, as explained in chapter 2, of providing quantitative information about the microscopic properties of the emitting regime.

4.2.1 TYPICAL BEHAVIOUR OF COMPOSITE EMITTERS

Before embarking on an account of the detailed behaviour of the various emitting structures which were studied, it would be helpful to identify certain general features of their characteristics which are common to this type of emission regime. In particular, this approach provides an ideal framework within which to present the extensive experimental data obtained from this investigation.

Thus, Fig. 4.1 is a schematic representation of the typical current-voltage characteristic of a metal - insulator micropoint emitter. This is seen to be initiated by a switch-on process, whereby there is a threshold switching voltage V_{SW} at which the emission current changes abruptly from an effective zero - value to a saturated value I_{SAT} . The saturation current (I_{SAT}) then extends over a voltage range ΔV_3 (region 3 in the figure) which lies between the voltages V_{SAT} , i.e. $\geqslant 550$ Volts, to V_{MAX} , i.e. $\leqslant 5$ KV as limited by the maximum voltage which can be applied to the tip before it explodes. Such a tip explosion is believed to depend on the dimensions of the emitter tip metal core, the coating thickness and the emitter treatment as explained below. On progressively lowering the voltage through region 3, one first passes into the transition region 2, which starts at the bounded voltage V_{SAT} and extends over a voltage range $\Delta V_2 = V_{SAT} - V_L$, and then lastly into region 1 which is bounded by the voltage V_L and the threshold voltage V_{TH} , i.e. the minimum voltage required for detecting a finite emission current. In region 1 the I-V characteristic gives an approximately linear Log I/V^2 versus $1/V$ Fowler - Nordheim (F - N) plot (see section 2.2.3.1). If such an emitter is subsequently cycled through the same voltage range the current generally follows the "dashed" curves, i.e. showing a smooth

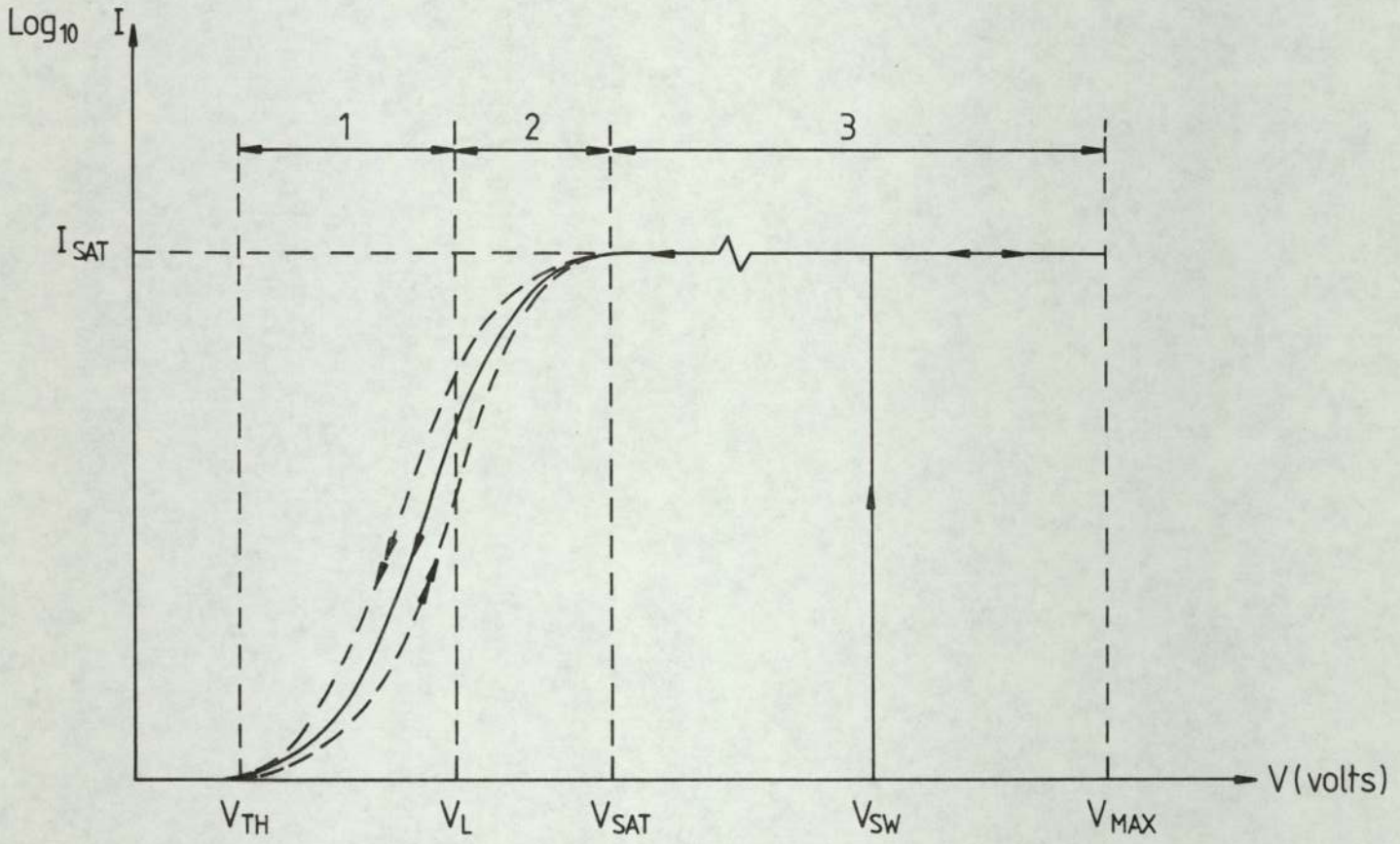

Fig. 4.1 The general form of current-voltage (I-V) characteristics of a composite emitter.

dependence of current on voltage but with a significant built-in hysterisis between the increasing and decreasing values.

As will be seen in the following sections, the relative values of the basic perameters defined previously, viz. I_{SAT} , V_{TH} , V_L , V_{SAT} , V_{SW} , $\Delta V_1 = V_L - V_{TH}$, $\Delta V_2 = V_{SAT} - V_L$ and $\Delta V_3 = V_{MAX} - V_{SAT}$, were found to be strongly dependent on the particular emitting regime.

It was also found that in some cases the behaviour of the I-V characteristic deviated significantly from the general form of Fig. 4.1, however these effects are thought to provide important additional information about the emission process, so they have been collected together to form a seperate section (4.2.4).

4.2.2 RESIN-COATED TUNGSTEN EMITTERS

As indicated in chapter 3, this type of composite emitter proved to be the most successful from two points of view. Firstly, it was possible to achieve a good control over the manufacturing procedure, and secondly, such emitters gave reproducible I-V characteristics between batches. Accordingly, experimental data from this system has been chosen to illustrate the typical emission behaviour of metal - insulator microemitters.

In Fig. 4.2, curves (A) and (B) compare respectively the I-V characteristics of the tungsten micropoint emitter shown in Fig. 3.12, "before" and "after" it was coated with a 0.2 μm thick layer of epoxy-lite resin.Fig. 4.2 (A) is typical of the steeply-rising reversible non-ohmic characteristics found for metallic field emitters following a field desorption cleaning procedure. Whilst Fig. 4.2 (B), which is for resin-coated tungsten emitter, has the same general shape as Fig. 4.1, but with the parameters V_{SW} = 700 Volts, V_{SAT} = 550 Volts, V_L =

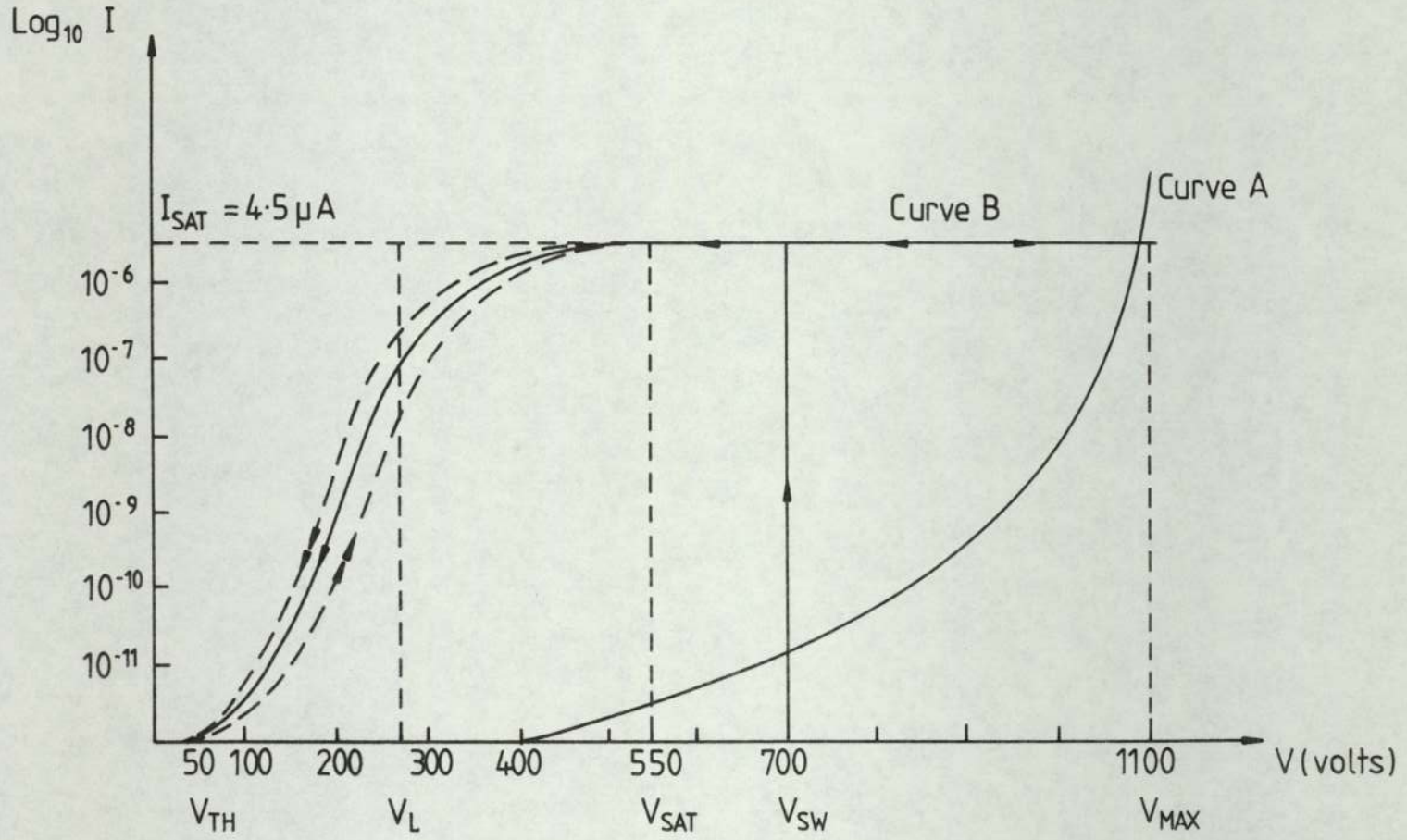

Fig. 4.2 A comparison of the I-V characteristics of an uncoated tungsten emitter of tip radius ~38 n m (curve A), and that obtained after coating with a 0.2 μ m thick layer of epoxylite resin (curve B).

280 Volts, V_{TH} = 50 Volts and V_{MAX} = 1100 Volts with I_{SAT} = 4.5 μ A; this is considerably different to the characteristics of the metallic emitter. The corresponding Fowler-Nordheim plots for the uncoated and coated tips are shown respectively as (A) and (B) in Fig. 4.3, this shows that the effect of the resin insulating coating is to reduce the slope of these plots from a value of m_W = 9870 for clean tungsten to a value of m_{W+R} = 2424 for the resin coated tungsten. The physical significance of the difference between these two plots will be discussed in chapter 5.

Another important observation from Fig. 4.2 , is that whereas ~1100 Volts is required to obtain an emission current of 1 μ A from the uncoated tip, a maximum of 550 Volts (= V_{SAT}) was required to obtain a "switched-on" saturated emission current of 4.5 μ A from the coated tip. In addition, V_{TH} for the coated tip was only 50 Volts compared with 400 Volts for the uncoated tip. A further practical consideration, from the point of view of electron sources, is that the coated emitter was not only more stable, but also gave a very much brighter electron optical source (see section 4.3.1). Subsequent cycling of the voltage resulted in the smooth and reversible hysterisis characteristics (shown in Fig. 4.2 by the double-arrowed dashed curves). This highlights the important property that the switch-on phenomenon was usually only seen with the first application of the voltage across virgin emitters.

For this type of emitter, the thickness of the insulating layer is clearly a very important parameter. Accordingly, a series of experiments were undertaken using emitters having resin coatings of varying thicknesses. Early experiments used very thick coatings, obtained by forming balls of resin on the tips, see Fig. 3.8 (a) where the estimated film thicknesses was 25 - 50 μ m. However, when

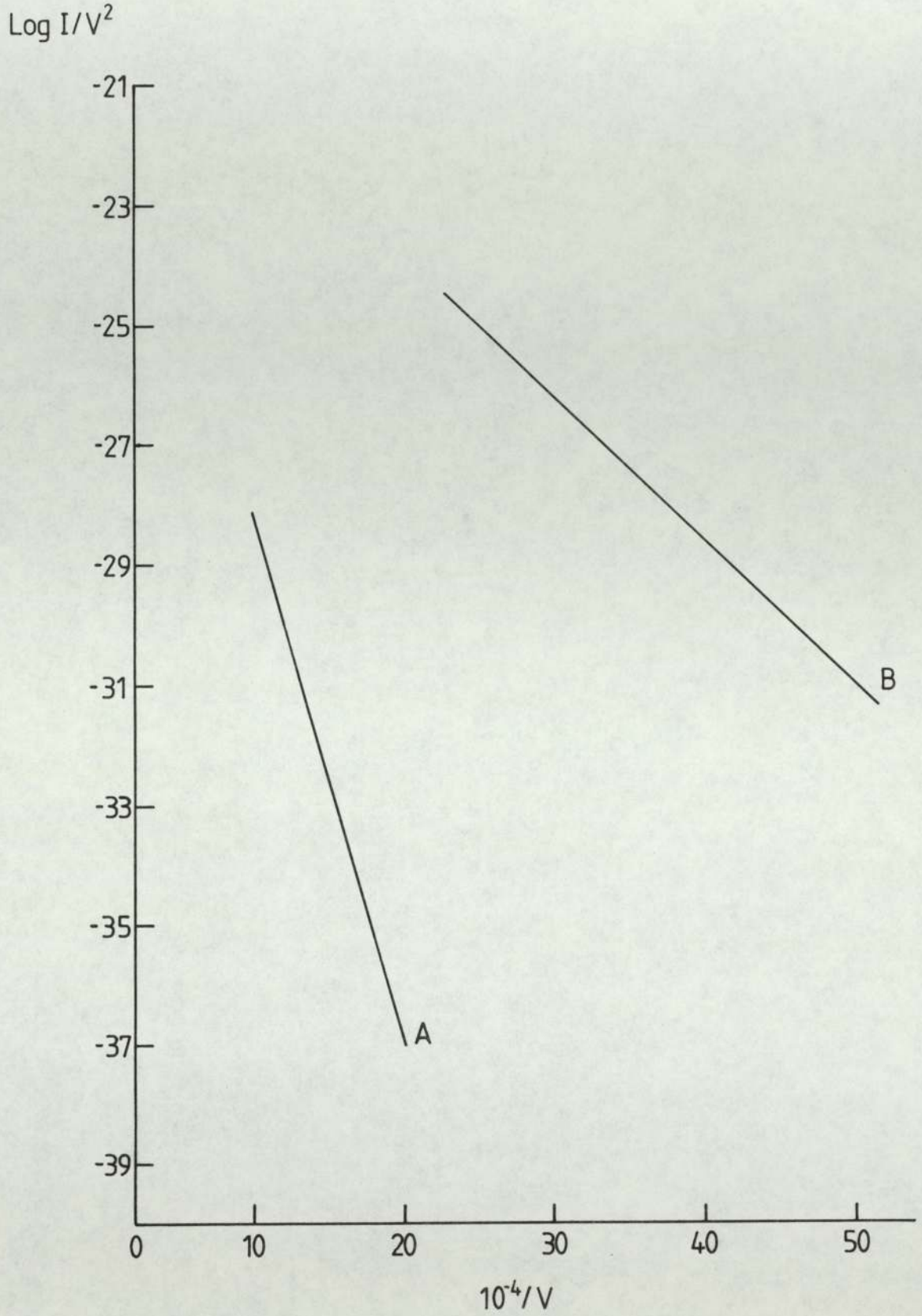

Fig 4.3 Fowler-Nordheim plots of the uncoated (curve A) and resin-coated (curve B) emitters whose I-V characteristics are presented in Fig. 4.2 .

mounted in the field emission microscope (F.E.M.), no field electron emission was obtained with this type of emitter for applied voltages up to 12 k V. Although attempts were made to achieve controlled reduction in the thickness of such coatings using ion beam etching (see section 4.5), this approach was considered to be basically unsatisfactory since large image distortions in the optical microscope (see section 3.2.1.4), prevented an accurate measurement of the effective insulating layer over the metallic tip. Subsequent experiments therefore concentrated on the sub-micron coating technique used to prepare emitters with characteristics as given in Figures 4.2 and 4.3 . Thus Table 4.1 presents the collated emission data which was recorded under identical experimental conditions from a series of "as - prepared" tips having resin coatings of thicknesses (Δd) varying between 0.04 and 0.2 μ m. It will be noted however that this table only presents information about the parameters V_{SW} , I_{SAT} , V_{SAT} , V_{MAX} , V_L , V_{TH} , m_W , m_{W+R} , tungsten tip radius r, E_{SW} ($\alpha\ V_{SW} / r$) and E_{SAT} ($\alpha\ V_{SAT} / r$). This is because the "transition" part of the characteristic frequently exhibited deviations from the "typical" behaviour of Fig. 4.1 (see the later section 4.2.4), which no longer allowed it to be described by all the originally defined parameters.

The relations between Δd and the more reproducible parameters used to characterise the emission data are presented graphically in Figures 4.4 , 4.5 and 4.6 . From Fig. 4.4 it is seen that even though there is considerable scatter in the measurements of the switching field (defined as $V_{SW} / K r\varepsilon$) due to the difficulty of accurately measuring the tip radius and the probable variability of the dielectric constant ε form specimen to specimen, the experimental points lie on a hyperbolic curve. It should be noted that the actual

Resin thickness Δd (μ m)	V_{SW} Volt	I_{SAT} μA	V_{SAT} Volt	V_{MAX} Volt	V_L Volt Approx	V_{TH} Volt	m_W	m_{W+R}	Tungsten tip radius "r" nm Estimated	E_{SW} $x10^9$V/m	E_{SAT} $x10^9$V/m
0.2	700	4.5	550	1100	280	50	9870	2424	38	18.42	14.47
0.19	800	4.5	600	1200	300	100	13363	2314	42	19.05	14.29
0.155	1400	5	900	2000	550	250	11595	2292	69	20.29	13.04
0.13	1950	5.5	1300	2500	650	200	14562	3058	71	27.465	18.3
0.112	700	2.5	500	950	-	-	-	-	32	21.875	15.625
0.11	2450	7	1800	3100	290	200	10023	2215	93	26.3	19.35
0.106	2550	8.5	1900	3300	1200	400	11018	2378	48.7	53.36	39.01
0.082	2600	7	1600	3100	750	550	12984	2092	110	23.64	14.55
0.078	2500	10	2100	5000	840	400	9811	2104	100	25.0	21.0
0.0585	1800	5	1500	2900	500	250	12833	2969	70	25.71	21.43
0.051	1500	4	1200	2200	450	25	11756	2138	54	27.8	22.22
0.048	1350	2.5	950	2050	400	100	10117	2413	42	32.14	22.62
0.043	1200	1.5	900	1750	500	100	13672	2395	33	36.4	27.27
0.04	1140	1.2	900	1600	690	500	18641	3007	25	45.6	36.0

TABLE 4.1 Emission data obtained from composite emitters having various thicknesses of a resin coating.

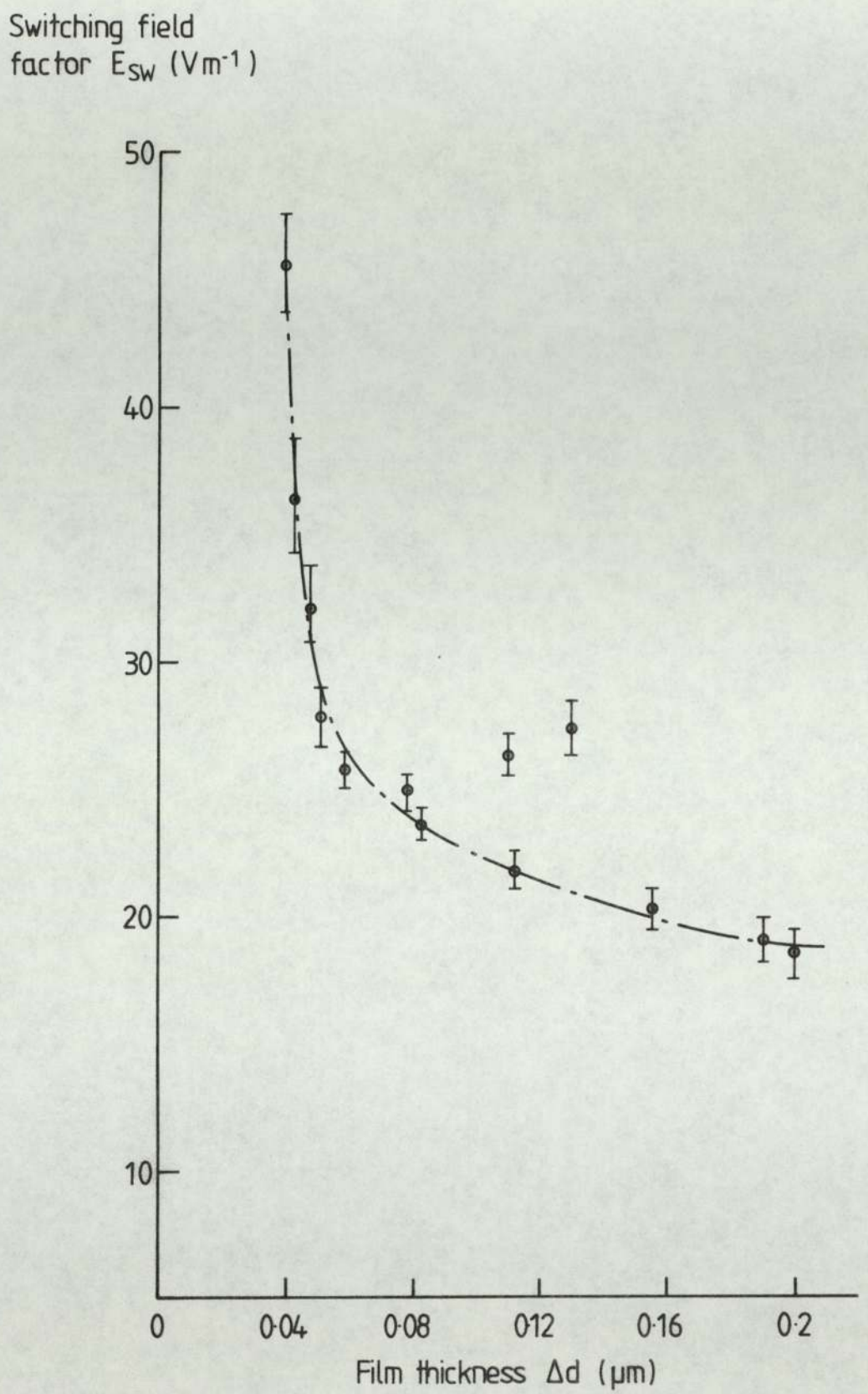

Fig. 4.4 The relation between the film coating thickness Δd and the tip switching field factor E_{SW} ($\propto V_{SW} / r$).

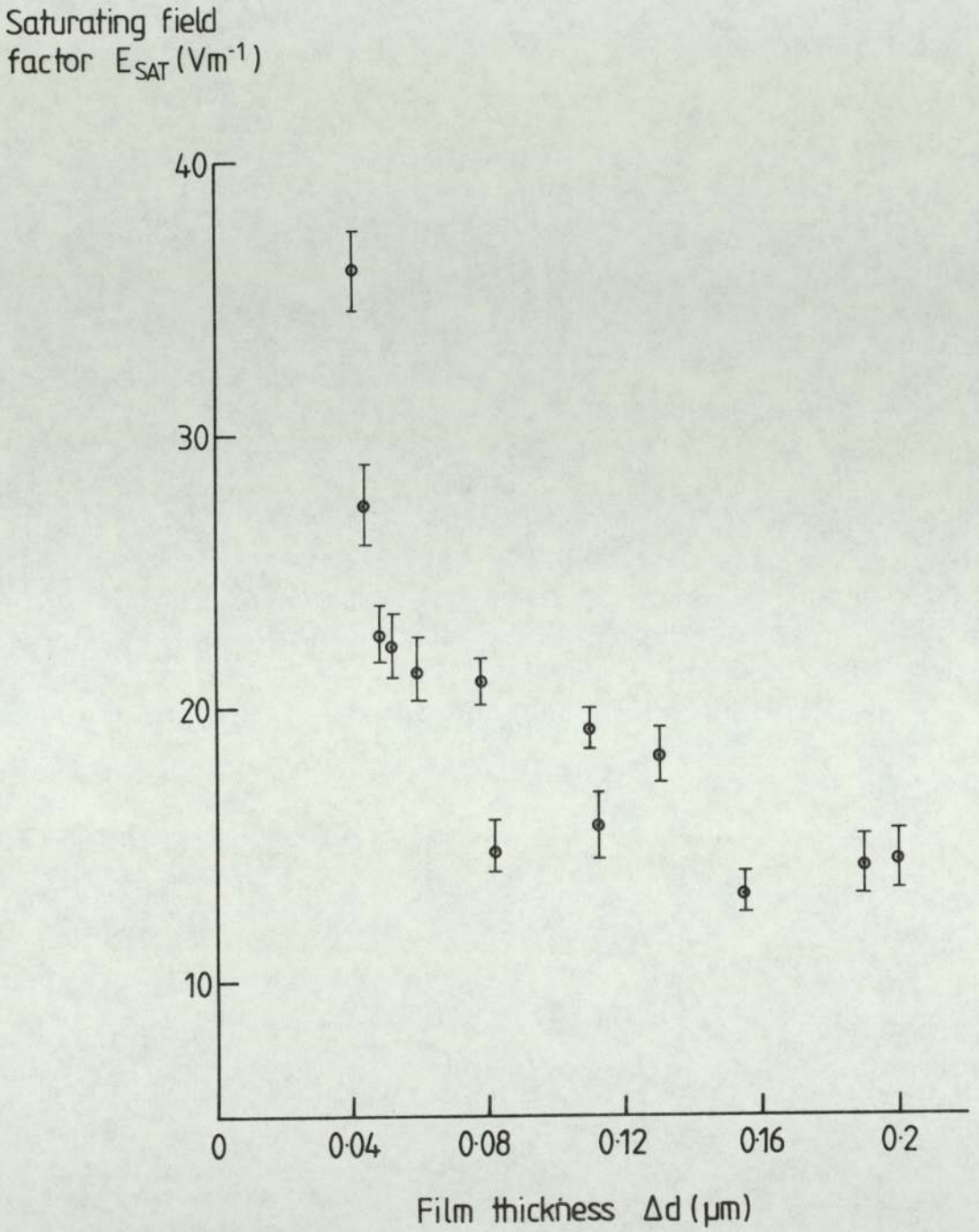

Fig. 4.5 The relation between the film coating thickness Δd and the tip saturation field factor E_{SAT} (α V_{SAT} / r).

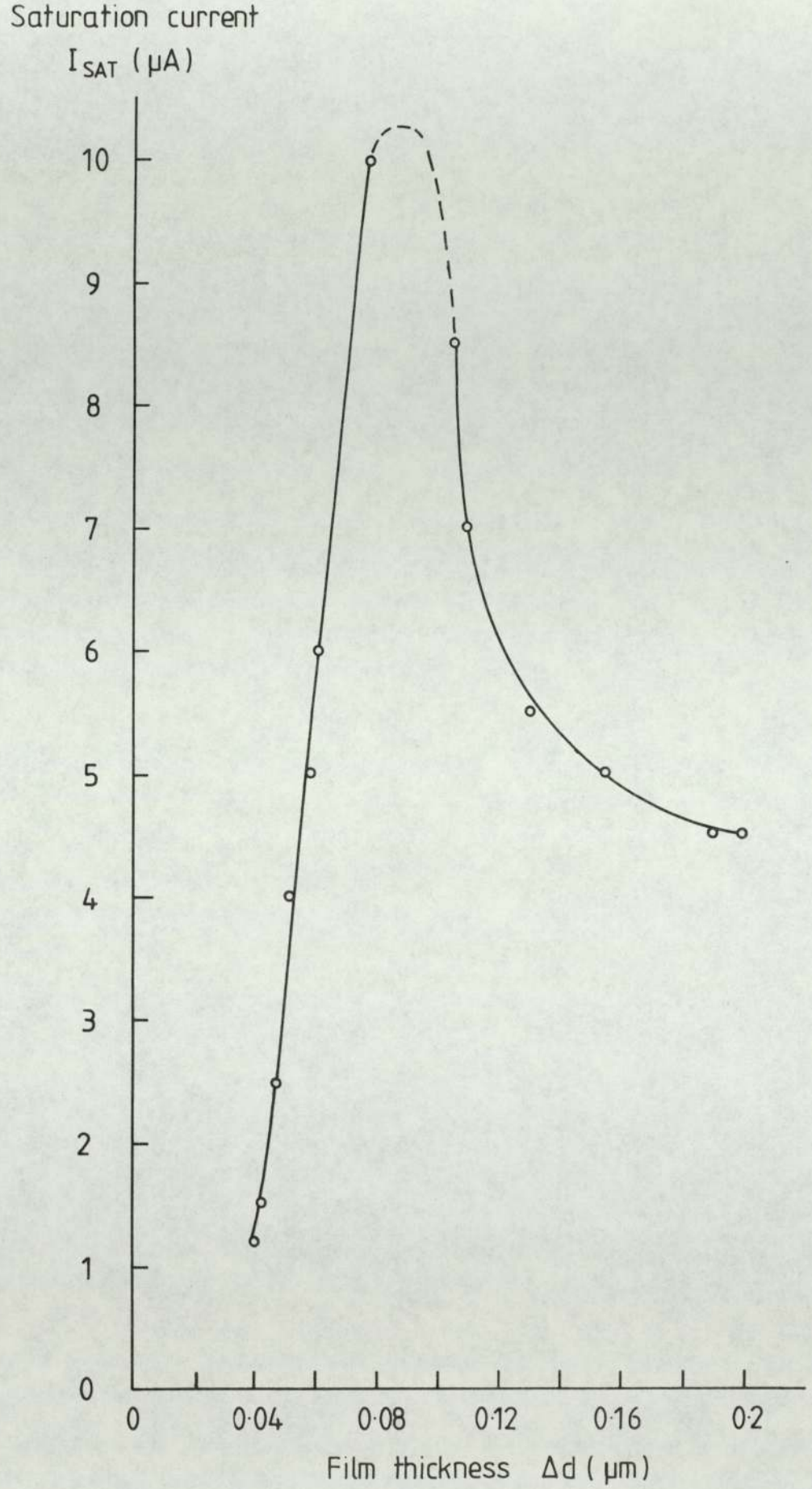

Fig 4.6 The relation between the film coatings of thicknesses Δd and the saturated current I_{SAT} .

field at the metal surface has been taken as $E_{SW} / K\varepsilon$, where K is a factor determined by the geometry of the emitter, and the thickness of the insulating layer. Since these parameters are difficult to determine, it follows that a large uncertainty would be introduced into the estimation of tip field. Hence to avoid these complications $E_{SW} \alpha V_{SW} / r$ was plotted against film thickness. The hyperbolic form of the experimental relationship between E_{SW} and Δd will be shown later to have a theoretical basis. Likewise, the saturation field can be defined as $V_{SAT} / K r\varepsilon$. It can be seen, in Fig. 4.5 , that the E_{SAT} curve had considerable scatter which makes a determination of its functional relationship to Δd difficult, but, a slight hyperbolic form is just discernable. Finally, from Fig. 4.6, it is seen that I_{SAT} increased almost linearly with Δd, and then passed through a maximum at Δd approximately 0.09 μ m, but fell off at a steep rate as Δd approached approximately 0.2 μ m.

THE EFFECTS OF IN-SITU, U.H.V. BAKING.

The investigation was at a relatively advanced stage when it was discovered that the effects of an initial in-situ thermal processing of a coated microemitter could have a very significant influence on its subsequent emitting properties. Accordingly, only a small proportion of the total number of emitters studied, were investigated from this point of view. However, sufficient data was accumulated to identify the following general trends:

(a) "Tip explosions" were significantly reduced. This was an effect which occured widely with unbaked emitters, being observed as a visual "flash" that resulted in the destruction of a tip, as illustrated in the micrographs of Figures 4.17 and 4.18 or in a less drastic form "tip explosion" could result in either the electrons

being emitted at wide angles from sites on the side of the cone, or causing "tip deformation" as illustrated in Fig. 4.13 .

(b) The saturation current I_{SAT} was found to be more stable. This occured even at pressures $\sim 10^{-7}$ mbar, a property that greatly facilitated the recording of noise-free electron energy spectra (see section 4.4).

(c) Electron emission tended to be concentrated in a narrow paraxial beam. As a result of this the electron source had a brightness that was typically six times higher than that obtained from an uncoated emitter with the same total emission current (see section 4.3.1).

As a quantitative illustration of the advantages to be derived from this baking procedure, three tungsten micropoint emitters were coated with a similar thickness ($\sim$ 0.2 microns) of resin and were then baked at three different temperatures for the same length of time (12 hours). The resulting switch-on voltages V_{SW} and saturated emission currents I_{SAT} for these three emitters are summarised in Table 2. It will be seen that there is a marked decrease in V_{SW} with increasing baking temperature, while at the

Baking Temperature of Emitter (°C)	V_{SW} (Volts)	I_{SAT} (μ A)
100	1200	1.7
140	850	3.5
200	700	4.5

TABLE 4.2 The collated experimental data obtained from three tungsten microemitters coated with similar thickness of resin (0.2 μ m) and baked at different temperatures.

same time there is an increase in I_{SAT} ; similar general trends were observed for at least two of the other composite emitting regimes which are described in the following section 4.2.3 (e.g. tungsten coated with either hydrocarbon or lacomit).

4.2.3 COLLATED DATA FROM A SELECTION OF COMPOSITE EMITTING STRUCTURES.

In this section, a survey will be given of the emission characteristics of the other metal-insulator micro-structures which were fabricated using the techniques described in chapter 3. Thus, Table 4.3 presents the data in broadly the same format as that used previously in Table 4.1 for the resin-coated tungsten emitters. However, for several of these coatings it was not possible to make accurate measurements of the film thickness; accordingly, the terms "thin", "medium" and "thick" will now correspond to estimated layer thicknesses (Δd) of $\leqslant 0.15\,\mu m$, $0.15 \leqslant \Delta d \leqslant 0.5\,\mu m$ and $0.5 \leqslant \Delta d \leqslant 3\,\mu m$ respectively. An exception to this was the case of the hydro-carbon coating which will be highlighted below. As has been shown in Table 4.1 , all of the emitters exhibited a "switch-on" effect and gave a saturated current I_{SAT} which then remained constant over an anode voltage range ΔV_3 . Equally, most of these emitters exhibited behaviour as typified in Fig. 4.1; however there were exceptions, as in the case of some resin-coated tungsten emitters, and these deviations will be briefly described in the following section. It was also found that whenever the baking procedure was applied to these types of composite emitters it resulted in very similar improvements in the emission characteristics to those found for resin-coated tungsten. (see section 4.2.2).

Type of insulator	Insulator thickness μ m	V_{SW} Volt	I_{SAT} μ A	V_{SAT} Volt	V_L Volt Approx	V_{TH} Volt
Hydrocarbon	0.0231	3000	3.2	2600	1600	800
" B	0.0280	2600	1.2	2500	1900	1200
"	0.0305	2500	8.2	2300	1400	300
"	0.0595	650	1	600	400	100
"	0.158	5000	12	-	-	-
			1.2	3800	2900	1900
Lacomit E (baked at 240°C)	thin	1000	3	-	600	100
Lacomit (baked at 200°C)	thin	1200	1.5	1100	750	300
Lacomit (baked at 140°C)	thin	2100	1	2000	1600	1000
Lacomit	medium	2400	9	1900	1200	75
Glass tip (Electrodag film)	thick	18000	0.08	14000	11500	9000
Glass tip (Tin)	thick	14500	0.04	11500	8500	2000
Glass tip (Gallium film)	thick	10000	0.5	9250	8000	4000
Glass tip A (Electrodag film)	thick	18000	10	6000	5000	3000
Glass tip D (Electrodag film)	thick	6300	5	5750	5400	4000

TABLE 4.3 Collated emission data obtained from a range of composite emitter regimes.

HYDROCARBON COATING.

Because of the ease with which controlled layers of this material could be deposited in-situ in a T.E.M. (see section 3.2.1.5), it was possible to make an additional investigation of the influence of the coating thickness on the emission characteristics. However, unlike the previous study on resin-coated emitters (see figures 4.4 , 4.5 and 4.6) this used emitters which had been baked up to a temperature of 140°C, with the consequent improvement in stability and reproducibility of the emission current. The increased brightness of this type of source following baking was particularly marked; in fact the phosphor screen became "burnt", presumably due to ion bombardment resulting from the evaporation of hydrocarbon from the emitter due to the high emission current densities. However, whilst baking to 200°C was found to give a somewhat improved stability, a bake out at $\sim 350^{\circ}$C was found to have destroyed the switching characteristics of the emitter. In the particular case of these hydrocarbon emitters, the baking procedure also led to an increase in emission current which was observed before switch-on occured. Initially, this pre-switch on current had measured values as low as $\leqslant 10^{-11}$ A prior to baking at temperatures $\geqslant 140^{\circ}$C, but after baking currents as high as 10^{-9} A were easily detected.

INTERNALLY-CONDUCTING GLASS TIPS.

As will be recalled from chapter 3 (section 3.2.2), these emitters had a structure that differed markedly from the rest of the "coated" systems. Accordingly, it is appropriate to give a brief account of their properties, i.e. supplementary to the data contained in Table 4.3 .

Firstly, they exhibited the normal switch-on phenomenon although the switching voltage V_{SW} was generally high and showed a wide variation (5000 - 18000 Volts) between the various glass emitters: This finding is believed to reflect the unpredictable form of the metal-glass micro-structure at the tip of such emitters. In particular, it was found that the type of internal coating used (gallium, electrodag ... etc) had a major influence on the values of the parameters V_{SW} , I_{SAT} ... etc and the stability of the emission. This is thought to reflect on how effectively the coating produced a good conducting substrate directly beneath the emitting surface; in this respect, the best results were obtained from emitters using the electrodag metallising technique. For a "good" emitter, where the metal coating penetrated to within $\sim 2\,\mu$ m of the glass tip, it was possible to obtain a switching voltage as low as 500 Volts, with $I_{SAT} \sim 2.5\,\mu$ A which was stable over a period of hours, and a voltage range $\Delta V_3 \sim 4500$ Volts. Furthermore, these sources exhibited even higher electron beam brightnesses than that found for the resin-coated baked emitters. Unlike the metal-coated sources, these glass-internally coated emitters also exhibited an associated optical effect in the form of a pin-point of light at the emitting tip. This was thought to be electroluminescent in origin, although no confirmatory Alfrey-Taylor plots of the intensity variation with applied voltage were made (64). Finally, it should be mentioned that attempts to vary the thickness of the glass overlayer by using a hydrofluoric acid etching technique were unsuccessful, in the sense that such a treatment invariably suppressed any further emission. This was probably due to the observation that the etched end of the glass tip was invariably roughened to such an extent, that the field distribution arround the tip was then altered and its field

intensifying properties lost.

4.2.4 ATYPICAL EMISSION CHARACTERISTICS.

As already mentioned, most of the emitter types studied occasionally exhibited atypical characteristics, particularly in region (1) and (2) of Figure 4.1 . Therefore, to conclude this account of the I-V characteristics of composite emitters, it is appropriate to present a brief survey of the range of effects that can be observed. These are summarised in Figures 4.7 to 4.11 in such a way that the sequences of current-voltage cycles are mostly self-evident. However, to clarify and highlight certain features of these characteristics, a brief description is given below of the five types of deviant behaviour which were observed. The physical significance of these findings will then be discussed in the following chapter.

Referring to Figure 4.7 , Type A behaviour will be characterised by an apparently "first order" discontinuity between the "on" and "off" states. The phenomenon was repeatable between successive cycles of voltage, although there was the normal hysterisis between the "upward" and "downward" characteristic. Emitters exhibiting this type of behaviour are indicated by a suffix "A" in Tables 4.1 and 4.3 . The second deviation viz. Type B behaviour is shown in Figure 4.8 . This was characterised by a series of up to five current plateaux or steps as the voltage was slowly cycled. Subsequent recycling of the voltage led to exhibiting the typical characteristic having a well defined V_{TH} . Emitters which exhibited this type of behaviour are indicated by a suffix "B" in Table 4.3 .

Type C atypical behaviour was mainly associated with those emitting regimes that were formed by immersing metallic tips in

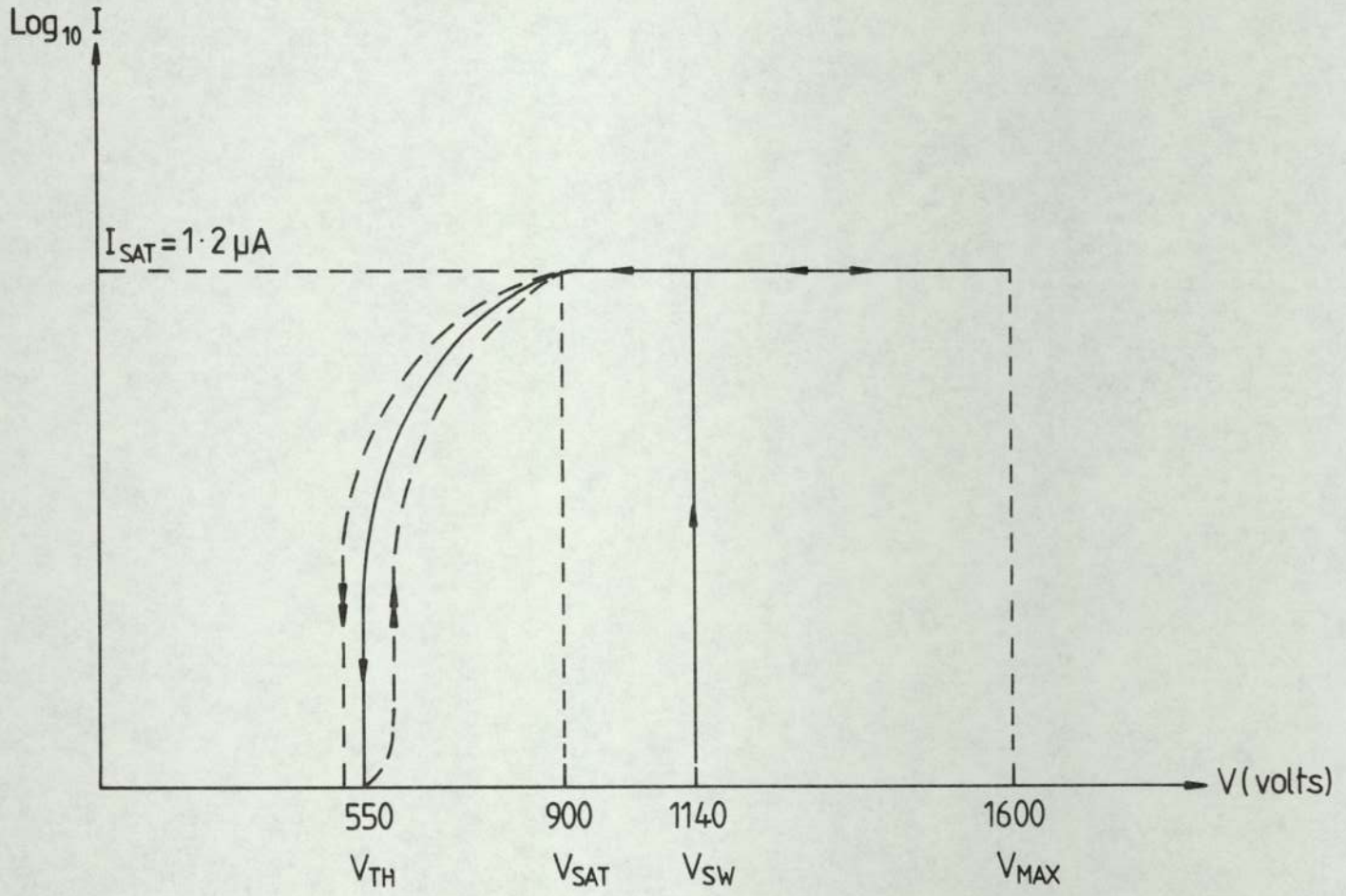

Fig. 4.7 I-V plot of 'type A' atypical behaviour.

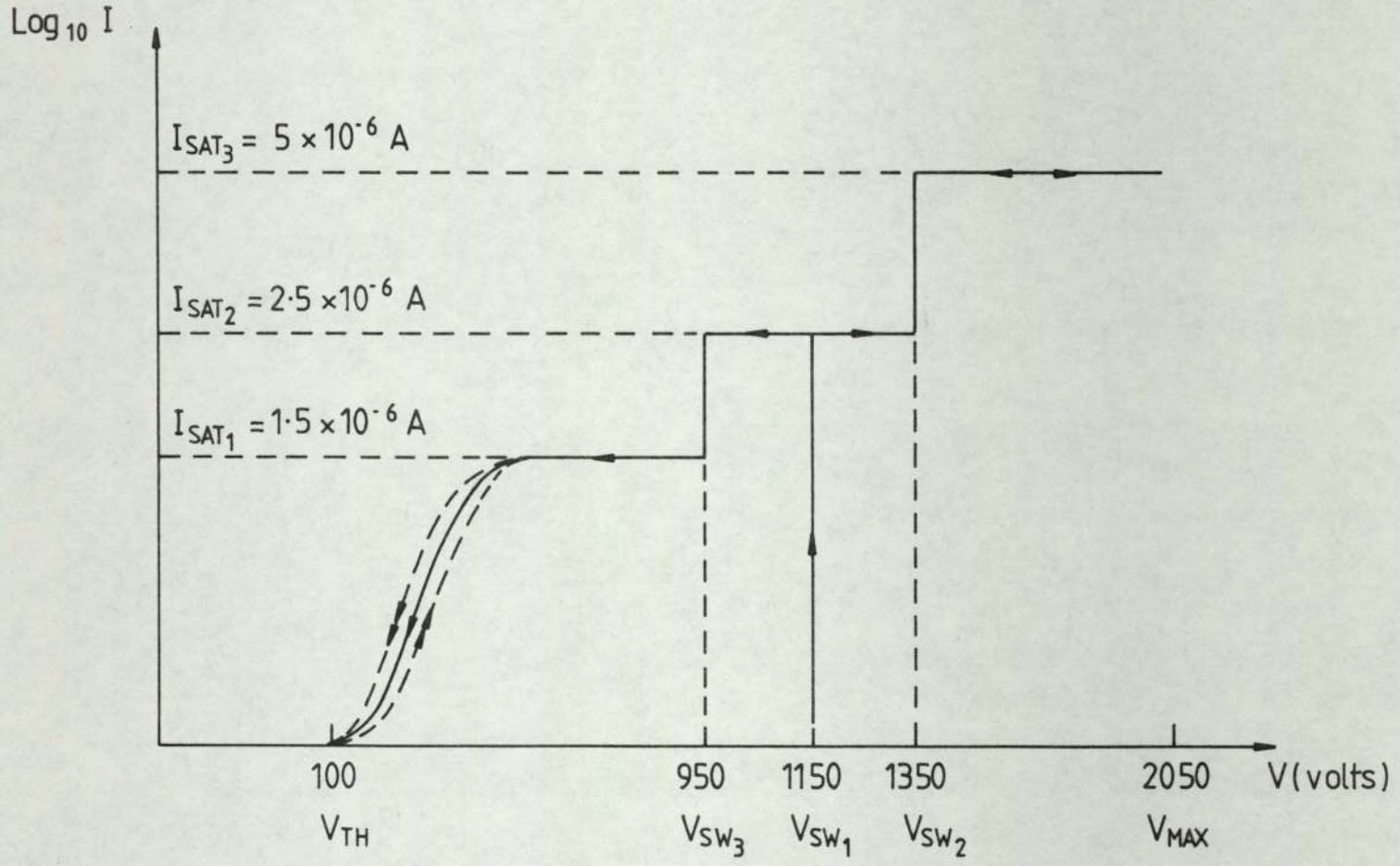

Fig. 4.8 I-V plot of 'type B' atypical behaviour.

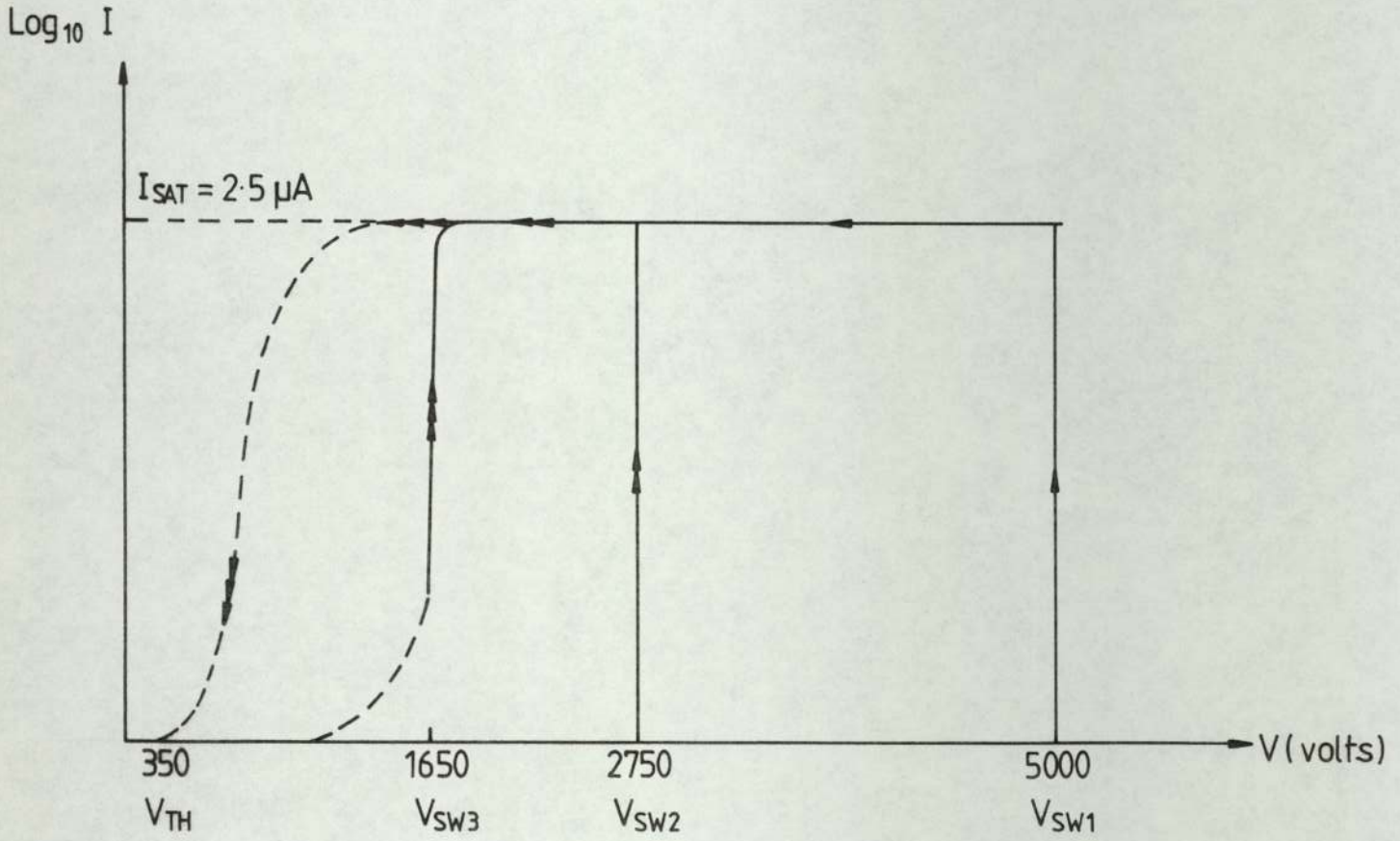

Fig. 4.9 I-V plot of 'type C' atypical behaviour.

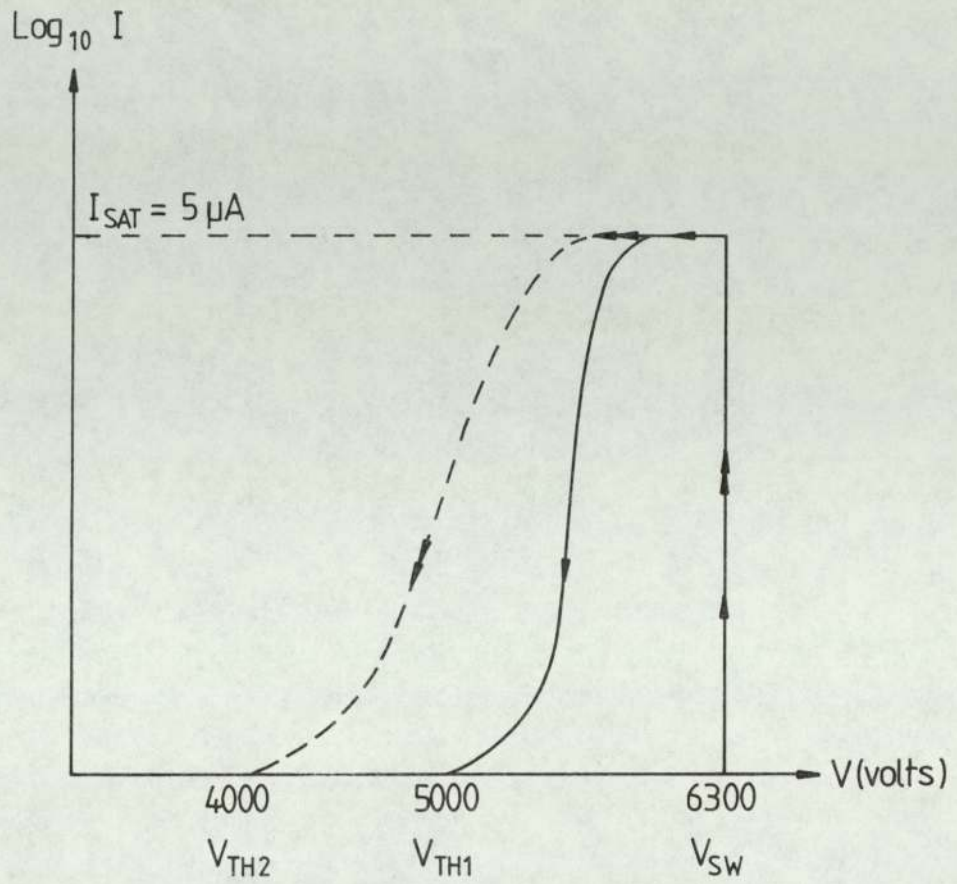

Fig. 4.10 I-V plot of 'type D' atypical behaviour.

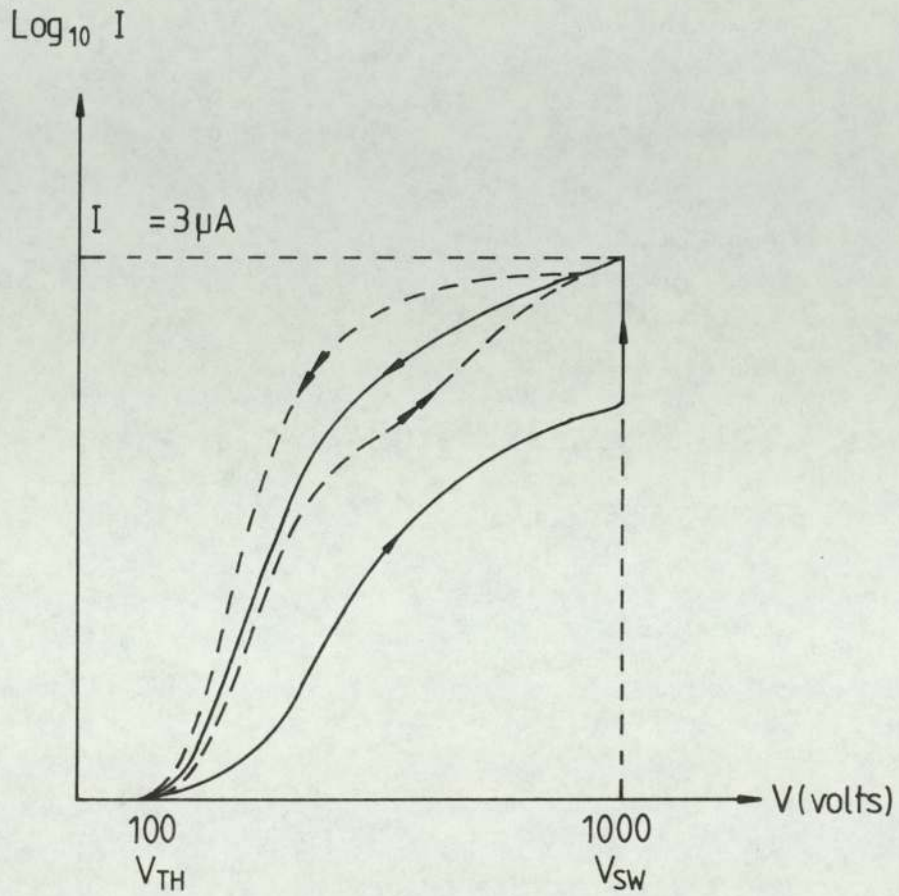

Fig. 4.11 I-V plot of 'type E' atypical behaviour

insulating "balls" of material (see 3.2.1); i.e. where it was reasonable to assume that a "thick" insulating layer ($\gtrsim 200\ \mu$ m) was involved. For these systems, a high conventional initial switch-on voltage V_{SW} is required, but on lowering the voltage, the saturation current I_{SAT} of region 3 extended from say 7000 Volts to very low voltages ($\leqslant$ 100 Volts). However, as shown in Fig. 4.9 on re-cycling the voltage, switch-on effects were again observed, although at progressively lower voltages $V_{SW\ 2}$ and $V_{SW\ 3}$. Eventually though, after three to four cycles, the emitter characteristic approached a "typical" form with a smooth reversible shape and a well defined V_{TH}. The data obtained from this type of emitter is collated in Table 4.4 (see page 176).

Referring to Fig. 4.10 , the fourth type of atypical behaviour (Type D) was somewhat similar to type C, but was characterised by a progressively lowering value of V_{TH} and a corresponding extension of the I_{SAT} region as the voltage was re-cycled; i.e. the value of V_{SW} remained approximately constant. As with type C, the emitter eventually approached the "typical" behaviour after three or four voltage cycles. Emitters of this type are indicated by a suffix "D" in Table 4.3 . The final type of atypical behaviour (Type E) is shown in Fig. 4.11 . In common with other composite emitters, this is characterised by an initial switch-on effect; however, in this case there was no extended saturation region, rather the emission current showed a smooth decrease with applied voltage. After one or two successive voltage cycles the emitter also approached the "typical" behaviour. This type of emitter is indicated by a suffix "E" in Table 4.3 . A possible explanation for this, and also of types A to D will be discussed in the following chapter.

It was occasionally noted that, during the traditional I-V cycling, a negative resistance behaviour occured at high emission currents($\geqslant 10\mu$A).

4.3 EMISSION IMAGES OF COMPOSITE EMITTERS.

The conventional field emission microscope described in section 3.4 has been extensively used in this investigation, firstly, to obtain information about the physical processes involved with these types of emitters, and secondly, to provide a means of measuring such practical electron source parameters as beam brightness, current stability and life time. Experimental data is therefore presented in this section in order to compare the general character of the emission images obtained under identical conditions from the various composite emitting regimes studied, and also how such factors as the insulating layer thickness and thermal treatment influence the properties of a given type of emitters (e.g. the resin-coated tungsten species). As with the case of the I-V data of section 4.2 , a physical explanation of the image behaviour will be given in the following discussion chapter.

4.3.1 AXIALLY-SYMMETRICAL SINGLE-SPOT IMAGES.

Following the format used in section 4.2 when presenting the I-V data, a comparison will first be made between axially symmetric emission images obtained from a clean metallic (i.e. tungsten) tip and as-prepared switched-on composite emitters under similar experimental conditions; i.e. corresponding to the I-V characteristics of Fig. 4.2 . These are shown respectively in the typical example of Fig. 4.12 (a) and (b), from which it will immediately be seen that the emission from the composite emitter (in this case a tungsten tip coated with a 0.2 μ m layer of resin) is very much more concentrated with no apparent structure within the image. Thus, for a given total emission current, the composite emitter image appeared

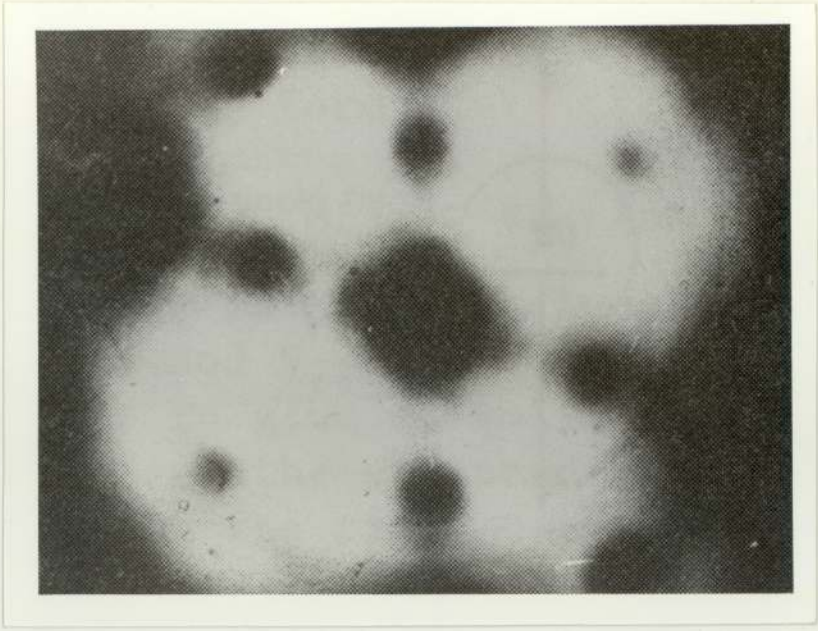

(a)

10mm

(b)

10mm

Fig. 4.12 Projection images obtained from (a) a clean tungsten emitter and (b) after coating with a 0.2 μ m layer of resin. Both images were recorded with the same tip-to-screen separation and the same emission current of 4.5 μ A.

very much brighter. In quantitative terms, the electron optical brightness of the two sources of Fig. 4.12 are respectively in the ratio of one to six. At the operating pressure of $\sim 10^{-8}$ mbar, both images exhibited random fluctuations in intensity : for the metallic emitter, the brightness of individual spots changed abruptly, whilst for the composite emitter the whole image changed in intensity, with sometimes, an accompanying change in the spot-size. However, it was generally found that the stability of most composite emitter images could be greatly improved by in-situ baking to $\sim 140^{\circ}$ C or still better to $\sim 200^{\circ}$ C, for several hours. Any instability which may remain after baking could usually be eliminated by a conditioning procedure; this was carried out by either running the emitter at constant current, for a period of approximately 30 minutes (occasionally a few hours were required) or by leaving it to go through a relaxation process i.e. by turning off the anode voltage and leaving the emitter under vacuum for approximately 24 hours. Baking also greatly reduced the risk of an unstable emitter being destroyed by spontaneously "exploding"; this would be observed as an intense flash of emission, after which there was usually no further current unless higher voltages were applied to the tip. If such exploded emitters were subsequently examined in the T.E.M. , the profile of the tip was usually found to have been deformed as shown in Fig. 4.13 .

To further highlight the effects of baking on the emission image from a 0.2 μ m resin-coated tungsten emitter, the five image sequence shown in Fig. 4.14 illustrates the increased stability of the emission following baking and voltage cycling. This also illustrates that the image spot-size was found to show a strong dependence on the current, when the emission followed the I-V characteristic of Fig. 4.1, i.e. as the voltage applied to the composite emitter was lowered. This finding

Fig. 4.13 A T.E.M. micrograph of deformed tungsten microelectrode coated with resin after tip "explosion". (Magnification = 64800X).

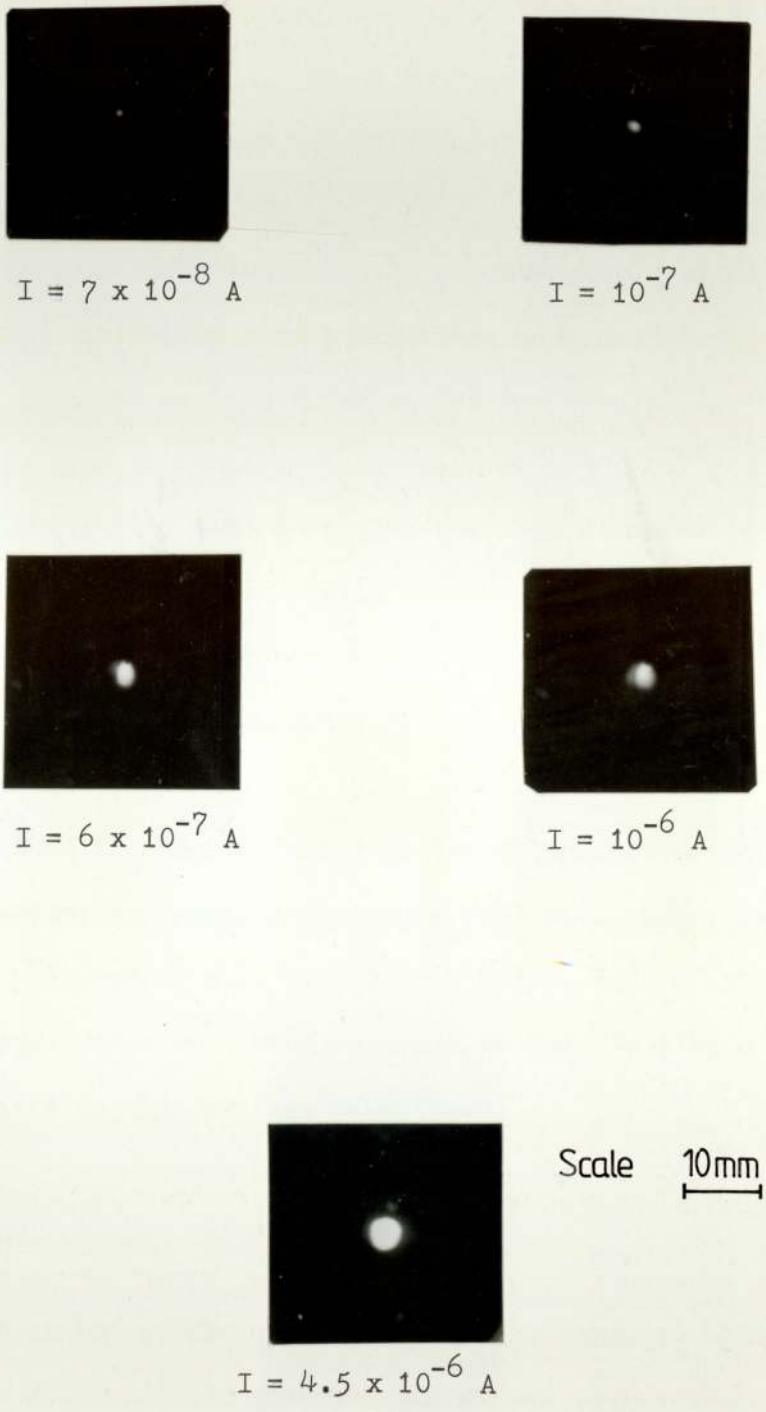

Fig. 4.14 A sequence of projection images showing how the spot size changed with emission current.

has important physical implications which will be discussed in chapter 5 . In fact, the emission image at the highest current (switching current I_{SW}) in Fig. 4.14 remained unchanged over a period of more than 100 hours running at a current of 4.5 μ A, including several "off" periods. These were general findings for the emitters tried; such properties are potentially interesting for commercial electron sources.

However, in order to routinely produce stable single-spot emitters it was found that three more precautions were necessary. Firstly, it was found that the optimum thickness of the insulating layer to obtain this type of emission image was $\sim 0.15 - 0.2$ μ m. Thinner layers, for example, tended to give the type of multiple-spot images described in the following section. Secondly, care needed to be taken with the axial alignment of the emitter to ensure that it was at least 10 mm from the phosphor screen anode (see also 4.2.2). Thirdly, great care had to be taken when initially applying the electric field in order to avoid any rapid current surges (even with a $10^8 \Omega$ series resistor, such surges were still possible). If all the above precautions were effectively taken, most of the composite emitter types which were studied could be made to give a single-spot image similar to that of Fig. 4.12 (b).

4.3.2 MULTIPLE-SPOT IMAGES.

In about 10% of the emitters tested it happened that the initial image of a switched-on composite emitter was more complex than that of Fig. 4.12 (b) in that the emission appeared to come from two or more well-defined sub-emission centres. Four examples of this phenomena are shown in the "before" sequence of images of Fig. 4.15, i.e. before the emitter was subjected to any treatment, where in each

"Before" "After"

(a) Resin Coating

(b) Hydrocarbon Coating

(c) Lacomit Coating

(d) Glass Coating

Fig. 4.15 A sequence of images showing emission originating from more than one sub-emission centre "before" and "after" various tip "conditioning" treatments.

case, the individual spots exhibited independent and random fluctuations of intensity. It will also be seen that in (a) and (b), the emission was directed off-axis, suggesting that it originated from sub-centres that were located away from the geometrical apex of the emitter. The incidents of this latter phenomenon could however be controlled by minimising the axial divergence of the electric field in the vicinity of the tip by increasing the axial distance between the tip and screen. In practise it was found that this parameter needed to exceed 10 mm.

Multiple-spot images were mostly a feature of emitters that had thin insulating layers of less than 0.15 μ m thickness. This is illustrated by Fig. 4.16 which is a sequence of eight cine-film frames taken at a speed of twenty four frames per second. Clearly, the image is very complex with its detailed structure changing rapidly with time. This latter property could be clearly observed, for example, by noting the switching "on" and "off" of the sub-centre located at twelve o'clock. Also, the sub-centre located at three o'clock had the sequence of switching: "on" (c), "off" (d) and "on" again (f) in less than quarter of a second. This behaviour will make the process of obtaining stable distributions from such emitters very difficult. In fact, these images bear a strong resemblance to the characteristic image of a "dirty" tungsten emitter; this therefore suggests that for very thin layers, the electrons "hop" and / or tunnel through it so that the resulting emission image is largely characteristic of the emissivity of the underlying substrate rather than a property of the layer itself.

In cases where muliple-spot images were obtained with thick layers (i.e. $\geqslant 0.15\ \mu$ m), it was often possible to subsequently obtain a single-spot image by processing the emitter using a combin-

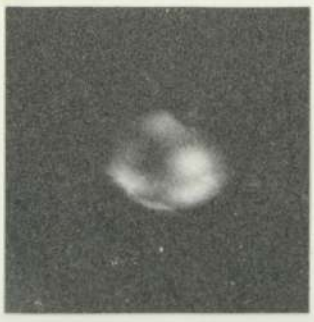

(a) t = 0.04 sec

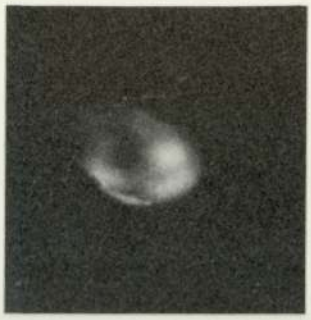

(b) t = 0.05 sec

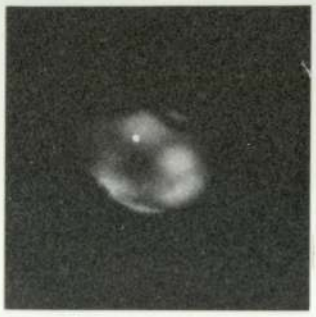

(c) t = 0.96 sec

(d) t = 1 sec

(e) t = 1.08 sec

(f) t = 1.2 sec

(g) t = 1.5 sec

(h) t = 1.9 sec

Fig. 4.16 A sequence of cine-film frames showing the change with time (t) in the muliple-spot images of thin insulating layers.

ation of low-temperature external baking and voltage cycling. Thus the "after" image of Fig. 4.15 (a) was obtained by simply lowering the voltage until the smaller emission centre "switched-off", with an accompanying step-like fall in the emission current (see Fig. 4.8). Subsequent baking at 140°C for approximately 12 hours both stabilised the emission from the larger centre and reduced its emitting area, thus effectively increasing the source brightness. The coalesced "after" image of Fig. 4.15 (b) and (c) were obtained by external baking (for a period $\geqslant$ 20 hours at 140°C), apparently involving some form of annealing process, whilst the final "after" image of Fig. 4.15 (d) was obtained by running the emitter at constant voltage over an extended period of time ($\sim$30 minutes). The brightness of this latter glass source represented one of the highest values encountered in this investigation i.e. its electron optical brightness is ten times higher than that of clean tungsten. Unfortunately, from a practical point of view this type of emitter had a very limited life time, in that they frequently "exploded" after a period which could range from only a few minutes up to a few days at the maximum of emission at approximately 1 μ A. To illustrate the physical consequences of such an event, Fig. 4.17 presents optical micrographs of a tip "before" and "after" explosion, while in Fig. 4.18 two micrographs of exploded tips are shown. The effect of the "relaxation process" in eliminating the multi-spot emission and producing a single-spot emission is illustrated in Fig. 4.19 (a) and (b). In addition, this process also produced perfect stability to both the emission image and current of the 0.2 μ m resin-coated tungsten emitter.

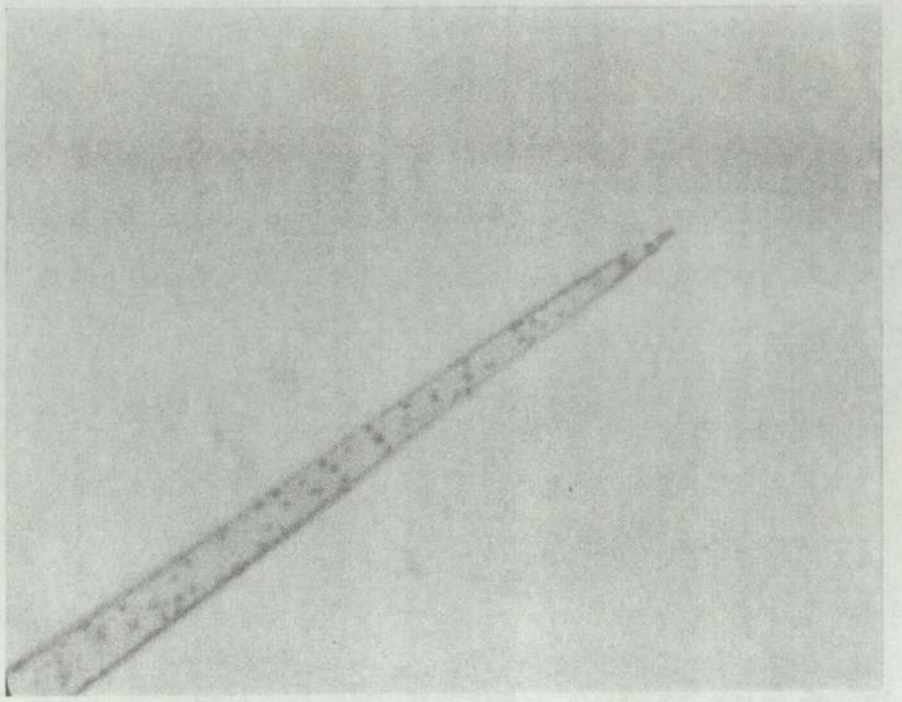

(a)

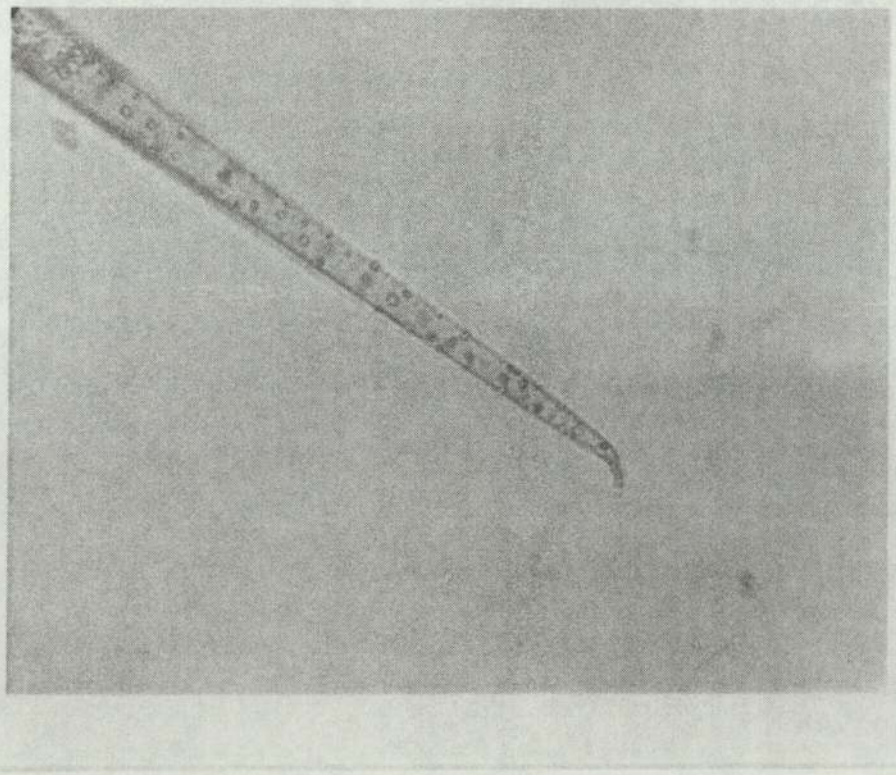

(b)

Fig. 4.17 Micrographs of an internally conducting glass tip (1)

(a) before exploding and (b) after exploding.

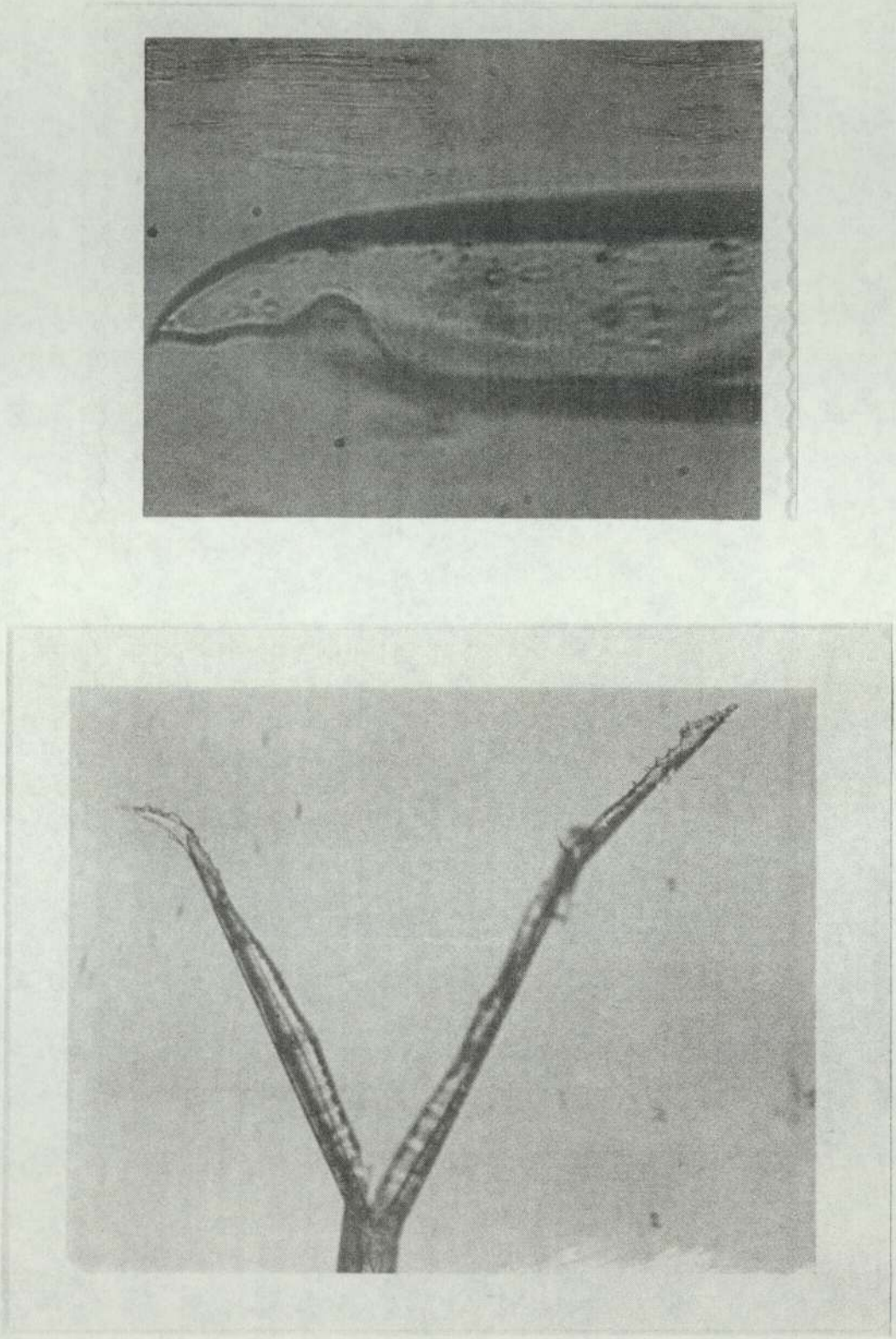

Fig. 4.18 Micrographs showing glass tips (2 and 3) after exploding.

(a)

(b)

Fig. 4.19 (a) Multi-spot emission image obtained from tungsten microemitter coated with 0.2 μ m resin coating.

(b) The same image after 24 hours relaxation process.

NB The images are superimposed over the spectrometer probe hole.

4.4 ELECTRON ENERGY SPECTRA OF COMPOSITE EMITTERS.

As indicated already in this thesis, the vital importance of these measurements lies in the information they contain about the physical nature of the mechanism operating with these composite emitters. The instrumental facility developed for these measurements has already been described in detail in section 3.3 . It will be recalled that this was basically a Van Oostrom retarding potential analyser with the electronic systems modified to give a differential output. This output thus gives the electron energy spectrum from which it is possible to obtain the spectral half-width, i.e. defined as the full width at half maximum (F.W.H.M.), and the peak shift from the substrate Fermi level. By calibrating the energy scan of the spectrometer in terms of the known energy distribution of a reference electron source (in this case a clean tungsten field emitting tip), it is subsequently possible to identify the Fermi level of the cathode substrate on the spectrum of any other electron source. Since however, a spectrum typically required approximately ten seconds to be recorded it has in fact only been possible to record the spectra of the composite emitters that gave stable emission currents over periods in excess of ten seconds.

4.4.1 SPECTRA OF SINGLE-SPOT SOURCES.

The spectra of clean tungsten and resin-coated emitters were compared in Fig. 3.41 , while their current-voltage characteristics and emission images were shown respectively in Figures 4.2 and 4.12 . From this data, it was clear that the spectrum obtained from the composite emitter was distinguished by several features when compared to a clean tungsten spectrum: (a) it was displaced towards lower energies

by 0.7 e V with respect to the Fermi level of a metallic cathode; (b) it had a larger F.W.H.M., and (c) it was more symmetrical than the tungsten spectrum. A sequence of spectra from a resin-coated tungsten emitter is illustrated in Fig. 4.20 which shows the effect of increasing the emission current from $\sim 1\ \mu$ A to the saturation current of such emitter, i.e. $I_{SAT} \sim 4.5\ \mu$ A, corresponding to an increase of tip - to - anode voltage from 390 to 550 Volts. Fig. 4.21 then shows the resulting spectral shifts and the half-widths (F.W.H.M.) as functions of the emission current . The spectral shift was clearly increased considerably by increasing the emission current up to I_{SAT} , while the F.W.H.M. initially had values less than that for a clean tungsten emitter i.e. ~ 0.23 e V, which slowly increased with current up to 0.29 e V as the saturation current of $4.5\ \mu$ A was approached. However, when the current was restricted to the saturation region, neither the spectral shift nor the F.W.H.M. were found to vary with the applied external electric field.

4.4.2 SPECTRA OF MULTI-SPOT SOURCES.

In the case of the multi-spot images, such as shown in Figures 4.15 or 4.19 (a), each spot could be positioned over the sampling anode probe hole, to show that they produced independent single-peaked spectra which were uniquely positioned with respect to the cathode Fermi level at any given applied voltage. A typical result is shown in Fig. 4.22 , where the spectra of the three dominant spots have been superimposed on the same photographic plate. It was also found that the shift from the Fermi level of each peak varied independently with the applied anode voltage, so that the relative separations of the peaks did not generally remain constant when the voltage was cycled.

Fig. 4.20 A sequence of spectra obtained from tungsten microemitter coated with 0.2 μ m resin, illustrating how the shift and half-width (F.W.H.M.) vary with the emission current (increasing from 1.1×10^{-6} A to 4.5×10^{-6} A).

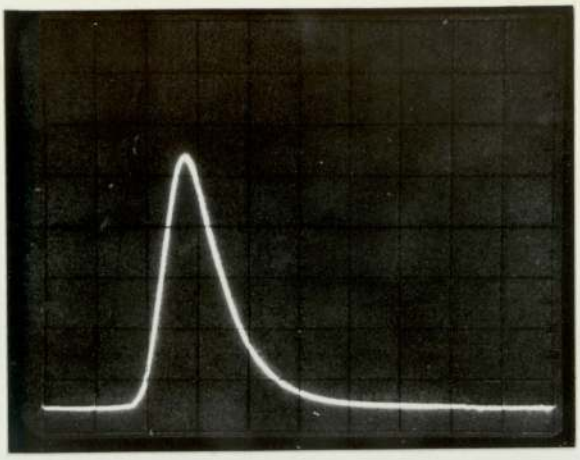

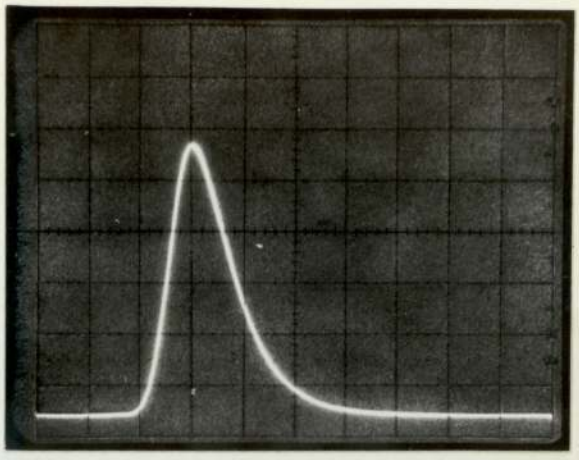

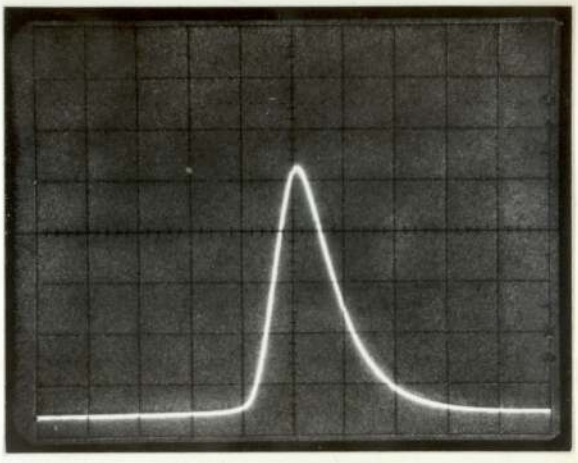

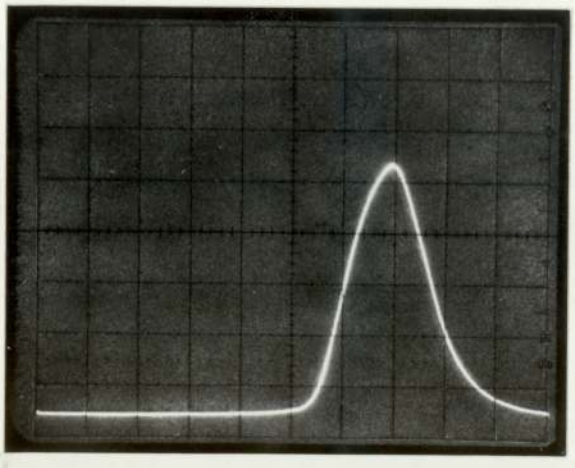

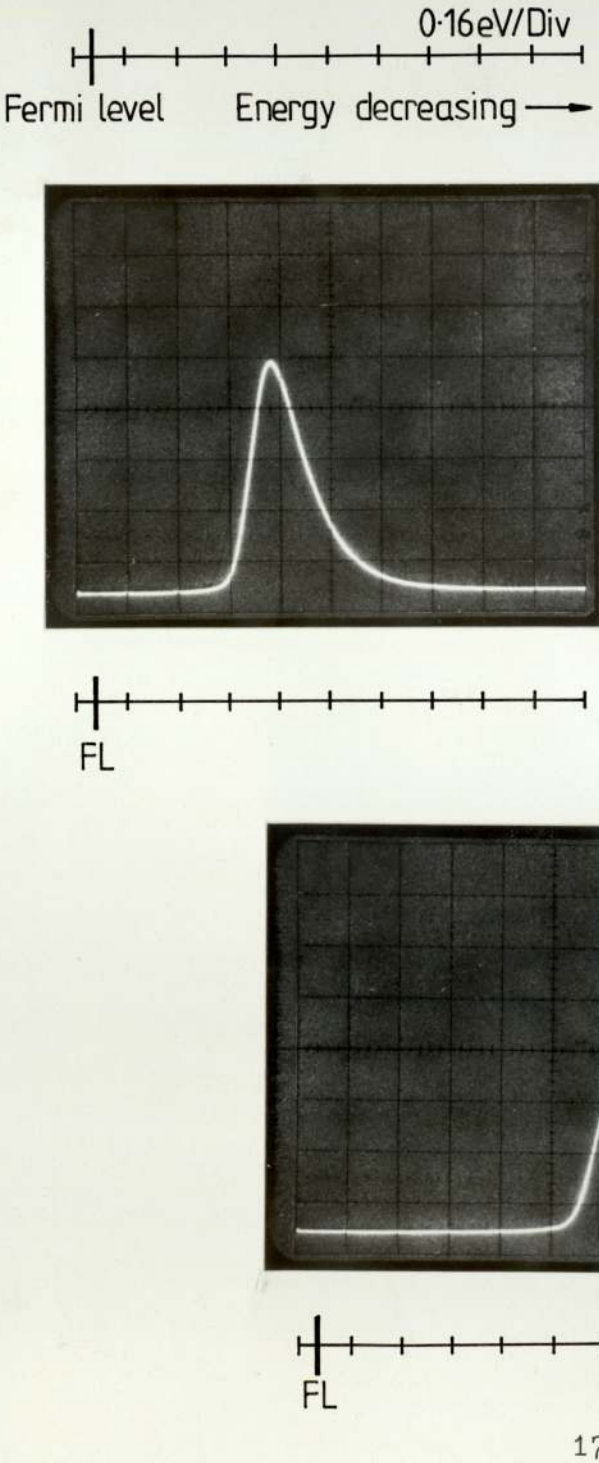
0·16eV/Div
Fermi level
Energy decreasing
FL
FL
FL
FL

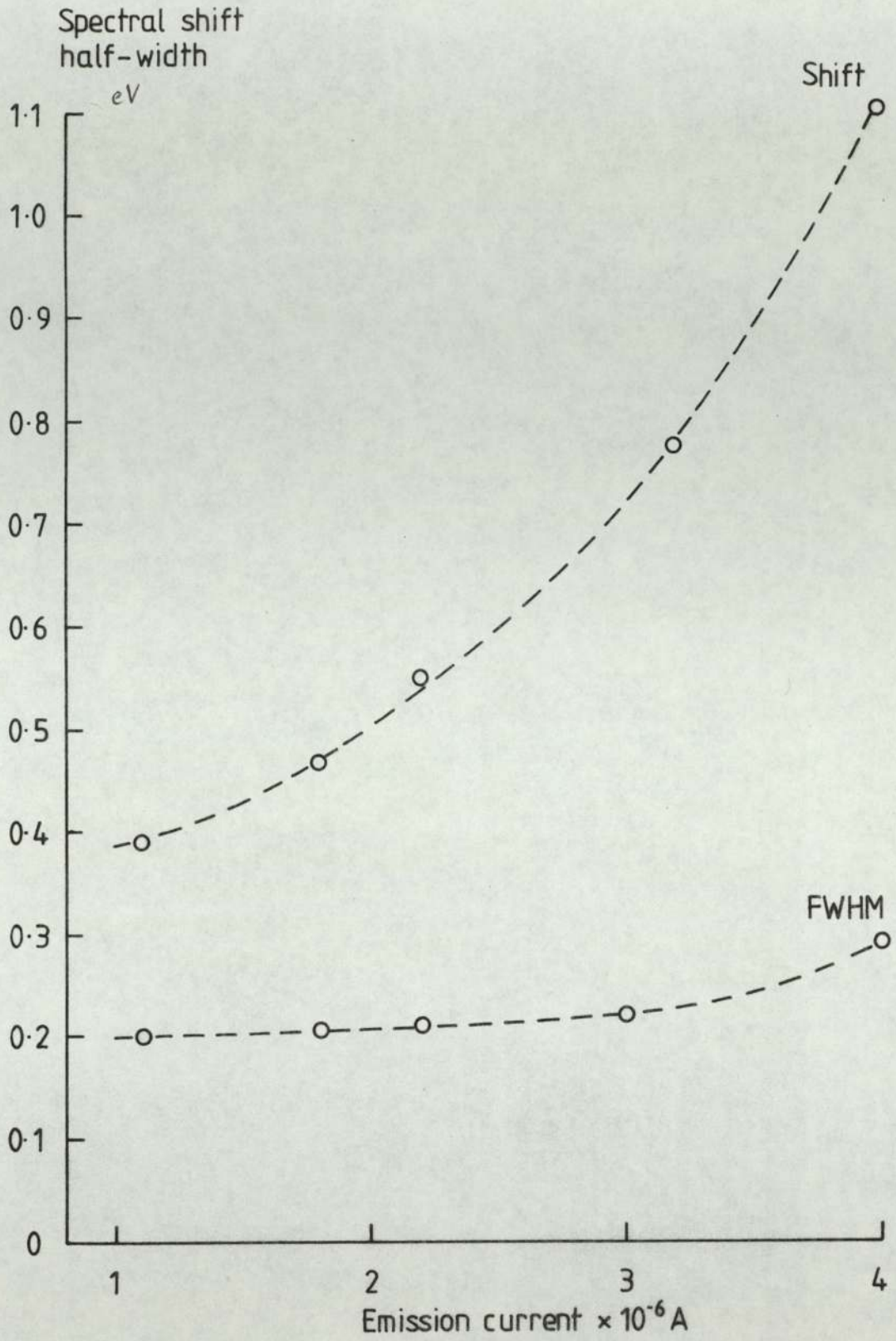

Fig. 4.21 Plot shows the variation of the spectral shift and the half-width (F.W.H.M.), with respect to the tungsten substrate Fermi level, with emission current.

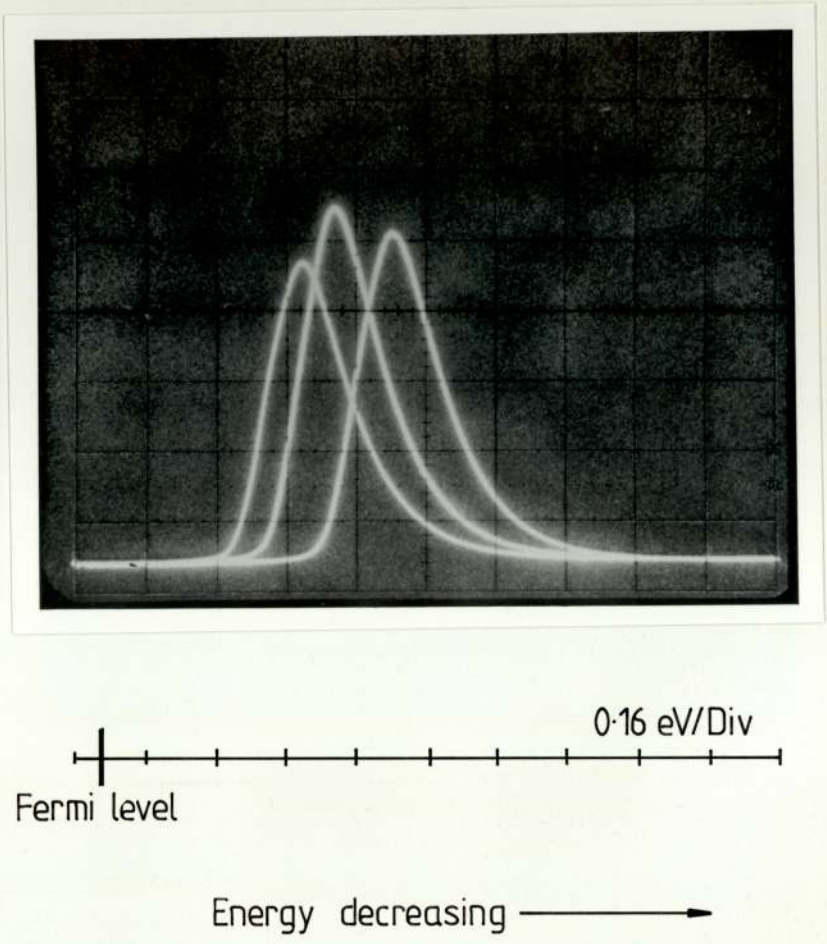

Fig. 4.22 The superimposed energy spectra recorded at constant applied voltage from the individual spots of the emission image shown in Fig. 4.15 .

4.5 EFFECT OF ION BEAM ETCHING.

Although attempts were made to use the facility described in section 3.2.1.4 for controlling the thickness of insulating layers, the technique did not prove to be very satisfactory, mainly because the procedure tended to introduce a high level of instability into the emitted current. However, two examples of the effects of this treatment will be briefly described.

In the first case "extensive" etching was applied to the tungsten emitter coated with a thick ball of resin, shown in Fig. 3.8 (a), which initially gave no emission for the applied voltage up to 12 k V. However, after etching, this tip switched-on at 7 k V during the first voltage cycle and at $\sim$6 k V on subsequent cycles, after which the I-V characteristic closely resembled that of Fig. 4.8. For the second example, "light" ion etch was applied to a tungsten emitter coated with a layer of araldite resin a few microns thick. This initially switched-on at 1900 Volts with I_{SAT} $\sim$1 μ A, but after etching, the switch-on voltage was significantly lowered to $\sim$1700 Volts; in addition, the magnitude of the saturated emission current was three times higher than that obtained before etching producing a similar I-V characteristic to that shown in Fig. 4.2 . From this limited experience, it was concluded that ion beam etching could only be a useful support tool for emitter fabrication, provided a complementary procedure could be developed for "annealing out" the surface changes responsible for the increased current instability.

Type of insulator	Insulator thickness	V_{SW1} Volt	I_{SAT} μA	V_{SAT} Volt	V_{SW2} Volt	V_{SW3} Volt	V_{TH} Volt
Wax ball	thick	10000	8	1300	3300	3300	400
Lacomit ball (without baking)	thick (~300 μm)	8000	5	1300	4500	1500	200
Zinc oxide ball	thick	7000	10	3000	7000	3000	50
Plastic ball	medium	2750	2	300	2600	-	50
Araldite resin ball	thin	1900	1	300	1100	-	75
Glass tip (Electrodag) film	thin	2750	2.5	1300	1600	500	350

TABLE 4.4 Collated experimental data from emitters exhibiting ' Type C ' atypical behaviour.

CHAPTER 5

DISCUSSION

5.1 Introduction

To provide a focus for the discussion of the experimental data, the most important of the findings presented in the previous chapter will first be briefly summarised.

(1) Composite microemitters exhibit a switch-on process whereby, as an electric field is slowly applied to a virgin emitter, no emission is observed until a certain threshold field ($\geqslant 3 \times 10^{8}$ V m^{-1}) is reached; experimentally this is recorded as the threshold switching voltage, V_{SW} . At switch-on, the emission current suddenly jumps from an effective zero-value to the saturated current, I_{SAT} , typically ranging between 1 and 10 μ A. If the field is then progressively lowered, the current at first remains constant at I_{SAT} , but then starts to decrease as the field is further lowered below V_{SAT} . However, a continuous emission was obtained for fields down to perhaps one or two orders of magnitude lower than the switch-on field: i.e. the initial cycling of the field gave a large hysterisis in the emitted current. A subsequent cycling of the field gave a smooth I-V characteristic with a small, but significant, "secondary" hysterisis between the increasing and decreasing curves.

(2) The Fowler-Nordheim plots of the current-voltage characteristics are found to be approximately linear for emission currents $\leqslant 10^{-7}$ A, although there is a marked deviation at higher currents. The slopes of the plots are typically four to six times lower than those obtained for the uncoated metal tips; i.e. corresponding to a lowering of the substrate metal work function from ~ 4.5 e V to ~ 1.8 e V.

(3) The emission images obtained from composite microemitters with relatively thick insulator coatings ($\gtrsim 0.15\ \mu$ m) generally consist of a stable concentrated bright spot with no apparent substructure. However, if the insulator coating was relatively thin ($\lesssim 0.15\ \mu$ m), the image breaks up into several discrete spots, each of which tend to intermittently switch on and off. As the emission current increases the image size also tends to increase, but more will be said about this later.

(4) Secondary switching processes, involving step-like changes in the emission current, are occasionally observed during the initial voltage cycling; i.e. after the initial switch-on effect. Each of these step-like changes are accompanied by the appearance of new spot on the screen; i.e. the switching on of another emission centre.

(5) The low-temperature ($\lesssim 200^{\circ}$ C) baking of microemitters is found to improve their performance: i.e. the field required to extract a given current is typically lowered by a factor of 3 to 4 , whilst the emission images become more stable and bright with a corresponding stabilisation of the emitted current. Other tip "conditioning" treatments, such as running them at constant current for approximately 30 minutes, or the relaxation process described in section 4.3.1 has similar effects. In fact, the relaxation process can sometimes cause multi-spot images to become single-spot.

(6) The electron energy spectra obtained from composite microemitters depart markedly from those to be expected for metallic emitters; i.e. they are always displaced towards lower energies with respect to the Fermi level of a metallic cathode. In addition, both this shift and the F.W.H.M. of the distributions display a non linear increase with current and field, with the spectral shape becoming progressively more symmetrical. At field levels $\gtrsim 5 \times 10^{8}$ V m^{-1} the F.W.H.M.

eventually exceeds the value obtained from a metallic emitter.

(7) Single-peaked electron spectra are obtained from each of the spots composing in a multi-spot emission image, where the spectral shifts from the Fermi level of each peak vary independently with the applied field.

(8) There is an optimum thickness of the insulator resin coating on the W-microemitters of $\sim 0.09\ \mu$ m for producing the highest I_{SAT} values.

The experimental findings which were summarised above, and the additional results reported in chapter 4 , have important implications to both the technological applications of field emission electron sources, and the fundamental physical understanding of the emission mechanism operating with this type of composite micro emission regime. Accordingly, it will be convenient to present separate discussions of these two aspects.

5.2 TECHNOLOGICAL IMPLICATIONS.

The manufacture and testing of various types of composite field-emitting micropoint electron sources has been described in chapter 3.2 . These consisted of two main types: firstly, tungsten micropoint emitters that were coated with a variety of insulating materials, such as the epoxylite resin and hydrocarbon, and secondly, the internally-conducting glass microemitters. Sufficient data was obtained to make the following critical appraisal of the performance of these sources compared with the more conventional metallic (generally tungsten) field emitting micropoint electron sources. This appraisal considers important practical factors such as source brightness, electron energy spread, emitter life-time and current stability. A brief account will also be given of the possible uses and recent advances in the technol-

ogical applications of field emission electron sources.

5.2.1 THE FIELD EMISSION ELECTRON SOURCE.

5.2.1.1 BACKGROUND AND DEVELOPMENT.

Due to the requirement of producing a high electric field E (i.e. $\gtrsim 10^9$ V m^{-1}) at the surface of a metallic field emission cathode (F.E.C.) with a reasonably low extraction voltage, (say < 1 K V) it is necessary to use a micropoint cathode with an extremely small tip radius, typically between 10 and 100 n m. With such an arrangement a current density "J" of about 10^5 A cm^{-2} can easily be obtained, whose field dependence is governed by the Fowler-Nordheim equation 2.17. Since this value is about 10^3 times higher than the upper limit obtainable from a thermionic source, much research effort has been made to develop the field emission cathode as a practical source of electrons for a variety of technological applications. Originally, their application was investigated by the Dyke group in the 1950s, and in the early 1960s, at the Linfield Research Institute (36, 112, 113). In summary, the interest in field emission sources stems from their following well known properties (114): (1) they are "cold" electron sources, theoretically capable of operating at temperatures as low as T = 0 K; (2) they can deliver a large current density J $\simeq 1 \times 10^8$ A cm^{-2}; (3) they have a small optical source size (20 to 30 A°) of high brightness ($\gtrsim 10^9$ A cm^{-2} sr^{-1}); (4) they have a highly nonlinear I-V characteristics; and (5) they have a relatively narrow energy distribution ($\sim$ 250 m e V).

Any application of a F.E.C. requires ultra high vacuum conditions, i.e. pressure of $\lesssim 10^{-9} - 10^{-10}$ mbar, in order to obtain current stability and long emitter life-times. These stringent vacuum

requirements deterred the extensive applications of the F.E.C. until, on the one hand, the recent advance in vacuum technology, and on the other, the development of alternative types of cathode which are less sensitive to environmental conditions [115]. Much research has taken place [116 - 120] to identify the exact effect of pressure on emission current stability, and on the emitter itself. From the results obtained by Van Oostrom [120] it may be deduced that the operational life-time of a W-field emitter would be practically without limit at a vacuum of the order of a 10^{-14} mbar. At this pressure the stability of the emission current would also be more than sufficient to satisfy the requirements demanded of a source for most practical electron optical instruments. However, for technical and economic reasons, it is more usual to find such instruments operating with a vacuum in the emitter region lying in the range 10^{-8} to 10^{-10} mbar. Under these conditions, the emitter will: (1) adsorb residual gas atoms at the tip surface; (2) be bombarded by positive ions formed as a result of electron-gas atom interactions; and (3) be subject to face migration of admolecules and adatoms. These processes may occur at rates sufficient to significantly affect operation. Thus it becomes necessary to periodically "flash" the emitter at an elevated temperature in order to remove the layer of adsorbed gas which accumulates, and to smooth out the surface irregularities which may build up as a result of ion bombardment [119].

Crewe et al [9] and later Swann and Smith [119] illustrated how the mean emission current varies, at constant applied voltage, during a typical operating cycle of a W-emitter. Thus referring to Fig. 5.1 , the flat stable region is where the emitter may successfully be used as a source. This region lasts for a time which is dependent on vacuum conditions, after which, the current starts to

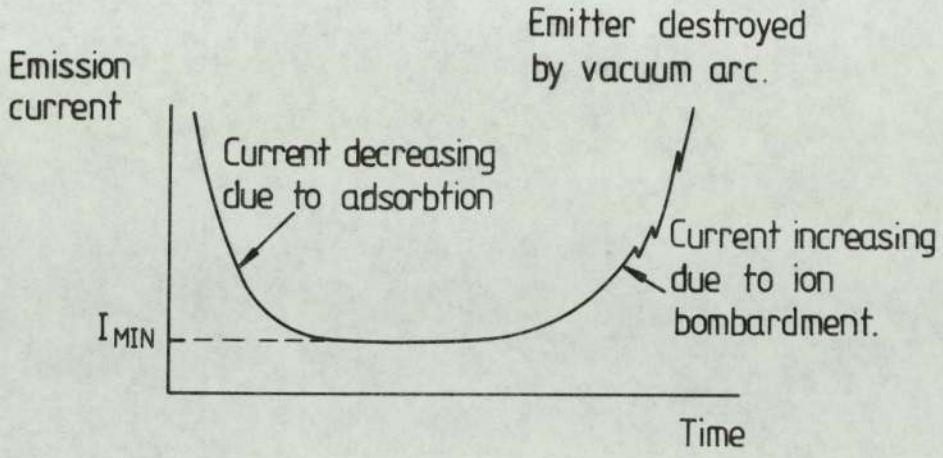

Fig. 5.1 Illustrating I_e variations and cyclical life-time criterion, of constant applied potential.

rise and becomes increasingly unstable until operation is no longer possible. The emitter then has to be reflashed, whereafter the cycle can be repeated. During the operating period of the cycle, the emission current exhibits random fluctuations, which appear as noise on the beam entering the electron optical system e.g. a S.E.M.

5.2.1.2 EMITTER TYPES AND RECENT ADVANCES.

The use of a heated tungsten point cathode as an electron source of smaller size and higher brightness than the conventional thermionic cathode, was first proposed by Hibi [121] in 1955. The sizes of the emitter radii, and the applied field strength, suggests emission enhancement due to Schottky effect was the primary mechanism in Hibi's early work [114]. Cosslett and Haine [122] compared the tungsten hairpin thermionic and field emitting cathode, and concluded that the F.E.E. cathode was superior for image spot diameters less than ~1000 A°. Later Drechsler et al [123] refined these considerations, and compared the behaviour of pointed cathodes under conditions of cold

field emission, T F (temperature-assisted field emission) and Schottky emission and concluded that aberrations in the lens systems used to image the source were the primary limit on image spot size in each case. Everhart [124] performed a rigorous analysis of the optical properties of a "cold" field emitter and Schottky tungsten point source emitter, by combining the point source model with a simple analytical model for the lens action. Lauer [125] also made similar calculations for thermionic emission guns. A more realistic analysis of the source optics of a pointed cathode was later carried out by Wiesner [126], using a model of a field emitter consisting of a sphere-on-an orthogonal-cone (S O C).

In past decades, many analytical models for determining the magnitude of the electrostatic field at the tip of a micropoint cathode and a normal planar anode have been developed. Muller [127] and Haefer [128] assumed a cathode of hyperbolic shape in front of a plane anode, while Drechsler and Henkel [129] improved this model by superimposing the field due to an appropriately located point charge system in order to get a better approximation to the real cathode shape. Dyke and co-workers [42], Wiesner [126], Wiesner and Everhart [130] and Kern [131] used the S O C model, to calculate the field; for the details of the model see Kasper [132].

Very briefly, field emission electron sources take the form of either diode or triode gun systems. Diode guns are formed by the micropoint cathode and a concentric anode aperture, known as the extractor electrode, and is similar to the geometry used by Muller [75] in the field emission microscope, or later in the field ion microscope [133]. This type of device produces a highly magnified image, where the image formation process has been fully investigated by Muller and Tsong [134]. In a triode F.E.E. gun, the point-

cathode is followed by two co-axial anode apertures which have a lens action for focusing of the emitted beam [132]. This type of system has been subject of numerous investigations, including those of Butler [135], Crewe et al [9], Munro [136, 137], Tonomura [138], Riddle [139] and Orloff and Swanson [140].

The stability required of the field emission current is an important factor in choosing the type of gun system to be used. However, this choice is not easy, since the stability depends on mechanical, thermal, electrical and chemical considerations, all of which are interdependent. Investigations of this complex question, which is impossible to treat exactly, are so numerous that they cannot all be cited. However, a review of many of the earlier studies has been given by Swanson and Bell [114], whilst the investigation of Ranc et al [141] is representative of more recent work on the stability of W-microemitters.

The high applied electric field E exerts a mechanical stress on the tip which must be balanced by elastic stresses in the material. For this reason only materials of high mechanical strength, such as tungsten and glassy carbon, may be used for cathodes. In addition to this, other requirements, such as high melting point, low vapour pressure and relatively high electrical and thermal conductivity, resulted in tungsten being used for the emitters in most high field emission work. The characteristics of such a source are now well known, having been successfully applied in high resolution scanning transmission electron microscopy S.T.E.M. by Crewe and co-workers [8, 142] and later by Swann and Smith [119], and will be compared in section 5.2.2 with those of the sources developed in this work. Attempts have been made to improve the performance of the W-emitter by means of an oxygen-enhanced thermal-field shaping method, which

requires the processed tip to be operated at 900°C [143, 144]. The deposition of various materials on the tungsten to improve its stability have also been extensively investigated, e.g. thin monolayer films of geranium [145], carbon [146, 147, 148] Zirconium [115, 149, 152]. In addition to tungsten, molybdenum fine tips were coated with thin films (0.5 - 2.0 monolayers) of transition metals (Re, Cr, Ti, Sc, Th, Y) by Davydova et al [118], where they improved the emitter current decay between 10% and 85% . In contrast, the work by Bolin and Trump [153] suggested that the coating of tungsten with epoxy resulted in large reduction in emission current (approximately 5 orders of magnitude). Apart from depositing a monolayer of carbon on tungsten, a variety of other carbon materials have been used as field electron sources. These generally have work functions of 4.5 e V, a low ion etching rate, low rate of gas adsorption, and hence the emission characteristics of the tip will be less affected by physisorption of gases [154, 155].

By using carbon fibre as a field emission cathode, it was possible to obtain a current stability comparable to that of tungsten, but at a pressure of only $\sim 10^{-8}$ mbar [7, 11, 156 - 161]. Glassy carbon F.E.E. sources were also manufactured [154, 162 - 164] and excellent characteristics were reported [154]. This material seems promising and therefore the possibilities of developing its use in the future will be discussed in the Conclusion. Lanthanum hexaboride ($La B_6$), which was first investigated by Lafferty [165], has been used as a field emitter because of its favourable physical properties, i.e. it is a refractory metal and consequently hard and resistant to ion bombardment [166 - 168]; it also has a low work function (~ 2.7 e V). Windsor et al [169] and more recently, Mulvey [170] described its emission properties in detail. Several other types of material have

been used as field electron sources; e.g. TiC needles by Adachi et al [171], GaAs and GaP sharp emitters by Ohno et al [172] and SiC whiskers have been investigated by Nishida [173], Baker [174] and Baker et al [156, 175]. In some cases [172] their I-V behaviour, including the hysterisis effect, is strikingly similar to that reported in section 4.2 for composite emitters. Finally, ZrC, WC, TaC and LaB_6 emitters were investigated by Elinson and his co-workers [176, 177], who were also interested in the effect of different electrode geometries on the ionic bombardment of the emitter [178].

Arrays of emitters, have been developed by Spindt using semi-conductor technology [15, 179], and their emission capabilities evaluated by Forman [16]. Similar arrays of emitters have been studied by Stewart and Wilson [180]. A thin field emitter of tantalum carbide with a sharp knife-edge, has also been described by Shirokov [181]. In an alternative approach, a thin silicon oxynitride film metal-insulator-metal system, which relies on a hot-electron mechanism, has been reported by Yankelevitch [17]. Finally considerable effort has been expended on developing negative electron affinity cold cathode devices [18, 182, 183].

In contrast, very little work has been reported on glass-based field emission sources. Roynet and Mignolet [184] investigated field emission from metal tips coated with glass, but found to give very low emission currents. Hibbert and Robertson [185] used a broken glass tip in contact with a murcury pool, but no measurable emission current was obtained. Later they tried to obtain emission from borosilicate glass in the presence of residual gases [186]. A comparison of the characteristics of these types of emitter, with those of the systems described in chapters 3 and 4, will be presented

in section 5.2.2 .

5.2.1.3 USES AND APPLICATIONS.

A field emission source, because of its special properties outlined in the previous section, offers major advantages in electron beam equipment requiring high brightness and coherence. The most successful exploitation of such sources has been in the manufacture of compact, very-high-powered X-ray tubes (Fexitrons) by Dyke [36]. Such tubes are pulsed with voltages ranging from 70 k V to 2 M V and widths from 10^{-7} - 2 x 10^{-8} s, and give peak powers varying from 147 to 10000 M W, with spot sizes of 2 to 5 mm diameter [187]. As a result, the Fexitron is extremely useful in high-speed X-ray photography [36, 187 - 189]. As mentioned already, field emission sources have been successfully incorporated in a high resolution S.T.E.M. by Crewe and co-workers [8, 9, 142, 190]. In addition to S.T.E.M., the F.E. source has been applied to a range of other electron beam instruments, such as the electron-probe microanalysers, electron beam fabrication systems, Auger analysis system, transducers, flash X-ray devices [113], X-ray microprobe analysers, switch tubes, cathode ray tubes [7, 157]. The future should see further important applications in electron diffraction, holography, microrecording and other electron-probe instrumentation.

Various workers, e.g. Fontana and Shaw [191], Dyke [36], Froome [192], Dyke and Charbonnier [113] Pushpavati and Van de Ziel [193], have investigated the use of field emitters in microwave devices. Dyke and co-workers developed highly compact, fixed-frequency, microwave generators-which they named 'Femitrons'. These devices have been used in the 3 - 8 cm region as amplifiers, mixers, and multipliers operating at high powers with efficiencies of 40 - 80%

(thermionic tubes have efficiencies of around 30%). The operating pressure within these valves was 10^{-7} - 10^{-10} mbar (see reference 157). Field emitting cathodes can also be used in computers and microminiature valves [194]. Developments along these lines have been made by Hansen [195] and Koyama and Kawai [196], who constructed a miniature triode. Both Spindt [197] and Cline [198] have investigated the possibility of making miniature multi-array electron beam devices. Mention should also be made of the magnetic field emission gun [199], which can be easily adapted to any kind of electron microscope, and is available in a commercial form: this gun was originally developed by Tryon and Laberrigue [200].

5.2.2 A COMPARISON OF THE PERFORMANCE OF COMPOSITE MICROEMITTERS WITH THAT OF CONVENTIONAL METALLIC MICROPOINT EMITTERS.

For the reasons outlined in the previous section, there is much technological interest in the development of F.E. sources. Thus it is important to assess the practical potential of the composite microemitters developed in the course of the present study. In the following sections, the performance of this new type of sources will be critically compared with the more conventional metallic micropoint emitter.

5.2.2.1 SOURCE BRIGHTNESS.

According to Borries and Ruska [201], the average brightness $\overline{B}$ of an electron beam is defined as the emission current ΔI per elemental area ΔA normal to the beam and per unit solid angle $\Delta\Omega$, i.e. $\overline{B} = \Delta I / (\Delta A . \Delta\Omega)$. The beam brightness increases linearly with the emitted current density J from the cathode

(i.e. $J = \Delta I / \Delta A$) and with the accelerating voltage, but inversely with the lateral kinetic energy of the electrons. For tungsten micropoint emitters, a value for J of 10^6 A cm^{-2} was obtained by Dyke and Trolan (202), and is now an accepted average value (141, 154). Swanson (115) achieved, with his zirconiated W-emitter, a $\overline{B}$ of $\sim 10^{10}$ A cm^{-2} sr^{-1}, while Lea (158) reported 10^8 A cm^{-2} sr^{-1} for carbon fibre emitters. This leads to a value of $\overline{B}$ which is usually taken as $\simeq 10^{10}$ A cm^{-2} sr^{-1} although various other values have been given by different researchers working under somewhat different experimental conditions. Thus, the value of $\overline{B}$ has been given by Crewe et al (142) as 7×10^{11} A cm^{-2} sr^{-1}, Ranc et al (141) as $\simeq 10^9$ A cm^{-2} sr^{-1} and by Van der Mast (203) as 10^9 A cm^{-2} sr^{-1} (at 100 K V). No higher value for $\overline{B}$ has been reported for any of the various types of sources reported in 5.2.1.2 .

In contrast, the composite emitters developed during this work invariably achieved a higher $\overline{B}$ than that of clean tungsten for a given total emission current. Thus, the resin-coated tungsten micropoint emitter gave a value of $\overline{B}$ that was $\sim$ six times higher, the internally-conducting glass microemitters gave a value of $\sim$ ten times higher beam brightness (see sections 4.2.2 and 4.2.3), whilst the W-microemitters coated with hydrocarbon gave approximately the same brightness.

5.2.2.2 EMISSION IMAGES.

The emission image provides valuable information about different practical parameters such as brightness (see previous section), current stability and life time (see section 4.3). The only aspects which will be compared here are the image structure and stability.

A well known characteristic of the tungsten image is its fragmented

appearance (see Fig. 4.12 (a)), where stability depends on many factors. The flickering of the individual spots is a problem which many researchers have tried to solve by different means; these include treating the tip by periodic field desorption and flashing processes [119, 160]. However, this image instability was reported to persist even after oxygen-enhanced thermal processing [143]. These problems were also encountered with glassy carbon tips [163] and carbon fibre [7, 156]. The emission images of all the conventional emitters are reported to consist of multi-spots images which mostly flicker and change in intensity with time [7, 163, 171].

In contrast, the typical emission image of the composite emitters reported in this thesis, generally consists of a single-spot image of uniform intensity (see Figures 4.12 (b), 4.14 and 4.19 (b)); i.e. it has no apparent sub-structure within the image. Also, it is highly stable with time, after the initial switch-on process.

5.2.2.3 EMISSION CURRENT.

For conventional emitters, the emission current increases with applied voltage in the manner shown in curve 'A' of Fig. 4.2 for clean tungsten. In contrast, the typical behaviour of a composite microemitter (see Fig. 4.1) involves an initial switch-on of the emission current from an effectively zero-value to a saturated value ranging between 1 and 10 μ A. This current is typically very stable, which is reflected by the stable emission image mentioned above. With all the major types of the new composite microemitters, i.e. W-microemitters coated with resin, hydrocarbon, lacomit and internally-conducting glass tips, it was possible to obtain a given value of emission current at a field that was typically $\lesssim 0.5$ that required to draw the same current from the various types of conventional

emitters discussed in earlier sections. As an example, a clean W-emitter in a given electrode geometry required $\sim$ 1100 Volts to draw a current of 1 μ A, while a resin coated tip, only required $<$ 500 Volts to give the same current. The only microemitter known to give a comparable performance to this, is the carbon fibre which can give a 1 μ A emission current at less than 1 K V, however, the emission image is unstable i.e. it flickers (7, 156). It should be noted that the F-N plots of the composite emitters were generally linear for emission currents $\leqslant 10^{-7}$ A, which is in reasonable agreement with published results for materials such as Zr / W (115), LaB_6 (169) and carbon fibre (158).

5.2.2.4 STABILITY.

The problem of stability, discussed in 5.2.1.2 , has been a major handicap for all previous field emission sources, and despite many efforts, is still to be overcome. However, the composite sources reported here are believed to be a major advance towards solving the stability problem, especially the resin-coated tungsten with its extremely stable emission current and image; with no significant noise recorded during an emission period $\sim$ 100 hours.

5.2.2.5 ENERGY SPREAD OF EMITTED ELECTRONS.

It is well known from studies on conventional emitters that the spectral half-width is very sensitive to the presence of contaminant ad-atoms on the surface of the emitting tip. In fact, it is only by taking the maximum precautions to obtain an atomically clean tip that it is possible to approach the value of $\sim$ 230 m e V. In contrast the electron energy distribution measurements reported in

section 4.4 , indicate that composite emitters typically have a spectral half-width of $\lesssim$ 300 m e V for emission currents $\lesssim 5\,\mu$ A; i.e. as a matter of routine without any special precaution. In this respect therefore, composite emitters have a significant advantage over conventional emitters.

It should also be remembered that the spectral characteristics of composite emitters also differ from say W-tips (e.g. Young [48]) by exhibiting a field dependent shift towards lower energies with respect to the F.L. of a metallic cathode. In addition, the F.W.H.M. also increased with field, eventually exceeding the value for a metallic emitter. These results agree with those obtained from carbon fibre [11] and Zr / W [115]. In the majority of studies with conventional emitters, no such field-dependent shift has been noted, although Veneklasen and Siegel [143] reported an increase in the F.W.H.M. for O / W tips compared with those of clean tungsten.

5.2.2.6 LIFE-TIME.

The life-time of an electron source accompanied by a constant stability of emission current and image, is a vital consideration in determining whether such a source has potential technological applications. Thus, a life-time test of more than 100 hours was carried out on a resin-coated W-emitter and revealed perfect stability in both emission current and image, with negligible recorded noise. In contrast, published work on the behaviour of W-emitters under U.H.V. conditions indicate that current fluctuations and flicker noise appear after only few hours operation, so that they require intermittent treatment such as flashing [119, 160]. As already mentioned, Van Oostrom calculated that, at a pressure of 10^{-14} mbar, a clean W-emitter could possess unlimited life [120].

However, for pressures of less than 10^{-7} mbar, a life time of 1000 hours is possible. Such life-times have been reported for Zr-coated (115) and oxygen-processed tungsten (143), and also for LaB_6 (169). However, all these showed current changes and instabilities during the test. Similar current fluctuations were also reported to be associated with emission from from glassy carbon tips (154, 163). Carbon fibre tips have a life-time of 2400 hours at 10 μ A emission current and 500 hours for 100 μ A (156) although a high level of noise was still a feature of this type as well.

As with the resin-coated W-emitter referred to above, it was also found that the internally-conducting glass tips had a life-time of several days, which was an enormous improvement over previously reported results (185), where a life-time of only 30 seconds was found for a W-tip coated with glass. On the basis of these findings it is believed that composite emitters offer very considerable practical advantages.

5.2.2.7 EMITTER PROFILE.

Not surprisingly, it was also found that the profile of composite emitters remained constant during operation, even after running for periods exceeding 100 hours. In contrast, the onset of instabilities with W-and carbon fibre tips (204) has been associated with a degradation of the emitter profile. Similar changes have also been reported by Futamoto et al (164) glassy carbon fibre tips. The most probable explanation for the stability of composite emitters is that the emission is controlled by the "protected" metal-insulator interface existing between the tungsten and resin (see section 5.3), rather than by the dynamic distribution of surface states as in the case of conventional emitters.

5.2.2.8 EASE OF FABRICATION.

The fabrication of the composite emitters has been shown to be simple and cheap. In this respect, they are certainly comparable with conventional W-emitters, but have many advantages over the often more costly fabrication processes of other emitters such as glassy carbon (154) or GaAs and GaP (172) or LaB_6 (169).

5.3 THEORETICAL IMPLICATIONS.

Before considering possible theoretical interpretations of the emission characteristics of composite microemitters, it could be helpful to list their main characteristics.

(1) They exhibit a switch-on effect, typically at fields $\gtrsim 3 \times 10^8$ V m^{-1}.

(2) Their F-N plots are usually linear for currents $\lesssim 10^{-7}$ A.

(3) Their emission current typically saturates following the switch-on.

(4) Their I-V characteristics show a hysterisis effect, between the increasing and decreasing curves, for secondary voltage cycling.

(5) Secondary switching processes, are sometimes observed involving step-like changes in the emission current.

(6) I-V characteristics corresponding to a negative resistance behaviour are occasionally observed at high emission currents ($\geqslant 10^{-6}$ A).

(7) They give stable and concentrated single-spot images for thick coatings, and multi-spot images for thin coatings that tend to flicker intermittently with time; i.e. switch on and off.

(8) Their electron spectra shift with increasing field towards lower energies; typically, the minimum spectral shift from the substrate Fermi level is $\gtrsim 0.2$ e V.

(9) Their F.W.H.M. increases non linearly with applied field from ~ 0.2 e V at $\sim 6 \times 10^{8}$ V m^{-1} to ~ 0.3 e V at $\sim 10^{9}$ V m^{-1}.

(10) Their spectra are more symmetrical than that of a clean W-emitter.

As a first possible explanation of the observed emission behaviour, the model illustrated in Fig. 5.2 will be considered. It will be recalled from Hurley's conducting filament model [70] (see section 2.4.2) that a filament may be electroformed through an insulating layer which will then behave as a metal-like whisker and give rise to a local field enhancement at the vacuum interface that could be sufficient to promote field electron emission. By analogy, one could imagine that a similar filamentary structure is "formed" in the insulating layer and similarly gives rise to a local enhancement of the field. Such an effect would explain the observation of Fig. 4.2 that emission occurs at lower fields than is found with uncoated emitters. This model would also explain the linearity in the F-N plots for low fields. However, whilst attractive, it does not apparently provide an adequate explanation of the observed behaviour since the emitted electron energy distributions were not of a metallic type. In particular, the spectra exhibit a field (and current) dependent shift away from the F.L. towards lower energies, but with the shift not varying linearly with emitted current; thus suggesting evidence that the filament is not behaving metallically i.e. ohmically.

This filamentary model can however be used for estimating the channel dimensions, which from Fig. 5.2 has a height h $\simeq 0.2$ μ m, equivalent to the thickness of the insulator. An estimate of the channel diameter 2r can be made from the observation that the work function ϕ of the emitter has been effectively reduced by the insulator layer

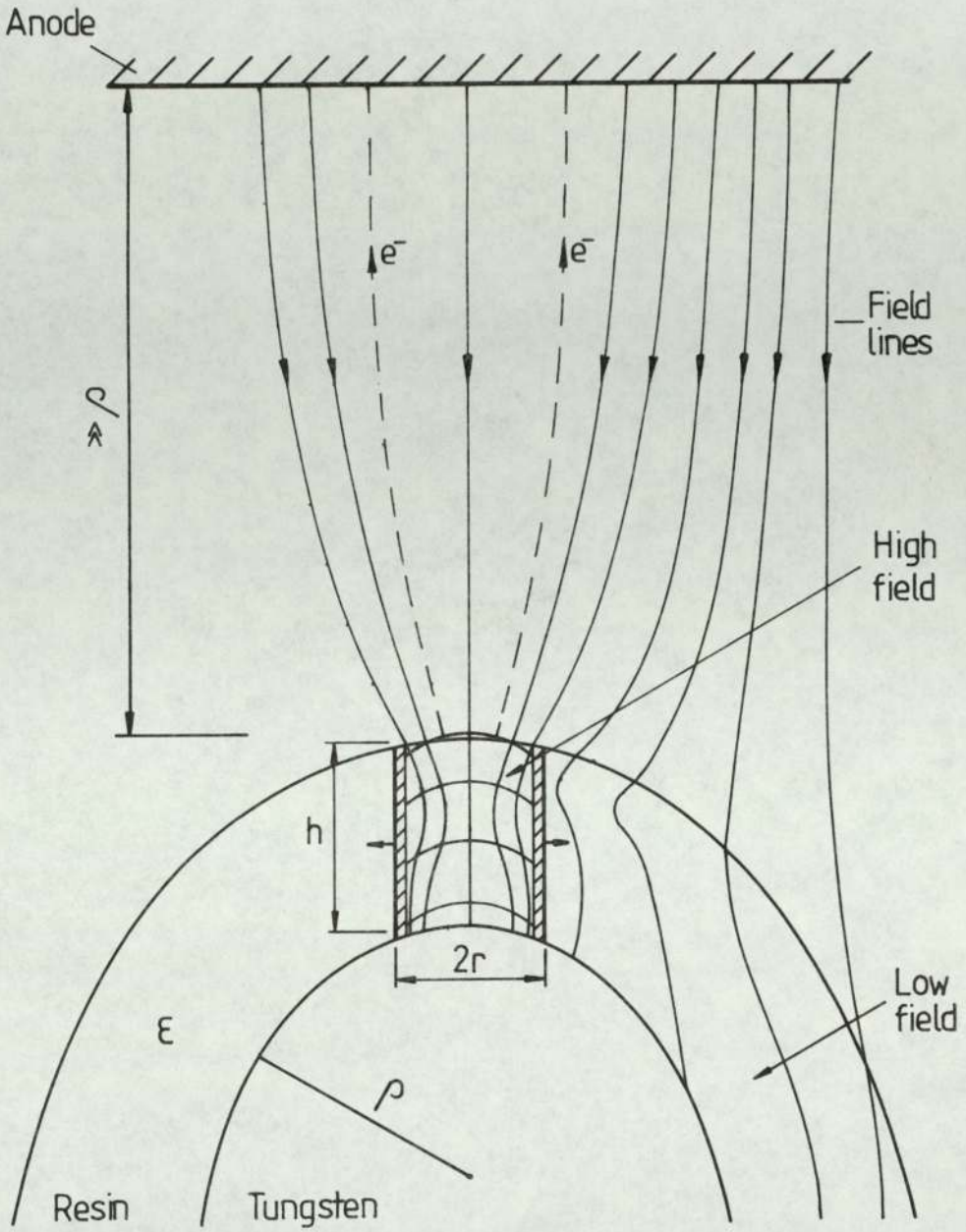

Fig. 5.2 A schematic illustration of how electron emission results from the formation of a conducting channel in the insulating layer. The associated electron field distribution is also shown.

from ~ 4.5 e V to ~ 1.8 e V (see Fig. 4.3). Thus, from equation 2.17 this reduction in ϕ could be interpreted as the result of a local field enhancement β by the emitter, where here β would have a value of ~ 2.5 . Hence, using the general relation [205]

$$\beta \simeq \frac{h}{r} + 2$$

one has

$$\frac{4.5}{1.8} \simeq \frac{h}{r} + 2$$

or

$$r \simeq 0.4 \, \mu \, m$$

so that the channel diameter $2r \simeq 0.8 \, \mu$ m. This value is in good agreement with those quoted for the channels formed in metal-insulator-metal switching devices, such as Cook [206] and Dearnaley et al [4].

Of the emission models which were analysed in section 2.4, the only one which appears to explain most of the observed characteristics of composite microemitters is the hot-electron mechanism proposed by Athwal and Latham [67]. This is similarly based upon the formation of a conducting channel in the dielectric layer and so can also be explained with reference to Fig. 5.2 . According to this model, when an external electric field of $> 10^8 - 10^9$ V m^{-1} is applied to a composite microemitter, the field will penetrate through the insulator down to the metal surface and create the possibility of electrons tunnelling from the metal into the insulator. If this occurs, the electron will be heated by the penetrating field and give rise to an avalanche process that results in the insulating medium locally switching to a conducting state, i.e. such as was originally identified by Ovchinsky for M I M devices [72]. The switching process is very fast, generally $\sim$ nanoseconds, although sometimes can be as long as microseconds at lower fields: also, the process is generally associated with the electro-forming of a filament or channel in the

insulating medium as illustrated in Fig. 5.2 . According to the later ideas of Adler et al [5] this forming process involves some form of local crystalisation with a consequent reduction in the interband trapping states. As will be discussed below, the cross-sectional dimensions of the "formed" channel depend on the insulating material and the current carried by the channel.

In contrast to the earlier model where the channel was treated as a simple metallic filament, the Athwal and Latham emission model [67] envisages the channel to have a very much more complicated electronic structure (see section 2.4.3). Thus following many of the concepts developed by Adler et al [5], it was assumed that electrons were emitted over the surface potential barrier of the insulator as a result of having been heated by the penetrating field in a narrow surface region. The strong field-dependence of the spectral shift and half-width can then be broadly explained in terms of increased electron-phonon scattering. Another important feature of this model is the concept that channels are "dynamic" structures, in that their cross-sectional dimension are determined firstly by the density of trapping centres and subsequently by the magnitude of the emission current. This property will be referred to again later when discussing the characteristics of emission images. In fact, as will be outlined in the following paragraphs, most of the properties of composite microemitters described in chapter 4 can be at least qualitatively explained in terms of this model.

The linearity of the F-N plots at low currents ($\lesssim 10^{-7}$ A) is thought to be attributable to the tunnelling process occuring in region 1 of Fig. 2.17 . This low-current region also has a small hysterisis effect associated with it (see Fig. 4.1), which is thought to result from relaxation effects associated with the changing

cross-section of the conducting channel. The non linear F-N plots which were observed at higher currents ($\gtrsim 10^{-7}$ A) were initially assumed to be due to a space charge limiting effect existing within the filament, similar to that found with thermionic emitters. However, more recently [207] the effect has been attributed to a change in the conduction characteristics of the insulator, as the current is increased. The step-like discontinuities in the I-V characteristics and deviations from the "typical" form can be attributed either to the thermal rupture and possible reforming of the filaments that are contributing to the total emission; or to the forming of new filaments when the field is progressively raised. This same process would result in the appearance of new emission spots on the screen. In particular, such images tend to be produced if the emitter is placed too close to the anode aperture ($\lesssim 5$ mm), or if the tip is surrounded by an anode as shown in Fig. 5.3 . A similar effect could arrise from the non-uniform surface field resulting from irregularities existing on the microemitter as illustrated in Fig. 5.4 .

The current stability of composite emitters is most probably due to the fact that the emission is controlled by the "protected" metal-insulator interface existing between the tungsten and resin, rather than by the dynamic distribution of surface states as in the case of conventional emitters. Also, it is known that the current density required in the threshold switching model is so high that it can cause disintegration of the solid; i.e. unless the material has a particularly stable character, as is the case for chalcogenide glasses where the valence electrons do not take any part in the bonding. Thus for the case of the composite emitter, which had an unchangeable profile before and after switching, it can be deduced that resin has

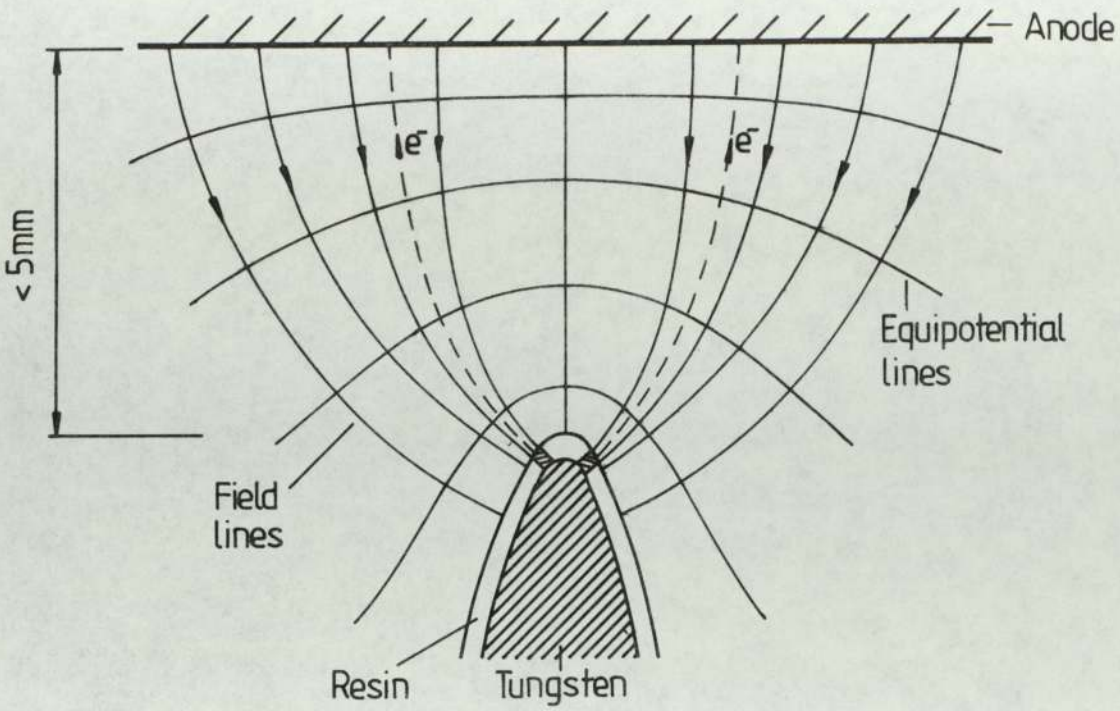

Fig. 5.3 A schematic illustration of how the divergent field associated with close proximity anode can lead to multi-spot images.

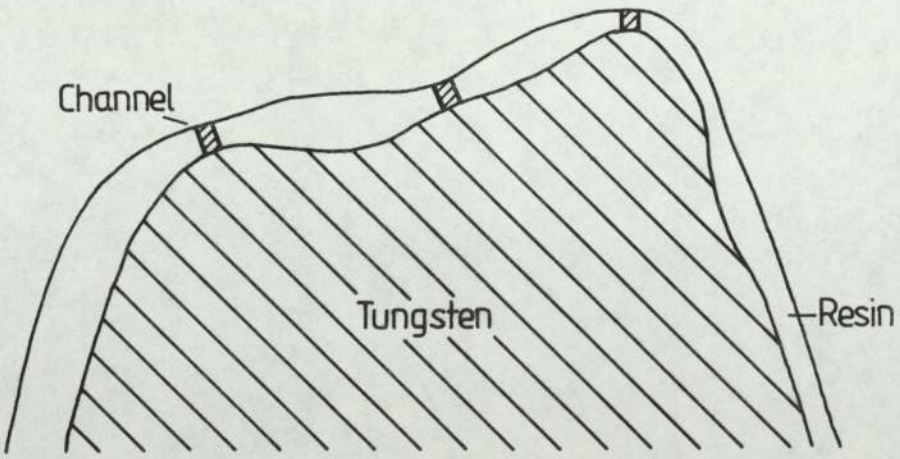

Fig. 5.4 Schematic illustration of how the irregularities of the substrate tungsten emitter could lead to a non-uniform surface film and formation of more than one channel.

stable properties similar to that of chalcogenide glasses. This is further supported by the stability of the single-spot emission image of the composite emitters.

The emission image size dependence, which was found to increase with both current and field, could be due to two possibilities. Firstly, it could be "physical" in origin and attributed to the suggestion of Ovchinsky [72] that in the ON-state the current density in the conducting channel might be constant, with the cross-section increasing with increasing current. Experimental evidence of that was provided by Henisch and Pryor [208, 209]., as well as by Peterson and Adler [210]. Mott [211] has shown that the dynamic space charge regime at the metal / insulator junction requires a constant current density. Therefore he postulated that for the current to increase the cross-sectional area will increase. Secondly, it could have a "subjective" explanation being associated with the variation over the image spot. The intensity of the image tends to decrease towards the edges making it difficult to define its exact size. This effect becomes more important at low currents and could have resulted in a fictitiously rapid fall-off of image size with emission current. This effect has been demonstrated by using long time exposures, where the image size can appear to increase by as much as $\sim 20\%$.

From the discussion of section 2.4.3, it will be recalled that the shift of the F.W.H.M. of the electron energy distribution from the Fermi level is seen to be the sum of three components of lost energy. Since each of these losses may be expected to increses with increasing current, total spectral shift should be strongly dependent on the applied field. Thus, if it is assumed that the hot-electrons escape over the work function barrier, the F.W.H.M. of the emitted

distribution will be predominantly due to phonon scattering of those electrons in region 3 of Fig. 2.17 . The fact that the initial value of the F.W.H.M. is only ~ 0.2 eV is not surprising, when it is appreciated that the electrons are emitted by two entirely different mechanisms. Thus for a clean tungsten emitter, the electrons leave the emitter surface at wide angles, whereas with coated emitters, the emission of electrons occurs through a small channel so that the energy spread of the electrons is likely to be less than that of clean W-emitters.

It is also evident that the composition of the insulator plays a vital role not only in the forming process [17], but also in the electronic processes. For example, the dielectric constant ε , which controls the field penetration is here assumed to have a value of ~ 4 for resin, but could vary by a factor of 2 from sample to sample. Another important parameter is the band gap: thus Simmons [212] noted that for insulators having energy gaps $\geqslant 3$ e V, the main concern is with the electron rather than the hole carriers, and gave two main reasons for this. Firstly, the hole mobility is usually much lower than the electron mobility and thus the hole contribution to the conductivity can usually, but not always, be neglected. Secondly, in practical insulating films, where the trapping density is high, the tendency is for free holes to be trapped quickly and thus become immobilised. However, Adler et al [5] pointed out that there are circumstances when the injection of holes plays an important role in the hot-electron emission process. It should be noted that both the initial formation and subsequent properties of a channel are strongly influenced by the density of donar or trapping states. For example, it is probably this parameter that is responsible for the differing threshold switching field observed with the present resin films and the chalcogenide glass films studied in M I M devices.

Lastly, the hyperbolic form of the curve of the switching field

versus the insulator thickness (presented in Fig. 4.4) has been explained as follows [207]: the emission from an electrode surface through an insulating layer cannot begin to occur until the field at the metal-insulator junction reaches a value at least high enough for electron tunnelling to take place. Thus the potential at the vacuum-insulator interface, due to the penetrating field plus the contact potential, must be sufficient to depress the conduction band edge below the metal F.L.. The contact voltage necessary to do this is $V_c \gtrsim \phi_I - \chi$, where ϕ_I is the work function and χ is the electron affinity of the insulator. In this case V_c will be equal to the electrostatic potential difference across the insulator due to the penetrating field, which is then given by $\frac{V}{Kr}\ \frac{d}{\varepsilon}$,

i.e. $V_c = \frac{V}{Kr}\ \frac{d}{\varepsilon}$

hence, $\frac{V}{Kr}\ \frac{d}{\varepsilon} \gtrsim \phi - \chi$

therefore,

$$\frac{V}{r} \gtrsim \frac{K \varepsilon (\phi_I - \chi)}{d}$$

which is of hyperbolic form .

CHAPTER 6

CONCLUSION

This final short chapter has two objectives: firstly, to present a brief statement outlining the principal conclusion of the investigation, and secondly, to indicate the direction that any future study should follow.

6.1 PRINCIPAL EXPERIMENTAL CONCLUSIONS.

The original concept of the project was to simulate, under controlled conditions, the metal-insulator microregime that is responsible for the field-induced electron emission currents that flow between broad-area high voltage electrodes at gap fields > 5 M V m^{-1}. For this purpose, a range of composite emitter structures were fabricated, all based on a micropoint geometry consisting of a conducting substrate overlayed by a sub-micron thick insulating medium. Of these, the most successful of these structures consisted of an electrolitically etched tungsten micropoint, such as is conventionally used in the field emission microscope (F.E.M.), which was then overlayed by a 0.04 - 0.2 μ m thick layer of epoxy resin. The emission characteristics of these composite microemitters were evaluated using a specially designed instrumental facility incorporating a F.E.M. and an electron spectrometer.

From an extensive series of measurements, it was concluded that there were both striking similarities and marked differences between characteristics of the purpose-fabricated emitters and the naturally occuring emission sites. Thus both processes exhibit an initial current switch-on phenomenon, and thereafter have a reversible low-field

current-voltage characteristic that gives a linear Fowler-Nordheim plot. Also, both emission processes have electron spectra that have a strong field-dependent shift towards low energies. However, in contrast to the natural process , the current delivered by the simulated emitters rapidly saturates with increasing field: a difference that is thought to indicate that the electronic properties of resin (e.g. the density of donor or trapping states) must be significantly different to those of the dielectric materials present on the surface of high voltage electrodes. A further difference between the two processes was that the emission image of the simulated emitters at current levels of $\sim 1\ \mu$ A generally consisted of a stable and bright single-spot, whereas the image of the natural process is multi-spot in character and unstable at comparable current levels. Here again though, the difference can be explained in terms of the electronic properties of the insulating material. By making a more appropriate choice of materials in a second generation of emitters, it could reasonably be hoped to eliminate many of these differences.

On the basis of the above experimental evidence, it was concluded that electrons are emitted from the simulated emitters by the same hot-electron emission mechanism that is thought to operate at naturally occuring sites. This model is based on the formation of a conducting channel in the insulating medium, i.e. similar to that occuring in M I M switching devices, where, from the experimental evidence, the typical cross-sectional dimensions of the channels in these simulated emitters is $\sim 0.8\ \mu$ m. This value is in good agreement with those quoted for the channels formed in metal-insulator-metal switching devices, which further supports the belief that the present simulated emitters are operating by the hot-electron mechanism.

Since it was also recognised that this new type of composite

emitter could be of technological importance, their performance has been evaluated in terms of the practical parameters conventionally used to characterise electron sources. Thus, whilst the source size is comparable with that of a normal uncoated tungsten micropoint field emitter, the source brightness can be over five times higher; i.e. a consequence of the electrons being emitted in a single cone of very small divergence. Equally important, the emission from these composite sources is extremely stable, even at pressures of $\sim 10^{-7}$ mbar; correspondingly they also have long life-times, without the need of intermittant reforming "flashing" procedures. However, to achieve this type of performance, it has been necessary to evolve procedures for accurately controlling the thickness of the insulating film, and to develop a range of "conditioning" pre-treatments, including low-temperature baking, voltage cycling, thermal relaxation and running the emitter at a constant current for an extended period.

6.2 FUTURE WORK.

It is suggested that a follow-up study should concentrate its attention in two parallel directions. Firstly, a broader investigation of the possible new materials, fabrication techniques and pre-treatments that could profitably be applied to composite emitters, and secondly, the development of more sophisticated analytical techniques for obtaining more detailed quantitative information about their physical properties. To illustrate these themes, some specific outline suggestions will now be given.

ALTERNATIVE COATINGS FOR W-MICROPOINTS.

The first type of material to be considered would be the chalcogenide glasses which are well known to exhibit stable and reproducible switching behaviour in M I M devices (5, 213). It is anticipated that the ability to achieve a controlled thickness of chalcogenide glass on a tungsten tip would lead to the production of a high performance microemitter, in particular, one requiring a lower switching field. The second set of promising materials are the glassy carbons, since it has already been demonstrated that W-micropoints coated with a layer of amorphous carbon, up to 0.15 μ m thickness gives composite emitters with good emission characteristics. In this context Hitachi (154) and Futamoto et al (164) and Yamamoto et al (162) discuss the use of glassy carbons as field emission tips, and also the use of monolayer coatings of high molecular mass hydrocarbons on tungsten (147, 148) and Ti (171). Another interesting material is zirconium oxide, since, as a conventional micropoint emitter, this material is known to give a source of high brightness and emission current; furthermore, there is at the moment much world wide interest in its development (115, 214). For similar reasons, it may also be profitable to consider the possibility of using a LaB_6 for coating.

INTERNALLY-CONDUCTING GLASS MICROEMITTERS.

This type of emitter has been shown to have particularly promising characteristics: e.g. a very high brightness (ten times that of clean W-microemitter), a high saturated emission current (up to 10 μ A), and a favourably low switching-on voltage ($\lesssim$ 500 Volts). At present however, it does have a short life-time, but this may be increased by improving the quality of the inner conducting coating.

This might be done by depositing a conducting film on the inner wall of the glass tube and then "pulling" the coated tubes to form glass microelectrodes with a conducting filament extending to the extremity of the tip. Such a film could be deposited, for example, by heating a gold wire that passes through the tube, or depositing Ag from a suitable electrolytic solution.

Factors such as saturation current, the relaxation process, image stability and structure, and the effect of baking may be studied for all these combinations of materials.

INFLUENCE OF EMITTER PRE-TREATMENT.

The processing of emitters, such as baking, running the emitter at constant current for a period of time, voltage cycling and the relaxation process, have been shown to have very important effects on the emission characteristics, particularly the stability. This therefore leads one to the belief that a further investigation of the influence of these processes, could well provide valuable information that would assist in the goal of manufacturing better electron sources.

INSTRUMENTAL AND ANALYTICAL IMPROVEMENTS.

To facilitate the practical evaluation of emitters, and to gain more insight into the fundamental microscopic processes associated with composite field emission sources, the following instrumental and analytical improvements are recommended for any future investigation.

(1) The establishment of a demountable electron optical bench for more readily investigating the performance of microemitters in practical imaging systems such as a cathode ray tube (215).

(2) The development of a technique for the in-situ study of emitters

in a T.E.M.. Here, one of the principal aims would be to investigate the possibility of seeing the formation of channels between the metal surface and the insulator vacuum interface.

(3) The application of various analytical techniques, such as an X-ray analysis, to help study properties of the insulator coating before and after switching.

(4) To accurately assess by means of a computer program, the effect of the insulator film coating on the field distribution in the vicinity of the tip.

(5) To improve the sensitivity of the spectrometer facility; eg. its electrometer detection system should be replaced by an electron-multiplier single electron counting system.

REFERENCES

1. Latham R. V., High Voltage Vacuum Insulation: The Physical Basis, Academic Press, London/Newyork, (1981).

2. Latham R. V., I E E E , Transactions On Electrical Insulation, E I - 18, 194 - 203, (1983).

3. Latham R. V., *Vacuum* , 32, 137 - 140 , (1982).

4. Dearnaley G., Stoneham A. M. and Morgan D. V., Rep. Progr. Phys., 33 , 1129 - 1191 , (1970).

5. Adler D., Henisch H. K. and Mott N., Rev. Mod. Phys., 50 , 2 , 209 - 220 , (1978).

6. Athwal C. S. and Latham R. V., J. Phys. D: Appl. Phys., 17 , 1029 - 1043 , (1984).

7. Latham R. V. and Wilson D. A., J. Phys. E: Sci. Instrum., 15 , 1083 - 1092 , (1982).

8. Crewe A. V., Sci. Amer., Vol. 224 , 4 , 26 - 35 , (1971).

9. Crewe A. V., Eggenberger D. N., Wall J. and Welter L. M., Rev. Sci. Inst., 39 , 576 - 583 , (1968).

10. Crewe A. V., Isacoon M. and Johnson D., Rev. Sci. Instrum., 40 , 241 - 246 , (1969).

11. Latham R. V. and Wilson D. A., J. Phys. D.: Appl. Phys., 16 , 455 - 463 , (1983).

12. Prohaska R. and Fisher A., Rev. Sci. Instrum., 53 , 1092 - 1093 , (1982).

13. Erichson G. F. and Mace P. N., Rev. Sci. Instrum., 54 , 586 - 590 , (1983).

14. Adachi H., Fugii K., Zaima S., Shibata Y., Oshima C., Otani S. and Ishizawa Y., Appl. Phys. Lett., 43 , 702 - 703 , (1983).

15. Spindt C. A., Holland C. E. and Stowell R. D., Appl. Surf. Sci., 16 , 268 - 276 , (1983).

16. Forman R., Applns. Surf. Sci., 16 , 277 - 291 , (1983).

17. Yankelevitch Yu. B., Vacuum, 30 , 3 , 97 - 107 , (1980).

18. Bell R. L., Negative Electron Affinity Devices, Clarendon Press, Oxford, (1973).

19. Solymar L. and Walsh D., Lectures On The Electrical Properties Of Materials, Oxford University Press, (1979).

20. Sommerfield A., Z. Physik, 47 , 1 - 32 , (1928).

21. Kittel C., Introduction To Solid State, John Willey and Sons, (1976).

22. Dekker A. J., Solid State Physics, Macmillan and Co. Ltd., (1969).

23. Frohlich H., Electronen Theorie Der Metalle, Springer, Berlin, 11, (1936).

24. Pointon A. J. and Elwell D., Physics For Electrical Engineers, William Clowes and Sons Ltd., (1970).

25. Murphy E. L. and Good R. H., Phys. Rev., 102, 6 , 1464 - 1473 (1956).

26. Fowler R. H. and Nordheim L. W., Proc. Roy. Soc., London, A119 , 173 - 181 , (1928).

27. Richardson O. W., The Emission Of Electricity From Hot Bodies, Longmans Green and Co., London, (1921).

28. Nordheim L. W., Proc. Roy. Soc., London, A121 , 626 - 639 , (1928).

29. MacColl L. A., Phys. Rev., 56 , 699 - 702 , (1939).

30. Schottky W., Phys. Z. 15 , 872 - 877 , (1914).

31. Seitz F., The Modern Theory Of Solids, Mc Graw - Hill (1940).

32. Sommerfield A. and Bethe H., Handbuch Der Physik, Berlin, 24 , N2 , 333 - 442 , (1933).

33. Guth E. and Mullin C. J., Phys. Rev. 61 , 339 - 349 , (1942).

34. Dolan W. W. and Dyke W. P., Phys. Rev. 95 , 2 , 327 - 332 , (1954).

35. Dyke W. P., Barbour J. P., Martin E. E. and Trolan J., Phys. Rev. 99 , 1192 - 1195 , (1955).

36. Dyke W. P., Field Emission, A Newly Practical Electron Source, I R E Trans. Mil. Electron. M I L - 4 , 38 - 45 , (1960).

37. Gomer R., Field Emission And Field Ionization, Oxford University Press, (1961).

38. Good R. H. and Muller E. W., Handbuck Der Physik, Berlin, 21 , 176 - 231 , (1956).

39. Van Oostrom A. G. J., Philips Research Reports Supplements, 1 , 1 - 102 , (1966).

40. Miller H. C., J. Franklin Inst, 289 , 347 - 351 , (1969).

41. Haefer R., Z. Physik , 116 , 604 - 622 (1940).

42. Dyke W. P., Trolan J. K., Dolan W. W. and Barnes G., J. Appl. Phys.,24 , 570 - 576 , (1953).

43. Dyke W. P., Trolan J. K., Martin E. E. and Barbour J. P., Phys. Rev.,91 , 1043 - 1054 , (1953).

44. Muller E. W., Z. Physik.,102 , 734 - 761 , (1936).

45. Muller E. W., Z. Physik.,120 . 261 - 269 , (1943).

46. Muller E. W. and Bahadur K., Phys. Rev.,102 , 624 - 631 , (1956).

47. Young R. D. and Muller E. W., Phys. Rev.,113 , 115 - 120 , (1959).

48. Young R. D., Phys. Rev.,113 , 110 - 114 , (1959).

49. Bennet G. A. G., Electricity And Modern Physics, Edward Arnold Ltd., (1970).

50. Stratton R., Proc. Roy. Soc. London,B 68 , 746 - 757 , (1955).

51. Stratton R., Phys. Rev.,125 , 67 - 82 , (1962).

52. Baskin L. M., Lvov O. I. and Fursey G. N., Phys. Stat. Sol., B 47 , 49 - 62 , (1971).

53. Stratton R., Phys. Rev.,135 , 794 - 805 , (1964).

54. Arthur J. R., Surface Science,2 , 389 - 395 , (1964).

55. Hughes O. H. and White P. M., Phys. Stat. Sol.,33 , 309 - 316 , (1969).

56. Salmon L. T. J. and Braun E., Phys. Stat. Sol.,A 16 , 527 - 532 , (1973).

57. Lewis B. F. and Fischer T. E., Surface Science,41 , 371 - 376 , (1974).

58. Modinos A., Surface Science,42 , 205 - 227 , (1974).

59. Handler P., J. Phys. Chem. Solids, 14 , 1 - 8 , (1960).

60. Shepherd W. B. and Peria W. T., Surface Science, 38 , 461 - 498 , (1973).

61. Sykes D. E. and Braun E., Phys. Stat. Sol., B 69 , 137 - 140 , (1975).

62. Rihon N., Surface Science, 70 , 92 - 100 , (1978).

63. Cox B. M., J. Phys. D: Appl. Phys., 8 , 2065 - 2073 (1975).

64. Hurley R. E. and Dooley P. J., J. Phys. D: Appl. Phys., 10 , L 195 - L 201 , (1977).

65. Allen N. K. and Latham R. V., J. Phys. D: Appl. Phys., 11 , L 55 - L 57 , (1978).

66. Allen N. K. and Latham R. V., Proc. 8th Int. Symp. On Discharges And Electrical Insulation In Vacuum, Albuquerque, B 3 , 1 - 13 , (1978).

67. Athwal C. S. and Latham R. V., Physica, 104 C, 189 - 195 , (1981).

68. Duke C. B. and Alferieff M. E., J. Chem. Phys., 923 - 937 , (1967).

69. Gadzuk J. W., Phys. Rev., B 1 , 2110 - 2129 , (1970).

70. Hurley R. E., J. Phys. D: Appl. Phys., 12 , 2229 - 2246 , (1979).

71. Hurley R. E. and Dooley P. J., J. Phys. D: Appl. Phys., 10 , L 195 - L 201 , (1977).

72. Ovshinsky S. R., Phys. Rev. Lett., 21 , 1450 - 1453 (1968).

73. Boer K. W. and Ovshinsky S. R., J. Appl. Phys., 41 , 2675 - 2681 , (1970).

74. Lee S. H., Appl. Phys. Lett., 21 , 544 - 546 , (1972).

75. Muller E. W., Z. Physik, 106 , 541 - 550 , (1937).

76. Pearson J. M., The Preparation Of Tungsten Field Emission Tips Using The Automatic Switch, Aston Univ. In Birmingham, (1976).

77. Simmons E. N., A Dictionary Of Metal Heat-Treatment, 127 , Frederick Muller Ltd., (1974).

78. Metallographic Technique For Aluminium Alloys, Table 3 , P 124, Dept. Of Metallurgy, Aston Univ. In Birmingham.

79. Mc Graw - Hill Encyclopedia Of Science And Technology, Vol 4 , P 606.

80. Clark Electromedical Instruments, Instructions For The Use Of Epoxylite Resin For Insulating Microelectrodes, England.

81. Frank J., Ion Tech. Ltd. British Patent Appl. No 44718/78 (1973).

82. Khorossany M. and Fitch R. K., Vacuum, 27 , 159, (1975).

83. Vanner K. C., Jackson N. F. and Rhodes S. J., Applications Of Polyimides In Microelectronics, "Resin And Chips", Phys. Bull., V 36 , (1984).

84. Gaubi H., Facultte Des Sciences De Tunis,"The Institution Of Electrical Engineering, Science, Education And Technology Division", Conference, (1983).

85. Scientific And Research Instruments Ltd., Puller For Glass Electrodes, Cat. No 2001 , England.

86. Kuyatt C. E. and Plummer E. W., Rev. Sci. Instrum, 43 , 108 - 111 , (1972).

87. Braun E., Forbes R. G., Pearson J., Pelmore J. M. and Latham R. V., J. Phys. E: Sci. Instrum., 11 , 222 - 228 , (1978).

88. Young P.L. and Gomer R., J. Chem. Phys., 61, 4955 - 4972 , (1974).

89. Kempin H.F., Klapper K. And Ertl G., Rev. Sci. Instrum., 49, 1285 - 1287 , (1978).

90. Dionne N.J. And Rhodin T.N., Phys. Rev.,B 14 , 322 - 340 , (1976).

91. Isacoon M. and Gomer R., Appl. Phys., 15 , 253 - 256 , (1978).

92. Henderson J. E. and Badgley R. E., Phys. Rev., 38 , 590 - 632 , (1931).

93. Henderson J. E. and Dahlstron R. K., Phys. Rev., 55 , 473 - 481 , (1939).

94. Barnes S. C. and Singer K. E., J. Phys. E., 10 , 7 , 737 - 740 , (1977).

95. Swanson L. W. and Crouser L. C., Phys. Rev., 163 , 622 - 641 , (1967).

96. Workowski C. J. and Czyzewski J. J., A 39 , 523 - 529 , (1971).

97. Workowski C. J. J. Phys. E: Sci. Instr., 13 , 67 , 1 - 22 , (1980).

98. Adachi H., Sase M., Zaima S. and Shibata Y., J. Phys., 14 , 769 - 778 , (1980).

99. Whitcutt R. D. B. and Blott B. H., Phys. Rev. Lett., 23 , 639 - 640 , (1969).

100. Plummer E. W. and Young R. D., Phys. Rev., B 1 2088 - 2109 , (1970).

101. Lea C. and Gomer R., J. Chem. Phys., 54 , 3349 - 3359 , (1971).

102. Allen N. K., Ph.D. Thesis, Aston Univ. In Birmingham, (1979).

103. Athwal C. S., Ph.D. Thesis, Aston Univ. In Birmingham (1981).

104. Wysocki J. K., Phys. Rev. B, 28 , 2 , 834 - 841 , (1983).

105. Coughlin R. F. and Driscoll F. F., Operational Amplifiers And Linear Integrated Circuits, Prentice - Hall Inc., (1977).

106. Ahmed H. and Spreadbury P. J., Electronics For Engineers, Cambridge Univ. Press, (1978).

107. Delaney C. F. G., Electronics For The Physicist, Penguin Books, (1971).

108. Jones M. H., A Practical Introduction To Electronic Circuits, Cambridge Univ. Press, (1977).

109. Bowman R., Ned. Tydshrift Voor Vacuumtechnick, 11 , 37 - 48 , (1973).

110. Russel A. M. and Torchia D. A., Rev. Sci. Requirements, 33 , 4 , 442 - 444 , (1962).

111. Pelmore J. M., Internal Report No 1 , Aston Univ. In Birmingham, (1975).

112. Dyke W. P. and Dolan W. W., Advan. Elect. & Elect Phys., 8 , 89 - 183 , (1956).

113. Dyke W. P. and Charbonnier F. M., 6th Nat. Conf. Electron Tube Techniques, 199 , (1963).

114. Swanson L. W. and Bell A. E., 32 , 193 - 309 , (1973).

115. Swanson L. W., J. Vacuum Sci. Technol., 12 , 6 , 1228 - 1233 , (1975).

116. Juttner B., Proc. Of The VI Int. Symp. On Discharges And Electrical Insulation In Vacuum, 101 - 106 , (1974).

117. Oshima C., Souda R., Aono M. and Ishizawa Y., Appl. Phys. Lett., 43 , 6 , 611 - 612 , (1983).

118. Davydova E. I., Karpenko A. D. and Shishkin V. A., Sov. Phys. Tech., 49 , 11 , 1307 - 1309 , (1979).

119. Swann D. J. and Smith K. C. A., Proc. Of The 6th Annual S.E.M. Symp., U.S.A., 41 - 48 , (1973).

120. Van Oostrom A., J. Appl. Phys., 33 , 10 , 2917 - 2922 , (1962).

121. Hibi T., J. Electron Microscopy, Japan, 3 , 15 , (1955).

122. Cosslett V. E. and Haine M. E., Proc. 3rd Int. Conf. Electron Microscopy, 639 , (1954).

123. Drechsler M., Cosslett V. E. and Nixon W. C., Proc. 4th Int. Conf. Electron Microscopy, Berlin, 13 - 20 (1958).

124. Everhart T. E., J. Appl. Phys., 38 , 4944 - 4957 , (1967).

125. Lauer R., Z. Naturforsch, 23 A, 1 , 100 - 108 , (1968).

126. Wisner J. C., Electronics Research Lab., Univ. Of California, Report No. E R L, 70 - 76 , (1970).

127. Muller E. W., Z. Phys., 108 , 668 - 680 , (1938).

128. Dobretsov L. N. and Gomoyunova M. V., Emission Electronics, Keter Press, (1966).

129. Drechsler M. and Henkel E., Z. Angew. Phys., 6 , 341 - 346 , (1954).

130. Wiesner J.C. and Everhart T. E., J. Appl. Phys., 44 , 2140 - 2148 , (1973).

131. Kern D., Ph.D. Thesis, Tubingen, Germany, (1978).

132. Kasper E., Advances In Optical And Electron Microscopy, 8 , 207 - 260 , Acad. Press, London, (1982).

133. Muller E. W., Z. Phys., 131 , 136 - 142 , (1951).

134. Muller E. W. and Tsong T. T., Field Ion Microscopy, Elsevier Inc. Newyork, (1969).

135. Butler J. W., Proc. 6th Int. Congr. Electron Microscopy, Kyoto 1 , 191 , (1966).

136. Munroe E., Proc 5th Europ. Congr. Electron Microscopy, Manchester, 22 , (1972).

137. Munroe E., "Image Processing And Computer-Aided Design In Electron Optics", (ed. P.W. Hawkes), 284 , Acad. Press, (1973).

138. Tonomura A., Jap. J. Appl. Phys., 12 , 7 , 1065 - 1069 , (1973).

139. Riddle G. H. N., J. Vac. Sci. & Technol., 15 , 857 - 860 , (1978).

140. Orloff J. and Swanson L. W., J. Appl. Phys., 50 , 2494 - 2501 , (1979).

141. Ranc S., Pitval M. and Fontaine G., Surface Sci., 57 , 667 - 678 , (1976).

142. Crewe A. V., Wall J. and Welter L. M., J. Appl. Phys., 39 , 576 - 583 , (1968).

143. Veneklasen L. H. and Siegel B. M., J. Appl. Phys., 43 , 1600 - 1604 , (1972).

144. Veneklasen L. H., Optik, 36 , 4 , 410 - 433 , (1972).

145. Sokol'skaya I. L. and Mileshkina M. V., Sov. Phys. Solid State, 6 , 1401 - 1410 , (1964).

146. Sukonnik M. S. and Shishkin V. A., Abstracts, 14th All-Union Conf. On Emission Electronics, FAN, Tashkent, (1970).

147. Saitou N. and Yamamoto S., Appl. Surface Sci. Netherlands, 5 , 4 , 374 - 387 , (1980).

148. Radon T., Acta Phys. Pol. A,Poland, A 58 , 4 , 377 - 382 , (1980).

149. Fursei G. N. and Shakirova S. A., Sov. Phys. Tech. Phys., 11 , 6 , 827 - 833 , (1966).

150. Shrednik V. N., Sov. Phys. Solid State, 3 , 6 , 1268 - 1279 , (1961).

151. Swanson L. W. and Crouser L. C., J. Appl. Phys., 40 , 4741 - 4749 , (1969).

152. Swanson L. W. and Martin N. A., J. Appl. Phys., 46 , 5 , 2029 - 2050 , (1975).

153. Bolin P. C. and Trump J. G., Proc. 3rd Int. Symp., 50 - 55 , (1968).

154. "Field Emission Cathode And Method Of Preparation Thereof, Patent Specification", Hitachi Ltd., Tokyo, Japan, (1978).

155. English T. H., "S.E.M.; System And Applications", Conf. Series No. 18 , The Institute Of Physics London And Bristol, 12 - 14 , (1973).

156. Baker F. S., Osborn A. R. and Williams J., Nature, 239 , 96 - 97 , (1972).

157. Baker F. S., Osborn A. R. and Williams J., J. Phys. D: Appl. Phys., 7 , 2105 - 2115 , (1974).

158. Lea C., J. Phys. D: Appl. Phys., 6 , 1105 - 1114 , (1973).

159. Braun E., Smith J. and Sykes D. E., Vacuum, 25 , 9/10 , 425 - 426 , (1975).

160. Prohaska R. and Fisher A., Rev. Sci. Instrum., 53 , 1092 - 1093 , (1982).

161. Erickson G. F. and Mace P. N., Rev. Sci. Instrum., 54 , 586 - 590 , (1983).

162. Yamamoto S., Hosoki S., Fukuhara S. and Futamoto M., 734 - 742 , (1979).

163. Hosoki S., Yamamoto S., Futamoto M. and Fukuhara S., Surface Sci., 86 , 723 - 733 , (1979).

164. Futamoto M., Hosoki S. and Kawabe U., Surface Sci., 718 - 722 , (1979).

165. Lafferty J. M., J. Appl. Phys., 22 , 299 - 309 , (1951).

166. Windsor E., Proc. 11th Annual Field Emission Symp., Cambridge, (1964).

167. Johnson R. W. and Daane A. H., J. Phys. Chem., 65 , 909 - 915 , (1961).

168. Samsonov G. V., Nespor V. S. and Khrenova L. M., Phys. Metals & Metallography, 8 , 137 - 144 , (1959).

169. Windsor E. E., Ing C. and M. I. E. E., Proc. IEE, 116 , 3 , 348 - 350 , (1969).

170. Mulvey T., J. De Physique, CC2 , 2 , 45 , C2-149 - C2-154, (1984).

171. Adachi H., Fujii K., Zaima S. and Shibata Y., Appl. Phys. Lett., 43 , 7 , 702 - 703 , (1983).

172. Ohno Y., Nakamura S. and Kuroda T., Surface Sci. 91 , 636 - 654 , (1980).

173. Nishida J., J. Appl. Phys., 38 , 5417 - 5419 , (1967).

174. Baker F. S., Nature, 225 , 539 - 540 , (1970).

175. Baker F. S., Osborn A. R. and Williams J., Explosives Res. Div. Est. MOD, Tech. Rep., 132 , (1973).

176. Elinson M. I. and Kudintseva G. A., Radio Engng. Electron. Phys., 7 , 1417 , (1962).

177. Elinson M. I. and Vasil'ev G. F., Radio Engng. Electron., 2 , 3 , 126 - 129 , (1957).

178. Elinson M. I., Gor'kov V. A. and Vasil'ev G. F., Radio Engng. Electron., 2 , 1 , 107 - 127 , (1957).

179. Spindt C. A., Brodie I., Humphrey L. and Westerberg E., J. Appl. Phys., 47 , 12 , 120 - 126 , (1974).

180. Stewart D. and Wilson P., Vacuum, 30 , 11/12 , 527 - 532 , (1979).

181. Shirokov E. G., Sov. Phys. Tech. Phys., 14 , 8 , 1134 - 1139 , (1970).

182. Howarth J. R., Surridge R. K. and Palmer I. C., Internal Report-English Electric Valve Co. Ltd, Chelmsford England.

183. James L. W. and Moll J. L., Phys. Rev., 183 , 740 - 753 , (1969).

184. Roynet H. and Mignolet J. C. P., Bull. De La Societe Roy. Des Sci. De Liege, 38 , No. 5 - 6, 274 - 279 , (1969).

185. Hibbert D.B. and Robertson A. J. B., Proc. R. Soc. London, A, 349 , 63 - 79 , (1976).

186. Hibbert D. B. and Robertson A. J. B., Int. J. Electronics, 48 , 4 , 301 - 303 , (1980).

187. Rodewald H. J., Microtecnic, 20 , 381 - 383 , (1966).

188. Dyke W. P., Scient. Amer.210 , 108 - 118 , (1964).

189. Olin T. and Carlsson C., Radiologe, 2 , 451 - 455 ,(1962).

190. Crewe A. V. and Wall J., J. Molec. Biol., 48 , 375 - 393 , (1970).

191. Fontana J. R. and Shaw H. J., Trans. Amer. Inst. Elec. Engrs., 81 , pt 1 , 43 - 48 , (1962).

192. Froome K. D., Nature, 192 , 895 - 960 , (1961).

193. Pushpavati P. J. and Van De Ziel A., IEEE Trans. Electron Div. ED , 14 , 280 , (1967).

194. Shoulders K. R., Adv. Computers ed F L Alt, 2 , 135 - 293 , Acad. Press, London, (1961).

195. Hansen W. W., Contract DA-36-039 Sl - 84526, Task No. 3A99-13-001-01, Signals Corpse. Res. Div. Labs. QPR Nos 1-4 (U.S. Army), Stanford Res. Inst. (1960).

196. Koyama M. and Kawai H., Rev. Sci. Instrum., 37 , 1159 - 1161 , (1966).

197. Spindt C. A., J. Appl. Phys., 39 , 3504 - 3505 , (1968).

198. Cline H. E., J. Appl. Phys., 41 , 76 - 81 , (1970).

199. "Magnetic Field Emission Gun", O P E A, Vincennes, France.

200. Troyon M. and Laberrigue A., J. Microsc. Spectrosc. Electron, 2 , 7 - 11 , (1977).

201. Borries B. V. and Ruska E., Z. Techn. Phys., 20 , 225 - 235 , (1939).

202. Dyke W. P. and Trolan J. K., Phys. Rev., 89 , 799 - 808 , (1953).

203. Van Der Mast K. D., J. Of Microscopy. 130 , 309 - 324 , (1983).

204. Wilson D., Ph.D. Thesis, Aston Univ. In Birmingham,(1981).

205. Vibrans G. E., Tech. Rep. 353 , Lincoln Lab., M I T (NTIS ESDTOR 64 - 327), (1964).

206. Cook E. L., J. Appl. Phys., 41 , 551 - 554 , (1970).

207. Bayliss K., Ph.D. Thesis, Aston Univ. In Birmingham, (1984).

208. Henisch H. K., Ovchinsky S. R. and Pryor R. W., Proc. Int. Cong. Thin Films, Cannes, (1970).

209. Pryor R. W. and Henisch H. K., Appl. Phys. Lett., 18 , 324 , (1971).

210. Peterson K. E. and Adler D., Appl. Phys. Lett., 25 , 211 - 213 , (1974)

211. Mott N. F., Phios. Mag., 32 , 159 - 171 , (1975).

212. Simmons J. G., J. Phys. D: Appl. Phys., 4 , 613 - 657 , (1971).

213. Peterson K. E. and Adler D., J. Appl. Phys., 47 , 256 - 263 , (1976).

214. Mulvey T., Private Communication.

215. Salim M. A., Ph.D Thesis, Aston Univ. In Birmingham, (1984).

ACKNOWLEDGEMENTS

I have the pleasure in acknowledging my sincere gratitude to my supervisor Dr. R. V. Latham for his encouragement and enthusiasm throughout the course of this work. I am indebted for his invaluable guidance and useful discussions.

My thanks are due to Dr. R. K. Fitch for his help and advice and to professor T. Mulvey for his helpful discussions.

Mr. T. Reynolds, Mr. R. Keen and Mr. H. Arrowsmith have given useful technical assistance, to them I am most grateful.

Finally I would like to thank Miss D. Lymer for converting my handwriting to the form presented in this thesis.

APPENDIX

A SUBSIDIARY PROJECT

A similar retarding potential analyser to that described in chapter 3.3 was also employed for making the first accurate measurements of the energy distribution of the positive ions emitted by a liquid gallium ion source. Full details of this study are given in the appendix paper. These results further demonstrate the potentiallities of this type of analyser.

J. Phys. D: Appl. Phys., **16** (1983) L209–L213. Printed in Great Britain

LETTER TO THE EDITOR

Beam-energy distribution measurements of liquid gallium field-ion sources

G L R Mair, D C Grindrod, M S Mousa and R V Latham
Department of Physics, University of Aston in Birmingham, Gosta Green, Birmingham, B4 7ET, UK

Received 18 July 1983

Abstract. Measurements are reported on the energy distribution of the ion beam produced by Ga liquid metal ion sources, for a range of emission currents, $i \sim 1$–$50\ \mu$A. The full width at half-maximum (FWHM). $\Delta E_{1/2}$, of the energy distribution curves varies from ~4.5–5 eV at ~1 μA to ~35 eV at 50 μA. Three regions can be detected in the $\Delta E_{1/2}$ versus i curve. In the first region, between ~0.6 and 2 μA, $\Delta E_{1/2}$ varies very slowly with current. In the second region, above ~2 μA and extending up to ~25 μA, the curve rises steeply with current, in fairly good agreement with the predicted $\Delta E_{1/2} \propto i^{2/3}$ relation. For $i \geqslant 25\ \mu$A the curve deviates markedly from this relation, and tends to flatten. Although a tentative explanation for the deviation from theory at high currents may be given in terms of gross instabilities of the anode, the deviation at very low currents (where $\Delta E_{1/2}$ is almost constant with i) is not understood.

Energy deficits of ~4.5 eV have been observed on average, and this value is consistent with mechanisms of surface field ionisation (e.g. field evaporation). Finally, no significant difference in energy spread was found for ion sources of markedly different i–V characteristics, suggesting that impedance to flow has no important effect on the value of the energy spread.

The measurement of the energy distribution of Ga^+ ions emitted from a Ga liquid metal ion source (LMIS) is not new, although not many systematic studies have been published to date (Swanson *et al* 1980). Nevertheless, in view of the importance of the value of the energy spread of the ion beam, with regard to vacuum technology (for example, ion beam lithography), further investigations are of value, especially if these investigations add to existing knowledge. The present work also aims at comparing the results with the theoretical predictions of Knauer (1981) who attributes the energy spread in LMIS to collisionless coulomb interactions in the beam. Finally, the results have been obtained with an analyser hitherto unused for ions (see below).

Two of the three 'needle' type (Clampitt and Jefferies 1978)† ion sources used in the present study were of very similar construction, and hence displayed very similar i–V characteristics and onset voltages; the third ion source, having a high flow impedance, produced relatively flat i–V curves. A wide range of measurements was taken over a period of about two months, with a view to testing the reproducibility of the results.

In the 'needle' configuration, the ion-emitting anode consists of a W needle

† The ion sources were supplied by Culham Laboratory (UKAEA).

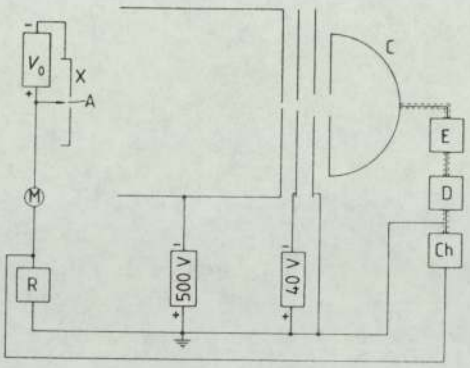

Figure 1. Schematic diagram of the system used for the energy analysis of the ion beam emitted from liquid Ga field-ion sources. V_0: extraction voltage; A: liquid Ga anode; X: extractor electrode; R: ramp generator; M: μA-meter; C: collector; E: electrometer; D: differentiator; Ch: chart recorder.

sharpened to a point (apex radius of order 1–10 μm) and covered by a liquid metal film. The lower half of the needle is immersed in a capillary reservoir filled with liquid metal, and thus liquid metal is continuously fed to the tip. On application of a high electric field between the tip and an apertured extraction electrode, the liquid film at the tip deforms into a cone (Taylor 1964) and emission commences (see e.g. Mair 1980).

The analyser used was of the van Oostroom type (van Oostrom 1966). This analyser has been extensively used for electrons, but here we have, for the first time, used it to obtain the energy distribution of an ion beam. Before introducing the ion source into the system, the analyser was tested using electron beams produced both thermionically and by field emission (the experimental resolution of the analyser is $\leqslant$30 meV for electrons). Details of the analyser can be found in the literature and, hence, here we shall only outline some of its fundamental features.

The van Oostrom analyser (figure 1) is a retarding field analyser, where the beam is analysed at the surface of a hemispherical collector kept at earth potential. The extractor

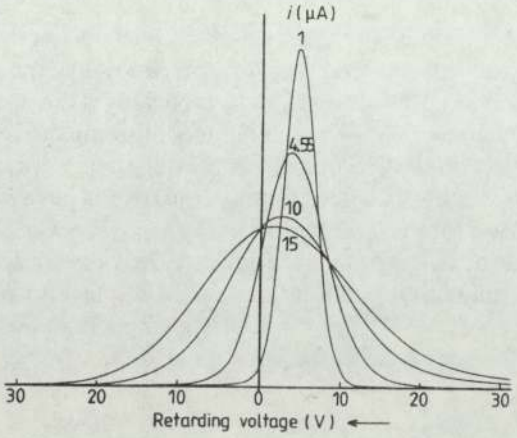

Figure 2. The energy distribution of the Ga^+ ion beam for different emission currents, $i(\mu A)$.

is kept at a high negative potential ($\gtrsim$5.5 kV) with respect to the anode which is in turn scanned with a negative-going ramp-voltage for recording the energy spectra. The retardation curves obtained were differentiated electronically to yield the energy distribution of the Ga ion beam, which, as established by many authors, consists essentially of Ga^+ ions (see e.g. Mair and von Engel 1979).

Figure 2 shows some typical energy distribution curves obtained with the system described above. At the lowest obtainable currents of ~1–2 μA, an energy deficit, ΔE, of ~4.6 eV was observed on average, with a few extreme values of ~4 eV and ~5 eV. These values are in good agreement with theoretical predictions (Swanson *et al* 1980) consistent with surface field ionisation (probably field evaporation) at the liquid anode; viz:

$$\Delta E = \Lambda + I - \varphi_c. \tag{1}$$

In equation (1), Λ is the heat of evaporation of Ga, I its ionisation potential, and φ_c the work-function of the retarder. Taking, therefore, $\Lambda = 2.808$ eV and $I = 6.0$ eV, for Ga, and with $\varphi_c \sim 4.5$ eV† for stainless steel (or Cr) (Kaye and Laby 1973), one has $\Delta E \sim 4.3$ eV.

Also seen in figure 2 is a tendency for the peak of the distribution to move toward higher energy (i.e. smaller energy deficit) values with increasing current (there is no substantial shift in the peak position between ~1–2 μA). In the case of collision dominated coulomb interactions in the beam, this shift has been shown by Zimmerman (1970) to be a consequence of the broadening of the energy distribution curve. It is not unnatural to imagine that a similar effect would take place in our case, where it is believed that the broadening is due to collisionless coulomb interactions (Knauer 1981).

Figure 3 shows a graph of the full width at half-maximum (FWHM), $\Delta E_{1/2}$, of the

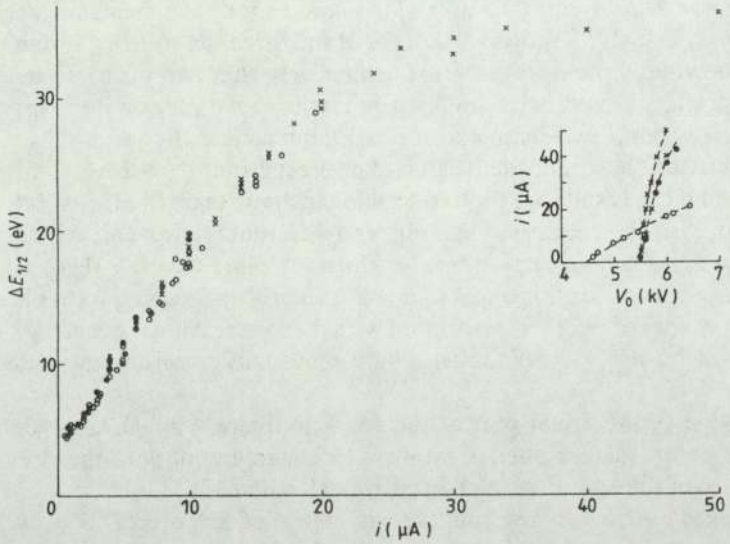

Figure 3. Graph of the full width at half-maximum, $\Delta E_{1/2}$, versus emission current, i, for the three Ga ion sources used (each symbol signifies a different ion source). Inset: Current–voltage characteristics of the three sources.

† Since Ga has a work-function of 4.45 eV (Kaye and Laby 1973) gradual coverage of the collector's surface with Ga will not affect this calculation significantly.

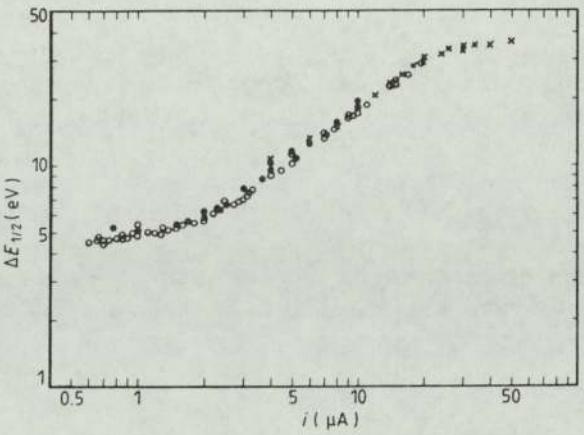

Figure 4. The results of figure 3 plotted on a log–log scale.

energy distribution, plotted as a function of the emission current, i‡. It can be seen that the curve rises steeply at first—following in fact fairly closely the predicted $\Delta E_{1/2} \propto i^{2/3}$ relation (Knauer 1981)—before it changes its slope, rather abruptly, at high currents. The change in slope occurs at ~25 μA, or so, and this may be significant, since it roughly corresponds to the emission level at which the current develops fast fluctuations (~30 μA) (Mair and von Engel 1979, Mair 1980). These fluctuations are thought to be due to gross ablation—and probably oscillation—of the field-elongated apex of the anode (Aitken 1976, Gaubi *et al* 1982). It is highly unlikely that a theory which assumes no path-crossing for the ions—as Knauer's theory does—should apply to an emission regime where the ion-emitting apex of the liquid anode is in mechanical turmoil.

The inset in figure 3 shows i–V curves of the three ion sources, obtained at the same time as the energy measurements. It can be seen that two of the sources display very similar electric characteristics, indicating that they have very similar impedances to flow.

At first sight only two distinct regions are detectable in the graph of figure 3. However, close inspection shows another region of interest around ~1–2 μA. This region is more clearly seen if the results are plotted on a logarithmic scale (figure 4). It is quite obvious that below 2 μA the energy spread follows a different relationship with current, namely it tends to approach an approximately constant value (as does the energy deficit; see above). The reason for this behaviour is not clearly understood, but it is unlikely that a minimum spread of ~5 eV is associated with the ion creation mechanism; in the absence of other effects, field-ion emission mechanisms usually entail energy spreads of a fraction of 1 eV.

The slope of the linear part of the curve in figure 4 is ~0.72, as determined by a least-squares fit; this number is within <10% agreement with the predicted $\frac{2}{3}$ power dependence of the energy spread on current (Knauer 1981).

Our measurements agree roughly with those of Swanson *et al* (1980), who report energy spreads of ~5–30 eV for emission currents of ~1–30 μA, although the values measured by these authors appear to be consistently somewhat lower than ours.

‡ In view of the fact that the extractor is charged to a high negative potential (≥5.5 kV), no secondary electrons can return to the anode from the ion-collecting surfaces and contribute to the emission current. Excluding, therefore, the small number of secondaries released by the extractor, which receives a small current (~1–2 μA) at the higher emission levels, the measured current, i, consists entirely of ions.

Finally, note that the ion source with the flat i–V characteristics in the inset of figure 3 displays the same energy spread as the other two sources with steep i–V curves. This suggests that, contrary to currently circulating ideas (Mair 1982, Wagner 1982), flow has no significant effect on the value of the energy spread—at least not up to ~20 μA.

Acknowledgments

This work was carried out under an SERC grant to Professor T Mulvey and Dr R G Forbes, to whom the authors are indebted for their continued interest and useful discussions. The authors wish to thank Culham Laboratory for kindly supplying the ion sources, and in particular Dr P D Prewett for many useful discussions. Thanks are also due to Mr A E Marriott-Reynolds for his excellent production of the drawings.

References

Aitken K L 1976 *Proc. Field Emission Day, Noordwijk (ESTEC)* pp 23–39
Clampitt R and Jefferies D K 1975 *J. Vac. Sci. Technol.* **12** 208
Gaubi H, Sudraud P, Tencé M and van de Walle J 1982 *Proc. 29th Field Emission Symp., Goteborg* (Stockholm: Almqvist and Wiksell)
Kaye G W C and Laby T H eds 1973 *Tables of Physical and Chemical Constants* 14th Edn (London: Longman)
Knauer W 1981 *Optik* **59** 335
Mair G L R 1980 *Nucl. Instrum. Methods* **172** 567
—— 1982 *J. Phys. D: Appl. Phys.* **15** 2523
Mair G L R and von Engel A 1979 *J. Appl. Phys.* **50** 5592
von Oostrom A G J 1966 *Philips Res. Rep.* Suppl. 1
Swanson L W, Schwind G A and Bell A E 1980 *J. Appl. Phys.* **51** 3453
Taylor G I 1964 *Proc. R. Soc.* A **280** 383
Wagner A 1982 *Appl. Phys. Lett.* **40** 441
Zimmermann B 1970 *Adv. Electron. Electron Phys.* **29** 251